UNIVERSITY OF SOUTHAMPTON

Faculty of Engineering and Physical Sciences
School of Electronics and Computer Science

A miniature 3D-printed Kibble balance for mass sensing applications

by

Emily F Edge

ORCiD: 0000-0003-4810-7598

A thesis for the degree of
Doctor of Philosophy

February 2026

University of Southampton

Abstract

Faculty of Engineering and Physical Sciences
School of Electronics and Computer Science

Doctor of Philosophy

A miniature 3D-printed Kibble balance for mass sensing applications

by Emily F Edge

Mass measurements are an essential part of every day life. Many transactions and tasks from paying a fair price for groceries to receiving a safe and effective dose of medicine rely upon accurate and traceable mass metrology. The redefinition of the International System of Units (SI) kilogram in terms of the Planck constant (h) in 2019 encouraged the implementation of directly traceable mass measurement at the point of need. One of the routes to traceable mass measurement is the Kibble balance principle which compares a mechanical force with an electromagnetic force. The updated mass definition presented an opportunity for improved measurement uncertainty at scales of less than a kilogram and also the introduction of traceable mass measurement at scales of less than a milligram. An analytical feasibility study of the electromagnetic Kibble principle suggested that it may be possible to achieve competitive mass measurement uncertainties at scales of 1 mg and extend the traceable range to 1 μg with an uncertainty of 0.5%. Three-dimensional (3D) printing is an emerging field in the development and fabrication of micro-electromechanical system (MEMS) devices. There are a number of benefits to 3D printing including the ability to rapidly produce prototype designs and the creation of fully 3D structures. The main aim of this work was to create a 3D printed prototype Kibble balance for masses between 1 g and 10 g with a measurement uncertainty of 0.25 % (at k=1) or less as a proof-of-concept device for miniaturisation to MEMS scale. Two options for generation of a 0.1 T radial magnetic field, anti-Helmholtz coils and opposing permanent magnets, were investigated through computer simulated models and laboratory experiment. The results showed that permanent magnetic material was a viable solution.

A “low cost” prototype system at the gram-level was designed based upon a single ring magnet with co-wound tare and bifilar main coils. Bespoke coils and 3D printed mechanical parts were manufactured and combined with commercially available components and National Physical Laboratory (NPL) produced hardware and software from the existing NPL Demonstration Kibble balance. This design was presented and published at the Joint International Measurement Confederation (IMEKO) TC3|TC5|TC16|TC22 Conference in 2022 [1]. The characteristics of the prototype system were measured and compared with the design estimates during the setup phase. Many of the key subsystems were calibrated individually to provide traceable measurements and estimates of uncertainty. The initial mass measurement performance of the prototype was determined using artifacts in the range 3.5 g to 6.0 g. The calculated uncertainty on the mass results was 0.2% (at $k = 1$). These results were compared with a traditional mass calibration of the artifacts performed at NPL to International Organization for Standardization (ISO) 17025 standard. This comparison revealed a +3.6% systematic error in the prototype system. Once identified, the source of this error can be eliminated to allow the device to be scaled to the micro-gram level within a target uncertainty of 0.5% (at k=1).

Contents

List of Figures

List of Tables

Acronyms

2D Two-dimensional

3D Three-dimensional

AC Alternating Current

ADC Analogue to Digital Converter

AFM Atomic Force Microscopy

AIP American Institute of Physics

BIPM International Bureau of Weights and Measures

C-Flex cross-flexure

CAD Computer Aided Design

CCM Consultative Committee for Mass and Related Quantities

CGPM Conférence Générale des Poids et Mesures

CIPM International Committee for Weights and Measures

CMCs Calibration and Measurement Capabilities

CotS commercial-off-the-shelf

csv comma-separated values

DC Direct Current

EFB Electostatic Force Balance

EMF electromotive force

FDM Fused Deposition Model

GCC GNU Compiler Collection

IC Integrated Circuit

IEEE Institute of Electrical and Electronics Engineers

IMEKO International Measurement Confederation

IOP Institute of Physics

IPK International Prototype Kilogram

ISO International Organization for Standardization

ITRI Industrial Technology Research Institute

JCGM Joint Committee for Guides in Metrology

JJA Josephson Junction Array

KC Key Comparison

KCRV Key Comparison Reference Value

KIBB-g1 Kibble Balance at the gram level version 1

KIBB-g2 Kibble Balance at the gram level version 2

KRISS Korea Research Institute of Standards and Science

LFB Low Force Balance

LNE Laboratoire national de métrologie et d'essais

MEMS micro-electromechanical system

MIKES Centre for Metrology

MJD Modified Julian Date

MPE maximum permissible error

MRA Mutual Recognition Arrangement

NdFeB neodymium-iron-boron

NIM National Institute of Metrology

NIST National Institute of Science and Technology

NMI National Metrology Institutes

NMIJ National Metrology Institute of Japan

NPL National Physical Laboratory

NRC National Research Council

OIML International Organisation of Legal Metrology

PB2 Planck Balance 2

PGI Post Graduate Institute

PLA polylactic acid

ppb parts-per-billion

ppm part-per-million

PRT Platinum Resistance Thermometer

PTB Physikalisch-Technische Bundesanstalt

PTFE polytetrafluoroethylene

PVA polyvinyl alcohol

QCM Quartz Crystal Microbalance

QCM-D Quartz Crystal Microbalance with Energy Dissipation

QHR Quantum Hall Resistance

RSS root-sum-square

RTC Real Time Computer

SET Sustainable Electronic Technology

SHM Simple Harmonic Motion

SI International System of Units

SmCo samarium–cobalt

SMOP Single Mode One Phase

SMTP Single Mode Two Phase

SPM Scanning Probe Microscopy

SRS Stanford Research Systems

TCR Temperature Coefficient of Resistance

TEOM Tapered Element Oscillating Microbalance

TMTP Two Mode Two Phase

UKAS United Kingdom Accreditation Service

VCA voice coil actuator

VoC Voice of Customer

XRCD X-Ray Crystal Density

Nomenclature

Symbols - Chapter 1

σ_{E1} Standard uncertainty of class E1 weights

k Confidence level

Symbols - Chapter 2

κ Sensitivity

ρ Density

a Acceleration

$A_r(^{28}\mathrm{Si})$ Relative atomic masses of silicon 28

a_{Si} Crystal lattice spacing

B Magnetic field

C Capacitance

C_f Sauerbrey sensitivity factor

D Change in energy dissipation

E Energy

F Force

f Frequency

g Local gravity

I Current

L Length

m Mass

$m(^{28}\mathrm{Si})$ Atomic mass of silicon 28

n Number of silicon atoms

P Power

Q Quality factor of the resonator

R Resistance

r Distance

T Torque

t Time

u Velocity

V Voltage

v Volume

w Weight

$A_r(e^-)$ Relative atomic masses of an electron

Subscripts - Chapter 2

a Air

b Buoyant

$diss$ Dissipation

$down$ Negative z-direction

off Off

on On

sph Sphere

$store$ Stored

up Positive z-direction

Symbols - Chapter 3

β Sensing coil mass scale factor

η Resistivity

γ Alignment factor

ρ Density

σ	Uncertainty
A	Coil profile area
A	Gain
a	Wire area
B	Magnetic field
d	Diameter
d	Wire diameter
g	Local gravity
H	Coil profile height
h	Maximum displacement
H_{mag}	Magnet height
I	Current
L	Length
m	Mass
N	Number of turns of the coil
n	Number of turns in sensing coil
P	Power
p	Coil packing factor
R	Resistance
r	Distance
r	Radius
S_{mag}	Magnet separation
s_{sph}	Sphere of air layer thickness
t	Time
u	Velocity
V	Voltage
W	Coil profile width

Subscripts - Chapter 3

AH	Anti-Helmholtz
c	Coil
Cu	Copper
HH	Helmholtz
M	Moving
m	Mass
mag	Magnet
max	Maximum
sph	Sphere
$target$	Target
W	Weighing

Symbols - Chapter 4

α	Phase alignment
β	The change in magnetic field
κ	Torsional spring constant
μ	Mass sensitivity
ρ	Density
θ	Angular deflection
A	Area
A	Gain
a	Acceleration
B	Magnetic field
B_0	Magnetic field of the permanent magnet
d	Depth
E	Young's Modulus
F	Force

f_z	Force in the z direction
g	Local gravity
h_c	Distance/Height of coil
I	Current
I	Second moment of area
i	Current
J	Torsional Coefficient
L	Length
l	Length
m	Mass
N	Number of turns
n	Number of clamps
n	Number of turns per unit height
p	Applied load
R	Resistance
r	Radius
s	Width of the balance arm slot
t	Time
u	Velocity
V	Voltage
w	Width

Subscripts - Chapter 4

1	Coil 1
2	Coil 2
b	Bearing
$coil$	Coil
Cu	Copper

external External (magnetic field)

M Moving

mc Main coil

mf Moving Frame

min Minimum

off Off

on On

s State (Moving or Weighing)

t Tare

tare Tare

tc Tare coil

W Weighing

Symbols - Chapter 5

α Temperature coefficient

κ Spring constant

σ Standard deviation

D Input division ratio

F Force

f Frequency

G Gain

g Local gravity

I Current

l_r Distance between the pivot point on the support frame

m Mass

N Number of data points

n Josephson Junction Array step number

n_{HP} Non-integer step number of the Josephson voltage according to the HP nanovoltmeter

R	Resistance
T	Temperature
u	Standard uncertainty
V	Voltage
z	Position on z axis

Subscripts - Chapter 5

$+$	Positive
$-$	Negative
$20°C$	Certified value at $20°C$
$3458A$	3458A Voltmeter
av	Average
$corr$	Corrected
$EB2H$	EB2 High Gain
$EB2L$	EB2 Low Gain
HP	Nanovoltmeter
ind	Indicated
J	Josephson
mf	Moving frame
o	Offset
PP	Peak to Peak
$step$	Step
T	Temperature
t	Tare
W	Weighing

Symbols - Chapter 6

ρ	Density
σ	Standard deviation

σ_{AB} Covariance of A and B

A Measurand

B Magnetic field

B Measurand

f Result

g Local gravity

I Current

L Length

m Mass

N Number of weighing phases

n Number of data points

t Time

u Velocity

V Voltage

v Volume

z Position on the z axis

Subscripts - Chapter 6

A Measurand

B Measurand

f Result

m Test mass

off Mass state off

on Mass state on

s Mass state

W Weighing

Physics constants

c Speed of light in a vacuum

e	Elementary charge
h	Planck constant
m_{e^-}	Mass of an electron
K_J	Josephson constant
N_A	Avogadro constant
R_K	von Klitzing constant
R_∞	Rydberg constant
α	Fine-structure constant
$\Delta\nu_{Cs}$	The unperturbed ground-state hyperfine transition frequency of the caesium-133 atom
μ_0	Permeability of free space
π	Pi

Units

A	Ampere
g	gram
l	litre
m	meter
N	Newton
T	Tesla
£	pound sterling

Prefixes

k	kilo
c	centi
m	milli
μ	micro
n	nano

Declaration of Authorship

I declare that this thesis and the work presented in it is my own and has been generated by me as the result of my own original research.

I confirm that:

1. This work was done wholly or mainly while in candidature for a research degree at this University;
2. Where any part of this thesis has previously been submitted for a degree or any other qualification at this University or any other institution, this has been clearly stated;
3. Where I have consulted the published work of others, this is always clearly attributed;
4. Where I have quoted from the work of others, the source is always given. With the exception of such quotations, this thesis is entirely my own work;
5. I have acknowledged all main sources of help;
6. Where the thesis is based on work done by myself jointly with others, I have made clear exactly what was done by others and what I have contributed myself;
7. Parts of this work have been published as: E. Webster, I. A. Robinson, H. Chong, and S. Davidson. Kibble balance for gram level mass measurements. *IMEKO Procedings TC-3*, Oct 2022
8. I was previously known as E. Webster (2014 to 2023).

Signed:..... Date:.....

Acknowledgements

There are many people who deserve recognition, from those who provided technical guidance and expertise to those who took an interest and cheered me on from the sidelines. And everyone in between! I faced many challenges over the last five years and I am truly grateful to each person for the unique part they played in supporting me. I hope to be able to thank everyone in person. It may take a while! Until then, a big and heartfelt thank you. Know that your time, knowledge, kindness, and understanding really made all the difference!

There are some key people and groups I will acknowledge here.

Thank you to my primary academic supervisor Harold Chong for his expert guidance and support throughout. My research skills developed significantly due to his enthusiasm, encouragement, and professionalism. Thank you also to my second academic supervisor Ruomeng Huang for his support. Thank you to the Sustainable Electronic Technology (SET) group for welcoming me and continuing to provide hybrid meeting options after the pandemic restrictions were eased. I appreciated being able to take part in group meetings even though I was based remotely.

Thank you to my industrial supervisor Ian Robinson for supporting me every step of the way. I benefited immeasurably due to his knowledge, experience, and generally being an all-round "good guy".

Thank you to the Mass Metrology group and the Materials and Mechanical Metrology department at National Physical Laboratory (NPL) for funding and facilitating this project, especially Bruce Duncan, Stuart Davidson, Rain Irshad, and Pete Theobald for their unwavering support. Thank you to the Presidential Scholarship Scheme at the University of Southampton for covering the cost of the university fees.

Thank you to the Post Graduate Institute (PGI) at NPL for their support. I enjoyed being a part of the community! Thank you to my PGI mentors Anna Subiel and Matt Cashmore whose sage advice, constant positivity, and limitless encouragement kept me going when things got tough.

Thank you to many colleagues at NPL without whom this project would not have been possible. Thank you to all past and current members of the Kibble balance team for the many hours of good company and fruitful conversation at Bushy House. Thank you to Chris Bull for his work on the Demonstration Kibble balance electronics, to Jack Berg for his work on the frequency counter, to Jean Morris for teaching me how to use the 3D printers, to James Berry for his assistance building and assembling the prototype, to Chris Pullen for helping to implement the mass lift, to David Szwer for his work on the data analysis software, to Charlie Jarvis for his advice on uncertainty budgets, to Stuart Davidson for his advice on mass metrology, to Nick Fletcher and Scott Wilkins for their assistance with the voltmeter calibration, to Peter Lovelock for generating Demonstration Kibble balance images, to Kevin Douglas for the loan of calibrated thermometers, to Perdi Potgieter for calibrating my marbles and assisting with magnet wrestling, and to Ian Robinson for his years of dedicated Kibble balance research upon which this project was built.

Thank you to my family and friends for being there for me always.

And finally, thank you to my partner Adam Swift for his love and infinite patience. There are no words that can sufficiently express my gratitude for everything he has done to support me in completing this thesis.

Note to self

My name's Em and I'm enough

Chapter 1

Introduction

1.1 Kibble Balance

A Kibble balance is an instrument that can realise the mass of an object directly from the International System of Units (SI) definition of the kilogram (kg). It was invented by Bryan P. Kibble at the National Physical Laboratory (NPL) in 1975 and was originally known as the "moving-coil watt balance" or "watt balance" for short [2]. Since then watt balances have been built by several National Metrology Institutes (NMI) and also at the International Bureau of Weights and Measures (BIPM) [3]. After Kibble's death in 2016 it was decided by the scientific community to adopt the name "Kibble balance" in his honour [4].

The NPL mark I watt balance was developed in the late 1970s for the purpose of realising the SI unit of current the ampere (A) to a higher level of precision and accuracy [5]. In the late 1980s this work led to international agreement of the conventional values of the Josephson constant (K_J) and the von Klitzing constant (R_K) used in the fields of precision voltage and resistance metrology respectively [6]. Later this balance was used to realise the SI watt and consequently determine the value of the Planck constant (h) [7].

The NPL mark II watt balance was built in the 1990s for the purpose of measuring the Planck constant. It was operated at NPL until 2009 when it was transferred to the National Research Council (NRC) in Canada [8]. In 2017 the NRC- NPL mark II Kibble balance contributed to the international effort to redefine the SI kilogram in terms of fundamental constants of nature including the Planck constant [9][10]. In November 2018 agreement was reached to fix the value of the Planck constant and adopt the new definition [11]. It came into use the following World Metrology Day on 20^{th} May 2019. This was a pivotal development in the field of mass metrology. With a fixed value of the Planck constant the Kibble balance technique allows the mass of any

object or substance to be measured with direct traceability to the SI definition anywhere in the world, at any time, and at any scale. The benefits include significantly shorter traceability chains, the elimination of calibrated mass standards, and the potential for reduced uncertainty at scales of less than 100 mg. To realise mass from the SI definition at small scales it will be necessary to create appropriately sized Kibble balance sensors.

1.2 Micro-electromechanical Systems

A micro-electromechanical system (MEMS) device consists of mechanical and electrical components constructed at the micron to millimeter scale. These devices are transducers that can change mechanical movement into an electrical signal or vice versa. MEMS are embedded into larger systems to fulfil a variety of functions such as pressure sensor, optical switch, accelerometer, or energy harvester. Traditional MEMS devices are created using micro fabrication techniques such as deposition of material layers on to a silicon substrate, photolithography, and wet and dry etching. These techniques are also utilised in Integrated Circuit (IC) chip fabrication, therefore the mechanical elements and associated electrical circuitry of a MEMS device can be constructed in the same process. Silicon is the preferred material for ICs. However MEMS can also be made from polymers, metals, and ceramics depending on the requirements for the application of the device. MEMS devices are low cost to produce in large volumes due to their physical size combined with well established batch production methods originating from IC fabrication [12] [13].

MEMS design can be limited by the prevalent fabrication methods. Firstly, the nature of the deposition, patterning, and etching techniques determines the types of structures that can be achieved. Usually MEMS are Two-dimensional (2D) or 2.5D at best. Complex Three-dimensional (3D) structures cannot be achieved. Secondly, traditional MEMS fabrication requires access to a clean room with expensive deposition and lithography equipment. This can slow the rate of prototyping and reduce opportunities for creating new designs.

By contrast, an emerging field in the development and fabrication of MEMS is 3D printing. There are a number of benefits to 3D printing MEMS devices including the ability to rapidly prototype designs and the creation of fully 3D structures. A range of techniques and methods have evolved over the past two decades such as Fused Deposition Model (FDM), stereolithography, and two-photon polymerisation that are capable of producing minimum feature sizes of around 200 μm, 50 μm, and $\leq$1 μm respectively [14]. Hybrid devices combining traditional MEMS with 3D printed parts were created initially. For example, silicon MEMS sensors embedded into 3D printed structures for gas sensing and fluid flow applications. More recently, complete MEMS

devices were created using modified or a combination of additive manufacturing techniques including MEMS switches that were 3D printed using two types of material, a conductive polylactic acid (PLA) and a water soluble polyvinyl alcohol (PVA) [14]. Other 3D printed electrical components such as resistors, capacitors, and inductors have been demonstrated. The component structure was manufactured using FDM techniques with channels or tubes printed in a sacrificial material. The electrical circuits were formed by injecting a "liquid metal paste" into the cavities created by the removal of the sacrificial material. These components were successfully used to demonstrate the implementation of a passive wireless sensor for detecting biochemical changes in milk kept at room temperature [15]. Differential capacitive sensing accelerometers are another example of 3D MEMS devices created through a combination of additive manufacturing and wet metalisation processes [16]. This work demonstrated that "fit-for-purpose" MEMS accelerometers could be created using these methods with the benefit of being individually customised. This flexibility is highly desirable for rapid prototyping of new sensors. If the technical limitations of 3D printing MEMS such as feature resolution can be overcome then it is likely that these methods will supersede the current MEMS fabrication methods.

A key milestone in the miniaturisation of Kibble balance technology to MEMS scale (sub-milligram level) is the creation of a 3D printed Kibble balance at the gram-level (1 g to 10 g). This proof-of-concept device will be used to inform the design of future micro-Kibble balances and act as a test bed for electronic and software subsystems that can be directly transferred.

1.3 Route to a 3D Printed MEMS Kibble Balance

The primary purpose of a 3D printed MEMS Kibble balance will be to function as a competitive alternative to existing micro-balances that are calibrated using transferable mass standards. The requirements of such a device include traceability to the SI, with a target relative uncertainty lower than can be achieved for International Organisation of Legal Metrology (OIML) class E1 weights calibrated by sub-division.

The level of traceable mass measurement uncertainty achievable by end users in some applications is currently limited by the uncertainty of the value assigned to the standard masses, commonly referred to as "weights", used in their process or methodology. The OIML recommends specifications for standard weights in document OIML R 111-1:2004. Weights are arranged into classes (E, F, and M) and the maximum uncertainty for each nominal mass is stated [17].

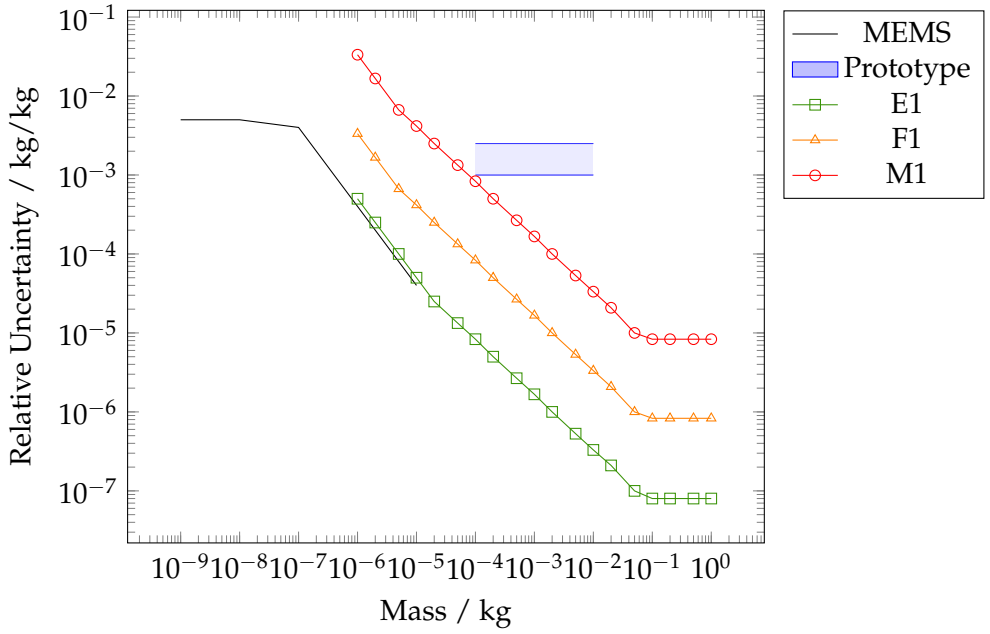

FIGURE 1.1: Target uncertainties for a future MEMS Kibble balance and a 3D printed prototype at the gram-level in comparison with the maximum permissible standard uncertainty ($k = 1$) of mass standards below 1 kg according to the OIML [17].

A typical end user at best only has access to class E1 weights with their associated uncertainties. For the majority of applications involving quantities of greater than 1 g this is acceptable as the level of uncertainty is less than or equal to 1.7 ppm (at $k = 1$). When working at sub-gram levels relative uncertainties increase sharply as shown in figure 1.1. This is the region of the mass scale where there are the biggest gains to be made in terms of reducing uncertainty. Figure 1.1 includes suggested target measurement uncertainties for a future 3D printed MEMS Kibble balance (black line) that aims to compete with traditional mass balances and a target measurement uncertainty for a proof-of-concept 3D printed prototype at the gram-level (blue shaded area). The MEMS targets were calculated in relation to OIML standard weight maximum permissible uncertainty also shown in figure 1.1. A total uncertainty of less than or equal to $0.8\,\sigma_{E1}$ between 10 mg and 100 μg and 0.5 % at less than 100 μg where traceable mass measurement is not currently available.

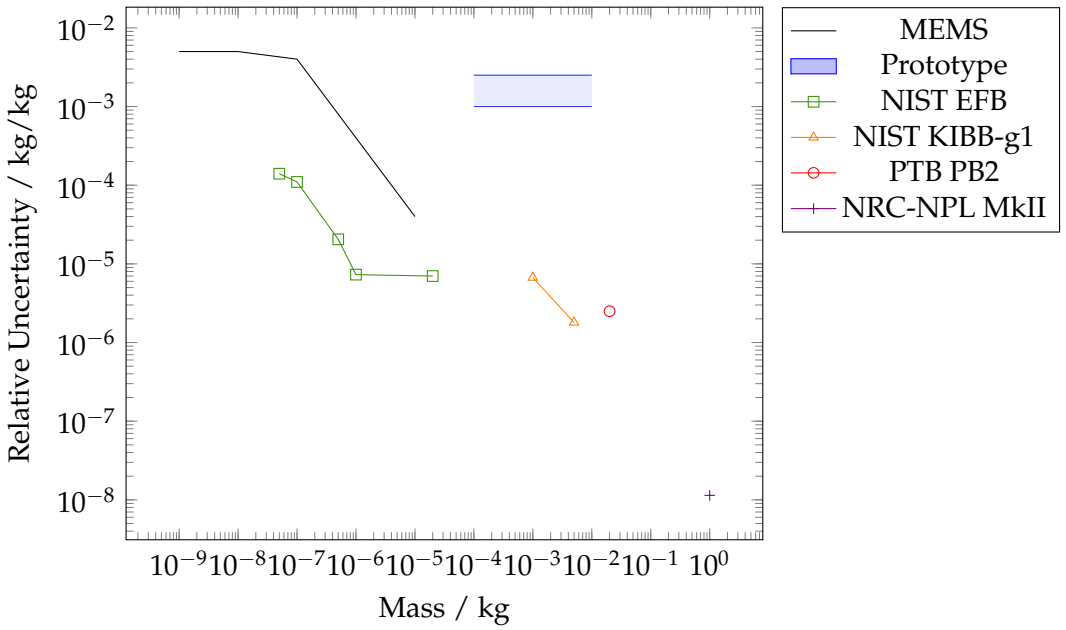

FIGURE 1.2: Target uncertainties for a future MEMS Kibble balance and a 3D printed prototype at the gram-level in comparison with examples of uncertainties (k=1) achieved by existing Kibble and electrostatic balances [3][18][19][20][21].

Figure 1.2 places the target uncertainties for a future MEMS Kibble balance and a gram-level 3D printed prototype in context with published mass measurement data from a selection of existing state-of-the-art Kibble and electrostatic balances. Each existing balance was designed to compete with mass standards in terms of measurement uncertainty at its respective operating mass range. The design details of each balance in figure 1.2 are presented and examined in chapter 2.

A 3D printed Kibble balance operating between 1 g and 10 g was not expected to compete with existing traditional electronic mass balances or state-of-the art Kibble balances in terms of measurement uncertainty due to limitations in affordable voltage measurement technology, low-cost 3D printing manufacturing, and operation in air. The primary focus of this device was to demonstrate the proof-of-principle as a stepping stone to a 3D printed MEMS Kibble balance at the milligram to microgram range.

The target standard uncertainty for the 3D printed prototype at the gram-level was selected to be between 0.1 % and 0.25 % ($k = 1$). If this measurement uncertainty could be achieved with a proof-of-concept device then it is likely that the 3D printed MEMS Kibble balance targets could be achieved upon further miniaturisation.

1.4 Motivation

Mass measurement affects all aspects of daily life. Everything from taxation on commodities, to safety on flights, to pricing of groceries in shops, to the dose of active ingredient in medicine, relies upon mass measurements made with appropriate accuracy and precision at a high level of confidence.

The redefinition of the SI kilogram in 2019 in terms of a fixed constant of nature, the Planck constant (h) [11], created the opportunity for improvement in the accuracy, precision, and confidence of mass measurement. In particular, measurements in the range from 10 mg downwards has the biggest prospect of improvement in uncertainty as a result of the new definition. Applications that involve measurements in this range occur across a variety of sectors such as pharmaceutical, environmental, commodities, and manufacturing.

1.5 Aim and Objectives

The aim of this work is to take a step towards enabling directly traceable mass measurements on the shop floor.

The primary objective is to produce and evaluate a low cost 3D printed Kibble balance for masses between 1 g and 10 g with a target standard uncertainty of 0.25% ($k = 1$) or less. This 3D printed balance is intended to act as a stepping-stone towards the development of a MEMS device capable of measuring mass at scales of less than or equal to 100 mg with a standard uncertainty of 0.5% ($k = 1$).

1.5.1 Current State-of-the-Art

Existing mass measurement technology and methodology is limited by virtue of being developed to utilise the previous artefact-based SI kilogram definition which had three major drawbacks.

Firstly, artefact-based definitions inherently limit the method of dissemination. In terms of mass, this means that calibrations typically involve physical mass standards (also known as “weights”) as the source of traceability. This method can occasionally create a barrier to traceability. If a sensor is not compatible with traditional standard weights, for example it can not accommodate a weight in terms of dimensions or other properties, then a secondary standard or method needs to be used. Either this method is not directly traceable to the SI or it introduces an extra step into the traceability chain. Additional steps in a traceability chains usually introduce additional relative uncertainty at each step.

Secondly, the best relative uncertainty on a mass measurement can only be achieved at one kilogram. By definition, the International Prototype Kilogram (IPK) always had a mass equal to exactly 1 kg with zero uncertainty. The method of determining the mass of any artefact, other than the IPK, was by direct comparison with an artefact of known mass. Hence a chain of mass comparisons, starting with the IPK, was formed in order to disseminate traceable mass values across the globe. The uncertainty incurred during a mass determination by comparison was minimised by ensuring that the mass of the two artefacts being compared were within a few milligrams and their volumes were within a few millilitres of each other. For artefacts of nominal mass not equal to 1 kg the method of comparison was adapted. Subdivision of the kilogram, specifically the method of assigning values to artefacts that have mass less than 1 kg, introduced increasing relative uncertainty with decreasing orders of magnitude by virtue of the nature of the iterative process. Typically, the relative uncertainty at 1 mg was at least five orders of magnitude higher than at 1 kg [17].

Thirdly, traceable measurement is not practical below 1 mg as the stability of standard artefacts is extremely poor at this scale due to issues of contamination and/or damage when in use. For example, the addition of dust particles has a much greater impact on the total mass than at the gram or kilogram level. Transfer mass standards at this scale are typically constructed from aluminium wire. The material properties and small physical size results in a delicate object that requires extremely careful handling to prevent loss of mass. In addition, the calibration history for standard artefacts at this scale is typically relatively short due to the ease at which they can be lost and hence were frequently replaced. The smallest commercially available standard masses are 50 μg [22].

Since May 2019, the definition of the SI kilogram has been based on a fundamental constant of nature, the Planck constant h, and does not imply or prescribe a method for realisation of the unit. Primary measurement (or realisation) of mass is no longer tied to a specific artefact at a single point on the scale. Any instrument that incorporates the fixed value of the Planck constant may be used. Therefore, SI mass can now be realised anywhere, at any time, and at any point on the mass scale. This presents a new opportunity to overcome the limitations of the artifact based definition discussed in this section.

1.5.2 Voice of Customer Survey

In 2018 a Voice of Customer (VoC) survey was carried out by the NPL. The aim of this activity was to identify current and future industry requirements for small mass and force measurement. Colleagues working in different scientific fields at NPL were consulted on existing applications for small mass and force measurement, gaps in the traceability chains, and the potential for a micro-Kibble balance to solve existing or

future measurement problems. This led to discussions and interviews with external contacts working in industry across a wide variety of sectors and applications.

It was found that the limiting factors and technical challenges of the pre-2019 SI kilogram definition (artefact basis discussed above) impact mass and force measurement capability in a number of applications. For example, there are many application specific sensors that are designed to make non-traceable relative mass measurements. These sensors allow small mass measurements to be made by difference at a reduced level of confidence. They generally rely upon non-traceable standards and/or the linearity of the sensor. Whilst these are practical and useful solutions for self-contained sets of measurements they have significant drawbacks in terms of verification and external comparison, specifically comparison of results that have been collected in different locations, at different times, or with different equipment cannot be made with confidence.

Jones [23] and Shaw [24] highlighted applications where the pre-2019 SI definition of the kilogram introduced limitations. Low concentration solutions are commonly produced by following a serial dilution method. Similar to sub-division of the kilogram, uncertainty is accumulated at each step of the method resulting in high relative uncertainty on the target solution. Many coating applications use differential measurement of mass to infer layer thickness during deposition or etching of materials. These are relative measurements and cannot be reliably compared with other relative measurements made elsewhere. Pipette calibration is carried out using small volumes of water and relies upon the linearity of a micro-balance in particular for volumes below 1 μl. Air quality monitoring methodology for particulate measurement employs differential weighing of filters. This is an example of a static measurement of a dynamic phenomenon which consequently limits the conclusions that can be drawn about the emissions that contributed to the result. Specifically, information about the rate of emission and/or time of day is not captured by these measurements. Micro-balances are used to measure the mass of micro diamonds during land surveys in the diamond mining industry. Typically, traditional micro-balances do not have enough resolution for this application and traceable mass standards do not exist in the micro-gram range. Atomic Force Microscopy (AFM), Scanning Probe Microscopy (SPM), and nano-indenter cantilevers require mass standards for traceable force calibration. However traceable mass standards in the lowest range ($<$1 μg) do not exist.

Table 1.1 summarises the findings of the VoC survey. To realise the potential of enhanced measurement capability in these applications new sensors and instruments that exploit the advantages of the 2019 SI kilogram definition need to be created.

TABLE 1.1: Summary of requirements for low scale mass metrology applications. Information drawn from voice of customer market research carried out by NPL.

Sector	Application	Mass/Force Scale	Challenge	Requirements
Pharmaceutical	Drug production	milligrams to grams	High throughput - 10s per second	Dynamic 'in-line' measurement. Regulatory type approval.
	Cell and gene therapy	micrograms to milligrams	High value powders. Low quantity batches. Continuous production methods.	High accuracy on very small quantities. Compatibility with powders. Regulatory type approval.
Environment	Air pollution - particulate monitoring	micrograms	Traceable real-time measurement. Many types of particulates - size and material.	Continuous measurement. Remote calibration. Compatibility with target particulate(s).
Commodities	Mining - diamonds, precious metals, rare earth elements.	micrograms	High value. Very small quantities.	High accuracy on very small quantities. Static measurements.
Manufacturing	Material testing - instrument calibration	nanonewtons	Calibration of Atomic Force Microscope (AFM) and indenter cantilever spring constant	Traceability to SI units. Very low scale forces

1.6 Thesis Layout

Selection of Approach

Chapter 2 comprises a literature review of the existing methods of mass realisation and measurement. The performance and features of state-of-the-art Kibble balance experiments and competing technologies across the mass scale are presented and evaluated. Examples of MEMS scale devices that include elements of Kibble balance devices are also included. The designs of these devices were used to inform and inspire the design of the 3D printed Kibble balance prototype in preparation for transfer to MEMS scale in the future.

Feasibility Study

Chapter 3 contains the details of an analytical feasibility study for an electromagnetic Kibble balance operating in the mass range 1 g to 10 g. A simplified model, simulations, and calculations based on assumed parameters are presented and evaluated against the aim of this work. The simulations were carried out in COMSOL Multiphysics® software. An assessment of suitability to scaling to MEMS scale was made.

3D Printed Prototype

Chapter 4 focuses on the design, analytical evaluation, and manufacture of a novel 3D printed Kibble balance at the gram-level. The prototype design was based upon the outcomes of the feasibility study, low cost 3D printed parts, off-the-shelf components, and NPL designed Kibble balance electronics and software subsystems. All 3D printed components were designed in SolidWorks Computer Aided Design (CAD) software and manufactured on FDM type 3D printers from PLA filament. Estimates of expected characteristics and performance of the prototype were calculated based on the mechanical and electromagnetic design and also the specification of the commercial-off-the-shelf (CotS) parts. Details of the manufacturing process, initial testing, troubleshooting, and design changes implemented to overcome issues are presented.

Prototype Calibration

Chapter 5 contains details of the verification of the 3D printed prototype characteristics against the design predictions presented in chapter 4. The results of individual subsystem calibration including estimated uncertainties are included.

Prototype Performance

In chapter 6 the results of mass measurements of five test pieces made using the 3D printed prototype are presented an analysed. The test pieces were glass marbles in the range 3.5 g to 6 g. Their masses were calculated from measurement sequences comprising weighing and moving data with both mass on and mass off. A detailed uncertainty budget was included.

Conclusions and Future Work

In chapter 7 the contents of this work are summarised. Conclusions are drawn on the measured performance of the 3D printed prototype against the target uncertainty stated in chapter 1. Recommendations of future work to optimise the performance of prototype are made and next steps for future work towards a 3D printed MEMS Kibble balance presented.

1.7 Novelty

The 3D printed Kibble balance presented in this work is unique in its combination of design features, low cost components, and principle of operation.

The mechanical design of the prototype balance was based on two symmetrical pivot arms containing four double-ended cross-flexure (C-Flex) bearings. The balance arms, support frame, and moving frame were all 3D printed from PLA plastic filament. This is the first example of the mechanical elements of a Kibble balance being reliant on the material properties and manufacturing quality of plastic 3D printed components in combination with double-ended C-Flex bearings.

The electromagnetic core of the balance was designed to be low cost and space efficient. The tare coil and bifilar main coil were co-located inside the same magnetic field. This reduced the number of magnets required and at the same time reduced the total volume of space occupied by the balance.

This prototype has made use of several subsystems that are part of the NPL Demonstration Kibble balance such as the linear encoder for position and velocity measurement, the magnet and magnet holder, the mass lift actuator for raising and lowering the mass under test, the electronics box (including voltmeter, current sources, coil switching, position sensing, frequency counter, mass lift) and the Real Time Computer (RTC) with its associated optical-fibre ring interface bus [25] and NPL Kibble balance software Nessus-2. Many of these components were designed and manufactured by NPL in small quantities for research purposes. When added to the cost of the CotS components used in the prototype the total cost was approximately £5000. This could be reduced if the prototype were to be manufactured at scale.

The prototype makes mass measurements by implementing a “single mode, two phase” methodology, specifically the bifilar main coil carries the weighing current in both the weighing and moving phases. This is the first Kibble balance to implement this methodology at the 1 g to 10 g range.

Chapter 2

Background

2.1 Mass Metrology

In physics "mass" is an abstract concept defined as an intrinsic property of a body. There are several physical theories that include the concept of mass spanning classical mechanics, relativity, and quantum mechanics. This has resulted in a few possible methods for measuring mass. However for centuries the underlying principle of mass metrology on planet Earth has been comparison of gravitational mass. The force exerted on an object (or substance) due to acceleration due to local gravity was compared to the force exerted on another "standard" object (or quantity of substance) of known or defined mass in the same gravitational field. Instruments such as the equal arm balance and force load cell were developed to enable these comparisons.

In Newtonian physics all bodies subject to acceleration a experience a force F that is proportional to their mass m.

$$F = ma \tag{2.1}$$

In the case of comparing the forces on two objects in air, if it can be assumed that they are made from material of the same density, then the difference in the force due to the acceleration of local gravity g is proportional to the difference in their masses.

$$F_1 - F_2 = (m_1 - m_2)g \tag{2.2}$$

The density ρ of a body is equal to its mass divided by its volume v.

$$\rho = \frac{m}{v} \tag{2.3}$$

If the objects being compared are made from materials of differing density, and hence have differing volumes, then air buoyancy effects need to be taken into account.

According to Archimedes principle buoyancy is a force that acts in opposition to gravity and is exerted on all bodies surrounded by a fluid. The buoyant force experienced by a body is proportional to the density of the fluid, the volume v of fluid displaced by the body and local gravity.

$$F_b = \rho_a v g \tag{2.4}$$

Where ρ_a is the air density at the time of the comparison.

This leads to the concept of "weight-in-air" which is frequently used interchangeably with mass in everyday life when high accuracy is unimportant.

$$w = F - F_b \tag{2.5}$$

$$w_a = (m - \rho_a v)g \tag{2.6}$$

For precision mass metrology it is necessary to correct measured weight-in-air for air buoyancy when comparing bodies of significantly differing volumes.

Throughout history humans have sought to improve mass measurement to meet the needs of society. Traditionally this has been achieved by implementing improved definitions based on artefacts with desirable characteristics. For example, artefacts that meet certain criteria such as universal availability (water), high consistency (carob seeds), and excellent stability with time (metal alloys) were successful candidates for achieving improved mass measurement.

2.2 SI Kilogram (1899 to 2019)

During the nineteenth century it became clear that a globally agreed system of units was needed to ensure fair trade between countries and regions. In 1875, seventeen nations signed the Convention du Mètre and founded the BIPM located on the outskirts of Paris [26].

2.2.1 Definition

At the first meeting of Conférence Générale des Poids et Mesures (CGPM) in 1889 a resolution was made to consider the object known as Le Grand K, or the IPK, as the definition of the unit of mass [27]:

> The kilogram is the unit of mass; it is equal to the mass of the international prototype of the kilogram.

(A) The IPK inside its three storage containers [28]. Image licensed by BIPM under CC BY 4.0.

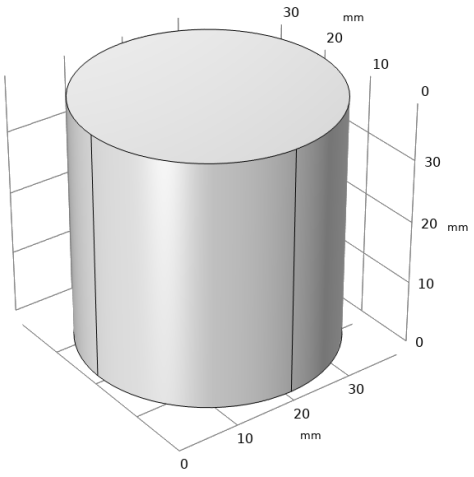

(B) Schematic diagram. The IPK is a cylinder of platinum iridium alloy (Pt:Ir, 90:10) with a diameter of 39 mm and height of 39 mm.

FIGURE 2.1: International Prototype Kilogram (IPK).

At the same time, 40 "national prototype" kilograms were sanctioned by the CGPM with the requirement that each copy should be as identical as possible to the IPK in terms of dimensions, material composition, and mass. At the time of manufacture, a mass within a few micrograms of the IPK was achievable for each copy. The national prototypes were allocated at random to the Member States of the Metre Convention and to the BIPM. This served two purposes, firstly to provide accessibility to the unit of mass on a global scale and secondly to prevent unnecessary wear, contamination, or damage to the IPK.

Since 1889, the national prototypes have returned to the BIPM on three occasions to be verified against the IPK directly. These measurement campaigns have shown that the masses of the national prototypes appear to be diverging from that of the IPK and each other. In the first verification (1946 to 1953) the standard deviation of the mass differences was found to be 25.8 μg and in the second verification (1989 to 1992) the standard deviation had increased to 153.1 μg. These results are shown in figure 2.2.

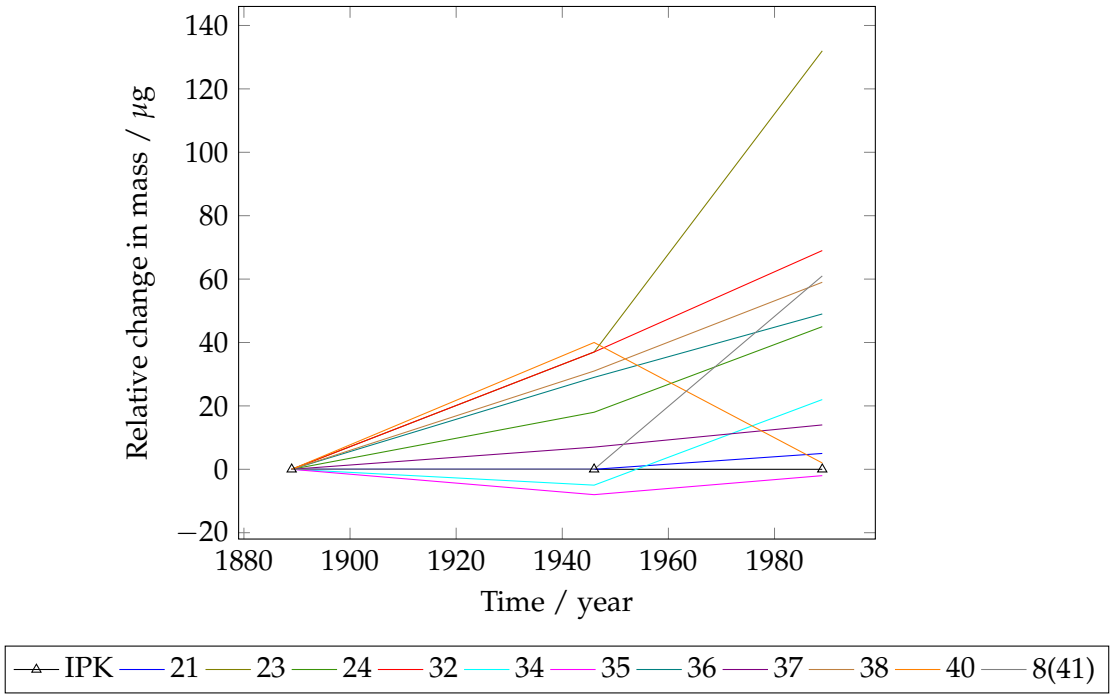

FIGURE 2.2: Change in 11 national prototype kilogram masses relative to the mass of the IPK from 1889 to 1989 denoted by their ID numbers. The initial 1889 starting value offsets relative to the IPK have been taken in to account. Reproduced from [29].

The majority of the national prototype kilograms appeared to be gaining mass relative to the IPK. However it was not possible to draw firm conclusions due the inherent problem of artefact based definitions, specifically the mass of the IPK itself could not be verified against an independent standard that was known to be stable.

The IPK could have been losing mass with respect to the national prototypes through a process of degradation (corrosion due to environmental conditions) or the national prototypes could have been gaining mass through contamination during use or storage. The mostly likely scenario was that a combination of processes, both degradation and contamination, were happening at different rates to all the artefacts simultaneously. However it was impossible to determine the exact causes of the observed effect. This conundrum coupled with the size of the drift in masses of the national prototypes (153 μg standard deviation in 1989, approximately 30 times larger than the typical assigned uncertainty at the time of 5 μg) highlighted the need for a new definition that guaranteed accuracy and stability over thousands of years.

2.2.2 Sub-division

When using an artefact based definition, the most accurate measurements of that quantity can only be made at the same nominal value as the artefact that forms the

definition. To make measurements at other scales a method of assigning values to objects at those scales is required. In the field of mass metrology, mass transfer standards (known as "weights") are used to calibrate mass measurement devices at a range of points on the scale.

The state of the art method by which all weights are calibrated with direct tracability to the kilogram is known as sub-division. A typical weight set contains nominal values in decades. There are six decades between 1 kg and 1 mg each comprising of four weights (nominal values 5, 2, 2 repeat, and 1). It is necessary to include a check weight at each decade and two 1 kg standards of known traceable value called "head weights". In total more than 110 comparisons of up to 38 weights are required to calibrate a 1 mg weight.

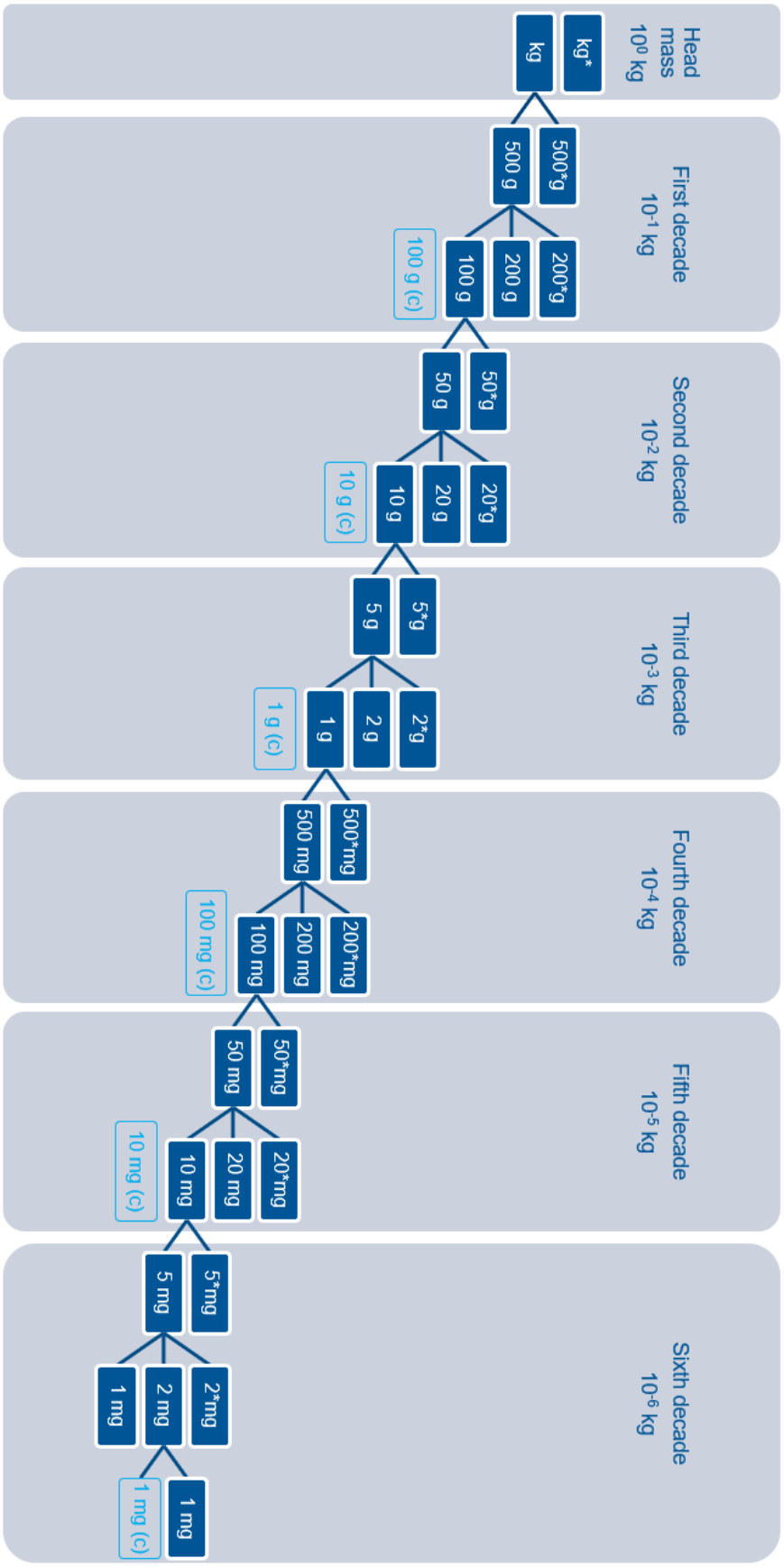

FIGURE 2.3: Diagram partially showing the comparisons required for sub-division of the kilogram. Repeat weights in each decade are denoted by an asterisk. Check weights are denoted by (c).

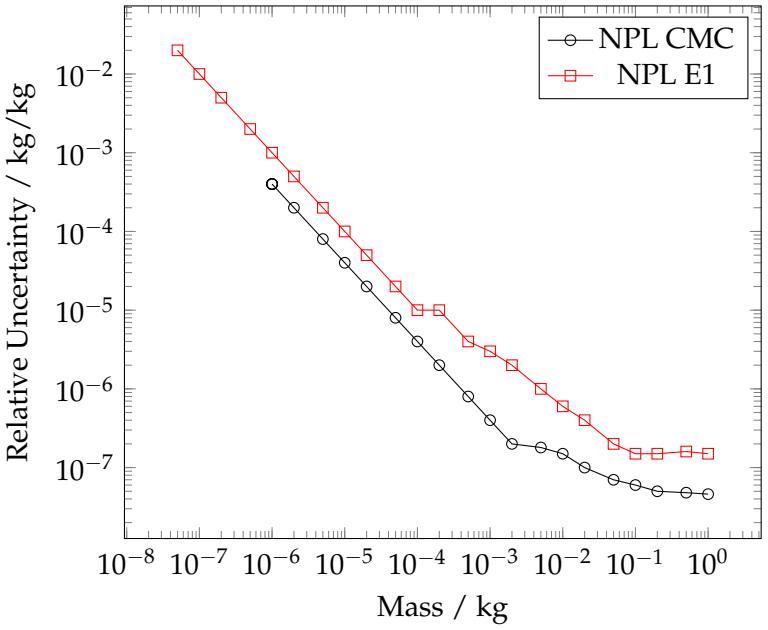

FIGURE 2.4: Relative uncertainty (k=2) of mass measurement below 1kg at NPL [30][31].

Figure 2.4 shows that sub-division introduces additional relative uncertainty at each step down the mass scale. NPL's best Calibration and Measurement Capabilities (CMCs) were peer-reviewed and approved under the International Committee for Weights and Measures (CIPM) Mutual Recognition Arrangement (MRA) framework. CMCs are the lowest achievable uncertainties for mass measurements by NMIs. NPL's capability for the calibration of E1 class weights is accredited to International Organization for Standardization (ISO) 17025 for Testing and Calibration Laboratories by the United Kingdom Accreditation Service (UKAS). Both of these capabilities are limited to objects of known properties, specifically mass standards complying to the OIML document R111-1 on the classification of weights [17].

Sub-division methodology is very labour and resource intensive. It requires up to three high quality mass comparators, several mass standard sets, and a skilled operator to achieve the lowest uncertainties. The purchase and maintenance of the required equipment is very costly particularly if you are only interested in smaller mass scales.

2.2.3 Dissemination

Outside of an NMI laboratory traceable mass measurements are made in direct comparison to calibrated weights or by using a balance that has itself been calibrated by weights of known value. This is relatively straight forward at moderate mass scales (1 g to 5 kg) as weights are typically made from stainless steel (density of 8000 kg/m^3) which means their volume is such that it is convenient for manipulation by a user.

When working at small mass scales (<1 g) there are a few factors to be taken into consideration.

The majority of sub gram weights are difficult to handle. Small tweezers with soft ends and an operator with a steady hand are required to move them in and out of storage containers or on and off a balance. This is particularly challenging for micro gram weights that are prone to moving in drafts and are difficult to grip gently with tweezers [32]. Therefore these mass standards are not convenient for use anywhere other than stable laboratory environments.

It is difficult to manufacture microgram weights of conventional nominal values, for example 50 μg, 20 μg, and 10 μg. Typically, sub-gram weights are made from thin aluminum wire bent into simple shapes convenient for handling and identification. Adjusting the mass of these standards is a task that requires skill, caution, and patience as it is very easy to remove more material than intended. Large deviations from the nominal mass value increases the uncertainty of measurement as balance linearity has to be taken into account.

The calibrated value of milligram and microgram mass standards tends to be unstable over time. This is due to the handing issues highlighted above causing damage and also contamination from dust and dirt. Cleaning these mass standards is not recommended as brushing or air cleaning could lead to damage or even loss [32] [33].

Taking the above factors into consideration and the high relative uncertainty accumulated during the sub-division process it is not possible to traceably calibrate standards below 50 μg using this method.

2.3 SI Kilogram (2019 to Present)

2.3.1 Definition

The 26$^{\text{th}}$ meeting of the CGPM held in November 2018 resolved to adopt a new definition of the SI kilogram based on a fixed value of the Planck constant h and on the existing definitions of the metre and the second [34]. This change was a monumental shift from the traditional paradigm of mass metrology. For the first time in history SI traceable mass measurements are no longer reliant on the properties of a physical artefact.

> The kilogram, symbol kg, is the SI unit of mass. It is defined by taking the fixed numerical value of the Planck constant h to be $6.626\,070\,15 \times 10^{-34}$ when expressed in the unit J s, which is equal to kg m^2 s^{-1}, where the metre and the second are defined in terms of c and $\Delta\nu_{Cs}$.

Where c is the speed of light in a vacuum and $\Delta\nu_{Cs}$ is the unperturbed ground-state hyperfine transition frequency of the caesium-133 atom. This definition is extremely powerful as it allows NMIs and other laboratories to realise the unit of mass independently. It also guarantees the stability of the unit over time as the fundamental constants underpinning the definition have fixed values.

Another important principle of the updated definition is that it allows for directly traceable mass measurement at any point on the mass scale, not just at 1 kilogram as was the case with the IPK definition. Any experiment or instrument that makes use of the fundamental constants included in the definition (h, c, $\Delta\nu_{Cs}$) can be used to realise mass. The scale at which this occurs is not prescribed or implied. This provides a new opportunity for traceable measurement of mass at small scales. The previous limit at around 50 μg was caused by the practicalities of producing, calibrating, using, and maintaining microgram transferable mass standards. If mass can be realised directly at the scale required then sub-division will not form part of the traceability chain and hence the effect of relative uncertainty inflation due to this process will not occur.

There are currently two routes to realising mass from the new SI definition at the 1 kg level with high accuracy: a Kibble Balance and X-Ray Crystal Density (XRCD) of a single-crystal silicon 28 sphere.

2.3.2 X-Ray Crystal Density Method

The XRCD method requires an artefact with specific properties in order to realise mass, typically a sphere of exceptional roundness and low surface roughness manufactured from high purity single-crystal silicon 28 is used.

$$m_{sph} = n\, m(^{28}\mathrm{Si}) \tag{2.7}$$

The basic principle is that the mass of a sphere m_{sph} can be determined by counting the number of silicon 28 atoms n inside volume v_{sph} and multiplying by the atomic mass $m(^{28}\mathrm{Si})$.

$$n = \frac{8 v_{sph}}{a_{Si}^3} \tag{2.8}$$

where a_{Si} is the lattice spacing between silicon 28 atoms.

$$m(^{28}\mathrm{Si}) = 2\frac{R_\infty h}{\alpha^2 c}\frac{A_r(^{28}\mathrm{Si})}{A_r(e^-)} \tag{2.9}$$

where R_∞ is the Rydberg constant, α is the fine-structure constant, h is the Planck constant, c is speed of light in vacuum, and $A_r(^{28}\mathrm{Si})$ and $A_r(e^-)$ are the relative atomic masses of silicon 28 and an electron respectively.

This method assumes that the volume of the sphere and the lattice spacing can both be measured very accurately and that the silicon crystal only contains the isotope silicon 28 arranged in a perfect diamond cubic lattice. In reality these conditions are not achievable and several corrections need to be applied. Silicon is highly reactive with oxygen and a silicon dioxide layer forms on the surface of the sphere. The mass of the surface layers can be determined by measuring their thickness and making some assumptions about the arrangement of the silicon dioxide molecules and the isotopes of oxygen present. The surface layer thickness is also used to adjust the measured diameter of the sphere to obtain the volume of the core of the sphere. The single-crystal lattice structure may not be perfectly populated and therefore have some "holes" where there are missing atoms. An assumed mass of missing silicon atoms is subtracted to account for this. The sphere is unlikely to contain only silicon 28 isotopes and therefore a correction needs to be made for the purity of the material. The average relative atomic mass is calculated and multiplied by the number of silicon atoms in the core of the sphere.

The XRCD method can only be applied to artefacts that meet strict criteria in terms of material properties and dimensions and therefore it can only be used to create primary artefacts against which other masses and objects need to be compared in order to determine their mass. This creates a barrier to fulfilling one of the aims of this work, specifically the capability to directly measure the mass of quantities of interest with traceability at the point of use. As the majority of mass measurements carried out worldwide concern objects or materials that do not meet the criteria for the XRCD method it was not considered further in this work.

2.3.3 Kibble Balance Principle

The primary principle of the Kibble balance technique is that it consists of two parts, a force comparison known as the "weighing phase" and an instrument characterisation known as the "moving phase" [7].

The models for two implementations will be detailed in this section, i) electromagnetic and ii) electrostatic approach.

Electromagnetic Approach

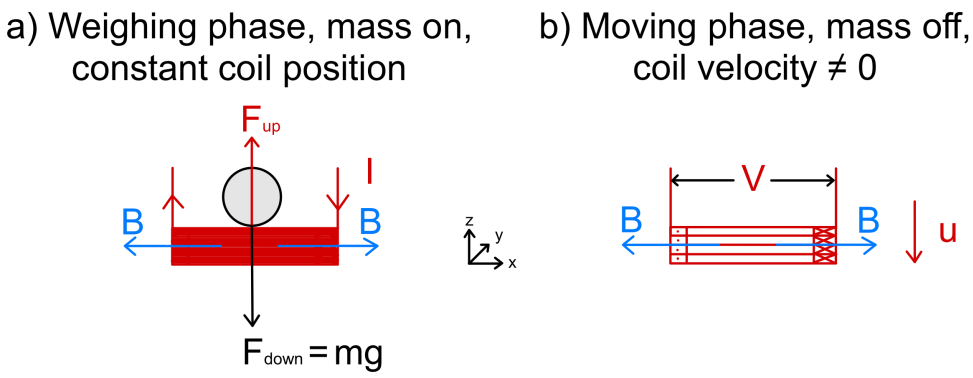

FIGURE 2.5: Schematic line diagram of the Kibble Balance Principle. a) Weighing phase: The mass under test (black sphere) is supported by a current carrying coil of wire (red lines) in a radial magnetic field (blue arrows). The coil is restricted to motion along the z-axis only and is maintained at a constant position during the weighing phase measurements. b) Moving phase: A voltage is induced in the coil of wire by moving it through the radial magnetic field along the z-axis at a constant speed u.

Part one, the weighing phase, is a comparison of forces as shown in part a) of figure 2.5. A mechanical force (F_{down}), specifically local gravity g acting on an object of mass m, is compared with an electromagnetically generated force (F_{up}). Typically the electromagnetic force is generated by a coil of length L carrying a current I in a magnetic field B [7].

$$F_{down} = mg \tag{2.10}$$
$$F_{up} = BLI \tag{2.11}$$
$$mg = BLI \tag{2.12}$$
$$m = \frac{BLI}{g} \tag{2.13}$$

Part two, the moving phase, is a characterisation step. As shown in part b) of figure 2.5, the coil used to generate the electromagnetic force in part one is driven through the magnetic field at a known velocity u in order to induce a voltage V. This allows the product BL to be determined without measuring the magnetic field and the length of wire in the coil independently by external methods.

$$V = BLu \tag{2.14}$$
$$BL = \frac{V}{u} \tag{2.15}$$

By combining the two parts of the experiment, equation 2.13 and 2.15, the mass of the object can be determined.

$$m = \frac{VI}{gu} \tag{2.16}$$

The BL product is the most influential characteristic of the Kibble balance device despite not appearing in the final equation for mass (2.16). The BL is a measure of the sensitivity of the device. Optimising this quantity is key to optimising measurement uncertainty as the device geometry and the magnitudes of V, I, and u are directly affected by it.

Traceability to SI

For the measurement of weighing current I and moving voltage V, traceability to the SI definition of the kilogram is established through quantum electrical standards (based on the Josephson effect and the quantum Hall effect) and Ohm's law [8]:

Josephson effect

$$V \propto \frac{h}{2e}\Delta\nu_{Cs}$$

Quantum Hall effect

$$R \propto \frac{h}{e^2}$$

Ohm's law

$$I = \frac{V}{R}$$

where h is the Planck constant, e is the elementary charge, and R is resistance.

For the measurement of local gravity and speed of the coil during moving, traceability to the SI kilogram is established through links to the SI units of time and length [34].

Gravity

$$g \propto c\Delta\nu_{Cs}$$

Velocity

$$u \propto c$$

Substituting these relations into equation 2.16 it can be shown that the Kibble balance experiment meets the requirement for direct realisation of SI mass:

$$m \propto \frac{\frac{h}{2e}\Delta\nu_{Cs} \cdot \frac{h}{2e}\Delta\nu_{Cs} \cdot \frac{e^2}{h}}{c\Delta\nu_{Cs} \cdot c} \propto \frac{h}{c^2}\Delta\nu_{Cs} \tag{2.17}$$

Electrostatic Approach

The original Kibble principle can be adapted to an electrostatic approach, specifically a capacitor can be used to generate a force instead of a current carrying coil in a magnet field [35].

The sensitivity κ of the device is given by the gradient of the capacitance in the z-direction multiplied by the potential difference V between the plates of the capacitor.

$$\kappa = \frac{dC}{dz}V \tag{2.18}$$

The electrostatic force between the plates of the capacitor is given by equation 2.19

$$F = \frac{1}{2}\kappa V \tag{2.19}$$

This is the equivalent of the force generated in the weighing phase in the electromagnetic approach (equation 2.13).

During the moving phase of the experiment a capacitor plate moves with velocity u and a current I is induced.

$$I = \kappa u \tag{2.20}$$

Equating electrostatic force F to the weight mg of the object under test and combining the two parts of the experiment, equations 2.19 and 2.20, the electrostatic equivalent of the electromagnetic Kibble equation can be formed.

$$m = \frac{1}{2}\frac{IV}{gu} \tag{2.21}$$

Comparison of equations 2.21 and 2.16 shows that the only difference between the approaches is a factor of a half. Traceability to the SI can be established through the parameters, I, V, g, and u as discussed earlier in this section on page 24.

2.3.4 Dissemination

20th May 2019 marked the start of a phased transition of the realisation and dissemination of the SI definition of the kilogram from the single artefact basis (IPK) to multiple independent realisation experiments linked to the Planck constant (h).

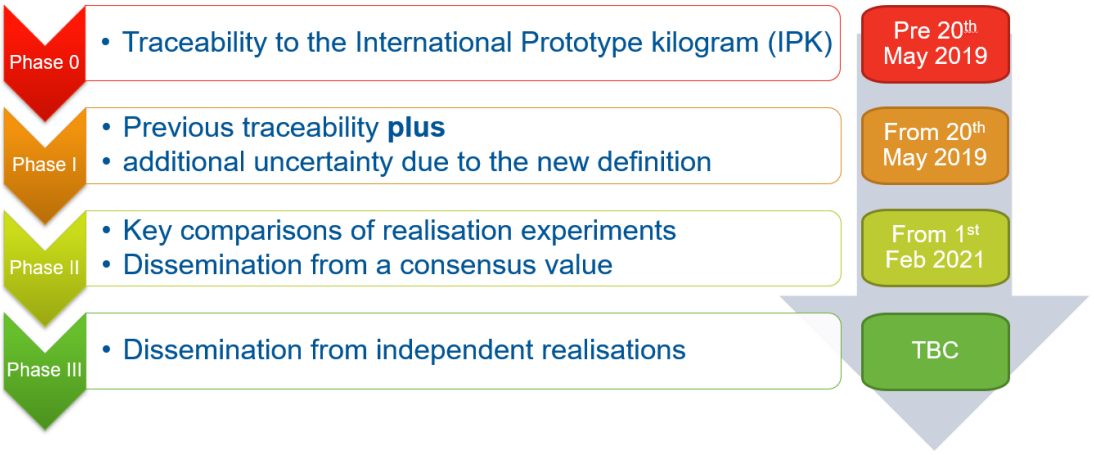

FIGURE 2.6: Flowchart outlining the phases of dissemination of the SI kilogram post redefinition in terms of the Planck constant [36].

Figure 2.6 shows the four phases of dissemination approved by the Consultative Committee for Mass and Related Quantities (CCM) at the BIPM in May 2019. At the time of writing phase two is in operation and traceability to the SI definition of the kilogram is taken from a "consensus" value. The consensus value can be considered an ersatz realisation experiment made up of the most recent three sets of data from international Key Comparisons. A new Key Comparison (KC) will be carried out approximately every two years allowing the consensus value to remain sufficiently current for dissemination purposes and also affords a relatively frequent opportunity for new realisation experiments to contribute. The three sets of data selected to calculate the first consensus value were the "Extraordinary Comparison of National Prototype kilograms with the IPK" in 2014 [37], the "Realisation Experiment Pilot Comparison" in 2016 [10], and the 2019 "Key Comparison of Realisation Experiments" (CCM.M-K8.2019) [38].

These data sets were selected to ensure continuity with the pre-2019 IPK definition of the kilogram and the data analysis has been specified such that there will be no step changes in the consensus value. This requirement will ensure stability of the international mass scale until such time as the reliability of and confidence in the results from individual realisation experiments is sufficient to assume equivalence. The second consensus value came in to use on 1st March 2023 and was calculated from the results of the most recent KC of realisation experiments (CCM.M-K8.2021) [3], the previous KC in 2019 and the Experimental Pilot Study carried out in 2016.

The date of transition from dissemination phase two to phase three has not yet been set. Instead there are several strict criteria which need to be met in order to move into the next phase, both on the individual realisation experiments, the latest KC data set, and the latest three KC data sets as a whole. Individual realisation experiments must achieve a maximum relative standard uncertainty of 40 x 10^{-9} on the KC result, be

consistent with the Key Comparison Reference Value (KCRV), and demonstrate stability of output results by producing consistent results for two consecutive KCs. The most recent KC must contain a minimum of five individual realisation experiments that meet the individual criteria, of those experiments a minimum of three should have relative standard uncertainties of 20 x 10^{-9} or less, and within the KC there should be a minimum of two independent routes to realisation, for example X-Ray Crystal Density (XRCD) and Kibble balance. The difference between the consensus value for the kilogram (as calculated from the latest three KCs) and the KCRV for the most recent KC should be less than 5 x 10^{-9}.

The results of the most recent KC (CCM.M-K8.2021) showed that steady progress is being made towards the implementation of dissemination phase three. The relative standard uncertainties of four realisation experiments were comfortably within 40×10^{-9} (NRC, PTB, NMIJ, NIST) and a further two realisation experiments achieved results just outside of this target (NIM, BIPM). Of the experiments that met the first individual criteria, two (NRC, PTB) were also comfortably lower than 20×10^{-9}. X-Ray Crystal Density (XRCD) and Kibble balance routes to realisation were included. The difference in the KCRV between 2019 and 2021 was +3.6 μg which is an indication of stability of the cohort of realisation experiments in recent years. However the weighted mean of the results was observed to change by -31 μg between the 2016 pilot comparison and the 2019 KC. Further KC studies are required to determine the longer term stability of realisation experiments and ensure that all of the transition criteria are met robustly before proceeding to dissemination phase three [3].

2.4 Mass Realisation Experiments

2.4.1 Primary Kibble Balances

TABLE 2.1: Summary of three state-of-the-art primary Kibble balance experiments that contributed to the 2021 KC of SI kilogram realisation experiments [3][9][39][40].

Experiment	Uncertainty at 1 kg k=1 (μg)	Mass Range (kg)	Operation	Guidance mechanism	Measurement coil
NRC- NPLMkII	11.4	0.25 to 1	TMTP	Balance beam	Single filar
NIST-4	27.4	0.50 to 2	TMTP	Balance wheel	Single filar
BIPM	41.1	1	SMTP	Gimbals and flexures	Bi-filar

Table 2.1 contains details of the top three Kibble balance experiments that took part in the 2021 KC of primary mass realisations (CCM.M-K8.2021) and contributed to the latest consensus value of the SI kilogram [3]. These Kibble balance implementations

operate in the mass range 500 g to 2 kg and are based on the electromagnetic Kibble principle. The NIST-4 and NRC- NPLMkII experiments are both capable of realising mass at more than one nominal mass value. This is beneficial for the dissemination of the mass unit, verification and linearity checks, and direct comparison between Kibble balance experiments.

The NRC- NPLMkII [9] and NIST-4 [39] experiments operate on a Two Mode Two Phase (TMTP) basis, specifically the weighing and moving data collection phases are carried out with the apparatus in different configurations called "modes". The restriction in operation is due to the design of the electrical system and the implementation requirements for precision measurement. The mechanical subsystem of the NRC- NPLMkII balance is based on a traditional mass comparator balance beam with a knife edge pivot point [44]. The measurement coil is suspended from one arm into the magnetic field. In "weighing mode" a tare mass on the opposite arm is required to counterbalance the mass of the measurement coil. This reduces the total electromagnetic force that the coil length, current, and magnetic field combination (BLI) has to produce to level the balance beam and consequently allows finer control of the coil position. Symmetrical currents can be generated between the test mass on and off states of the weighing phase ($I_{on} \approx -I_{off}$) by selecting a tare mass that applies a small additional force equivalent to half the weight of the test mass to the counterbalance. Operating with symmetrical currents during the weighing phase is beneficial for minimising changes in magnet temperature, and hence changes in the magnetic field, due to the constant power carried in the coil ($P = I^2R$). However changes in magnetisation due to the reversal of the current still need to be accounted for [9]. To perform moving phase measurements the balance has to be reconfigured into "moving mode" by removing the tare mass and test mass from the balance beams. This removes the weighing current from the coil and allows the induced voltage to be measured accurately during moving phase. The NIST-4 Kibble balance guidance mechanism consists of a balance wheel in place of a balance beam. The balance wheel approach was introduced to ensure a linear motion of the measurement coil along the z-axis during moving phase which has advantages for accelerating and decelerating the coil. The wheel sits inside a bespoke monolithic flexure block that allows translation of up to ± 0.5 mm in the $x - y$ plane. This adjustment facility allows the centre of the measurement coil to be accurately aligned with the magnetic centre of the permanent magnet [45]. In addition, an electrostatic torque compensation system comprising high voltage electrodes and grounded gold-plated glass plates was fitted to the measurement coil suspension rods to prevent rotation about the z-axis [46].

The BIPM Kibble balance operates on a Single Mode Two Phase (SMTP) scheme [40]. Its mechanical design was originally based on double and single axis gimbal mechanisms and flexures in a single stack with an electrical tare system at the top. There is no reconfiguration required during the operation of this balance therefore it

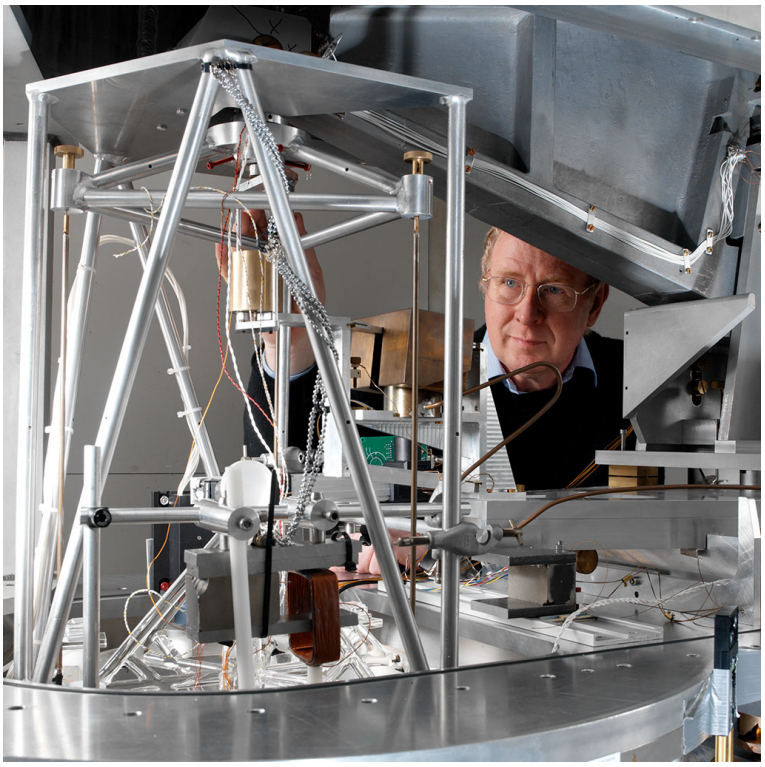

(A) NPLMkII prior to transfer to NRC [41]. Image courtesy of NPL.

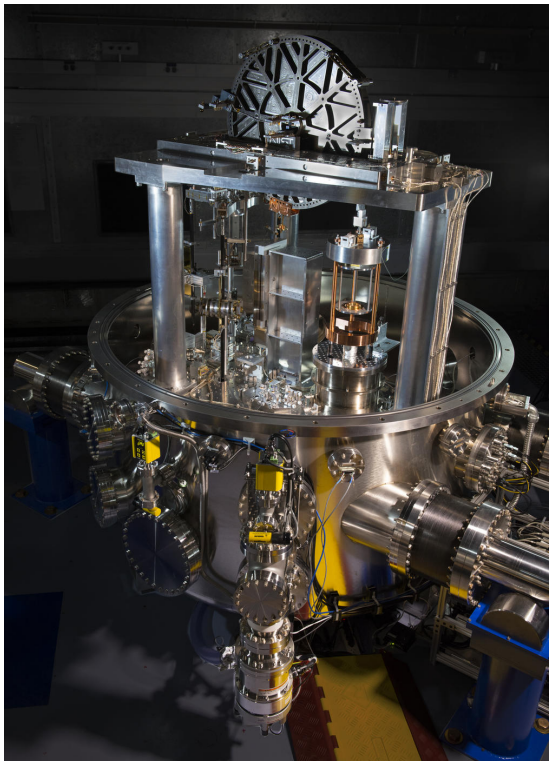

(B) NIST-4 [42]. Image by J.L. Lee, courtesy of NIST .

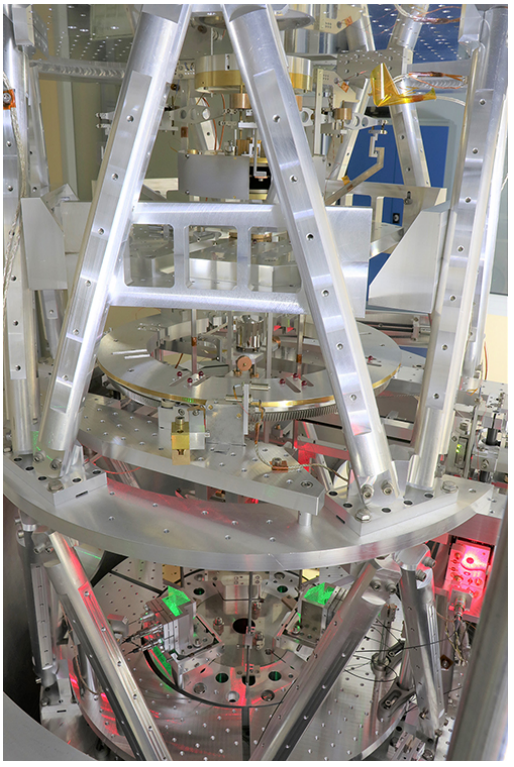

(C) BIPM Kibble Balance [43]. Image licensed by BIPM under CC BY 4.0.

FIGURE 2.7: Primary Kibble Balances.

only has one mode. The BIPM Kibble balance design originally intended to use a superconducting measurement coil. In theory this would have allowed weighing phase and moving phase data to be collected simultaneously as the weighing current and the moving voltage could be present at the same time without interference or cross-coupling of the signals [47][48]. In 2012 Robinson [49] proposed a bifilar coil as a method of achieving many of the advantages of simultaneous weighing and moving phases without the disadvantages of a superconducting coil such as the expense of operation at cryogenic temperatures. This method was trialled and eventually implemented in the BIPM Kibble balance [50][51]. A new mechanical guidance system is under development to remove parasitic motion of the measurement coil. A double-pan beam utilising a voice coil drive system at the centre and a servo controlled translation stage was proposed [52] and tested in air [53]. The system successfully reduced the parasitic motion of measurement coil however oscillation of the counter balance pan was observed. To mitigate this issue the design has been updated to a single-pan equal arm beam with a fixed dead-weight to counter balance the measurement coil.

All three Kibble balance experiments require operation under vacuum conditions, access to a Josephson Junction Array (JJA) primary voltage reference cooled to liquid helium temperature, and long measurement campaigns or large datasets to achieve state-of-the-art mass uncertainties for a single object, typically 1,000 measurements, 10,000 measurements, and a two week data block for the NRC- NPLMkII, NIST-4, and BIPM Kibble balances respectively. These requirements do not align with the needs of typical end users discussed in chapter 1 in terms of uncertainty, size, cost, and convenience.

2.4.2 Table-top Kibble Balances

This subsection summarises three state-of-the-art Kibble balance experiments that are based on the electromagnetic Kibble principle. All three balances are operated in air at masses of 100 g or less. The intended purpose of these balances is the direct calibration of OIML R111 classified weights by a “table-top” sized device.

NIST Kibble Balance at the gram level version 1 (KIBB-g1)

NIST’s KIBB-g1 was designed to operate in the range 10 g to 1 g [20]. Its electromagnetic core includes a samarium–cobalt (SmCo) 50.8 mm diameter disk magnet inside a custom-designed open yoke that houses two 73 mm diameter measurement coils. Similar to the NIST-4 primary Kibble balance, the KIBB-g1 incorporated a balance wheel as part of its mechanical mechanism. However, in this case a “dual diameter” balance wheel is used to ensure a more compact footprint

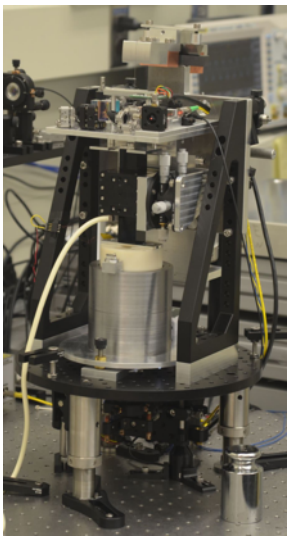

FIGURE 2.8: NIST KIBB-g1 table top balance prototype [54]. Image courtesy of NIST.

(approximately 30 cm diameter by 57 cm tall). The tare system consists of a separate coil and magnet in combination with a deadweight eddy damper. A square cross-section air bearing is used to connect the balance wheel to the mass pan and measurement coils. A Michelson heterodyne interferometer is used to measure position and velocity of the measurement coils. Various CotS devices were used to provide trigger pulses, frequency measurement, and voltage measurement. Two custom-made brass artefacts of nominal mass 5 g and 1 g were used as test weights. Brass was selected due its very low magnetic susceptibility resulting in a negligible correction due to interaction with stray magnetic field from the open main magnet. A magnet placed on the bottom of the mass pan to counter act the effect of stray magnetic field from the main magnet was proposed when measuring objects made from other materials. KIBB-g1 was run according to a SMTP measurement sequence over a period of 18 hours for each test weight. A non-sealed draft shield was placed over KIBB-g1 for the duration of the measurement. A standard relative uncertainty of 1.8×10^{-6} was achieved at 5 g and 6.3×10^{-6} at 1 g. These results were consistent with a traditional mass calibration of the test weights by subdivision to within calculated uncertainty. These results successfully met the uncertainty requirement of OIML R111 for class E2 weights. It was noted that while KIBB-g1 met its targets in terms of accuracy, uncertainty, physical size, and in air operation, it did not meet its target cost of $50,000 or less. This was mainly due to the need to access low uncertainty voltage references such as a JJA which are very expensive to buy and run.

The main advantage of the KIBB-g1 is the precision and accuracy of the mass measurements. However the cost and size of the CotS devices that make up the electronic measurement subsystems and the length of time required to obtain a result are significant disadvantages. Also, the mechanical design is a complex 3D structure

comprised of multiple components that do not lend themselves to MEMS manufacturing methods.

NIST Kibble Balance at the gram level version 2 (KIBB-g2)

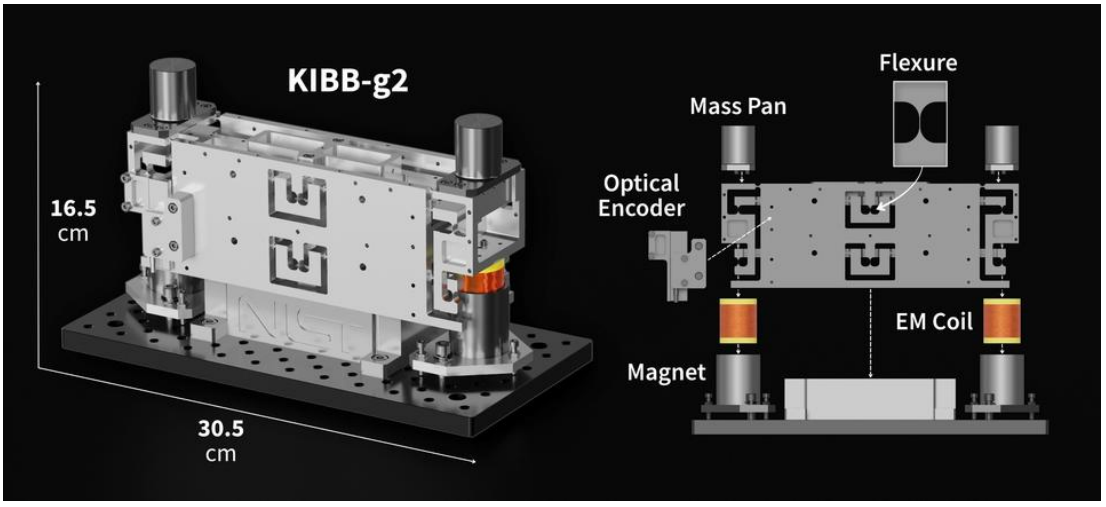

FIGURE 2.9: NIST KIBB-g2 table top balance schematic [55]. Image by Sean Kelly, courtesy of NIST.

The KIBB-g2 was developed by NIST for the United States Army to provide directly traceable calibration of standard weights at the point of use [56]. The target mass range was 50 g to 500 mg with a standard relative uncertainty of 30×10^{-6}. The end users also required a more compact, robust, and convenient to use instrument than KIBB-g1. To achieve these aims the KIBB-g2 mechanism is based on monolithic symmetrical four-bar linkage and hinged flexure design. Two identical bespoke voice coil actuator (VCA) manufactured by a commercial company are used for the electromagnetic measurement and tare systems. These VCAs comprise a single filar coil on a light weight plastic former around a permanent magnet. A CotS optical encoder is used for position and velocity measurements instead of an interferometer resulting space and cost savings. For simplicity the mass pan is connected directly to the guidance mechanism and measurement coils without a self centering gimbal in between. The total volume of the mechanical and electromagnetic subsystems of the instrument is approximately 4,000 cm^3 (estimated dimensions of 25 cm long by 8 cm wide by 20 cm tall). CotS devices such as a digital voltmeter, frequency counter, and computer were needed to complete the system. Analysis of data from KIBB-g1 showed that it could be possible for KIBB-g2 to achieve its target uncertainty of 30×10^{-6} within a few minutes of data collection rather than over a period of hours. This would fulfil the end user convenience requirement.

The main advantages of the KIBB-g2 are the compact mechanical components, fit for purpose measurement uncertainty, and convenient measurement times. The

monolithic guidance mechanism is a complex 3D design however it may be possible to adapt it to achieve a similar structure at MEMS scale.

PTB Planck Balance 2 (PB2)

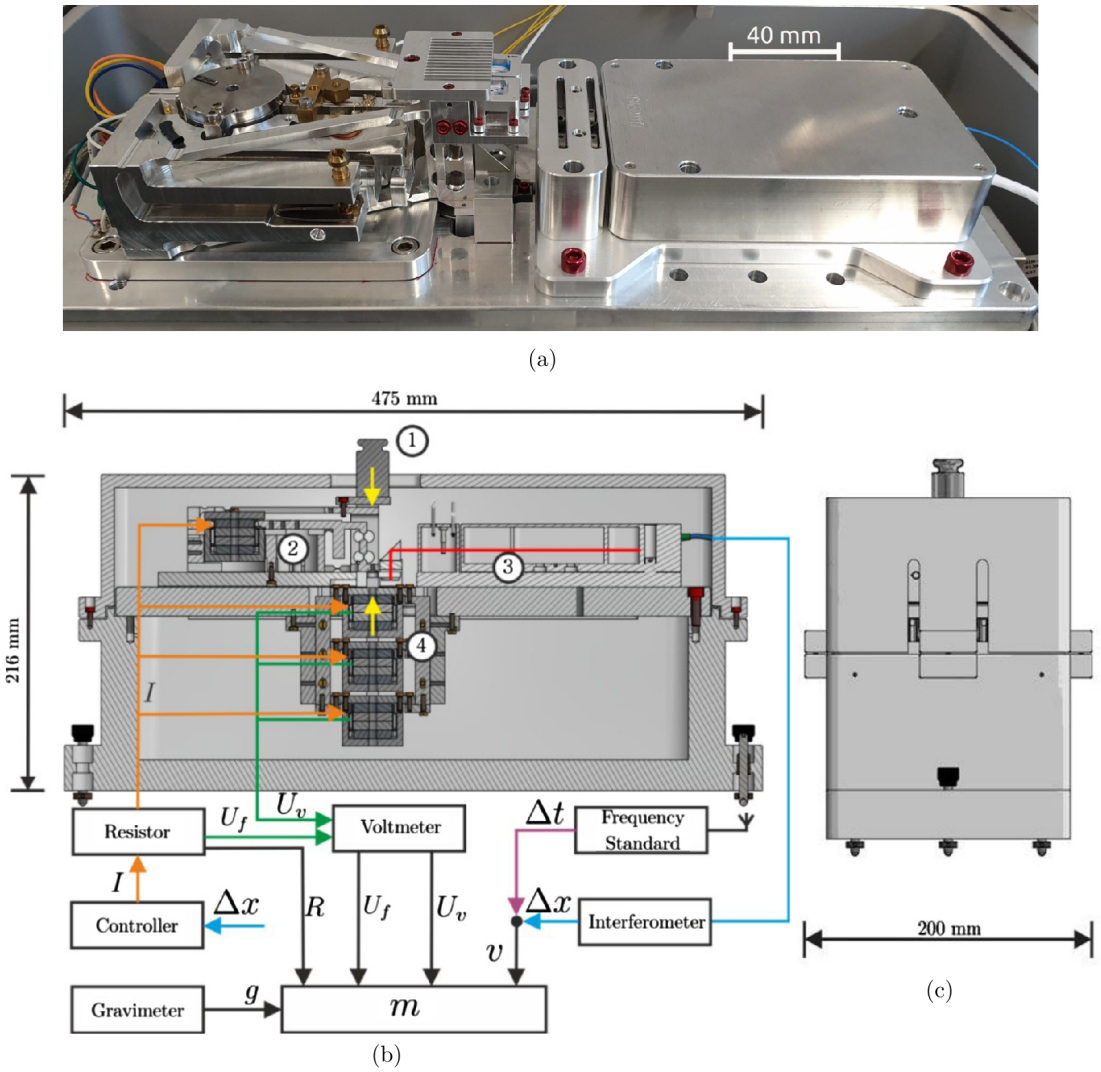

FIGURE 2.10: PTB PB2 table top balance. (a) Prototype viewed from above. (b) Schematic section view from long side side. (c) Schematic view from short side. Figure reproduced from [21]. Licensed by Vasilyan et al. under CC BY 4.0.

The PB2 instrument was developed by Physikalisch-Technische Bundesanstalt (PTB) in collaboration with Technische Universität Ilmenau [21]. The aim was to create an instrument that operated in the range 100 g to 1 mg with uncertainties commensurate with OIML class E2 requirements. From the outset the paramount design principle was that all parts of the system should be modular and comprised of CotS components where possible. The mechanical guidance and tare subsystem were provided by a CotS load cell from a traditional electromagnetic force balance. This design decision resulted in a maximum moving range of approximately 100 μm.

Several custom coil actuators were trialed for the main measurement magnet and coil subsystem. The designs included a single filar coil within an air gap of a closed circuit magnetic field guide with two SmCo permanent magnets. The trial coils had diameters between 29 mm and 32 mm and a height of 10 mm. They were made from 50 μm diameter wire with between 3,000 and 5,500 turns per coil resulting in a BL product of approximately 181 Tm. The position and velocity measurement is achieved using a homodyne differential interferometer with the coil displacement mirror attached to a platform that is connected to the coils by a frame passing through the closed magnet. The mass pan design is suitable for OIML shaped weights and could be adapted for spheres. The total volume of PB2 is approximately 20,500 cm^3 (47.5 cm long by 20 cm wide by 21.6cm tall) about half the volume of KIBB-g1 and five times the volume of KIBB-g2. PB2 was tested with a set of stainless steel OIML class E1 weights in the mass range 50 g to 1 mg. The balance was operated according to a SMTP measurement sequence with ABA cycles in both weighing and moving phases. During moving phase the measurement coil was oscillated according to a sinusoidal signal generating an induced AC voltage. The maximum displacement was 40 μm and frequencies between 0.5 Hz and 10 Hz were trialled. A correction was applied for the difference in BL product between the static position in weighing phase and the measured BL product over the range of motion during moving phase.

It was shown that the statistical standard error of the measurements were consistently lower than the maximum permissible error (MPE) for OIML class E1 weights for all test masses except at 10 mg. However, the systematic deviation of the measured result from the nominal value of the test mass was higher than the MPE for OIML class E1 weights for all test masses except at at 2 g and 50 g. However, the systematic deviation was consistently lower than the MPE for OIML class E2 weights except at 100 mg and below. Further work was proposed to investigate and reduce these discrepancies including a focus on weighing phase data collection and improvement of the Abbe error induced by the indirect measurement of the coil position.

The short range of motion ($<$100 μm) of the measurement coil excluded the possibility of DC voltage measurements due to the inherent time constraints. The measurement of the fundamental mode of the AC voltage over the range of motion was used to calculate the average BL product over that distance. It was acknowledged that any non-linearity in the magnetic field would create a bias in the calculation of BL. Further investigation of the AC induced voltage signal produced by PB2 in moving phase showed that the higher order harmonics could be used to estimate a correction [57]. It was found that this correction was suitable for the calibration of OIML class E2 weights. This is important knowledge for the miniaturisation of Kibble balance technology to MEMS scales.

2.4.3 Electrostatic Kibble Balances

This subsection summarises four state-of-the-art mass and force experiments that operate at 10 mg and below. They are all based on the electrostatic force principles and are traceable to the SI without a standard mass artefact. These balances are typically used for calibration of standard mass artefacts and force sensors such as cantilever probes for AFM [23] [24].

NIST Electostatic Force Balance (EFB)

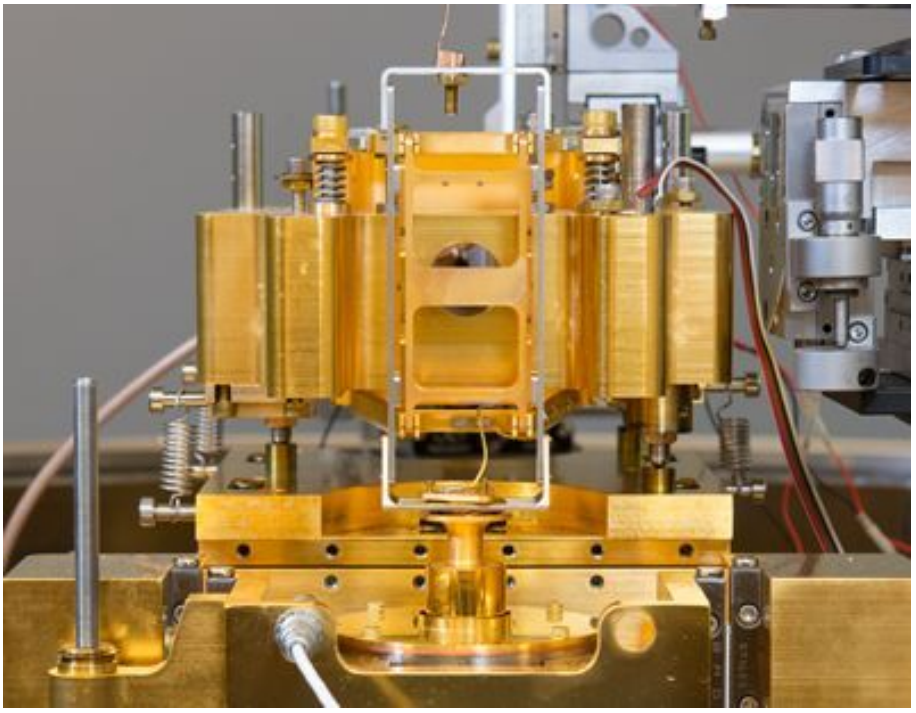

FIGURE 2.11: NIST Electrostatic Force Balance side view [58]. Image by J.L. Lee, courtesy of NIST.

NIST's EFB is comprised of a cylindrical capacitor with a 4-bar linkage guidance mechanism, interferometer length measurement and operates in a vacuum chamber [18]. It has a very low a measurement range of 10 pN to 0.3 mN and is capable of one part-per-million (ppm) relative uncertainty. These capabilities are currently unrivaled. The main additional benefit of this system is its self-contained SI traceability through the ability to calibrate subsystems or measurands such as the interferometer, capacitance, and voltage directly to SI units.

The main disadvantages of this balance, in terms of the aims of this work, are its three dimensional (3-D) capacitor design and practicality of operation. The 3-D capacitor does not lend itself to MEMS design and manufacture which favours two dimensional structures such as parallel plates or comb structures. Operating a balance

under vacuum conditions adds extra complexity and cost. Additional uncertainty from the vacuum-air transfer of standard weights will need to be added and the practicalities of artefact handling in a sealed system will need to be considered.

NPL Low Force Balance (LFB)

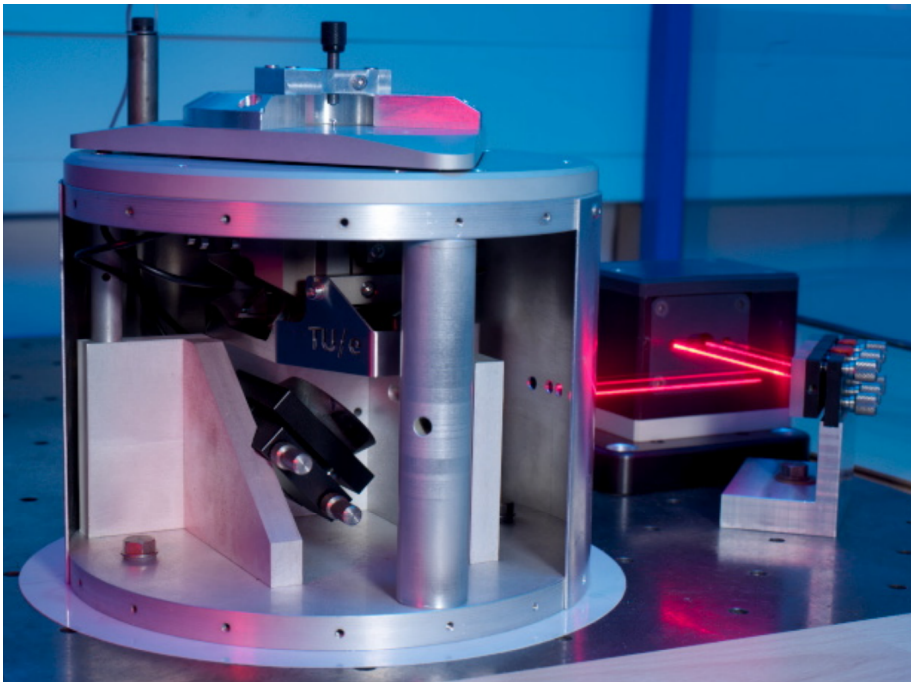

FIGURE 2.12: NPL Low Force Balance side view. Reproduced from [59], © Crown copyright 2008, National Physical Laboratory.

NPL's LFB operated in air and consisted of a 4-electrode capacitor with moving dielectric material connected to a monolithic 4-bar flexure guidance mechanism [59]. Similar to the NIST EFB it used an interferometer for length measurement. It operated at low forces from 10 nN to 10 μN and also benefited from self-contained SI traceability for its interferometer, and capacitance and voltage measurands. A differentiating feature of this system is that it was capable of bi-directional force measurement. This could be a powerful advantage for reducing measurement uncertainty and/or adapting the system to different applications.

Industrial Technology Research Institute (ITRI) Capacitor Balance

The core of ITRI's instrument is a 3-electrode parallel plate capacitor with monolithic flexure guidance mechanism as shown in figure 2.13 [60]. It can measure mass over a narrow range between 1 mg and 10 mg with a relative uncertainty of 100 ppm while operating in air. The performance and operation of this balance partially meet the requirements of this work in terms of mass range, relative uncertainty, and the ability

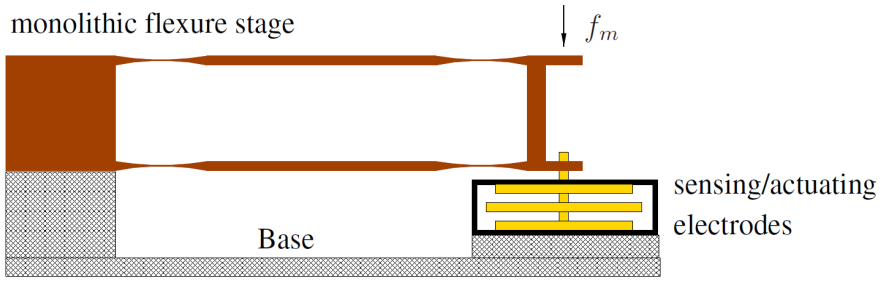

FIGURE 2.13: ITRI Capacitor balance schematic side view [60]. © IOP Publishing. Reproduced with permission. All rights reserved.

to operate in air with potential for scaling to smaller masses. Its parallel plate capacitor core in particular lends itself to scaling to MEMS. The main drawback of this system is that it requires periodic calibration using external equipment such as an interferometer which adds increased maintenance cost and effort.

National Institute of Metrology (NIM) Capacitor Balance

NIM's Capacitor Balance is a differential measurement system consisting of a cylindrical capacitor with a monolithic flexure guidance mechanism [61]. The balance was optimised for use at 1 mg and had a reported uncertainty of approximately 4 %. A few mechanical configurations were trialled prior to this version. In an attempt to reduce measurement signal noise an air damper system was implemented [62]. To increase the mass range of the balance a lever system was used [63]. The differential system proved successful at reducing measurement drift with time. The performance and operation of this balance partially meet the requirements of this work in terms of mass range and the ability to operate in air. However, the achieved relative uncertainty is significantly higher than the target for this work and the 3-D capacitor design of the device does not lend itself to scaling to MEMS.

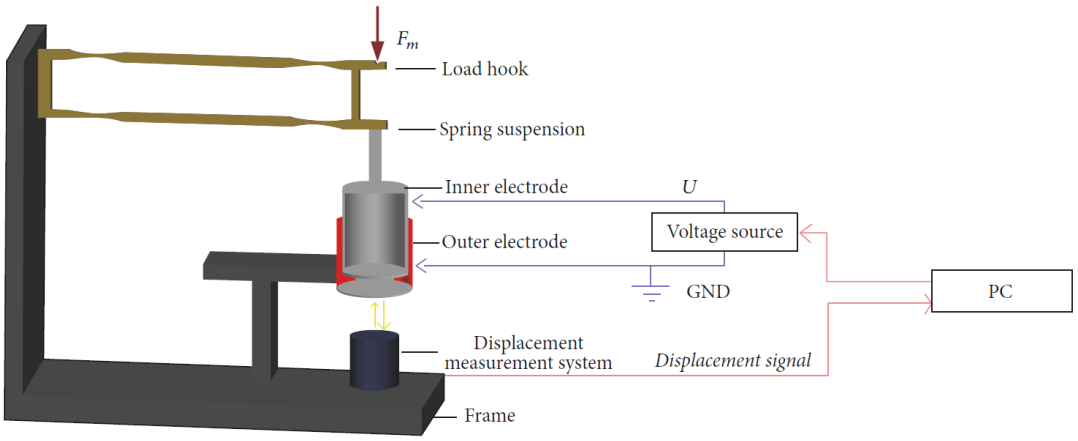

(A) Schematic diagram of single force measurement system.

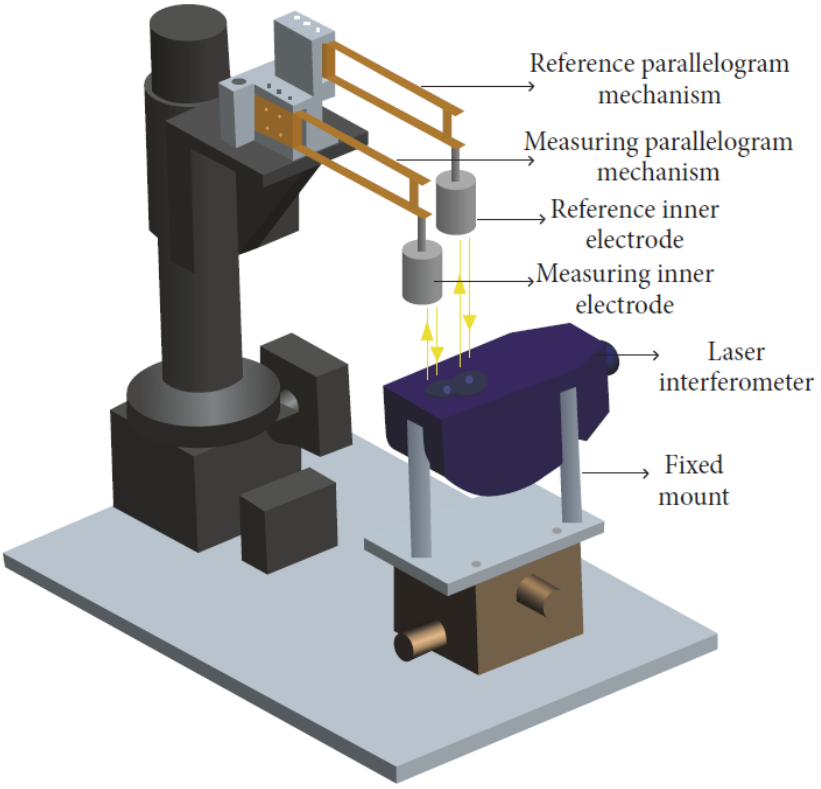

(B) Schematic diagram of differential measurement system.

FIGURE 2.14: NIM Capacitor balance. Figures reproduced from [61]. Licensed by Peiyuan Sun et al. under CC BY 4.0.

2.5 Artefact Based Traceability

2.5.1 State-of-the-Art Low Scale

Several NMIs and research groups have developed state-of-the-art low scale mass and force experiments which take their traceability to the SI from calibrated standard mass artefacts. This subsection summarises four experiments. The majority are based on force transducer technology and one on electrostatic force principles.

Adapted Commercial Microbalance

Korea Research Institute of Standards and Science (KRISS), Tianjin University, and Centre for Metrology (MIKES) have all developed facilities for the measurement and calibration of small forces. These are primarily for applications such as AFM and material indenter cantilever calibration. All three groups have utilised the core of a commercially a available microbalance, specifically the load cell, as the key sensing element of their facility. Load cells convert a force into an electrical signal which can be characterised and calibrated using standard mass artefacts. These instruments can measure masses up to a few grams (2.1 g at Tianjin University and 6.1 g at MIKES) with a resolution of 0.1 ng [64][63][65].

There are two main advantages to this approach. Firstly, it relies on a widely used existing technology which has reliability that has been proven over many decades. Secondly, it can operate and produce high resolution measurements in air. This significantly simplifies measurement methodologies and reduces the amount of support equipment required. The main disadvantage of this approach is that absolute measurement performance is limited by the availability, traceability, and uncertainty of standard weights below 1 mg.

Pendulum in an Electrostatic Field

PTB have developed a facility for very small forces that act perpendicular to gravity. It is based on pendulum principles and consists of a single crystal silicon bob in an electrostatic field. This system is capable of measuring forces that are less than a micro-Newton with a resolution of one pico-Newton. Traceability to the SI force is achieved indirectly through the mass of the pendulum bob (acceleration due to gravity, pendulum length and period). This facility has both the lowest operating range and the highest resolution in the literature. However its biggest drawback for mass measurement is that it can only measure forces that are perpendicular to gravity [66].

2.5.2 Competing Technologies

This subsection summarises and evaluates five types of commercially available precision low scale mass measurement devices based on alternative physical principles, piezo-electric resonators, oscillating glass tubes, strain gauges, and quartz fibre torsion. All devices require calibration with a standard mass artefact to gain traceability to the SI. Notably it is not possible to achieve this for Quartz Crystal Microbalance (QCM), Quartz Crystal Microbalance with Energy Dissipation (QCM-D), or Tapered Element Oscillating Microbalance (TEOM) based devices as standard artefacts small enough are not commercially available or included in the international standard for weight calibration requirements [17].

Quartz Crystal Microbalances

There are two types of Quartz Crystal Microbalance QCM and QCM-D. Both of these are based on Piezo-electric resonators which behave according to the Sauerbrey equation (2.22).

$$\Delta m = -C_f \Delta f \tag{2.22}$$

Where Δm is change in mass per unit area, C_f is the Sauerbrey sensitivity factor and Δf is frequency change [67].

The QCM-D instruments also include a change in energy dissipation measurement.

$$D = \frac{1}{Q} = \frac{E_{diss}}{2\pi E_{stored}} \tag{2.23}$$

Where D is the change in energy dissipation, Q is the quality factor of the resonator, E_{diss} is the energy dissipated, and E_{stored} is the energy stored by the system.

QCM instruments typically operate in the range 10 μg to 100 μg with a resolution of up to 1 ng/cm^2. They were developed for use in applications such as molecular interaction, film growth, oxidation, and corrosion (in vacuum and gas phase) monitoring. QCM-D instruments have similar specifications and are used to measure the properties of films such as viscosity, elasticity and density, and also observe the kinetics of molecular interactions (in liquid phase). All of these applications require the measurement of sub-microgram mass changes in real-time.

Tapered Element Oscillating Microbalance

The sensing element of a TEOM consists of an oscillating hollow glass tube with a filter on the moving end.

$$\rho = \frac{\frac{dm}{dt}}{\frac{dv}{dt}} \tag{2.24}$$

Where ρ is density, $\frac{dm}{dt}$ is change in mass with time, and $\frac{dv}{dt}$ is change in volume with time.

TEOM instruments were developed for air quality monitoring purposes and are used to detect aerosol and dust particles in real-time. They typically have a resolution of $0.1\mu g/m^3$ and an accuracy of $\pm 0.75\%$ [68].

Load-cell Microbalance

Commercially available microbalances are used in many analytical laboratories world wide. They cover the mass range from approximately 300 ng to 10.1 g. Microbalances are based on a load cell with strain gauges and translate a force into an electrical signal. Typical repeatability is between 0.15μg and 0.4μg [69].

The main benefit of a microbalance is that it can be calibrated using mass standards traceable to the SI kilogram over the majority of its measurement range. The main disadvantages are that mass standards at the very low ranges either do not exist or have high relative uncertainty (due to subdivision of the kilogram as discussed in Subsection 2.2.3) and dynamic (or real-time) measurement is not possible as load cells require time to settle in order to achieve repeatable measurements.

$$\Delta f \propto \Delta R \propto \Delta V \propto \Delta L \tag{2.25}$$

Where f is frequency, R is resistance, V is voltage and L is length.

Quartz Fibre Torsion Microbalance

This instrument is based on a traditional twin pan comparator and uses quartz fibre torsion difference measurement to achieve high sensitivity to small differences in mass. It operates on masses up to 1 g with a resolution of 0.1 μg. It is possible to calibrate this balance with traceability to the SI kilogram as far as standard mass artefacts allow. The main disadvantages are that a standard mass artefact is required

as a counterbalance, it requires optical alignment by the user, and it is not capable of dynamic (or real-time) measurement [70].

2.6 Electromagnetic MEMS Devices

MEMS devices that perform force measurement or generate forces contain many components in common with a Kibble balance. This makes them ideal candidates to inspire the design of a future MEMS Kibble balance. A selection of MEMS devices are presented and their design features evaluated for this purpose.

Magnetometer

In 2017 Punyabrahma and Jaynth developed a magnetometer for estimating the magnetic moment of magnetic micro-particles [71].

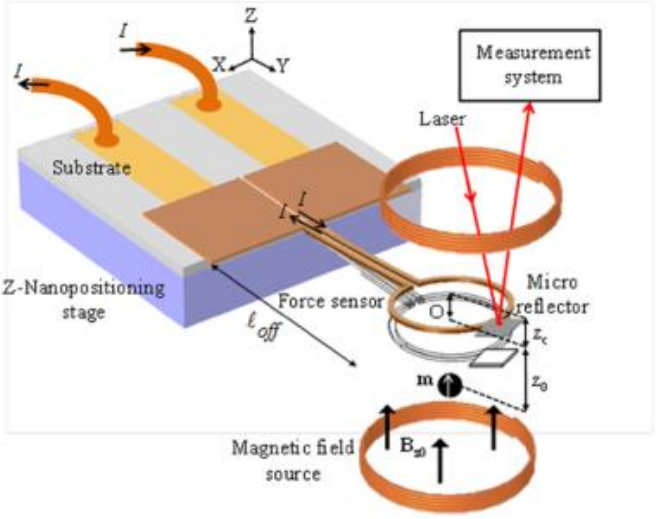

FIGURE 2.15: MEMS magnetometer schematic. Reprinted from [71], with the permission of AIP Publishing.

The design, shown in figure 2.15 , has several advantages that could be used to influence the design of an electromagnetic MEMS Kibble balance. It is suitable for very small force detection, uses planar coils to create a solenoid based magnetic field, and includes a traceable position measurement system (laser inteferometer). The main disadvantage of this device is its high relative uncertainty. The measured magnetic moments of particles only agreed to within 16% of theoretical values.

Energy Harvester

In 2009 Wang et al. created a micro-electro-magnetic low level vibration energy harvester for the purpose of converting ambient vibrations into electrical power (figure 2.16a). This device consists of many components found in a typical electromagnetic Kibble balance and has a planar structure which is suited to MEMS device design.

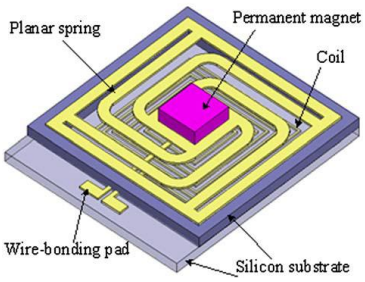

(A) Schematic structure of a low-level vibration energy harvester [72]. Reproduced with permission from Springer Nature.

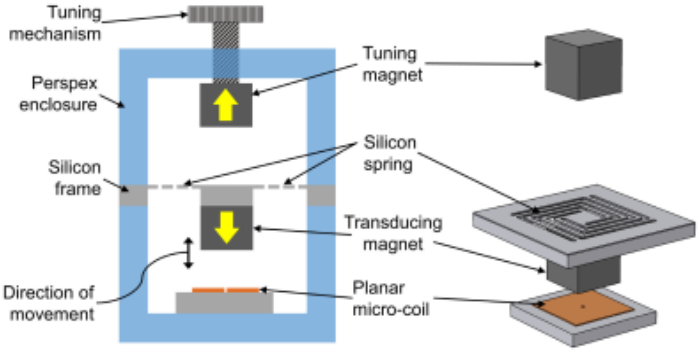

(B) Structure of a magnetically tuneable MEMS nonlinear vibration energy harvester comprising of silicon spring, NdFeB magnets and planar micro-coil [73] © 2017 IEEE.

FIGURE 2.16: Two examples of MEMS energy harvesters.

In 2017 Podder et al. developed a method for magnetically tuning a MEMS vibration energy harvester (figure 2.16b). In addition to the planar coil and silicon spring flexure, the main design feature of interest is the second (or tuning) magnet that can be adjusted to change the stiffness of the flexure system. This would be an advantage for a MEMS Kibble balance as it would allow the mass or force sensitivity of the device to be optimised. However it may also be a disadvantage due to the placement of tuning magnet directly above the main magnet. This would create a design challenge as it is not obvious where to place the mass under test.

Alternating Current (AC) Sensor

In 2009 Leland et al. created a self-powered AC sensor for monitoring energy use [74]. As shown in figure 2.17, the AC sensing part consists of a permanent magnet at the end of a piezoelectric cantilever. The two main features of interest are the creation of the very small permanent magnet ($\sim$150μm square by $\sim$100 μm tall, $\sim$0.4 T) and the potential use of the piezoelectric cantilever for displacement measurement.

The permanent magnet was made from a neodymium alloy. It was printed into position on the cantilever and was magnetised post production. Use of the piezoelectric cantilever for displacement measurement would be very convenient as it

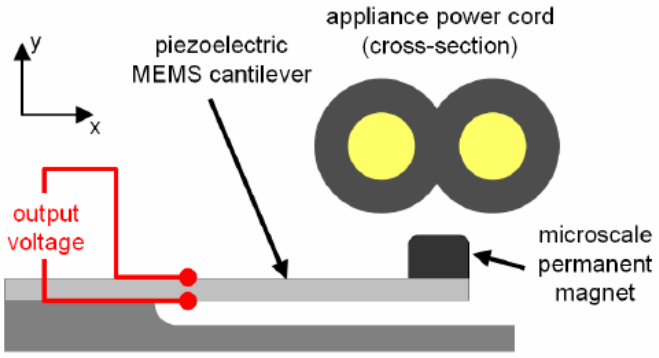

FIGURE 2.17: Side-view schematic of a self-powered MEMS AC current sensor (not to scale) [74] © IOP Publishing. Reproduced with permission. All rights reserved.

would contain the measurement in the spring system. This would remove the need for a separate displacement measurement method such as an interferometer and hence simplifies the design and reduces the number of components in the device.

Passive Wireless Sensor

In 2015 Kisic et al. developed a passive sensor to measure normal forces from commercially available components [75]. Figure 2.18 shows a cross section of the device and its operational principal.

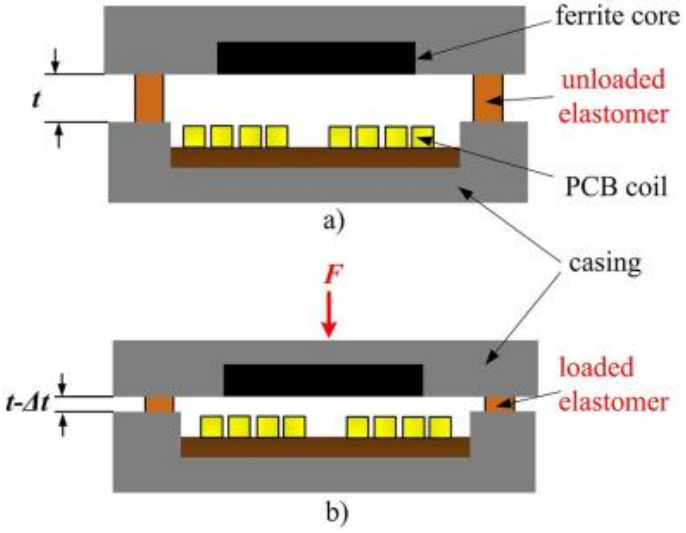

FIGURE 2.18: Passive wireless force sensor (a) without external force (b) with applied normal force [75] ©2015 IEEE.

The planar coil and magnet are an advantage for MEMS manufacture and the orientation of the force sensing components are compatible with mass measurement, specifically they are aligned in the z-axis. Another benefit is that the device is comprised of commercially available components. This reduces the cost of

construction and increases the reliability/robustness of the device. The main disadvantages of this design is that it not a directly traceable measurement of force, the forces detected are large (tens of Newtons) in comparison to the target range for a micro-Kibble balance ($\leq$100 mN) and it has a poor resolution.

Haptic Feedback System

In 2020 Berkelman and Abdul-Ghani created an electromagnetic position sensor and force feedback system [76]. This device consisted of two sets of overlapping flat rectangular coils rotated at 90° to each other and separated by a plate. These coils were used to generate Lorentz forces in any direction on an interaction magnet held above the surface of the device.

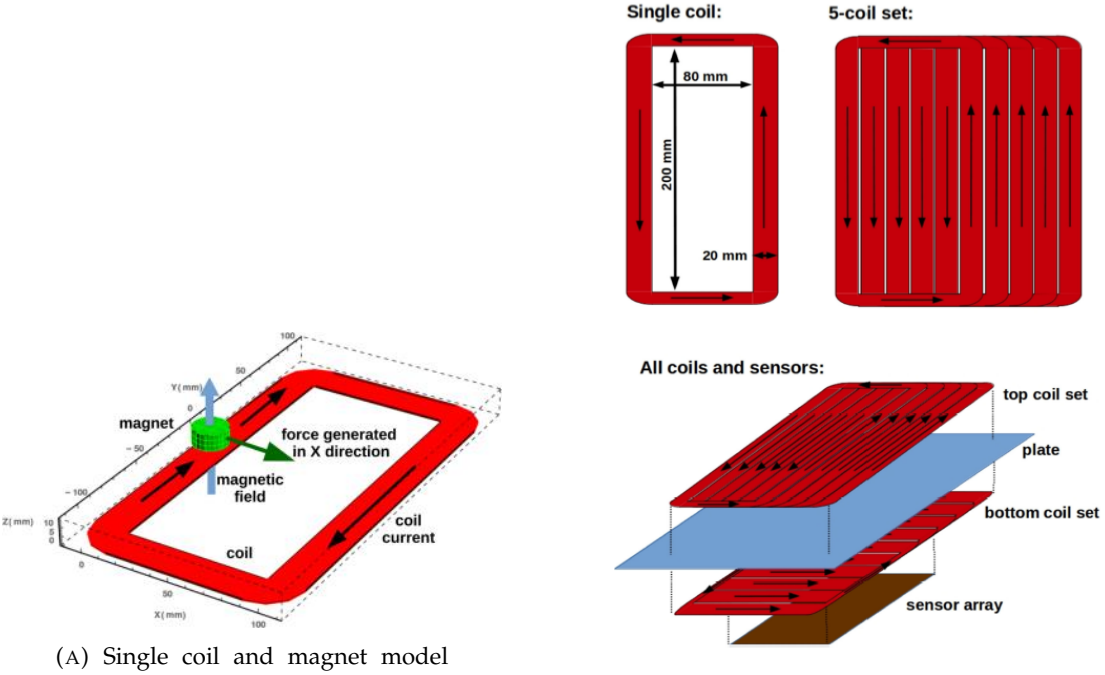

(A) Single coil and magnet model with current, magnetic field, and Lorentz force vectors in coil coordinate frame.

(B) Single coil, five coil set, and complete 10-coil sensor array configuration.

FIGURE 2.19: Electromagnetic haptic feedback system [76] © 2020 IEEE.

The main advantages of this design are the planar coils suitability for MEMS manufacture and the orientation of the force sensing is compatible with mass measurement in the z-axis. Plus there is an option for force measurement in the x-axis too. The main disadvantages of this sensor are a small force sensing range along the z-axis and off centre alignment of the magnet with the coil is required. In addition the device produces excess heat due to continuous current flowing in the coils. This could cause significant issues for mass measurements due to air currents causing drafts.

Micro-force generation

In 2020 Zhu et al. published the design for a new micro-force generating instrument under development at the National Metrology Institute of Japan (NMIJ) [77]. This instrument applies Kibble balance principles to a rotating device and is capable of transmitting a generated torque to a linear compression or tension force. As shown in figure 2.20a, the core of this instrument is a rectangular coil inside a moving magnetic field provided by two Neodymium magnets connected to the drive shaft of a motor under servo control. Figure 2.20b shows how the torque generated on the coil is transmitted to a balance beam which is resting on an air-bearing. A loading frame is connected to one end of the balance beam by a very thin hinge. The mass of the of the loading frame is manually counterbalanced using tare weights positioned in symmetry at the other end of the beam. Distance r, from the centre of the balance beam to the loading frame hinge is measured precisely to facilitate calculation of force from torque. The position and motion of the moving frame is measured using a laser interferometer.

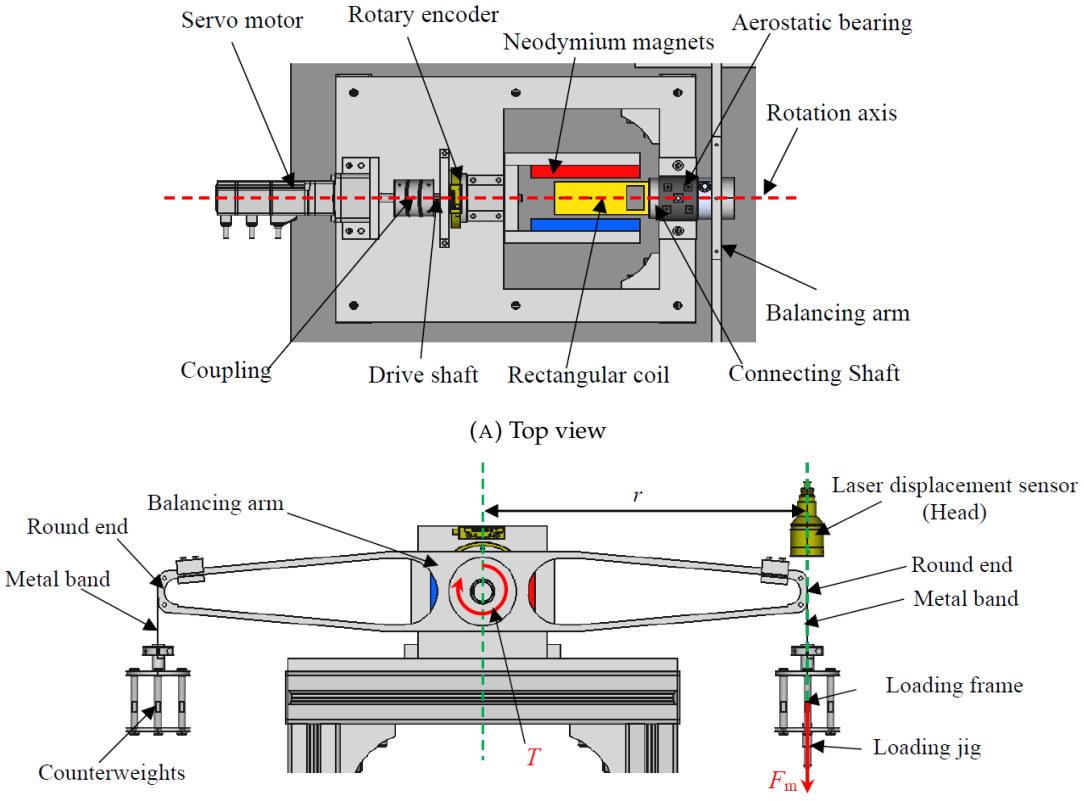

(A) Top view

(B) Front view

FIGURE 2.20: Electromagnetic micro-force generating machine transmission mechanism schematics. Figure reproduced from [77]. Licensed by Zhu et al. under CC BY 3.0.

This device operates following the Kibble principles by using two modes (static and dynamic) and has a planar coil however, in general, it does not have many features

that are suited to the design of a MEMS Kibble balance. In particular its balance beam mechanism and air-bearing are not suited to MEMS scaling.

2.7 Summary

In this chapter the concepts, implementations, and practicalities of modern mass metrology were reviewed. The change in the definition of the SI unit of mass, the kilogram, from an artefact basis (IPK) to a fundamental constant of nature (Planck constant h) in 2019 marked the start of a new era. The opportunity for mass to be realised from the definition at any scale and at any location was highlighted and the rational for pursuit of improved traceable mass measurement at the sub-gram level was presented.

The theory of the two main routes to realisation, the XRCD method and the Kibble principle, were introduced. The features of the XRCD approach were examined against the aims of this work and it was concluded that it could not meet the requirement of direct traceability at the point of use by a "typical" end user. By contrast a device based on either the electromagnetic or the electrostatic Kibble principle has the potential to achieve traceable mass measurement for any object at the point of use. In addition, Kibble balance devices are suited to "remote" calibration and dynamic measurement. These capabilities are inherent to the implementation of the Kibble principle and beneficial for many applications. For example, in hazardous environments where it is unsafe for a user to enter, or weights cannot be removed for re-calibration due to radioactive or other hazardous contamination, it would be preferable to have a device that could maintain traceability without user intervention or transfer of standard artefacts. On production lines, manufactured products are often produced at a faster rate than would allow for real-time measurement by an "inline" electronic load-cell balance. Typically the response and stabilisation time of this type of balance is a few seconds. A device based on the Kibble principle should be able to achieve high accuracy dynamic measurement of mass by analysing the time varying signal from the device and inferring the mass of the object in real-time. A comprehensive literature review of state-of-the-art Kibble balance experiments, indirectly traceable mass measurement devices, commercially-available competing mass measurement technologies, and electromagnetic MEMS devices was carried out.

The review of state-of-the-art Kibble balances covered mass scales from 1 kg to the sub-milligram range and both electromagnetic and electrostatic principles. It showed that a lot of progress has been made in scaling this technology. However, to achieve low measurement uncertainty compromises such as the inclusion of high cost components (JJA voltage reference) or the inconvenience of operating under vacuum conditions were required. Although the measurement range achieved has scaled to

sub-miligram masses in many cases the total volume of the instrument is significantly larger than commercially available indirectly traceable alternatives. All of the Kibble balances existing in the literature required precision engineered bespoke components for inclusion in subsystems such as the guidance mechanism or force actuator. Many of the designs and manufacturing techniques do not immediately lend themselves to further miniaturisation to MEMS scale.

Mass measuring instruments that obtain traceability to the SI definition of the kilogram through artefacts were also considered in the literature review as the current state-of-the-art available to "typical" end users. It is clear that these devices have advantages such as reliability, practicality, and familiarity as they have been developed over many decades and produced in high numbers for multiple applications. However these devices fall short in a few areas. For example, at sub-milligram scales traceable mass measurement is not easily accessible as standard weights below 1 mg are difficult to obtain and challenging to use. In addition, since the advent of the new SI definition in 2019, the opportunity to remove standard artefacts from the traceability chain is now a possibility. This highlights some of the other disadvantages of artefact based traceability such as the requirement for an operator to be present with the device for calibration. The Kibble principle by contrast allows for "remote" calibration.

It is clear that there is a gap in the market for a 3D printed MEMS Kibble sensor supported by an electronics system with a small footprint. The first step is to create a proof of concept 3D printed Kibble balance at the gram-level. To achieve this aim either the electromagnetic or electrostatic principle could be pursued. It is crucial that any prototype device produced should be capable of being scaled to MEMS. Therefore it is important to highlight MEMS manufacturing techniques, opportunities, and challenges of creating devices at this scale from the outset.

A few devices in the literature show that the electrostatic principle is a viable route to traceable mass and force measurement at low scales. If reliable and accurate fabrication of capacitors can be achieved at the appropriate size then this technology has the potential to be tailored to the requirements of the sensing application. For example, comb-drive actuators are an existing MEMS device that could be adapted to form the electrostatic core of a micro-Kibble balance.

The majority of Kibble balances in the literature are based on the electromagnetic principle utilising a permanent magnet and coil at the core. This is a proven route to miniaturisation as shown by the devices discussed in this chapter that operate at sensing scales from 1 kg to 1 mg. There are several examples in the literature of MEMS scale devices designed for other purposes, such as energy harvesting or detection of magnetic fields, that include elements of electromagnetic Kibble balances. A few examples are included in this chapter as inspiration for the development of an

electromagnetic MEMS scale Kibble balance. Due to the wealth of existing knowledge in both Kibble balance development and MEMS device fabrication this thesis will focus on the electromagnetic principle.

Chapter 3

Feasibility Study

In this chapter the feasibility of creating a 3D printed Kibble balance proof of concept was explored. A simple model based on the traditional Kibble Balance principle was evaluated analytically for masses in the range 10 g to 1 μg. The uncertainty at each mass range was estimated assuming that the electronic measurement subsystems were constructed from relatively low cost commercially available components. Contributions due to mechanical design and secondary effects were not modelled or estimated.

In a separate study, two options for generation of a magnetic field were simulated in COMSOL Multiphysics®, an anti-Helmholtz coil and a pair of opposed permanent magnets. The resultant predicted magnetic fields were evaluated for suitability for inclusion in a Kibble balance. The output of the opposed permanent magnet model simulation was verified experimentally in the laboratory.

3.1 Model and Assumptions

A simplified implementation of the Kibble Balance principle consisting of a single coil of radius r_c in a uniform radial magnetic field B as shown in figure 3.1 was assumed.

Calculations were performed using the following adaptation of equation 2.16:

$$m = \frac{\gamma V_W V_M}{RAgu} \tag{3.1}$$

where m is the mass of the object under test, V_W is voltage measured during weighing phase, R is the resistor used to convert current to voltage in weighing phase, V_M is the measured voltage induced during moving phase, A is the gain required to amplify the induced voltage for measurement, γ is an alignment factor due to differences in the

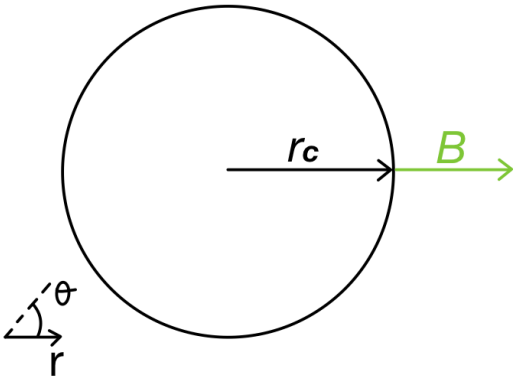

FIGURE 3.1: Simplified electromagnetic Kibble balance model showing a sensing coil of radius r_c in a radial magnetic field B from above.

guidance mechanism performance between weighing and moving phase, g is local gravity, and u is the velocity of the coil in moving phase.

The methods of magnetic field generation, guidance mechanism for moving parts, and counter balance for the coil mass were not considered in detail at this stage. However the following assumptions were made to facilitate the feasibility study.

The magnetic field B follows a radial distribution $\propto \frac{1}{r}$ with a constant magnitude at coil radius r_c and the variation in magnetic field along the z-axis at coil radius r_c is uniform. It was also assumed that the magnetic field was generated by circular components with axial symmetry about the z-axis.

It was assumed that the sensing coil was constructed from copper wire of diameter d and that the mass of the coil was directly proportional to the mass of the object to be weighed, by factor β.

The device parameters included in table 3.1 were assumed and allowed to vary over the values stated. Constant values for copper density, copper resistivity, and local gravity were also assumed as detailed in table 3.2. Equations 2.13, 2.15, and 2.16 were manipulated, as shown in table 3.3, to calculate the magnitudes of device and measurement parameters.

TABLE 3.1: Variable parameter upper and lower bounds for the electromagnetic analytical feasibility study.

Symbol	Description	Minimum	Maximum	Unit
m	Mass of the object to be measured	0.001	10,000	mg
B	Magnetic field	0.1		T
β	Sensing coil mass scale factor	2	1000	-
r_c	Sensing coil radius	20		mm
d	Wire diameter	25.4	50.8	μm
R	Current conversion resistor	1.00E+04	1.00E+07	Ω
u	Velocity of the sensing coil	0.1	10	mm/s
A	Amplifier gain	100	1000	-
h_{max}	Maximum displacement of the sensing coil	1		mm

TABLE 3.2: Constant values for the electromagnetic analytical feasibility study.

Symbol	Description	Value	Unit
ρ_{Cu}	Copper density	8960	kg/m^3
η_{Cu}	Copper resistivity	1.68E-08	Ωm
g	Local gravity	9.81	m/s^2

TABLE 3.3: Calculated parameters for the electromagnetic analytical feasibility study.

Symbol	Description	Equation	Unit
m_c	Mass of sensing coil	$m\beta$	mg
n	Number of turns in sensing coil	$2m_c/r_c\rho_{Cu}(\pi d)^2$	-
L	Length of sensing coil	$2n\pi r_c$	m
BL	Device characteristic	BL	Tm
R_c	Sensing coil resistance	$4\eta_{Cu}L/\pi d^2$	Ω
I_W	Weighing current	mg/BL	mA
V_W	Weighing voltage	$I_W R$	V
P	Power dissipated in the sensing coil (weighing phase)	$I_W^2 R_c$	μW
V_M	Moving voltage	BLu	V
t	Time available to obtain measurements (moving phase)	u/h_M	s

3.2 Predictions and Results

TABLE 3.4: Summary of the assumed and calculated parameters for an idealised model of electromagnetic Kibble balance in the range 10 g to 1 μg.

Symbol	**Unit**								
m_{target}	mg	10000	1000	100	10	1	0.1	0.01	0.001
Coil									
β	-	0.5	2	10	100	1000	1000	1000	1000
m_c	mg	5000	2000	1000	1000	1000	100	10	1
d	μm	50.8	50.8	50.8	50.8	50.8	25.4	25.4	25.4
n	-	2191	876	438	438	438	175	18	2
L	m	275	110	55	55	55	22	2.2	0.2
r_c	mm	20	20	20	20	20	20	20	20
R_c	Ω	2282	913	456	456	456	730	73	7.3
Magnetic field									
B	T	0.1	0.1	0.1	0.1	0.1	0.1	0.1	0.1
BL	Tm	27.5	11.0	5.5	5.5	5.5	2.2	0.22	0.02
Weighing									
I_W	mA	3.6	0.9	0.2	0.02	2E-03	4E-04	4E-04	4E-04
R	Ω	1E+03	1E+04	1E+04	1E+05	1E+06	1E+07	1E+07	1E+07
V_W	V	3.6	8.9	1.8	1.8	1.8	4.5	4.5	4.5
P	mW	29	1	1E-02	1E-04	1E-06	1E-07	1E-08	1E-09
Moving									
u	mm/s	0.1	0.2	0.2	0.2	0.2	0.5	5	10
A	-	1000	1000	1000	1000	1000	1000	1000	1000
V_M	V	2.8	2.2	1.1	1.1	1.1	1.1	1.1	0.2
h_M	mm	1	1	1	1	1	1	1	1
t	s	10	5	5	5	5	2	0.2	0.1
Uncertainty ($k = 1$)									
σ_m	kg	9E-07	9E-08	1E-08	1E-09	1E-10	1E-11	1E-12	4E-13
σ_m	ppm	86	86	113	113	113	107	121	373
Target uncertainty ($k = 1$)									
σ_{target}	ppm	2500	2500	2500	40	400	4000	5000	5000
$\Delta\sigma$	%	-97%	-97%	-95%	183%	-72%	-97%	-98%	-93%

The values of the variable and derived parameters of a simplified and idealised model of an electromagnetic Kibble balance including an estimate of the mass measurement uncertainty at each order of magnitude in the range 10 g to 1 μg are shown in table 3.4.

The values of the variable parameters were selected for each object mass m_{target} as follows. The sensing coil mass factor β was set such that it did not exceed 1000 and the mass of the coil m_c did not exceed 5 g. This was implemented in anticipation of designing a guidance mechanism in the next phase of this work. The aim was to reduce the impact of the sensitivity of the coil counter-balance mechanism on the total measurement uncertainty, specifically the larger the relative added mass of the object to be weighed, the higher the tolerance on the sensitivity requirement. The coil mass m_c and coil radius r_c of 20 mm were set to constrain the total size of the device to a footprint comparable with existing commercial micro-balances [69]. The diameter of the sensing wire d was chosen based on the coil mass. For $m_c \geq 1$ g a wire diameter of 50.8 μm was chosen to ensure a robust coil with a high number of turns. For $m_c < 1$ g, the wire diameter was halved to 25.4 μm to ensure a minimum number of turns ≥ 1. The magnitude of the magnetic field B was assumed to be 0.1 T at the coil radius r_c.

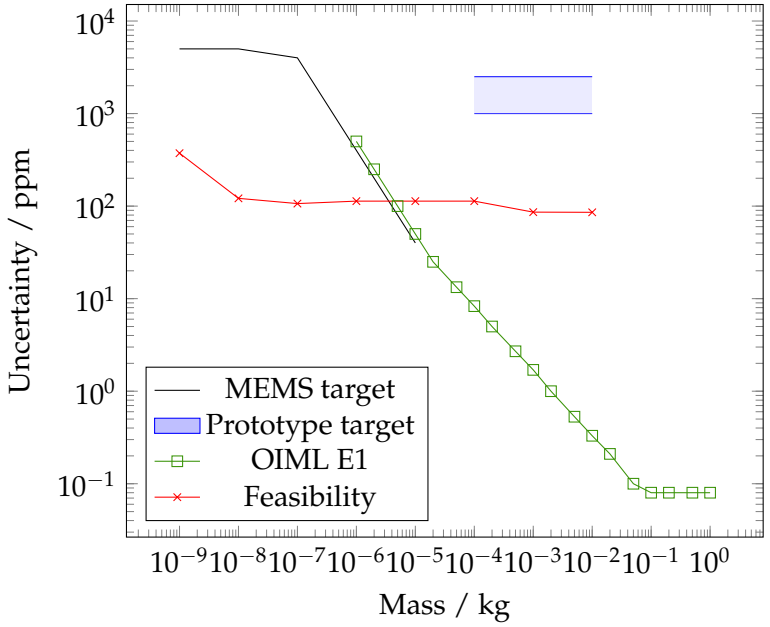

FIGURE 3.2: Comparison of uncertainty (at k=1) predicted by the feasibility study with OIML class E1 weights [17], and target uncertainties for a future MEMS Kibble balance and a 3D printed prototype.

Two options for generating a magnetic field were explored and the details reported in section 3.4. The maximum displacement h_{max} was set to 1 mm to ensure that the magnetic field uniformity assumption was met throughout the operation of the device. The value of resistor R was selected such that the weighing voltage V_W would be in the range 1 V to 10 V allowing a typical commercially available $\pm$10 V 20-bit ADC to be used for voltage measurement. The sensing coil was assumed to be driven at a constant speed during the moving phase such that the induced voltage V_M would be in the range 0.1 mV to 10.0 mV. The amplifier gain A was set to 1000 such that that the moving voltage V_M would be amplified into the measuring range of the ADC.

As shown in figure 3.2, the predicted total relative uncertainty in the range 10 g to 10 μg was more or less constant at around 100 ppm with a maximum variation of 35 ppm. The total relative uncertainty increased approximately four fold to 373 ppm at 1 μg. Details of the contributions to the uncertainty at 1 g, 1 mg, and 1 μg are included in tables 3.5, 3.6, and 3.7 respectively. The uncertainty evaluation was carried out in accordance with the JCGM document 'Guide to the expression of uncertainty in measurement'[78].

TABLE 3.5: Feasibility study uncertainty budget at 1 g.

Note	Contribution	Value	Unit	Unc. ($k = 1$)	Unit	Ratio	%
i	Gravity (g)	9.81	m/s^2	4.9E-04	m/s^2	5.0E-05	34%
ii	Phase alignment (γ)	1	-	5.0E-05	-	5.0E-05	34%
iii	Resistor (R)	1E+04	Ω	1.8E-01	Ω	1.8E-05	5%
iv	Weighing Voltage (V_W)	8.91	V	7.7E-05	V	8.6E-06	1%
iv	Moving Voltage (V_M)	2.20	V	7.7E-05	V	3.5E-05	16%
v	Amplification (A)	1000	-	1.4E-02	-	1.4E-05	3%
vi	Distance (h_M)	0.001	m	2.1E-08	m	2.1E-05	6%
vii	Time (t)	5	s	6.0E-05	s	1.2E-05	2%
		Total standard uncertainty ($k = 1$)				8.6E-08	kg
						86	**ppm**

TABLE 3.6: Feasibility study uncertainty budget at 1 mg.

Note	Contribution	Value	Unit	Unc. ($k = 1$)	Unit	Ratio	%
i	Gravity (g)	9.81	m/s^2	4.9E-04	m/s^2	5.0E-05	20%
ii	Phase alignment (γ)	1	-	5.0E-05	-	5.0E-05	20%
iii	Resistor (R)	1E+06	Ω	1.8E+01	Ω	1.8E-05	3%
iv	Weighing Voltage (V_W)	1.78	V	7.7E-05	V	4.3E-05	14%
iv	Moving Voltage (V_M)	1.10	V	7.7E-05	V	7.0E-05	38%
v	Amplification (A)	1000	-	1.4E-02	-	1.4E-05	2%
vi	Distance (h_M)	0.001	m	2.1E-08	m	2.1E-05	3%
vii	Time (t)	5	s	6.0E-05	s	1.2E-05	1%
		Total standard uncertainty ($k = 1$)				1.1E-10	kg
						113	**ppm**

TABLE 3.7: Feasibility study uncertainty budget at 1 μg.

Note	Contribution	Value	Unit	Unc. ($k = 1$)	Unit	Ratio	%
i	Gravity (g)	9.81	m/s^2	4.9E-04	m/s^2	5.0E-05	2%
ii	Phase alignment (γ)	1	-	5.0E-05	-	5.0E-05	2%
iii	Resistor (R)	1E+07	Ω	1.8E+02	Ω	1.8E-05	0%
iv	Weighing Voltage (V_W)	4.45	V	7.7E-05	V	1.7E-05	0%
iv	Moving Voltage (V_M)	0.22	V	7.7E-05	V	3.5E-04	87%
v	Amplification (A)	1000	-	1.4E-02	-	1.4E-05	0%
vi	Distance (h_M)	0.001	m	2.1E-08	m	2.1E-05	0%
vii	Time (t)	0.1	s	1.1E-05	s	1.1E-04	9%
		Total standard uncertainty ($k = 1$)				3.7E-13	kg
						373	**ppm**

i. The local gravity value was 9.81 m/s^2 [79] with an assumed uncertainty of 50 ppm based on determining local gravity by calculation rather than measurement. This allows the balance to be used without the prerequisite of a precise local gravity measurement which is essential to meet the requirement of a "low cost" device.

ii. Uncertainty due to difference in alignment of the sensing coil and the magnetic field between weighing and moving phase was assumed to be approximately 50 ppm [35]. This value was selected to take into account the repeatability of motion of the mechanical system manufactured from 3D printed PLA parts.

iii. Resistor uncertainty was calculated from the root-sum-square (RSS) combination of calibration, drift and temperature dependence uncertainties based on a Vishay HZ Series (Z-foil) resistor [80]. Calibration uncertainty was assumed to be 10 times NPL's UKAS accreditation [30]. A stability of 2 ppm (over 6 years unloaded) and temperature coefficient of 0.2 ppm/°C were specified for the resistor. Since the current applied to the resistor is very low the long term stability value has been assumed. A working temperature of 20 ± 20°C has been assumed for uncertainty due to a change in resistor temperature.

iv. Voltage uncertainty was calculated as the RSS of calibration, drift and ADC resolution. 20 bit ± 10 V Analogue to Digital Converter (ADC) calibrated against a high precision and stability voltage reference has been assumed. A conservative estimate of ADC calibration uncertainty of 5 ppm at 10 V based on NPL's UKAS accreditation schedule [30]. Long term stability of 10 ppm assumed based on a Linear Technology voltage reference [81]. ADC resolution calculated $\frac{10 \times 2}{2^{20}} = 19.07\,\mu$V [82].

v. Amplification of induced voltage during the moving phase was assumed to be carried out using a matched pair of Vishay HZ Series (Z-foil) resistors [83]. The calibration, drift and temperature uncertainty contributions were combined RSS. Calibration uncertainty based on ten times NPL UKAS accreditation schedule [30]. Matched resistors with a tracking temperature coefficient of 0.5 ppm/°C. A working temperature of 20 ± 20°C has been assumed for uncertainty due to a change in temperature of these resistors.

vi. Displacement uncertainty was based on an optical encoder system [84] assuming an absolute uncertainty of 20 nm plus a conservative relative uncertainty of 10 ppm of the displacement [35].

vii. The moving phase measurement time was assumed to be known with an absolute uncertainty of 10 μs plus a conservative relative uncertainty of 10 ppm [35].

3.3 Discussion

In the mass range 10 g to 100 μg, the number of turns in the coil n appeared sufficiently high ($\geq$175) to enable the manufacture of a robust coil with relative ease. Although at 100 μg it was necessary to select a wire of diameter $d = 25.4\,\mu$m instead of 50 μm which may cause a higher failure rate during manufacture. The high number of turns in the coil resulted in a BL product of between 2 Tm and 27 Tm which was an advantage during moving phase. The calculated BL enabled the velocity of the coil u to be kept relatively low (between 0.1 mm/s and 0.5 mm/s) resulting in between 2 s and 10 s to collect moving phase data. This time scale provides the opportunity to collect a higher number of data points. The induced voltage $V_M \geq$1.1 mV was amplified into the measurement range of the 10 V ADC with an assumed amplifier gain of 1000. This magnitude of amplification is not ideal as it has the potential to introduce a large source of uncertainty into the measurement. The calculated power P dissipated in the coil as a result of the weighing current I_W ranged from very low (29 μW) to negligible (10 pW) therefore self-heating effects are expected to be minimal at these mass scales.

At 10 μg and below, the coil with a wire diameter of 25.4 μm had fewer than 20 turns. This could cause significant performance issues in terms of reliability and alignment. The power P dissipated in the coil as a result of the weighing current I_W was exceptionally low $\leq$1 pW, therefore self-heating effects are expected to be negligible. As a result of the low number of turns in the coil, the BL product was less than 1. The velocity of the coil u needed to be higher than 1 mm/s to induce a voltage V_M that was inside the measurement capabilities of the assumed $\pm$10 V 20 bit ADC. This is a disadvantage as it reduces the amount of time t available to make the measurement to between 100 ms and 200 ms. This is likely to increase the signal to noise ratio.

Inspection of the 1 mg and 1 μg uncertainty budgets (tables 3.6 and 3.7) revealed that the higher total relative uncertainty at 1 μg was due to a significant decrease in the measured voltage during the moving phase from 1.1 V to 0.22 V respectively. The induced voltage was limited by the BL product, the velocity of the coil u, and the displacement distance. At 1 μg the BL product of the device was two orders of magnitude smaller than at 1 mg. The displacement distance was fixed at a maximum of 1 mm therefore the coil velocity was increased to compensate for the lower BL product. 10 mm/s was selected as the maximum velocity of the coil to keep the minimum time available for data collection feasible, specifically 100 ms resulting in $\sim$ 9% of the total uncertainty.

It is possible to reduce the uncertainty component due to coil velocity u in a number of ways such as increasing the BL product, increasing displacement h_{max}, or reducing the uncertainty component due to time measurement. However, all of these options result in compromises.

To increase BL product either a stronger magnetic field B or more turns n in the sensing coil are required. B is limited by magnetic material properties. In general a larger magnet will be required to increase B and, if coil mass scale factor β is to be maintained at ≤ 1000 a smaller wire diameter d will need to be used. Increasing the volume of magnetic material is not compatible with manufacturing a smaller device and a smaller wire diameter d is likely to result in reliability problems. Increasing the number of turns n would be an advantage in terms of increasing structural stability however it would result in a coil mass scale factor β of greater than 1000 which will have consequences for the required tare mass mechanism sensitivity and guidance mechanism performance.

Figure 3.2 shows the feasibility study uncertainties plotted against the target uncertainties for this work and commercially available OIML class E1 weights. As expected, the results confirm that a "low cost" Kibble balance will not be competitive in terms of uncertainty for masses greater than 10 mg. However, the results also show that there is a fair prospect of achieving competitive results with a future 3D printed MEMS Kibble balance developed for masses of 1 mg and below. The feasibility study calculations were based on simplified parameters and assumed an idealised model of the Kibble principles. Factors such as the guidance mechanism and measurement noise were not included. 3D printed parts are likely to introduce additional uncertainty due to manufacturing tolerances and unquantified or unpredictable material properties. It is likely that the uncertainty achieved with a 3D printed prototype at the gram-level will be higher than predicted by this feasibility study however these results show that there is a good prospect of achieving the target uncertainty of between 0.1% and 0.25%.

3.4 Magnetic Field Generation

The aim of this section was to evaluate options for generation of a magnetic field suitable for inclusion in a Kibble balance.

The generated magnetic field was required to be radial $\propto \frac{1}{r}$ with a magnitude greater than or equal to 0.1 T at the radius of the sensing coil. It was also required to be uniform along the z-axis over the range of motion of the sensing coil.

It was imperative that the quantity BL remains constant between weighing and moving measurement phases for the Kibble principle to apply. If the magnetic field follows a radial distribution then changes in the radius of the sensing coil during operation have no impact on the quantity BL. Uniformity along the z-axis is preferred to reduce measurement uncertainty. A magnitude greater than or equal to 0.1 T has been selected as a starting point value.

3.4.1 Helmholtz Coil

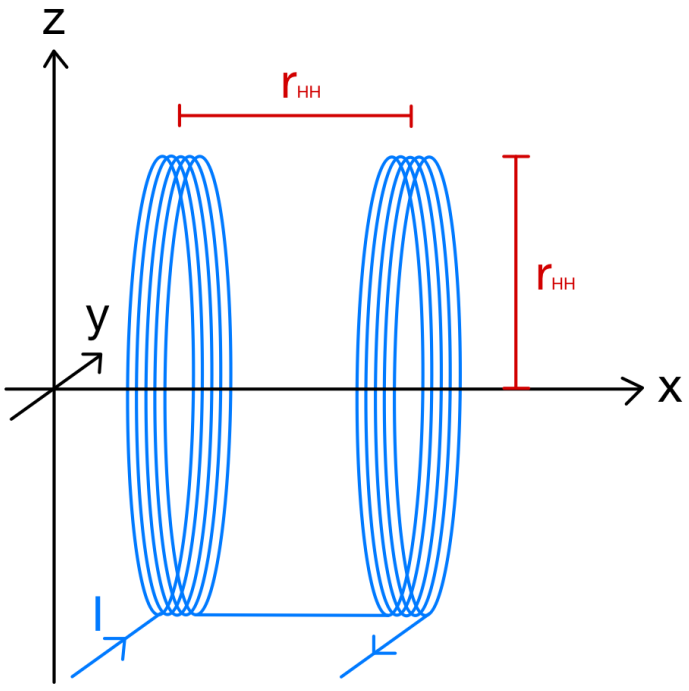

FIGURE 3.3: A Helmholtz coil of radius r_{HH} aligned to the x axis carrying current I.

A Helmholtz coil, as shown in figure 3.3, is a device that can be used to generate a uniform magnetic field. The field generated is a combination of two magnetic fields produced by identical circular current-carrying coils of wire aligned symmetrically on

axis and spaced at a distance equal to the coil radius. In a conventional Helmholtz coil the current carried in the coils is matched both in magnitude and direction. The resultant magnetic field along the axis of symmetry can be derived from the Biot–Savart law and is given by equation 3.2:

$$B = \left(\frac{4}{5}\right)^{\frac{3}{2}} \frac{\mu_0 N}{r_{HH}} I \tag{3.2}$$

Where μ_0 is the permeability of free space, N is the number of turns per coil, r_{HH} is the radius of the coils and I is the current carried in the coils.

3.4.2 Anti-Helmholtz Coil

The orientation and mathematical form of the magnetic field produced by a Helmholtz coil can be changed by flowing the current in the coils in opposite directions. This is called a reverse or anti-Helmholtz coil. In this configuration, the resultant magnetic field is parallel to the plane of the coils however it is non-trivial to solve analytically. COMSOL Multi-physics® simulation software was used to gain knowledge of the magnetic field produced by an anti-Helmholtz coil. Four geometries have been simulated as detailed in figure 3.4 and table 3.8.

TABLE 3.8: Summary of anti-Helmholtz coil simulation parameters. Four geometries A-D were simulated with four different currents. The direction of the current in the coils was in opposition to each other.

Symbol	Description	Unit	A	B	C	D
r_{AH}	Coil radius	mm	20	30	40	50
H_c/r_{AH}	Ratio - coil profile height to radius	-	0.1			
W/H_c	Ratio - coil profile width to profile height	-	1			
H_c	Coil profile height	mm	2	3	4	5
W	Coil profile width	mm	2	3	4	5
A_c	Coil profile area	mm^2	4	9	16	25
p	Coil packing factor	-	0.75			
N	Number of turns in the coil	-	350			
a	Wire area	mm^2	0.009	0.019	0.034	0.054
d	Wire diameter	mm	0.104	0.157	0.209	0.261
I_0	Current in the coil	mA	80, 160, 240, 320			
r_{sph}	Sphere of air radius	mm	200			
s_{sph}	Sphere of air layer thickness	mm	50			

The parameters were selected based on the following rationale. The coil radius r_{AH}, coil profile height to radius ratio H_c/r_{AH}, and coil profile width to height ratio W/H_c were chosen to keep the overall device dimensions comparable to existing commercial micro-balances. The coils were assumed to have been constructed by 'wild' winding and therefore a packing factor $p = 0.75$ was assigned. The number of turns per coil N was selected such that the resultant wire diameter would be greater than 100 μm for

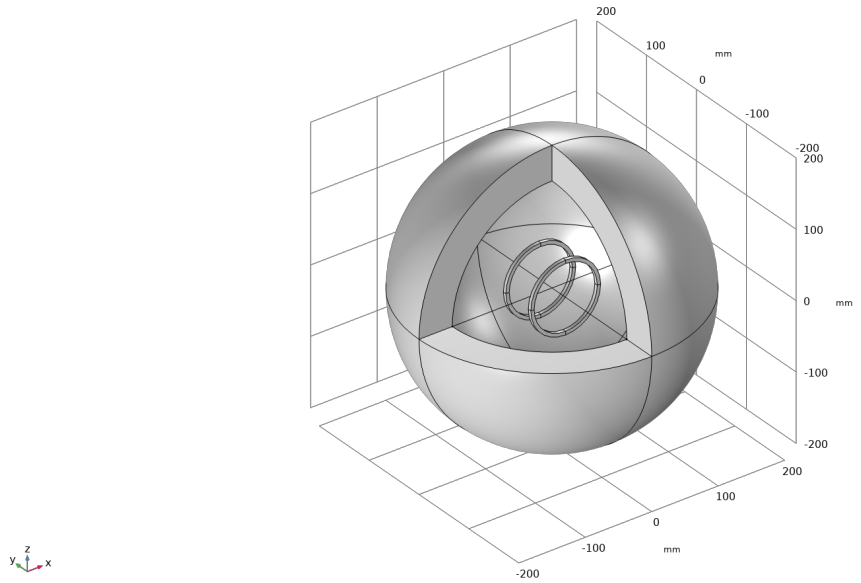

(A) Anti-Helmholtz coil pair centred inside a sphere of air with line segments along the x-axis and y-axis. The coils were spaced at a distance equal to the coil radius.

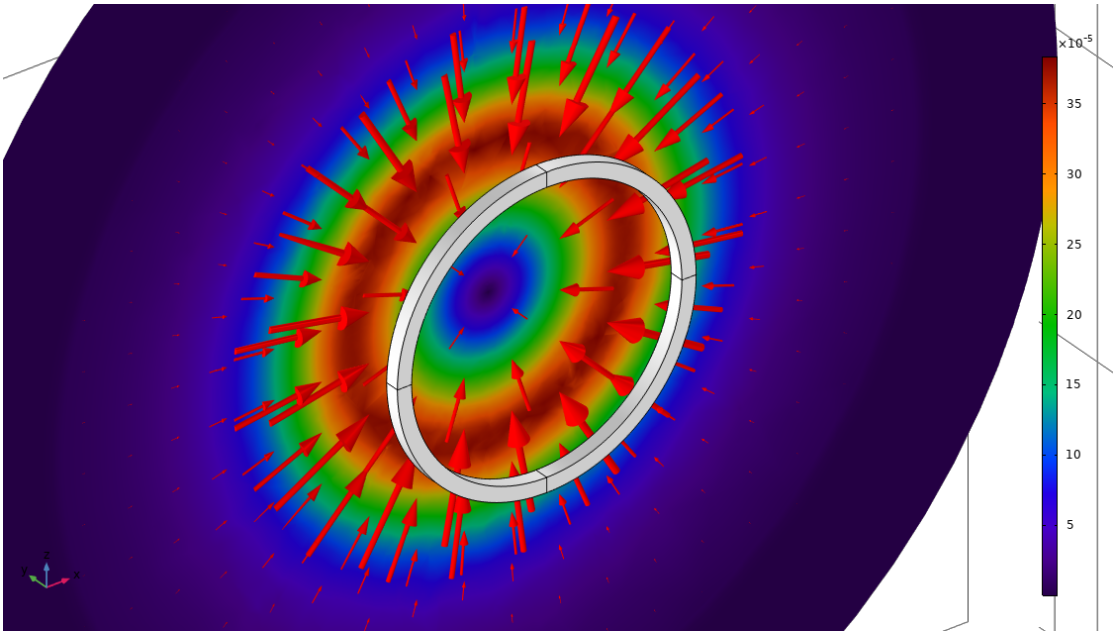

(B) Magnetic field arrows on the x-z plane between the anti-Helmholtz coil pair.

FIGURE 3.4: Anti-Helmholtz coil COMSOL Multiphysics® simulation geometry.

all geometries. The current carried in the coil I_0 was chosen to be 80 mA. This value was approximately the average maximum recommended current for the four geometries if constructed with wire diameter d as specified in table 3.8. Simulations in COMSOL Multiphysics® require a boundary condition to be set. A sphere of air of radius four times the radius of the largest coil was selected as the boundary condition for all geometries.

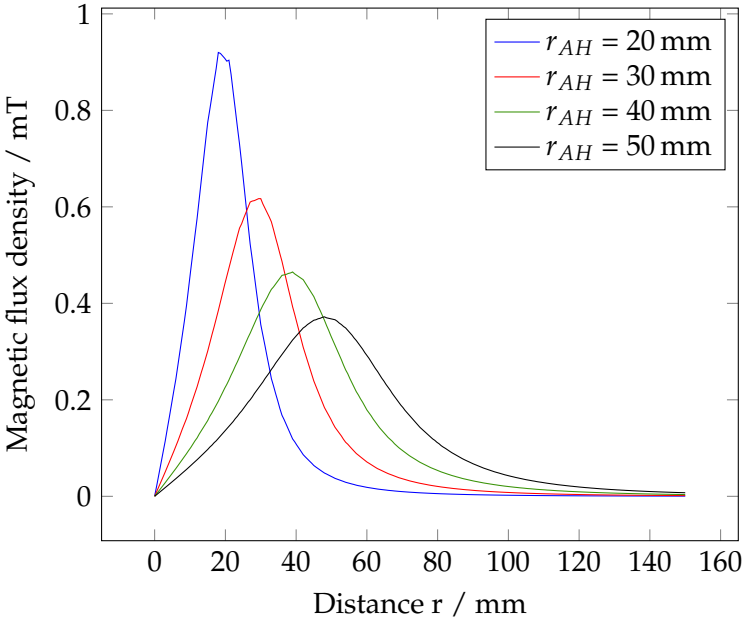

FIGURE 3.5: Anti-Helmholtz coil magnetic field along the radial axis equidistant between the coils for geometries A-D with I_0 = 80 mA.

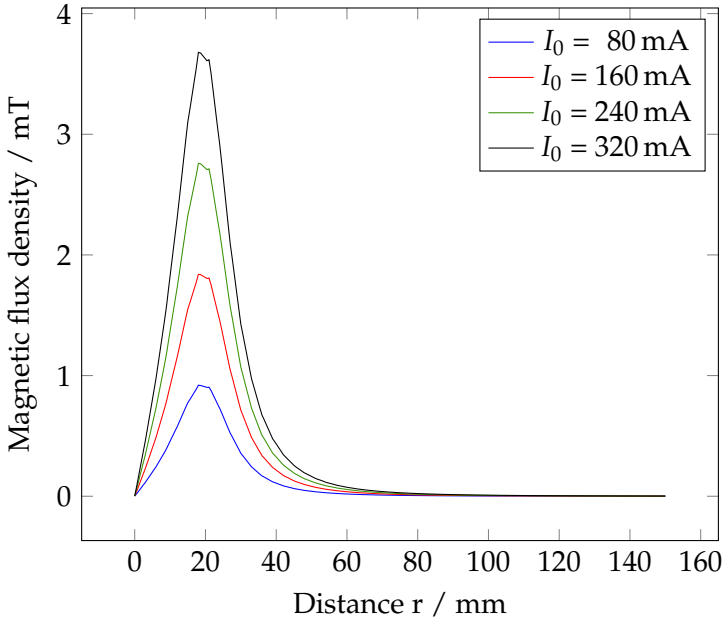

FIGURE 3.6: Anti-Helmholtz coil magnetic field along the radial axis equidistant between the coils for geometry A with I_0 set to four different values.

Figure 3.5 shows the predicted magnetic flux density along the axis parallel to and equidistant between the coils. From this figure it can be observed that the maximum predicted value of the magnetic field is less than 1 mT for all geometries and the maximum in each case is located at a distance r slightly greater than the coil radius r_{AH}. For constant current I_0, the maximum magnetic flux density decreases with increasing coil radius. At radii less than the coil radius r_{AH} the form of the magnetic field appears non-linear and complex. This does not fit the requirements for a Kibble balance and therefore the sensing coil cannot be placed in this region.

Magnetic flux density in the region $r > 1.5r_{AH}$ to r =150 mm, was fitted with four different equations.

TABLE 3.9: Results of fitting four equations to the magnetic flux density data in the region $r > 1.5r_{AH}$ from the anti-Helmholtz coil simulation with a current of 80 mA shown in figure 3.5.

Fit	Equation	Adjusted R squared			
		A	B	C	D
$1/r$	$c0 + c1(1/r)$	0.7424	0.8207	0.8815	0.9274
$1/r^2$	$c0 + c1(1/r) + c2(1/r^2)$	0.9840	0.9932	0.9975	0.9993
exp 1	$c0\exp(c1r)$	0.9862	0.9563	0.9795	0.9907
exp 2	$c0\exp(c1r) + c2\exp(c3r^2)$	0.9958	0.9996	1.0000	1.0000

The adjusted R squared statistics in table 3.9 suggest that the magnetic flux density in this region has a more complex relationship with distance than $\frac{1}{r}$ especially at smaller geometries. The shape of the magnetic field tends towards a $\frac{1}{r}$ relationship with increasing coil radius r_{AH} as shown by the increase in adjusted R squared from 0.7424 for model A ($r_{AH} = 20$ mm) to 0.9274 for model D ($r_{AH} = 50$ mm).

To investigate how the field changes with current, the simulations were run again with multiples of the original I_0 current. The results for geometry A are shown in figure 3.6.

The data in figure 3.6 showed that the magnitude of the magnetic field $|B|$ was directly proportional to the current I_0 on a one to one basis. Therefore, for geometry A (sensing coil radius of 20 mm) a current of approximately 22 A was required to generate 0.1 T of magnetic flux density at a distance of $1.5r_{AH}$. This current exceeded the recommended maximum current capacity for the wire (21.3 mA [85]) by over 1000 times. This result showed that an anti-Helmholtz coil was not a feasible method of magnetic field generation for a Kibble balance at the mass scales considered in this work. This conclusion is consistent with the consensus in the literature. Many if not all existing electromagnetic Kibble Balances utilise a permanent magnetic circuit [86]. Conventional coils such as the ones considered in this feasibility study are not used due to the low magnitude magnetic field produced. Superconducting coils such as those in the NIST-3 Kibble balance are extremely large, expensive, and time consuming to operate [87]. This system was rejected in favour of a yoke based permanent magnet when planning the NIST-4 Kibble balance [88].

3.4.3 Permanent Magnets

Identical circular permanent magnets positioned on axis and orientated with like poles facing each other can produce a magnetic field with similar characteristics to that generated by an anti-Helmholtz coil.

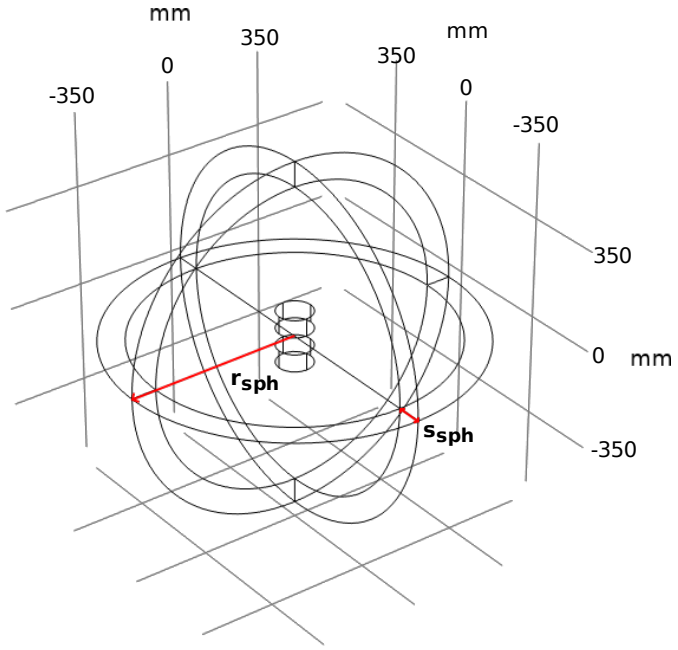

(A) Wire-frame view of identical cylindrical magnets centred inside a sphere of air with a line segment.

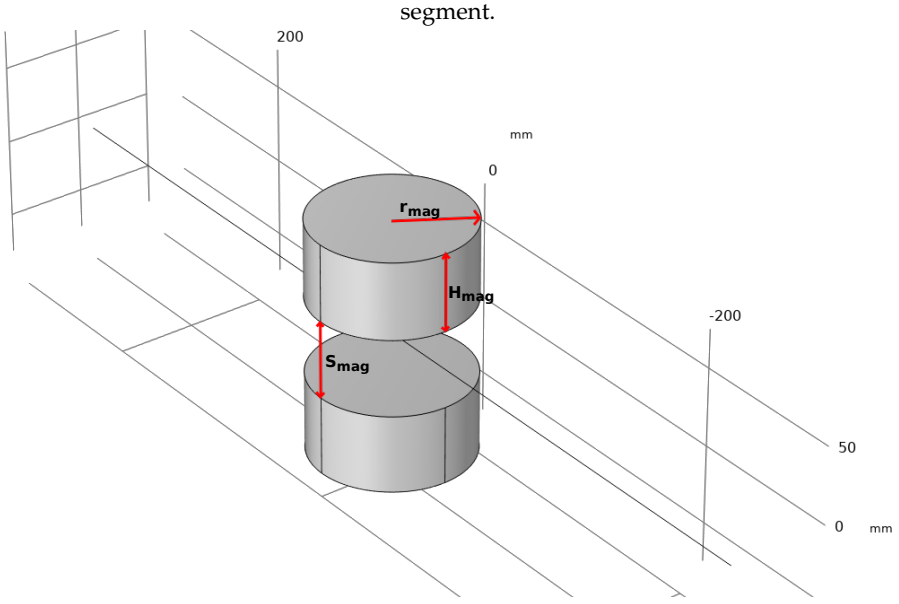

(B) Magnet pair spaced with a gap S_{mag} between their faces equal to their radius r_{mag}.

FIGURE 3.7: Permanent magnet COMSOL Multiphysics® simulation geometry.

Four geometries were simulated using COMSOL Multiphysics® as detailed in figure 3.7 and table 3.10.

Magnet radii r_{mag} and separation S_{mag} were selected to keep the overall device parameters comparable to existing commercial micro-balances and to allow a direct comparison with the anti-Helmholtz simulation. Magnet height H_{mag} was assumed to be equal to its radius as per a range of commercially available NdFeB disc magnets (from supermagnate.de [89]). The magnets were assigned the material properties of 'N45 (Sintered NdFeB)' selected from the COMSOL Multiphysics® library (1.05 recoil permeability and 1.35 T remanent flux density). The assumed remanent magnetic flux density was in agreement with the specification of a commercially available neodymium magnet [90]. A sphere of the air was used as a boundary condition. Its radius was set at seven times the radius r_{mag} of the largest magnet geometry.

TABLE 3.10: Summary of permanent magnet simulation parameters. The magnetic material was assumed to be N45 (Sintered NdFeB) and the default COMSOL library material properties used.

Symbol	Description	Unit	A	B	C	D
r_{mag}	Magnet radius	mm	20	30	40	50
H_{mag}	Magnet height	mm				
S_{mag}	Magnet separation (gap between faces)	mm				
r_{sph}	Sphere of air radius	mm	350			
s_{sph}	Sphere of air layer thickness	mm	50			

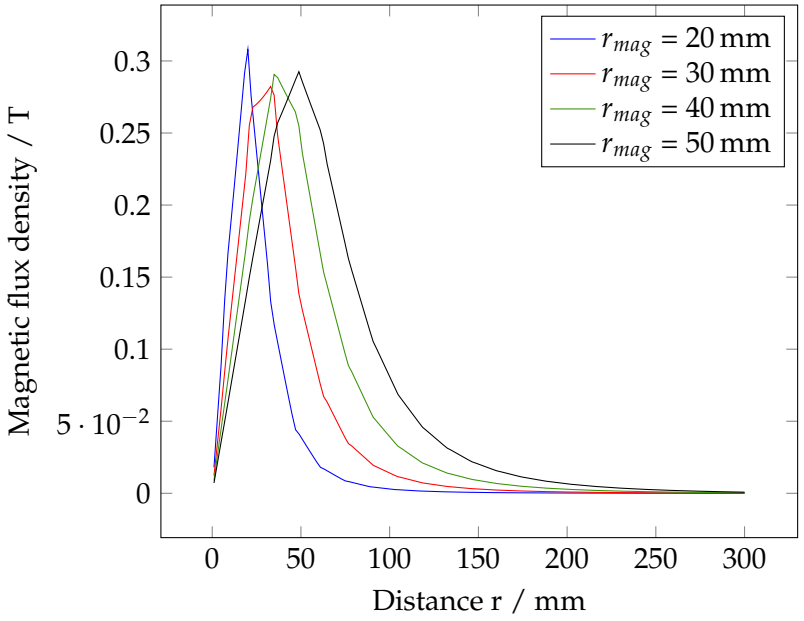

FIGURE 3.8: Magnetic field generated by permanent magnet pair along the radial axis equidistant between the magnets for geometries A-D.

Figure 3.8 shows the predicted magnetic flux density along the axis parallel to and equidistant between the magnets. It was observed that at radii less than the radius of the magnet $r < r_{mag}$ the form of the magnetic field appeared non-linear and complex. This did not fit the requirements for a Kibble balance and therefore the sensing coil should not be placed in this region. The peak magnetic flux density of each geometry was a similar magnitude with $|B_{max}| \sim 0.3$ T.

Data in the region $r > 1.5r_{mag}$ to r =300 mm was fitted with four different equations. The results are shown in table 3.11. The adjusted R squared statistics suggested that the magnetic flux density in this region had a similar form to the magnetic field generated by the equivalent radius anti-Helmholtz coil and changed in the same way, specifically it tended towards a $\frac{1}{r}$ relationship with increasing magnet radius r_{mag} with model D (r_{mag} = 50 mm) having the highest adjusted R squared value for this fit.

TABLE 3.11: Results of fitting four equations to the magnetic flux density data in the region $r > 1.5R_{mag}$ from the permanent magnets simulation.

Fit	Equation	Adjusted R squared			
		A	B	C	D
$1/r$	$c0 + c1(1/r)$	0.7775	0.8303	0.8735	0.9058
$1/r^2$	$c0 + c1(1/r) + c2(1/r^2)$	0.9959	0.9984	0.9993	0.9996
exp 1	$c0\exp(c1r)$	0.9975	0.9978	0.9981	0.9983
exp 2	$c0\exp(c1r) + c2\exp(c3r^2)$	0.9989	0.9996	0.9998	0.9999

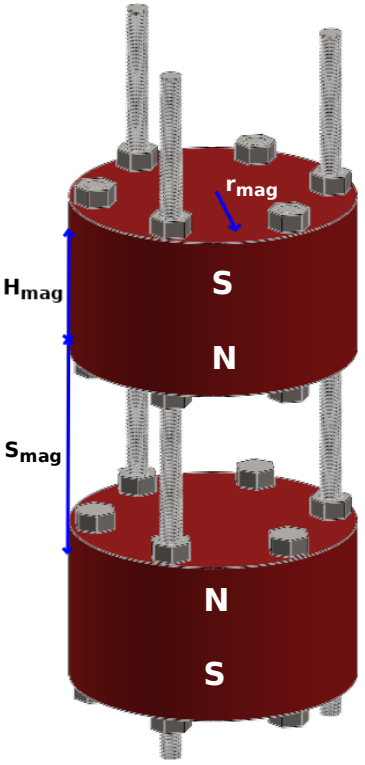

FIGURE 3.9: Permanent magnet experimental setup.

To verify the predicted magnetic field data produced by the COMSOL Multiphysics® simulations a simple magnet model was set up in the laboratory. Two neodymium, iron, and boron (NdFeB) alloy magnets [90] with radius r_{mag} and height H_{mag} of 35 mm were set up with like poles (north) facing each other at a separation distance S_{mag} of 55 mm and 65 mm. The magnets were encased in 3D printed plastic boxes with alignment holes. Stainless steel studding and nuts were used to align and space the magnets as shown in figure 3.9.

Magnetic flux density measurements were taken at 5 mm and 10 mm intervals in a radial direction on the plane midway between the magnet faces starting in line with outer edge of the plastic boxes. Taking into account the 13 mm wall thickness of the plastic boxes the first data point was collected at $r = 48\,\text{mm}$ (or $r = r_{mag} + 13\,\text{mm}$). An AlphaLab DC Magnetometer set to range 1999.99 was used to make the measurements. Data were collected with the probe in two orientations 180° apart. The average of the magnitude of these reading are reported and compared with the equivalent COMSOL Multiphysics® simulation data as shown in 3.10.

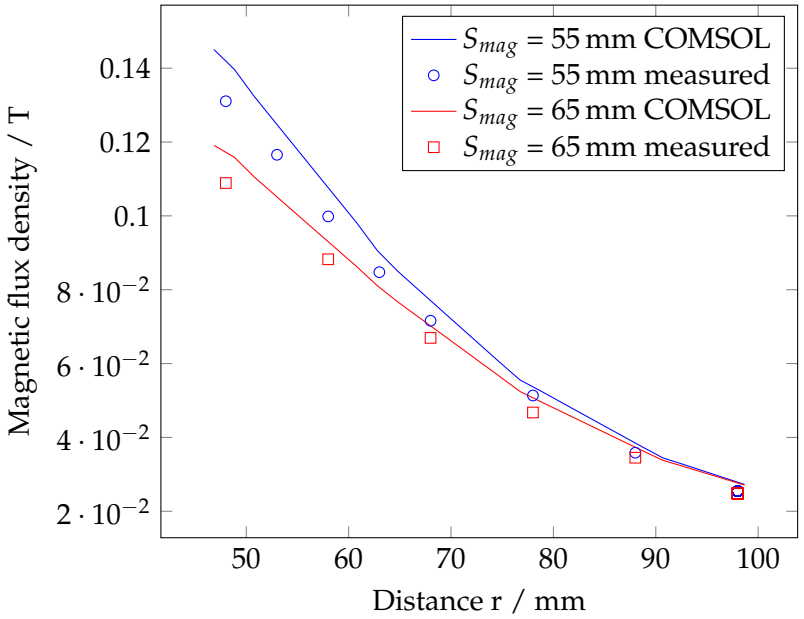

FIGURE 3.10: Comparison of permanent magnet predicted magnetic field with measured data for N45 NdFeB magnets of dimensions r_{mag} = 35 mm, H_{mag} = 35 mm at two separations S_{mag}.

Figure 3.10 shows that the COMSOL Multiphysics® predicted magnetic field data agrees to within $\sim$ 10% of the measured magnetic flux density at both magnet separations. In both cases the measured magnetic field was of lower magnitude than predicted, however a magnetic flux density of $\geq 0.1\,\text{T}$ at $r = r_{mag} + 15\,\text{mm}$ was observed which matches the assumed magnetic field magnitude used in the feasibility study. This experiment verified that the COMSOL Multiphysics® models are accurate to within $\sim$ 10% giving confidence in the feasibility study assumptions.

The permanent magnet feasibility studies indicated that a pair of permanent magnets could be used to generate a radial magnetic field of $\geq$0.1 T at coil radii required for a Kibble balance.

3.5 Summary

In this chapter the feasibility of creating a "low cost" Kibble balance device optimised for measurement of masses in the range 10 g to 1 μg was investigated.

A study focused on the scale of the sensing coil and consequent adjustment of the electrical measurement systems and operation parameters showed that there was a good prospect of achieving the target measurement uncertainty at sub-milligram masses.

A second study focused on methods of generating a magnetic field of 0.1 T or higher at the size of the sensing coil was carried out. The feasibility of two options, anti-Helmholtz coils and a pair of opposing permanent magnets, were explored. The results showed that anti-Helmholtz coils were not a feasible option for generating the required magnetic field magnitude with peak magnetic field values of less than 1 mT. The permanent magnet model was shown to generate a magnetic field of the required field strength and shape.

The results of the feasibility studies carried out in this chapter showed that there was a reasonable prospect of creating a working 3D printed Kibble balance at the gram-level with the potential for scaling to the sub-milligram level.

Chapter 4

Prototype

In this chapter the design, manufacture, assembly and initial testing of a 3D printed gram-level Kibble Balance is presented. Part of this work, specifically the mechanical design, was published at the Joint IMEKO TC3|TC5|TC16|TC22 International Conference in 2022 [1]. The design was based on some of parts and subsystems of the existing NPL Demonstration Kibble balance.

4.1 Background

The NPL Demonstration Kibble Balance (Figure 4.1) was developed for the celebration of the redefinition of the kilogram in 2019. Its primary purpose was to serve as a tool for public engagement and in the lead up to 20 May 2019 it was used to raise awareness of the significance of the redefinition of the kilogram by practical demonstration of the Kibble technique [91].

The Demonstration Balance system was designed to be portable and comprise all the components of a working Kibble balance such as a magnet, coil, tare mechanism, guidance mechanism, current source, voltage measurement, velocity measurement, real time computer, balance control software, and mass lift. The design was inspired by the planned NPL "Next Generation" Kibble balance [92] and thus benefits from the advantages of reduced alignment errors [93]. The Demonstration Balance differs from the "Next Generation" balance in a few important ways. Firstly, it operates in air removing the need for a vacuum chamber. Secondly, voltage measurements are made by conventional electrical and resistance standards rather than requiring a JJA and Quantum Hall Resistance (QHR) Standard held at the temperature of liquid helium (4.2 K). Thirdly, an encoder is used to make position and velocity measurements instead of a laser interferometer. Finally, spherical masses up to a nominal value of 50 g can be measured, five times less than specified for the "Next Generation" balance.

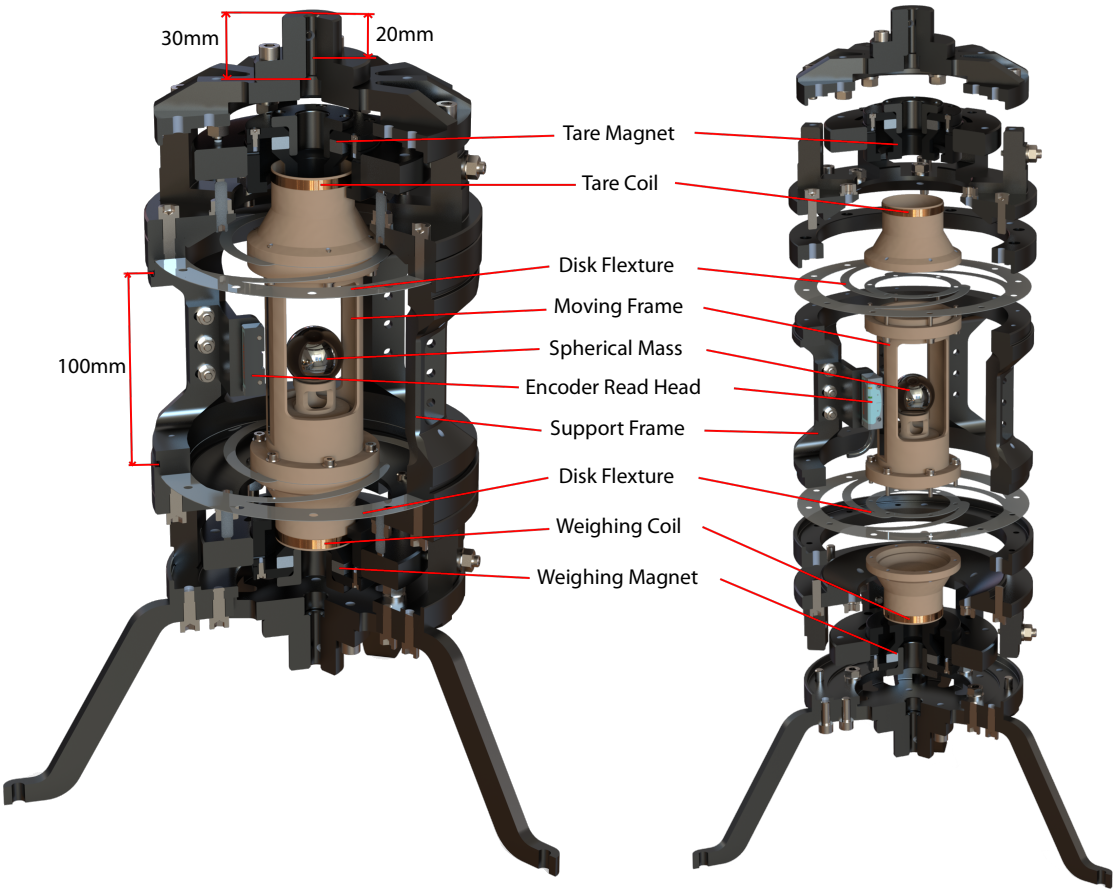

FIGURE 4.1: NPL Demonstration Kibble balance CAD section views.

Post redefinition a secondary purpose for the Demonstration Balance has come to the fore. This system can act as a stepping stone to the measurement of smaller masses via the Kibble principles. The balance is fitted with a bifilar measurement coil, the control software was updated to the same specification as the "Next Generation" balance, and a new simplified frequency counter which takes continuous velocity measurements (to match the measurements taken by the voltmeter) has been developed. This approach to velocity measurement was adopted to reduce the adverse effects of external vibration which is a common source of noise in Kibble balance measurement data [94]. The modified Demonstration Balance system has informed the design of a low cost 3D printed Kibble balance system aimed at measuring between 1 g and 10 g. The purpose of this prototype is to set the basis for future work on the development of a 3D printed MEMS micro Kibble balance with a target measurement range of 1 mg and below [35].

4.2 Design

One of the aims of the 3D printed prototype balance was to be a simplified and low-cost system for realising mass. To achieve these aims the Demonstration Balance system design was used as a baseline. Starting from a working system meant that the number of new parts to be designed and manufactured was significantly reduced. Some sub-systems and components were incorporated directly from the Demonstration Balance design including the RTC, software, electronics box, CotS optical linear encoder, magnet, and magnet holder.

This section will focus on the design of the components and sub systems created specifically for the 3D printed prototype balance. These include the moving frame, support frame, guidance and counterbalance mechanism, and coils and are shown in Figure 4.2, Figure 4.3 and Figure 4.4.

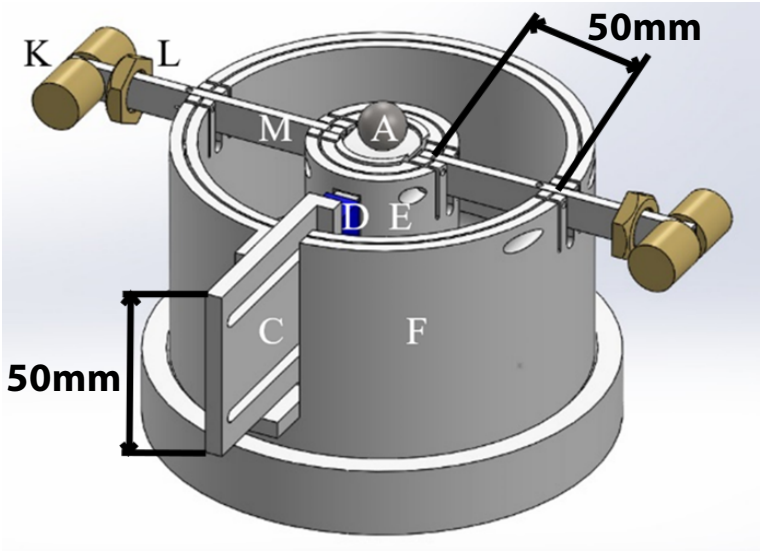

FIGURE 4.2: 3D printed Kibble balance external view. The support frame (F), moving frame (E), balance arms (M), encoder mount (C), and a spherical test mass (A) are shown in grey. The encoder read head (D) is shown in blue. The counterbalance tare masses (K), including fine adjustment nuts (L), are shown in yellow [1] © 2022 IMEKO.

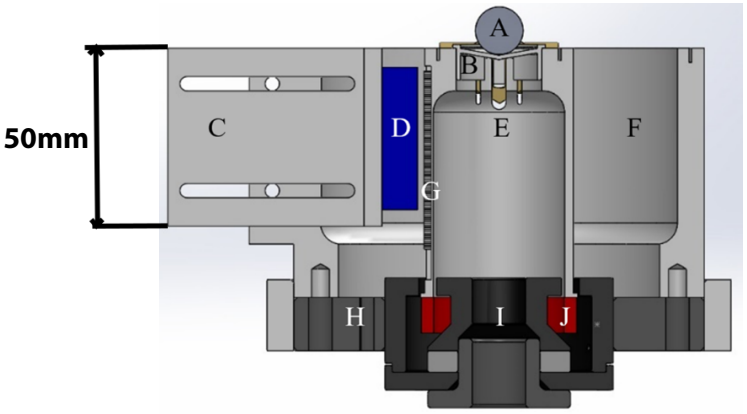

FIGURE 4.3: 3D printed Kibble balance cross-section shown perpendicular to the balance arms. The support frame (F), moving frame (E), balance pan (B), encoder mount (C), and spherical test mass (A) are shown in grey. The encoder read head (D) is shown in blue and the encoder scale (G) is shown in black and white. The magnet (I) and magnet holder (H) are shown in dark grey and black respectively. The tare and main coils assembly (J) is shown in red [1]

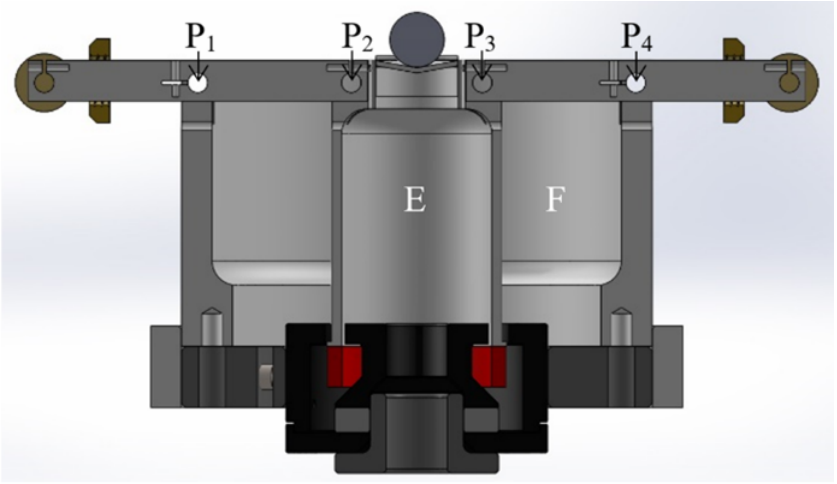

FIGURE 4.4: 3D printed Kibble balance cross-section shown parallel to the balance arms. The locations of four double-ended cross flexure bearings are indicated by P_1 to P_4. The support frame (F) and moving frame (E) have symmetrical geometry, therefore the distance between P_4 and P_3 was equal to the distance between P_1 and P_2 (50 mm) [1]

4.2.1 Magnet and Coils

The first simplifying design choice was to include only one magnet. The existing Demonstration Balance magnet was incorporated directly without any changes. Therefore, the new tare/drive coil and main coil were designed to fit inside the existing magnet gap and were wound one on top of the other forming a single unit, shown in red in Figure 4.3 and Figure 4.4.

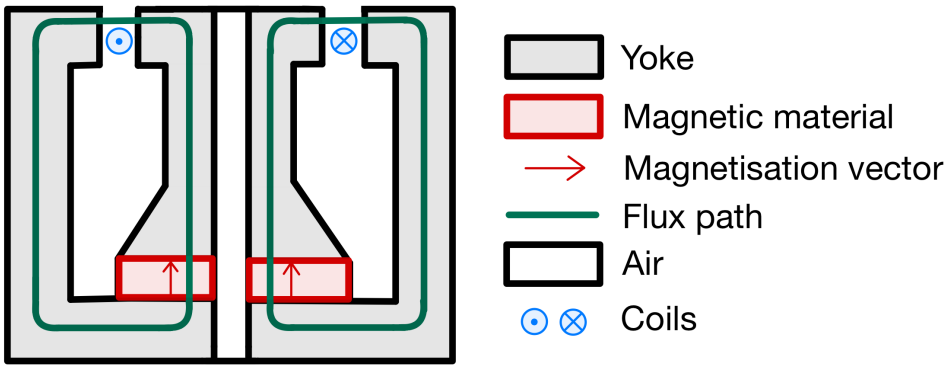

FIGURE 4.5: Simplified schematic diagram of the NPL Demonstration Kibble balance magnet. Not to scale.

The Demonstration Balance magnets were made from CotS ring-shaped NdFeB magnetic material and bespoke steel yoke pieces [95]. The system is closed at the base with the magnetic material attached to the inner yoke and the magnetic flux is guided through a single air gap. This design, shown in figure 4.5, is similar to the LNE type magnet [96] except for the position of the magnetic material and also equivalent to the lower half of a BIPM type magnet [97]. These designs and others are summarised in [86].

Both coils were constructed from the same 0.125 mm diameter insulated copper wire however the drive/tare coil consisted of a single strand of wire whilst the main coil was 'bifilar', specifically made from a twisted pair of wires. The two coil unit was 10 mm in height and approximately 30 g in mass. It was 'self supporting', with all wires secured together by an epoxy resin, and glued concentrically to the bottom face of the moving frame. The magnetic field B inside the gap of a typical Demonstration Balance magnet was approximately 0.17 T. The lengths of both coils were optimised to produce a BL product of approximately 2.5 Tm for the tare/drive coil (15 m) and 4 Tm for the main coils (24 m each).

4.2.2 Moving Frame

The moving frame was located inside the central structure (support frame) and supports the coils, encoder scale, and the mass pan. It was 3D printed using generic PLA material with a fill factor of 15% to keep the total mass of the moving frame assembly (coils, moving frame, encoder scale, mass pan) to approximately 80 g. The mass pan was conical to ensure spherical masses were positioned safely and centrally.

4.2.3 Support Frame

The support frame was the outer support structure for the encoder read head mount and the pivot points for the counterbalance mechanism. It was designed to fit on to the existing Demonstration Balance magnet holder which has the facility to adjust the relative position of the magnet with respect to the moving assembly. The support frame was also 3D printed from generic PLA material.

4.2.4 Guidance and Counterbalance Mechanism

The mechanical system was based on lever arm principles and contained four double-ended cross flexure pivot bearings. Two balance arms joined the moving frame to the support frame and held counterbalance (tare) masses. The purpose of this system was to allow the moving frame to move along the z-axis while minimising the motion in other directions. The balance arms were 3D printed from generic PLA material. The original design of the counterbalance masses included brass cylinders mounted on a threaded rod and fine adjustment masses made from a sliced brass M12 nut. C-Flex double-ended pivot bearings shown in figure 4.6 were selected for the pivot points on the support frame and at the connections to the moving frame.

The C-Flex pivot bearings were held in place using specifically designed clamps in the moving frame, support frame, and balance arms as shown in figures 4.7, 4.8, and 4.9 respectively. The clamps were included in the 3D print of each part and closed using nylon or stainless steel bolts. The support frame and moving frame clamps included “beam” components that could flex inwards to facilitate the motion of the moving frame. The end profile of the balance arm was 3 mm wide by 12 mm tall (11 mm excluding the “teeth” on the top and bottom of the arm shown in figure 4.22). The clamps shown in figures 4.7 and 4.8 were assumed to attach rigidly to the fixed sections of the C-Flex pivot bearing shown in figure 4.6. The balance arm clamps shown in figure 4.22 were assumed to attach rigidly to the rotating section of the C-Flex pivot bearing shown in figure 4.6.

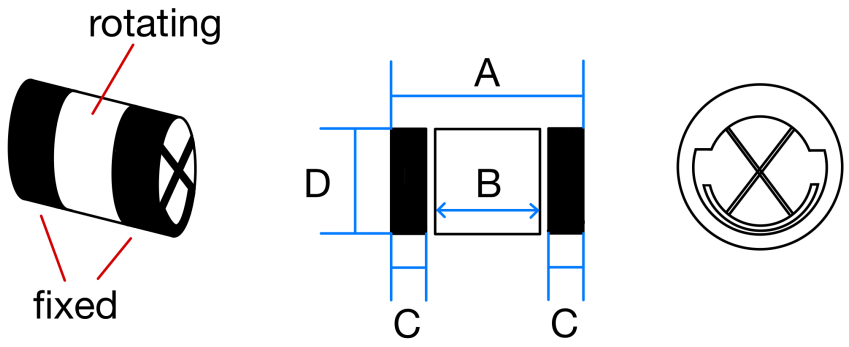

FIGURE 4.6: C-Flex double-ended pivot bearing diagram showing the fixed and rotational parts, dimensions, and end view. For CD-20, total length $A = 7.62$ mm, rotating section $B_{min} = 3.05$ mm, fixed sections $C_{min} = 1.52$ mm, and diameter $D = 4.76$ mm. Diagrams not to scale. Redrawn and simplified based on information from [98].

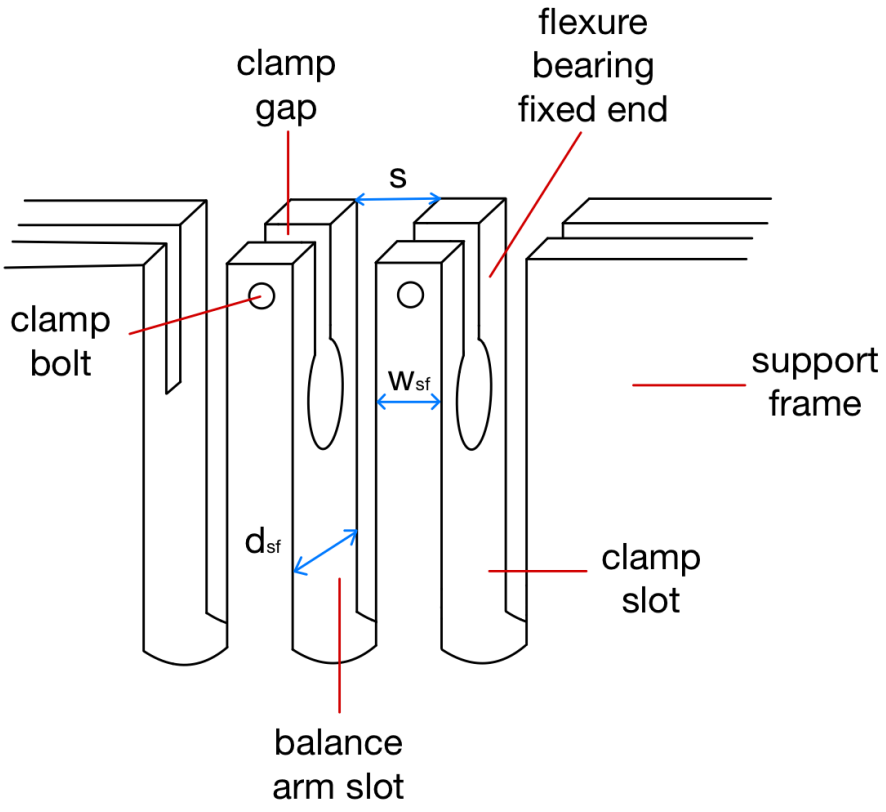

FIGURE 4.7: Support Frame C-Flex pivot bearing clamp diagram showing the features of the clamping mechanism including the width of the clamp $w_{sf} = 4$ mm, the width of the balance arm slot $s = 4$ mm, and the profile depth of the clamp beam $d_{sf} = 10$ mm. Diagram not to scale.

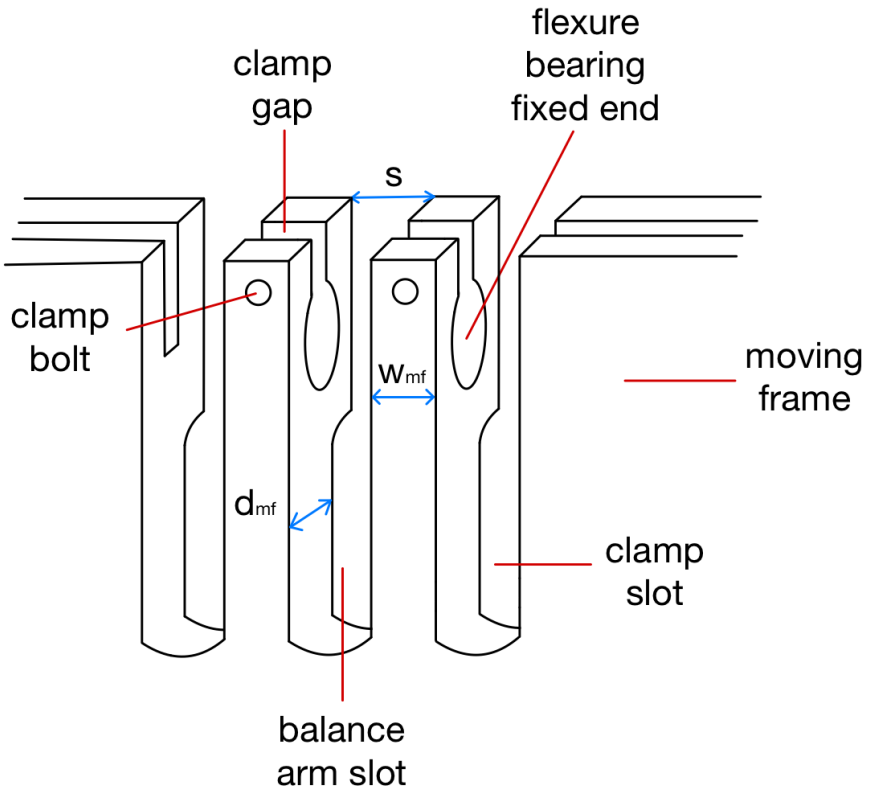

FIGURE 4.8: Moving Frame C-Flex pivot bearing clamp diagram showing the features of the clamping mechanism including the width of the clamp $w_{mf} = 3.2\,\text{mm}$, the width of the balance arm slot $s = 4\,\text{mm}$, and the profile depth of the clamp beam $d_{mf} = 3.11\,\text{mm}$. Diagram not to scale.

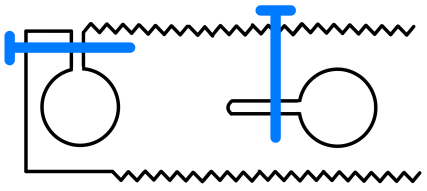

FIGURE 4.9: Balance arm profile diagram showing the concept of the clamping mechanism on to the rotational parts of the C-Flex pivot bearings. The clamps were closed by nylon bolts as indicated by the blue "T" shapes. Diagram not to scale.

4.3 Operation Theory

The 3D printed Kibble balance was based closely on existing electromagnetic Kibble balances and therefore the established Kibble principles and equations were used to analyse its expected performance. In 2012 Robinson [49] proposed a bifilar coil as a method of achieving weighing and moving phases in a single mode at room temperature (SMTP). This idea was a modification of the originally proposed Single Mode One Phase (SMOP) BIPM Kibble balance which used a superconducting coil cooled to cryogenic temperatures to carry the weighing current and induced moving voltage simultaneously without cross-coupling or interference [47]. The 3D printed Kibble balance was designed with a bifilar coil and was operated following a SMTP scheme of measurement.

4.3.1 Bifilar Coil Theory

A bifilar coil is constructed by winding a twisted pair of wires. This creates two separate coils that are almost identical in dimensions and position in space. When placed in a magnetic field it can be assumed that the difference in BL product between the two coils will be very small $(BL)_2 = (1+\delta)(BL)_1$. This setup allows one coil to carry the weighing current at all times during the weighing and moving phases whilst the second coil is used to measure the induced voltage during the moving phase. This has the advantage of keeping the two signals decoupled and keeping the difference between BL in the weighing and moving phases as small as possible. In this scheme the change in magnetisation of the magnet between weighing and moving phase due to the weighing current is minimised as the same magnitude of current is present in both phases.

As shown in figure 4.10, four measurement phases are required when performing mass measurements using a bifilar Kibble balance which create two virtual instruments, one for mass on and one for mass off. During the weighing phases, the tare coil system is used to apply a constant force (F_t) upwards (positive z-direction) and in all phases a weighing current is carried in one of the main coils.

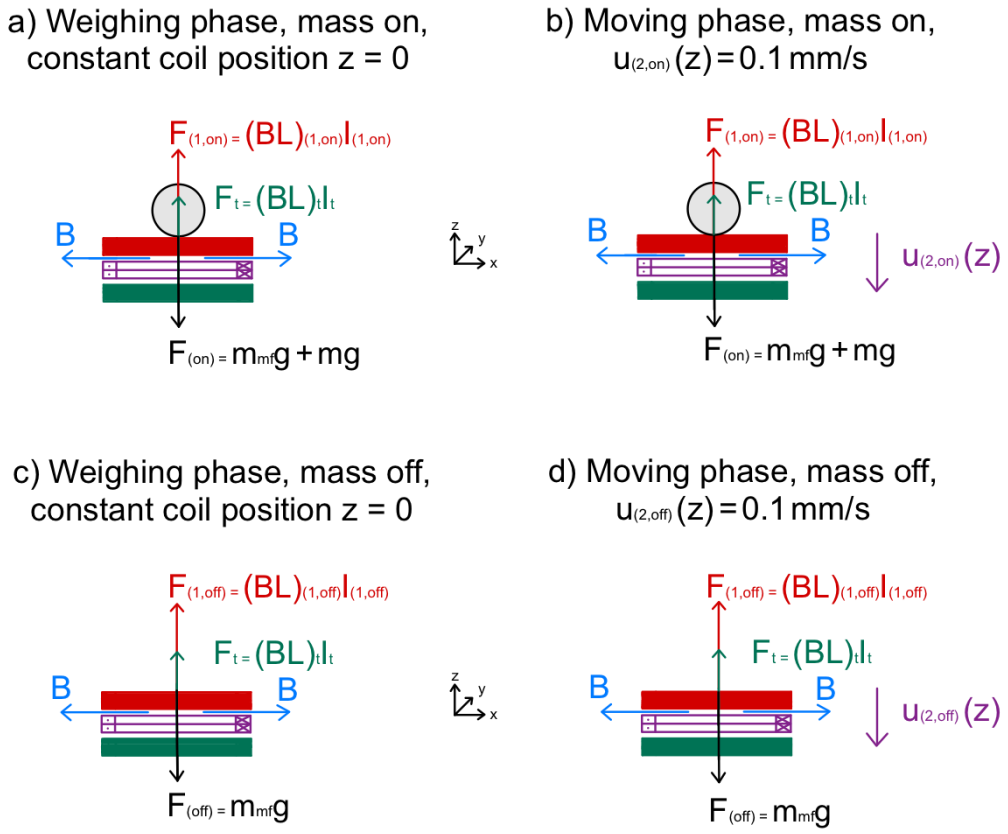

FIGURE 4.10: Schematic line diagram of the bifilar Kibble Balance Principle with co-located main coils (coil 1: red lines, coil 2: purple lines) and tare coil (green lines). Coils wound together or on top of each other but drawn separated here for clarity.

Forces - Mass On State

In weighing phase (figure 4.10 a) the system is in equilibrium with the coils held statically at the weighing position. In moving phase (figure 4.10 b) the system is also in equilibrium as the coils are moving at a constant velocity $u_{(2,on)}(z)$.

In both phases the forces are as follows:

$$F_{(on)} = F_t + F_{(1,on)} \tag{4.1}$$

$$m_{mf}g + mg = (BL)_t I_t + (BL)_1 I_{(1,on)} \tag{4.2}$$

Where $F_{(on)}$ is the sum of the weight of the Kibble balance moving parts (moving frame $m_{mf}g$ including the coils and the mass pan) plus the weight of the mass under test (grey sphere, mg), F_t is the tare force applied by the current in the tare coil ($(BL)_t I_t$), and $F_{(1,on)}$ is the force applied by the current in main coil 1 ($(BL)_1 I_{(1,on)}$) required to hold the balance at the weighing position.

Forces - Mass Off State

Similar to the mass on state, in the mass off state the balance is in equilibrium during the weighing (figure 4.10 c) and moving (figure 4.10 d) phases. The main difference is the absence of the mass under test resulting in a different weighing current in the main coil.

In both phases the forces are as follows:

$$F_{(off)} = F_t + F_{(1,off)} \tag{4.3}$$

$$m_{mf}g = (BL)_t I_t + (BL)_1 I_{(1,off)} \tag{4.4}$$

Where $F_{(off)}$ is the weight of the Kibble balance moving parts (moving frame $m_{mf}g$ including the coils and the mass pan), F_t is the tare force applied by the current in the tare coil ($(BL)_t I_t$), and $F_{(1,off)}$ is the force applied by the current in main coil 1 ($(BL)_1 I_{(1,off)}$) required to hold the balance at the weighing position.

Calculation of Mass

For each mass state (subscript s) the following measurements need to be taken. Firstly, data is collected with coil 1 assigned to the role of carrying the weighing current I at

all times and coil 2 assigned to the role of carrying the induced voltage V during the moving phase.

$$m_{1s}g_{1s} = (BL)_{1s}I_{1s} \tag{4.5}$$
$$V_{2s} = (1+\delta)(BL)_{1s}u_{2s} \tag{4.6}$$

Where m_{1s} is the mass measured by coil 1, g_{1s} is the acceleration due to gravity acting on the mass, $(BL)_{1s}$ is the product of the magnetic field B and the length L of coil 1, I_{1s} is the weighing current, V_{2s} is the voltage induced in coil 2 during the moving phase, $(1+\delta)$ is the correction term applied to account for the difference between $(BL)_{2s}$ and $(BL)_{1s}$ and u_{2s} is the velocity of coil 2 during moving phases.

The roles of the main coils are then reversed and the weighing and moving phases repeated.

$$m_{2s}g_{2s} = (1+\delta)(BL)_{1s}I_{2s} \tag{4.7}$$
$$V_{1s} = (BL)_{1s}u_{1s} \tag{4.8}$$

Each pair of equations can be combined according to the original Kibble principles discussed in Chapter 2 on page 24.

$$m_{1s}g_{1s}(1+\delta)u_{2s} = V_{2s}I_{1s} \tag{4.9}$$
$$m_{2s}g_{2s}u_{1s} = (1+\delta)V_{1s}I_{2s} \tag{4.10}$$

If δ is assumed to be constant over the period between measurement phases then equation 4.9 and 4.10 can be combined to eliminate $(1+\delta)$ resulting in the multiplication of the mass according to each coil.

$$m_{1s}g_{1s}u_{2s}m_{2s}g_{2s}u_{1s} = V_{2s}I_{1s}V_{1s}I_{2s} \tag{4.11}$$
$$m_{1s}m_{2s} = \frac{V_{1s}I_{1s}V_{2s}I_{2s}}{g_{1s}u_{1s}g_{2s}u_{2s}} \tag{4.12}$$

The mass in each state m_s can be calculated by taking the square root of equation 4.12.

$$m_s = \sqrt{m_{1s}m_{2s}} \tag{4.13}$$

To obtain a mass result m for the object under test equations 4.5 to 4.13 need to be carried out for both mass on and mass off states. The mass off m_{off} result should then be subtracted from the mass on m_{on} result.

$$m = m_{on} - m_{off} \tag{4.14}$$

4.3.2 Simplified Bifilar Coil Measurement Sequence

The bifilar coil theory outlined in section 4.3.1 requires a complex implementation in practice. The order of measurement phases needs to be carefully arranged to minimise the time between corresponding weighing and moving phases whilst also minimising potential thermal electromotive force (EMF) in the coil switching relays.

It is possible to simplify the implementation of the bifilar coil theory by assuming that the difference δ between the BL product of the two coils for a particular mass state is small during the period of time taken to record a weighing phase and a moving phase data set. Specifically if $(1 + \delta) \approx 1$ then $(BL)_{2s} = (BL)_{1s} = (BL)_s$. This assumption significantly reduces the total time taken to complete a measurement run as there is no need to repeat measurement phases with the roles of the coils reversed. In addition gravity can be assumed to be a constant value to within the target level of uncertainty for this work. Equations 4.5 and 4.6 can be modified as follows.

$$m_{1s}g = BLI_{1s} \tag{4.15}$$

$$V_{2s} = BLu_{2s} \tag{4.16}$$

Equations 4.15 and 4.16 can be combined as per the traditional Kibble principles and generalised to give m_s for each mass state.

$$m_s = m_{1s} = \frac{V_{2s}I_{1s}}{gu_{2s}} \tag{4.17}$$

Equation 4.17 is the simplified version of equation 4.13. The mass on (m_{on}) and mass off (m_{off}) results generated using this equation can therefore be combined according to equation 4.14 to calculate the mass (m) of the object under test.

For completeness, if measurement phases were carried out according to this simplified version of the theory with the roles of the coils reversed then additional repeat mass results m would be generated for the object under test.

4.3.3 Coil Current Effect

A wire carrying an electric current generates a magnetic field according to the Biot-Savart Law. A coil of wire can be considered as a stack of wire loops or a solenoid.

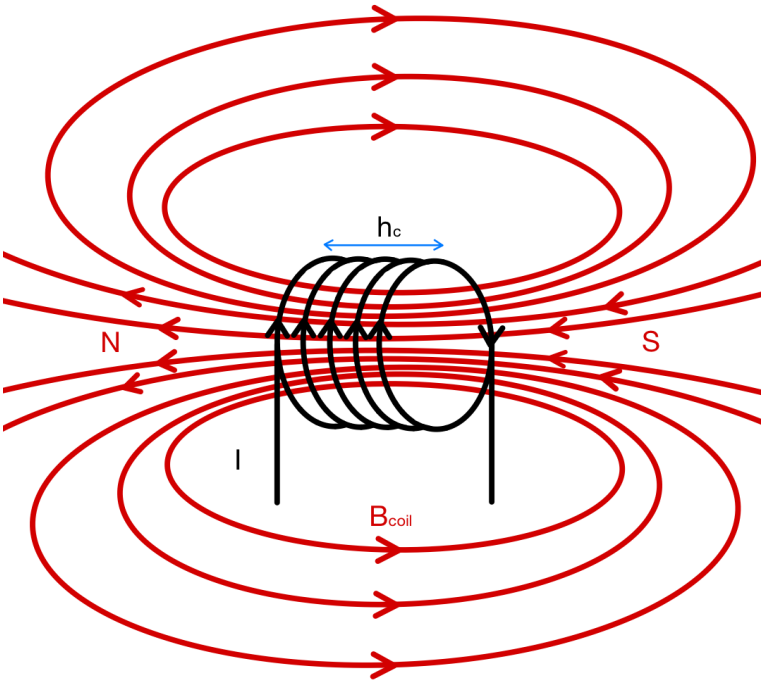

FIGURE 4.11: Magnetic field B_{coil} generated by a coil of N turns and height h_c carrying a current I. The north and south pole of the magnetic field are indicated by the red N and S respectively.

The magnetic field generated by a coil is given by equation 4.18.

$$B_{coil} = \mu_0 n I \tag{4.18}$$

where μ_0 is the permeability of free space, n is the number of turns N per unit height of the coil (N/h_c), and I is the current flowing in the wire.

If the current carrying coil of wire is located inside an external magnetic field, such as in a Kibble balance, then the two fields will interact through superposition.

$$B = B_{external} + B_{coil} \tag{4.19}$$

In a Kibble balance this is known as the coil current effect. Specifically, during the weighing phase the current flowing in the main coil directly affects the total magnetic field experienced by the coil which has an impact on its BL product. This effect is usually minimised by operating the Kibble balance in a specific way. For a classic TMTP Kibble balance with a single main coil, in weighing phase a tare mass is

selected such that the currents flowing in mass on and mass off states are equal and opposite ($I_{on} = -I_{off}$). In moving phase, there is no current present ($I = 0$). This arrangement ensures that the average BL product experienced by the coil during the weighing phase is measured during the moving phase [86].

For a SMTP Kibble balance with a bifilar main coil operating according to the measurement sequence detailed in section 4.3.2 it is not necessary to implement symmetric currents during the weighing phase. The BL product is measured in each mass state with the corresponding weighing current applied in one of the coils. The appropriate $(BL)_s$ is used to calculate the mass value m_s for each mass state and therefore the coil current effect is accounted for in the calculations. This assumption holds providing the weighing position coincides with the magnetic field centre of the Kibble balance magnet otherwise a correction will need to be applied [99].

As described in section 4.2.1, the main coils of the 3D printed Kibble balance were co-located with a tare coil inside a single magnet. This arrangement complicates the consideration of the coil current effect.

$$B = B_{external} + B_{main} + B_{tare} \tag{4.20}$$

Weighing Phase

During the weighing phase the tare coil carries a constant current I_{tare} which generates a force according to $F_{tare} = BL_{tare}I_{tare}$ (equation 2.12) to counterbalance the apparent weight of the moving frame w_{mf}.

$$w_{mf} = m_{mf}g + f_z \tag{4.21}$$

Where m_{mf} is the mass of the moving frame, g is acceleration due to local gravity, and f_z is the force in the z-direction due to the stiffness of the flexures in the guidance mechanism.

The tare current does not change between mass states therefore its own magnetic field B_{tare} is constant. However as the tare coil is inside the same magnetic field as the main coils it will be subject to the change in total magnetic field caused by the different weighing currents in the main coil in mass on and mass off states. The change in total magnetic field changes the BL product of the tare coil and hence the force applied in each mass state. The effect on the mass value of the object under test can be corrected according to the Magnetic Field Correction theory in section (4.3.4).

Moving Phase

During the moving phase the tare coil is used to drive the main coil at a constant speed through the magnetic field. This is achieved by changing the force applied to the moving frame by varying the current carried by the tare coil. The current applied to the tare coil is the sum of the current according to the predetermined "force profile" and any additional current required to accelerate the moving frame up to constant velocity or decelerate the coil to stationary for the turning points. The acceleration and deceleration zones are excluded from the BL product measurement range. The force profile is given by the sum of the forces required to hold the moving frame stationary at each position z along its moving range. If the weight of the moving frame ($m_{mf}g$) is counter-balanced by physical tare masses, such as parts K and L in figure 4.2, the force needed to hold the moving frame at different z positions is determined by the stiffness of the flexures in the guidance mechanism. This can be calculated analytically according to the mechanical theory in section 4.4.3. When the moving frame passes through the weighing position ($z = 0$) there will be no current in the tare coil because the force profile requires zero additional force to be applied at this position. Specifically, during moving phase at $z = 0$ the system is in equilibrium: the moving frame is moving at a constant velocity ($F = m_{mf}a = 0$ as $a = 0$) and the guidance mechanism flexures are at their respective resting positions ($F = \kappa z = 0$ as $z = 0$). Therefore, when $BL(z = 0)$ is measured during the moving phase the magnet-coil subsystem is momentarily in exactly the same "static" state as when it is at the weighing position during weighing phase.

4.3.4 Magnetic Field Correction

The magnetic field B was assumed to vary linearly according to current flowing in the coils. The current flowing in the tare coil during the weighing phase was fixed however the current flowing in the main coil changed between the mass off and on states. This required a correction term to be applied to the measurement of mass which is derived in [100].

$$B = B_0 + \beta I \tag{4.22}$$

Where B_0 is the magnetic field due to the permanent magnet plus the effect of the fixed current i in the tare coil and β is the change in magnetic field due to the change in current I flowing in the main coil.

The mass off state was assumed to be the origin state. The moving frame of mass m_{mf} was held at the zero position by the current i in the tare coil of length L_{tc}.

$$m_{mf}g = B_0 L_{tc} i \tag{4.23}$$

In the mass on state the test mass m was added to the moving frame and there was a change of current I flowing in the main coil of length L_{mc}.

$$m_{mf}g + mg = (B_0 + \beta I)L_{tc}i + BL_{mc}I \tag{4.24}$$
$$m_{mf}g + mg = m_{mf}g + \beta I L_{tc} i + BL_{mc}I \tag{4.25}$$
$$mg = \beta I L_{tc} i + BL_{mc}I \tag{4.26}$$

Equation 4.22 was rearranged to express the term βI as $B - B_0$. By substituting this expression, equation 4.23 and the length of the moving coil L_{mc} into equation 4.26 was transformed as follows.

$$mg = (B - B_0)L_{tc}i + BL_{mc}I \tag{4.27}$$
$$mg = \left(\frac{B - B_0}{B_0}\right) m_{mf}g + BL_{mc}I \tag{4.28}$$
$$mg = \left(\frac{BL_{mc} - B_0 L_{mc}}{B_0 L_{mc}}\right) m_{mf}g + BL_{mc}I \tag{4.29}$$

The BL products of the main coil in the mass off $B_0 L_{mc}$ and mass on BL_{mc} states were measured during the moving phases. The term $\left(\frac{BL_{mc} - B_0 L_{mc}}{B_0 L_{mc}}\right) m_{mf}g$ in equation 4.29 represents a correction to the usual expression for mass $mg = BL_{mc}I$. The fractional correction was calculated by dividing equation 4.29 by mg.

$$\left(\frac{m_{mf}}{m}\right)\left(\frac{BL_{mc} - B_0 L_{mc}}{B_0 L_{mc}}\right) \tag{4.30}$$

4.4 Estimated Performance

The simplified electromagnetic Kibble balance model defined in section 3.1 according to equation 3.1 was evaluated for masses in the range 1 g to 10 g based on the dimensions and characteristics of the gram-level Kibble balance design described in section 4.2.

4.4.1 Moving Phase

The tare coil was used to generate the motion of the moving assembly during the moving phase. The main coil velocity u was set to 0.1 mm s^{-1}. According to equation 4.16 a voltage of approximately 0.4 mV is induced in the main coil. To convert this voltage into the measurable range of the ADC ($\pm$ 10 V) an amplification A of 1000 is required, resulting in a measurable moving voltage V_M of approximately 0.4 V. The moving range was set to $\pm$0.5 mm about the weighing position resulting in a total displacement distance of 1 mm and a moving time of 10 s per direction. This distance was selected to check displacements an order of magnitude smaller than the lengths of the balance arms in preparation for miniaturising to MEMS scales.

4.4.2 Weighing Phase

The current I required to generate a force to oppose gravity acting on a mass in the range from 2.4 mA and 24 mA respectively. A resistance R of 100 Ω is required to convert these currents to a measurable voltage V_W in the range 0.24 V to 2.4 V. The current carried in the main coil will result in power dissipated ranging from 1.87 mW at 10 g to 0.02 mW at 1 g.

4.4.3 Guidance and Counterbalance Mechanism

The torsional specification of the pivot bearings selected for the guidance mechanism and the distance l_r between them have an impact on the performance of the balance [1]. The mechanical properties of the pivot bearing clamps also contribute to the total stiffness of the system.

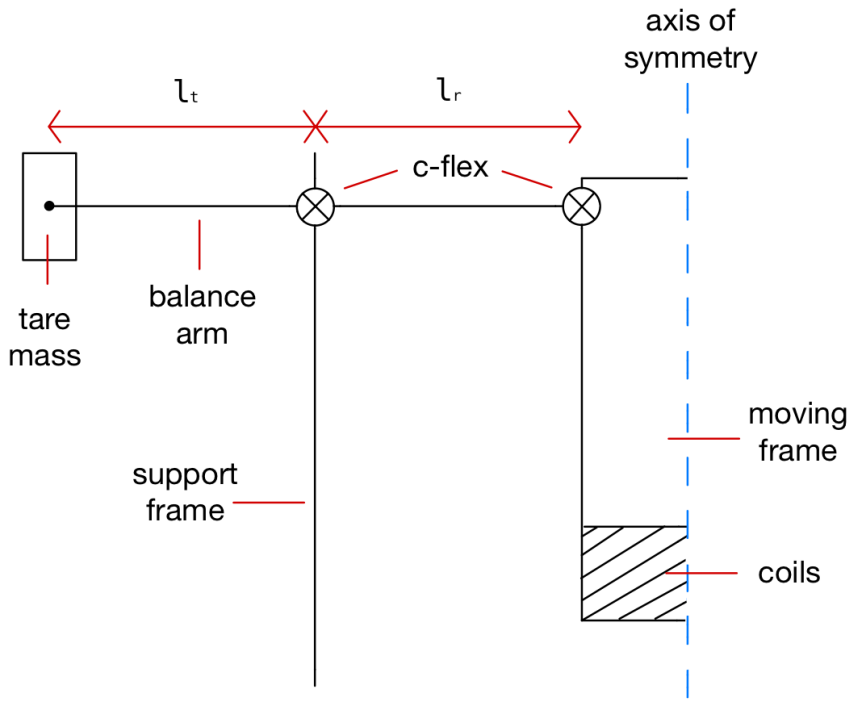

FIGURE 4.12: Cross-sectional line diagram of one half of the mechanical system at the origin position ($z = 0$). The distance l_r between the C-Flex pivots was fixed at 50 mm. The distance l_t between the tare mass and the C-Flex in the support frame can be varied to achieve equilibrium. Diagram not to scale.

Mechanical System Geometry in Motion

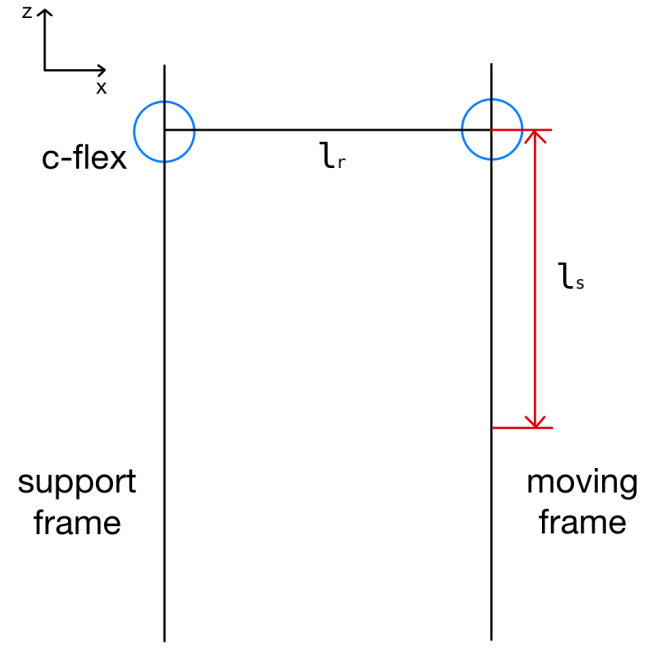

(A) Origin position (z= 0).

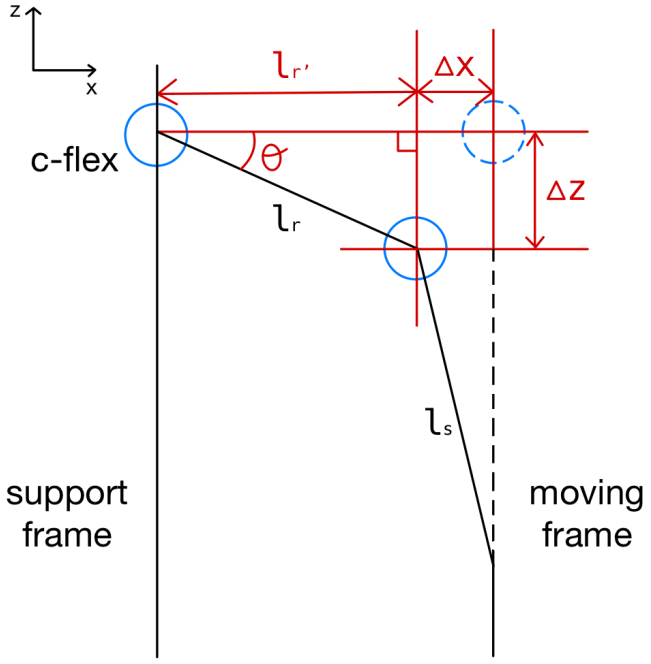

(B) Moving frame displacement (Δz).

FIGURE 4.13: Cross-sectional line diagram of one half of the mechanical system geometry at (A) the origin position and (B) with the moving frame displaced by Δz. The balance arm length and moving frame clamp length were fixed at l_r =50 mm and l_s =9.55 mm respectively. The C-Flex pivot bearing held in the moving frame clamp deflects towards the support frame by Δx. Diagrams not to scale.

According to simple harmonic motion the restoring force on a spring due a change in its length is given by 4.31:

$$F = -\kappa \Delta l \tag{4.31}$$

Where F is the restoring force, κ is the spring constant, and Δl is the change in length of the spring from its resting (non-stretched) position.

Clamp Spring Constant

The pivot bearing clamps can be considered as simple cantilever beam structures as shown in figure 4.14 with profile geometries shown in figure 4.15.

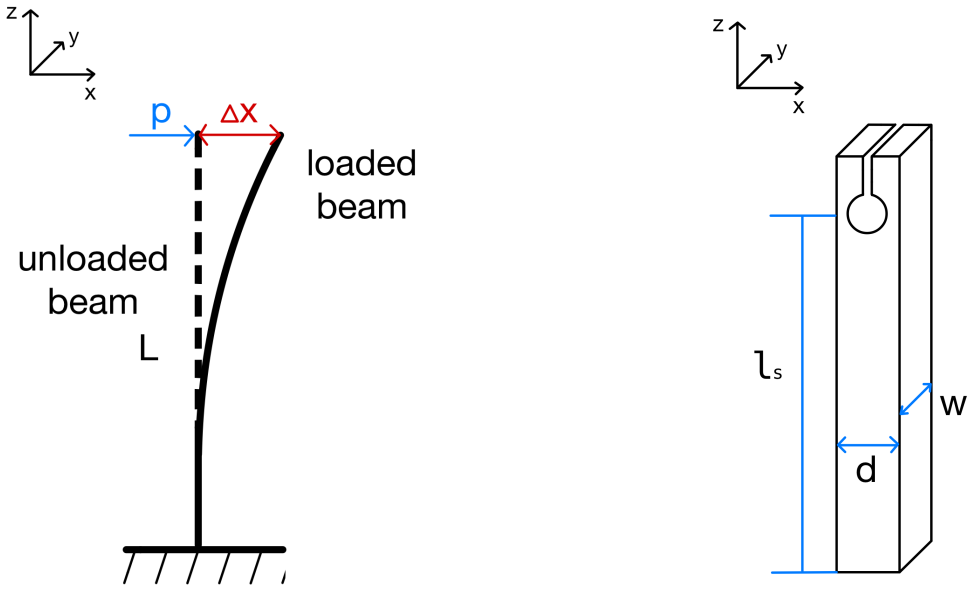

(A) Beam deflection. (B) Simplified clamp geometry.

FIGURE 4.14: Cantilever beam deflection and geometry. (A) A vertical cantilever of length L is deflected in the x-direction due to load p applied at the free end. (B) Clamp geometry showing beam length l_s, beam width w, and beam depth d. Diagrams not to scale.

The load required to deflect the cantilever beam by distance Δx can be calculated according to equation 4.32.

$$p = \frac{3EI\Delta x}{L^3} \tag{4.32}$$

Where p is the load applied, E is the Young's modulus, I is the second moment of area, Δx is the distance of deflection, and L is the length of the cantilever.

Comparison of equations 4.31 and 4.32 shows that the spring constant of a cantilever beam is given by $\frac{3EI}{L^3}$.

The second moment of area I is a geometric property of the cantilever beam that determines its resistance to deflection or bending. For the geometry shown in figure 4.14b the second moment of area with respect to the neutral axis I_y is calculated according to equation 4.33.

$$\begin{aligned} I_y &= \iint_R x^2 dA = \int_{-\frac{d}{2}}^{\frac{d}{2}} \int_{-\frac{w}{2}}^{\frac{w}{2}} x^2 dx dy \\ &= \int_{-\frac{d}{2}}^{\frac{d}{2}} w x^2 dx = \frac{w d^3}{12} \end{aligned} \tag{4.33}$$

As shown in figures 4.7 and 4.8, the pivot bearing clamps in the support frame and moving frame have different geometries. Figure 4.15 shows their respective profiles in closer detail. Their dimensions and calculated values of the second moment of area with respect to the y-axis are shown in table 4.1.

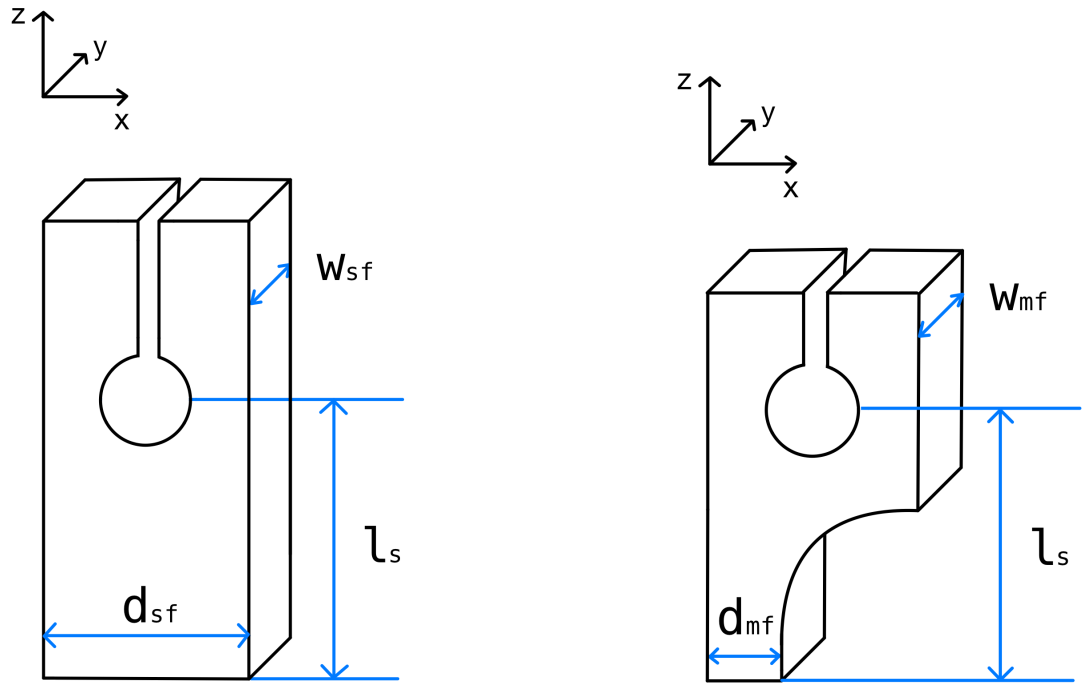

(A) Support frame. (B) Moving frame.

FIGURE 4.15: Pivot bearing clamp geometries. Diagrams not to scale.

The beam length l_s was equal to 9.55 mm for both geometries. It was assumed that the clamps would have a similar Young's modulus E given that they would be 3D printed from the same PLA material on the same 3D printer. By inspecting equation

TABLE 4.1: Pivot bearing clamp dimensions (as labelled in figure 4.15) and second moment of area with respect to the y-axis I_y.

Clamp ID	l_s mm	d mm	w mm	I_y m^4
Moving Frame (mf)	9.55	3.11	3.20	8.02E-12
Support Frame (sf)	9.55	10.00	4.00	3.33E-10

4.32, it was observed that the second moment of area was the most important factor impacting the relative stiffness of the two clamps. The moment of area for the support frame clamp $I_{(y,sf)} = 3.33 \times 10^{-10}\,m^4$ was more than 40 times higher than for the moving frame clamp $I_{(y,mf)} = 8.02 \times 10^{-12}\,m^4$. This indicated that the moving frame clamp was significantly less resistant to bending in the x-direction than the support frame. Therefore, for a given deflection Δx, the support frame clamp would require a force 40 times higher than the moving frame clamp. This allowed a simplifying assumption to be made for the analysis of the guidance mechanism motion. Specifically, as shown in figure 4.13, the support frame clamp was completely rigid and only the moving frame clamp would deflect when the guidance mechanism was in motion.

The total spring constant for the moving frame clamps k_{mf} was calculated according to equation 4.34.

$$k_{mf} = n_{mf}\frac{3E_{mf}I_{(y,mf)}}{l_s^3} \tag{4.34}$$

Where n_{mf} is the number of moving frame clamps in the system, E_{mf} is the Young's modulus of the moving frame material, $I_{(y,mf)}$ is the second moment of area with respect to the y-axis for the moving frame clamp, and l_s is the length of the cantilever.

According to the manufacturer's data sheet, the Young's Modulus of the generic PLA material used to manufacture all the 3D printed parts of the prototype was 3.31 GPa in the machined direction and 3.86 GPa in the transverse direction [101]. Studies of the mechanical properties of 3D printed PLA have shown that the 3D printing process can significantly reduce the Young's modulus from the manufacturers specifications [102][103][104]. A number of factors can influence the change in Young's modulus including infill density, infill pattern, printing speed, and printing orientation. In [102] the Young's modulus of test pieces was measured for a range of print parameters and combinations. The test pieces were made using generic PLA with a manufacturer specified Young's modulus of 3.31 GPa. It was found that infill density had the largest impact on measured Young's modulus closely followed by infill pattern. The study

included three infill densities (25%, 33%, 50%) and three infill patterns (grid, triangle, honeycomb). The observed Young's modulus ranged from 248 MPa to 796 MPa with a mean of 487.8 MPa. These values represent a 92.5%, 76%, and 85.3% decrease of the manufacturer's specification respectively. The prototype design described in sections 4.2.2 to 4.2.4 specifies an infill factor of 15%. The Young's modulus of 3D printed PLA with fill factors as low as 15% were not reported in the literature. However, given that PLA of the same manufacturer's specification was used in [102], a value of 248 MPa was assumed to calculate the total moving frame clamp spring constant $k_{mf} = 2.74 \times 10^4\,\mathrm{N{\cdot}m^{-1}}$ (with $n_{mf} = 4$).

The force acting on the moving frame in the z-direction due the moving frame clamps $F_{(z,mf)}$ is determined by resolving the force along the balance arm required to deflect the clamp into its component along the z-axis.

$$F_{(mf,z)} = -k_{mf}\Delta x \sin\theta \tag{4.35}$$

Where k_{mf} is the total spring constant of the moving frame clamps (equation 4.34), Δx is the deflection of the C-Flex pivot bearing towards the support frame, and θ is the angle of the balance arm deflection from the horizontal position.

Δx and θ are shown in figure 4.13b. According to trigonometry:

$$\begin{aligned}\Delta x &= l_r - l_{r'} \\ &= l_r - l_r\cos\theta \\ &= l_r(1-\cos\theta)\end{aligned}$$

Substituting this expression into equation 4.35:

$$F_{(mf,z)} = -k_{mf} l_r (1-\cos\theta)\sin\theta \tag{4.36}$$

Equation 4.36 can be simplified using the small angle approximations:

$$\begin{aligned}\sin\theta &\approx \theta \\ \cos\theta &\approx 1 - \frac{\theta^2}{2} \\ \theta = \arcsin(\frac{\Delta z}{l_r}) &\approx \frac{\Delta z}{l_r}\end{aligned}$$

$$F_{(mf,z)} = -k_{mf} l_r (1 - (1 - \frac{\theta^2}{2})\theta \tag{4.37}$$

$$= -k_{mf} l_r \frac{\theta^3}{2} \tag{4.38}$$

$$= -k_{mf} \frac{\Delta z^3}{2 l_r^2} \tag{4.39}$$

Pivot Bearing Spring Constant

The expected value of the linear spring constant of the pivot bearings in the mechanical system can be determined analytically from the number of pivot bearings, the torsional specification of the C-Flex flexures, and the distance between the pivot points.

$$k_b = \frac{n_b J}{l_r^2} \tag{4.40}$$

Where k_b is the total linear spring constant of the pivot bearings, n_b is the number of C-Flex flexures in the system, J is the torsional coefficient of an individual pivot bearing, and l_r is the distance from the moving frame to the pivot point.

There were a total of 4 CD-20 C-Flex pivot bearings in the system with a specified torsional coefficient J of 38.84 mN·m·rad^{-1} [98] and the distance between the pivot point and the moving frame was 50 mm. Therefore the calculated value of k_b according to equation 4.40 was 62.15 N·m^{-1}.

The force acting on the moving frame in the z-direction due the C-Flex pivot bearings $F_{(z,b)}$ is given by substitution into equation 4.31:

$$F_{(z,b)} = -k_b \Delta z = -\frac{4J}{l_r^2} \Delta z \tag{4.41}$$

Mass Sensitivity

$$\mu = \frac{F_z}{g} \tag{4.42}$$

To calculate the mass sensitivity μ of the prototype the total force in the z-direction F_z required to displace the moving frame by the minimum detectable distance needs to be divided by local gravity g.

The sum of the forces acting on the moving frame in the z-direction when it was displaced from the horizontal (origin) position was calculated according to the following equation:

$$F_z = F_{(z,b)} + F_{(z,mf)} + m_{mf}g - m_t g \tag{4.43}$$

Where F_z is the total force acting on the moving frame in the z-direction, $F_{(z,b)}$ is the total force from the C-Flex pivot bearings in the z-direction, $F_{(z,mf)}$ is the total force from the moving frame clamps in the z-direction, m_{mf} is the mass of the moving frame, m_t is the total mass of the tare masses, and g is local gravity.

The total value of the tare masses was selected to balance the mass of the moving frame. Substituting $m_t = m_{mf}$, $F_{(z,mf)}$ (equation 4.37), and $F_{(z,b)}$ (equation 4.41) into F_z (equation 4.43):

$$F_z = -k_b \Delta z - k_{mf} \frac{\Delta z^3}{2l_r^2} \tag{4.44}$$

The mass sensitivity of the prototype $\mu = 0.127\,\text{mg}$ was calculated according to equations 4.42 and 4.44 by setting Δz to the resolution of the linear optical encoder of 20 nm, $k_b = 62.15\,\text{N·m}^{-1}$, $k_{mf} = 2.74 \times 10^4\,\text{N·m}^{-1}$, $l_r = 0.050\,\text{m}$ and $g = 9.81\,\text{m·s}^2$.

Inspection of equation 4.44 shows that the moving frame clamps contribution ($-k_{mf}\frac{\Delta z^3}{2l_r^2}$) to the total vertical force on the moving frame is negligible in comparison with the force exerted by the C-Flex pivot bearings and therefore $F_z \approx F_{(z,b)}$.

By combining equations (4.41) and (4.42) it is observed that the mass sensitivity μ is directly proportional to torsional coefficient J and inversely proportional to the square of the distance between the pivot point and the moving frame l_r^2. C-Flex CD-10 bearings have the same diameter and length as CD-20 bearings but a lower torsional coefficient of $4.53\,\text{mN·m·rad}^{-1}$. Changing to CD-10 bearings is calculated to decrease μ by a factor of 10, to 0.015 mg.

4.4.4 Magnetic Field Correction

The presence of the counterbalance tare masses (labelled K) and fine adjustment nuts (labelled L) shown in figure 4.2 serve to reduce the effective mass of the moving frame (and all items attached to it) to zero. Therefore, the magnetic field correction according to equation 4.29 was assumed to be zero for the performance estimation calculations.

4.4.5 Uncertainty Budget

The prototype design calculations and assumptions were used to estimate the total relative uncertainty (at k=1) for 10 g, 5 g, 2 g and 1 g by building on the uncertainty analysis presented in table 3.5 in chapter 3.

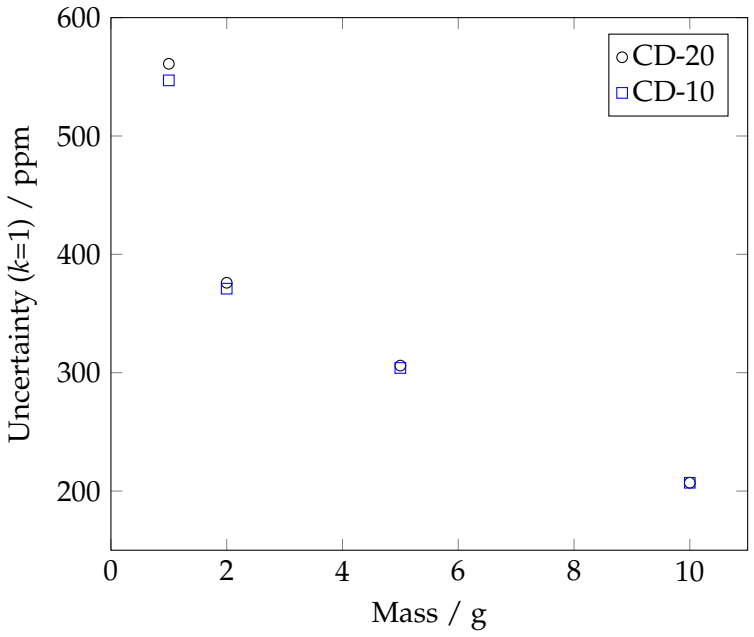

FIGURE 4.16: Predicted mass uncertainty for the prototype design (l_r = 50 mm) including a comparison of the effect of CD-20 and CD-10 C-Flex flexure bearings.

Figure 4.16 shows the expected uncertainty across the 3D printed prototype's working mass range and the effect of changing the flexure bearings from C-Flex CD-20 to CD-10. The difference in relative uncertainty varied from zero at 10 g to 14 ppm at 1 g. Therefore, as the expected difference in relative uncertainty was minimal, it was decided to use CD-20 flexure bearings during initial development of the prototype. The C-Flex CD-20 were made from slightly thicker material, indicated by their higher torsional coefficient, suggesting they were more robust and likely to withstand the rigors of initial testing.

Typical uncertainty for OIML class E1 mass calibration varies between 0.2 ppm at k = 1 for 1 g to 0.075 ppm at k = 1 for 10 g [105]. The estimated uncertainties for the 3D printed Kibble balance prototype presented in figure 4.16 show that this system cannot be competitive with existing traditional mass measurement in the range 1 g to 10 g. However there is a good probability that the prototype system will meet the target for this work of between 0.1% and 0.25%.

The results in figure 4.17 were calculated to investigate the effect of flexure stiffness on relative uncertainty when scaling the prototype design, specifically reducing the length of the balance arms l_r. Figure 4.17 shows that as the measured mass decreases

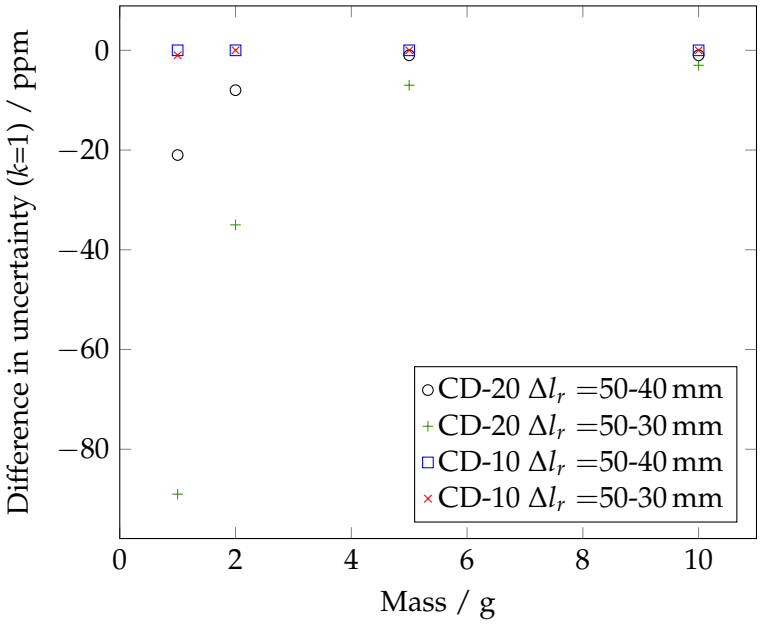

FIGURE 4.17: Effect of flexure stiffness and balance arm length on predicted mass uncertainty. Comparison between CD-10 and CD-20 C-Flex flexure bearings and three balance arm lengths l_r.

the selection of a lower flexure stiffness becomes more important, particularly at shorter balance arm lengths. This is due to the impact of the change in mass sensitivity μ calculated by equation 4.42. This effect highlights one of the challenges of scaling to MEMS, specifically the need to create a guidance mechanism with low stiffness in a single direction. In addition, the mass sensitivity equation also highlights the need for a length measurement system with higher resolution than 20 nm as the system is scaled to smaller sizes.

TABLE 4.2: Estimated uncertainty budget for the 3D printed prototype Kibble balance at 1 g based on the design and capability assumptions.

Note	Contribution	Value	Unit	Unc. ($k = 1$)	Unit	Ratio	%
i	Gravity (g)	9.81	m/s^2	4.91E-04	m/s^2	5.00E-05	1%
ii	Phase alignment (α)	1	-	5.00E-05	-	5.00E-05	1%
iii	Resistor (R)	100	Ω	3.22E-03	Ω	3.22E-05	0%
iv	Weighing Voltage (V_W)	0.24	V	1.12E-04	V	4.64E-04	68%
iv	Moving Voltage (V_M)	0.41	V	1.12E-04	V	2.77E-04	24%
v	Amplification (A)	1000	-	2.55E-02	-	2.55E-05	0%
vi	Distance (h_c)	1E-03	m	2.10E-08	m	2.10E-05	0%
vii	Time (t)	10	s	1.10E-04	s	1.10E-05	0%
viii	Flexure stiffness	0.001	kg	1.27E-07	kg	1.27E-04	5%
		Total standard uncertainty ($k = 1$)				0.561	mg

i. The local gravity value was 9.81 m/s^2 [79] with an assumed uncertainty of 50 ppm based on determining local gravity by calculation rather than measurement.

ii. Uncertainty due to difference in alignment of the sensing coil and the magnetic field between weighing and moving phase was assumed to be approximately 50 ppm [35]. This value was selected to take into account the repeatability of motion of the mechanical system manufactured from 3D printed PLA parts.

iii. Resistor uncertainty was calculated from the root-sum-square (RSS) combination of calibration, drift and temperature dependence uncertainties based on a Vishay HZ Series (Z-foil) resistor [80]. Calibration uncertainty was assumed to be 10 times NPL's UKAS accreditation [30]. A stability of 2 ppm (over 6 years unloaded) and temperature coefficient of 0.2 ppm/°C were specified for the resistor. Since the current applied to the resistor is very low the long term stability value has been assumed. A working temperature of 20 ± 20°C has been assumed for uncertainty due to a change in resistor temperature.

iv. Voltage uncertainty was calculated as the RSS of calibration, drift and ADC resolution. 20 bit ±10 V Analogue to Digital Converter (ADC) calibrated against a high precision and stability voltage reference has been assumed. A conservative estimate of ADC calibration uncertainty of 5 ppm at 10 V based on NPL's UKAS accreditation schedule [30]. Long term stability of 10 ppm assumed based on a Linear Technology voltage reference [81]. ADC resolution calculated $\frac{10 \times 2}{2^{20}} = 19.07\,\mu$V [82].

v. Amplification of induced voltage during the moving phase was assumed to be carried out using a matched pair of Vishay HZ Series (Z-foil) resistors [83]. The calibration, drift and temperature uncertainty contributions were combined RSS. Calibration uncertainty based on ten times NPL UKAS accreditation

schedule [30]. Matched resistors with a tracking temperature coefficient of 0.5 ppm/°C. A working temperature of 20 ± 20°C has been assumed for uncertainty due to a change in temperature of these resistors.

vi. Displacement uncertainty was based on an optical encoder system [84] assuming an absolute uncertainty of 20 nm plus a conservative relative uncertainty of 10 ppm of the displacement [35].

vii. The moving phase measurement time was assumed to be known with an absolute uncertainty of 10 μs plus a conservative relative uncertainty of 10 ppm [35].

viii. Mass resolution assuming C-Flex CD-20 double ended flexure bearings.

A detailed uncertainty budget for the 3D printed prototype predicted performance at 1 g is presented in table 4.2. It shows that the largest contributions to the total uncertainty are due to voltage measurement in both the weighing and moving phases. This prototype system utilises conventional room temperature electronics to comply with the requirements to be a low cost and compact system. The intention of this prototype is to provide a route to the further miniaturisation of Kibble technology to the milligram-level and below. At the milligram scale the relative uncertainty of currently available traditional mass measurement increases to a level which provides an opportunity for Kibble balances with conventional electronics [35].

4.4.6 Summary

In this section the design for a low cost gram-level 3D printed Kibble balance has been presented and evaluated analytically. The predicted results will inform the production and testing of a prototype at NPL. The analysis has also highlighted aspects of the design which will focus efforts on research and development to improve performance and guide further research on balances intended for measuring masses at the milligram-level.

4.5 Manufactured Prototype System

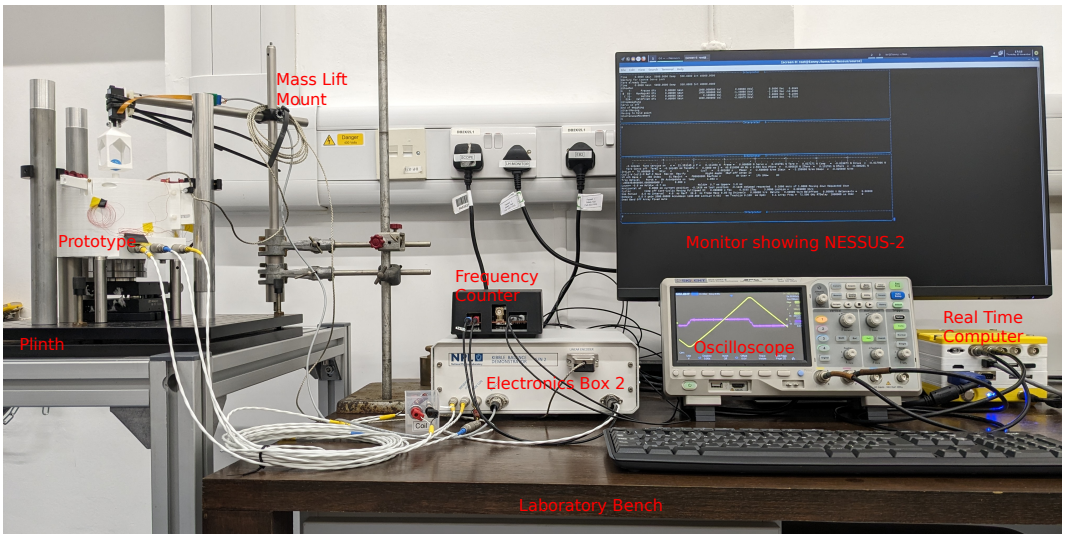

FIGURE 4.18: Assembled 3D printed Kibble balance prototype system.

Figure 4.18 shows the completed 3D printed Kibble balance system as setup in the laboratory for testing and evaluation. The prototype was placed on a light-weight plinth with the electronic subsystems, RTC, peripherals, and oscilloscope on an adjacent bench. The laboratory air was temperature controlled to 22±1°C. A draft shield was not used during evaluation and testing of the prototype system.

It was necessary to make several changes to the planned prototype design (section 4.2) during the manufacturing and assembly process. The main elements of the manufacturing process and important design changes are detailed in the following subsections.

4.5.1 3D Printing

A Prusa i3 MK3S+ was used to manufacture several key components of the 3D printed prototype balance including the support frame, moving frame, balance arms, balance pan, encoder mount, and mass lift. Generic polylactic acid (PLA) filament in combination with a 0.4 mm diameter print head was used for all components. The components were drawn in SolidWorks and prepared for 3D printing using PrusaSlicer Version 2.4.1+win64 software. The "g-code" print file settings included: 15% infill, brim on, and supports on build plate only. Other 3D print settings were kept at their default values. All parts were finished using hand tools to remove excess PLA, ensure holes of the correct size for the flexure bearings and to add threads to bolt holes where needed, for example at the back or bottom of flexure clamps.

4.5.2 Mass Lift

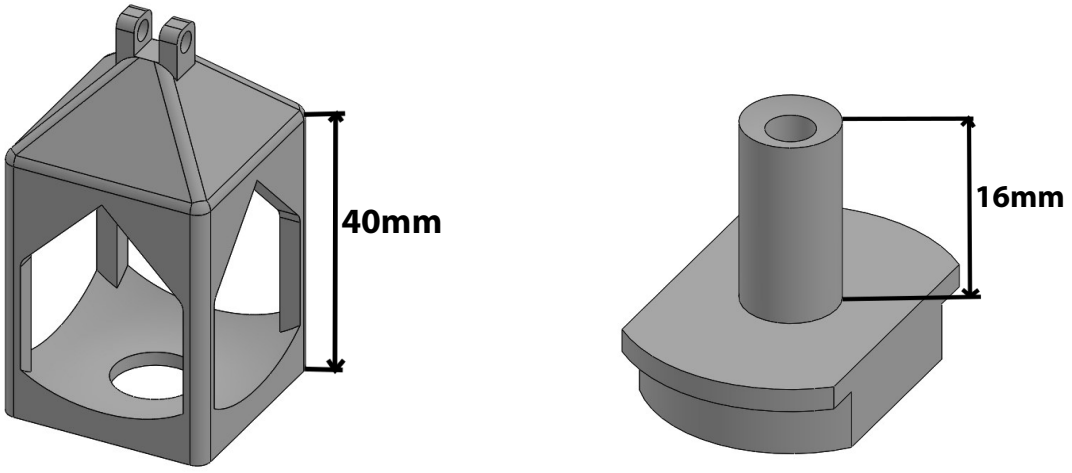

(A) Mass lift cradle. (B) Extended mass pan.

FIGURE 4.19: Mass lift component CAD models. 3D prints shown in figure 4.20.

The mass lift was a key component for automating the operation of the 3D printed Kibble balance. It was not considered in the original design however only a few modifications were required to integrate the existing Demonstration Balance mass lift actuator and software into the prototype system.

A cradle for spherical masses (shown in figure 4.19a was designed to hang from the actuator and the mass pan was modified (shown in figure 4.19b) to integrate with the central hole in the cradle and allow for the maximum moving range of the actuator. The actuator was attached to an adjustable arm mounted on a laboratory stand for positioning and alignment in three dimensions. The mass lift software required a reversal of direction to be implemented as the actuator was mounted in the opposite orientation to the actuator on the Demonstration balance. This allowed all mass lift operation commands written for the Demonstration balance to be utilised immediately.

Figures 4.20a and 4.20b show the mass lift and modified mass pan in operation with a Pale Blue spherical test mass. In “mass off” position the cradle is raised clear of the top of the mass pan. In “mass on” position the cradle is lowered to approximately half way down the mass pan extension. The hole in the centre of the mass lift cradle is large enough to ensure the mass pan is not in contact with the cradle in this position. Figure 4.20c shows how the mass lift cradle and actuator were mounted and supported by a laboratory stand placed on a bench adjacent to the plinth the

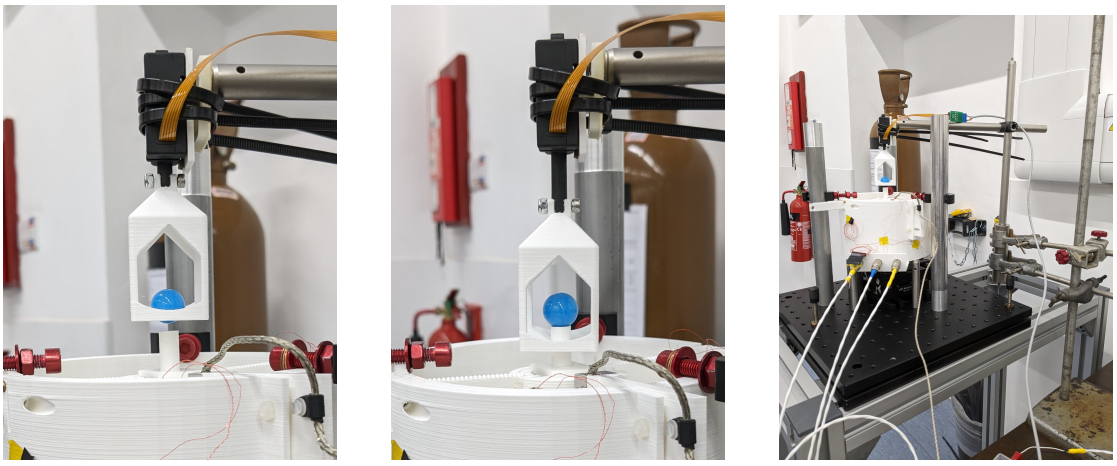

(A) Mass off. (B) Mass on. (C) Wide angle.

FIGURE 4.20: Mass lift system including mass lift cradle, actuator, adjustable support arm and modified mass pan.

prototype was placed on. This ensured that any vibration caused by the movement of the actuator would not affect the performance of the prototype.

4.5.3 Tare Mass

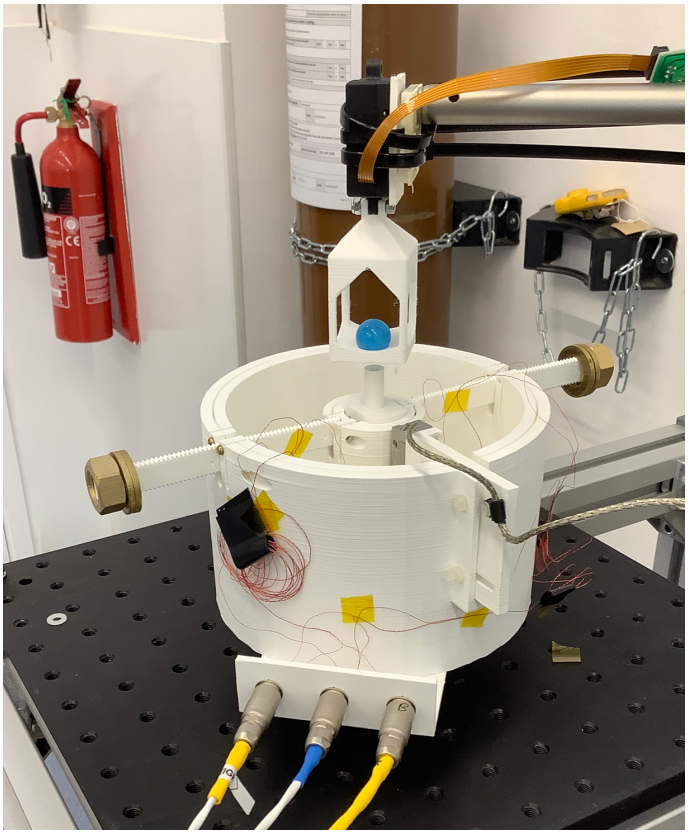

FIGURE 4.21: Brass tare weights counterbalancing the moving frame mass.

M12 brass nuts and brass washers, shown in position in figure 4.21, were selected as low cost tare masses for the end of each balance arm. The balance arm design was updated to include "teeth" on the top and bottom surfaces as shown in figure 4.22. These were sized and positioned to allow the M12 brass nuts to be threaded securely onto the end of each arm and provide controlled adjustment in and out as required to level the balance arms.

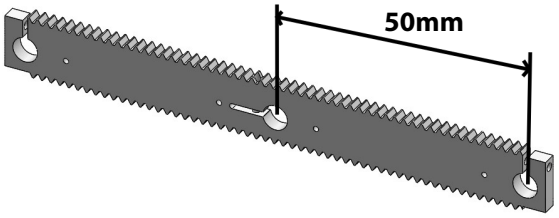

FIGURE 4.22: Updated balance arm CAD model that replaced part M in figure 4.2. 3D print shown in figure 4.21.

In the early stages of setting up and using the prototype balance it became clear that the brass tare masses were not required. When using current in the coils to change the balance offset position away from zero it was not possible move more than 0.3 mm below zero when the brass tare masses were in use. This was due to the asymmetrical nature of the current source used to supply the coils. The current source was originally designed for the NPL Demonstration balance which has a moving frame mass of approximately 200 g which is not permanently counterbalanced with physical masses. On start up the Demonstration balance moving frame is naturally positioned below the zero position due to the gravitational force on the moving frame being significantly larger than the mechanical force due to the stiffness of the flexures. Therefore the current source was designed to be uni-polar with a greater capacity to supply positive current than negative current. In terms of an electromagnetic Kibble balance this translates into a larger range of forces generated in the positive z-direction (pushing upwards) than in the negative z-direction (pulling downwards). Therefore, using the brass tare masses to offset the mass of the moving frame so that it was positioned close to zero when no current was applied caused the unintended consequence that movement in the downwards direction was limited. Increased motion in the negative z-direction was achieved by removing the brass tare masses from the balance arms to reduce the moving frame start position from 0.0 mm to -0.5 mm.

FIGURE 4.23: Modified mass pan with non-magnetic material added to the centre.

A trial was also carried out with a nominal 28.5 g of non-magnetic material added to the centre of the moving frame on a piece of studding screwed into the centre of the mass pan (figure 4.23). This reduced the start position to -1.7 mm. However this material was later removed as the additional mass appeared to cause instability during the weighing phase of measurements.

4.5.4 Coils

The coils were manufactured at NPL using a bespoke stepper motor wire twisting and winding system (Figure 4.24). This system was created in the mid-2010s for the development of the Next Generation Kibble balance coils and was also used to produce coils for the Demonstration Kibble balance. It is capable of producing twisted-pair wire and coils (either single or bifilar) when setup in different configurations.

In coil winding mode the software system takes a few variables to enable smooth operation such as wire diameter, coil diameter, coil height, winding speed, and starting position. During the coil winding procedure the operator must continually apply epoxy resin and monitor that the wire is being placed neatly, making adjustments where necessary. Both of these tasks were carried out using a small wooden stick. The software calculates and reports a few variables during the process such as the coil length and the current layer number. The software can be stopped or paused during winding.

A new coil former was designed in SolidWorks and produced from aluminium bar (Figure 4.25 and figure 4.24a). The diameter of the construction surface was designed

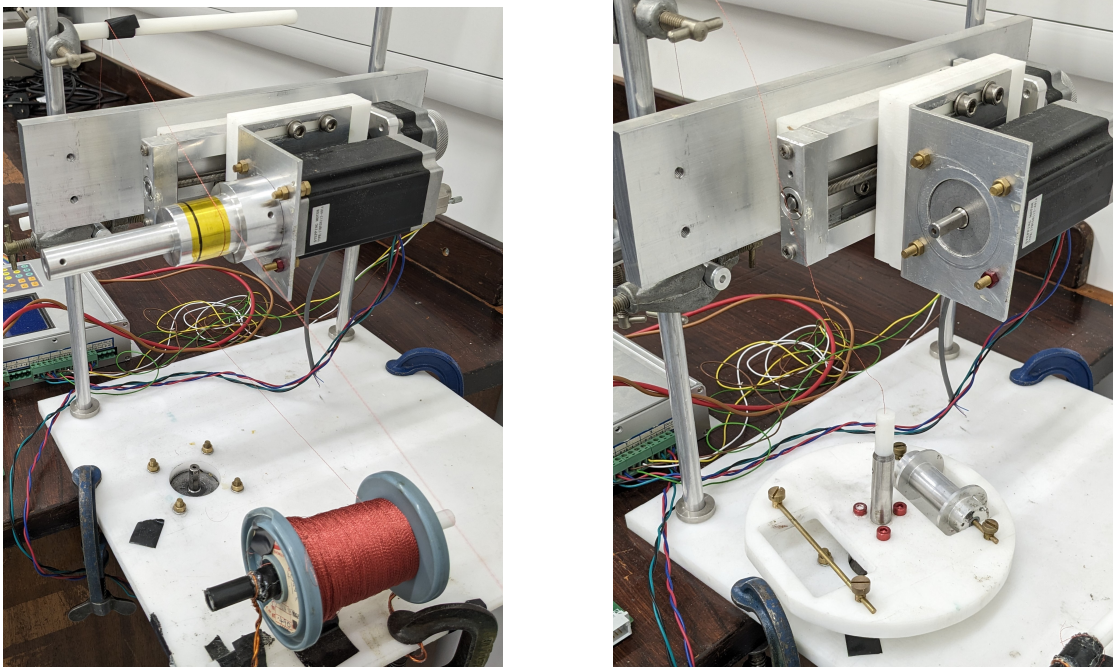

(A) Coil winding configuration. (B) Wire twisting configuration.

FIGURE 4.24: NPL wire twisting and coil winding system.

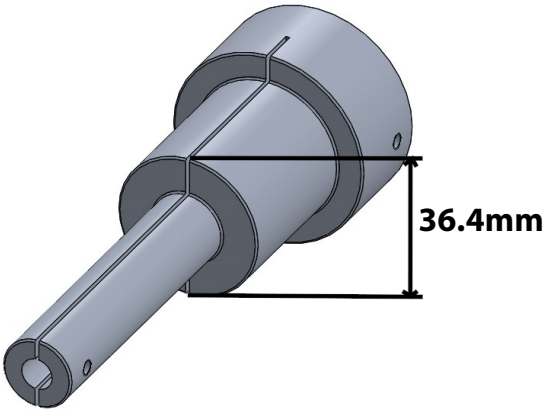

FIGURE 4.25: Coil former CAD model. Shown in place on the coil winder stepper motor in figure 4.24a.

to be fractions of a millimeter smaller than the required internal diameter of the prototype coils (36.5 mm). This allowed a thin film of Kapton tape and a layer of Teflon sheet to be placed underneath the coil during construction. This, plus the ability to clamp the end of the former in a vice and squeeze the central gap, facilitated removal of the coil from the former after the epoxy resin had cured.

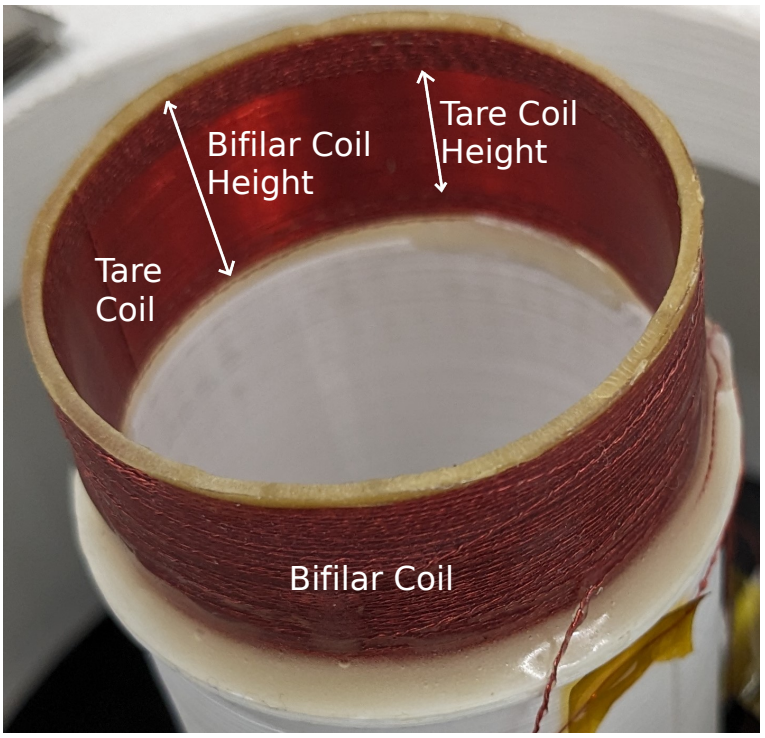

FIGURE 4.26: Co-wound single wire tare coil and bifilar main coils. Part J in figure 4.3.

The prototype coils (shown in figure 4.26) were all made from 0.125 mm diameter coated copper wire and Araldite® Ultra Strong epoxy resin. The tare coil was wound directly from a single strand. The main coils were made from a twisted-pair of the same wire. The methodology for the coil construction was adapted to take into account the co-location of the tare and main coils and the requirement for the loose ends of all the wires to finish at a similar location at one end of the coil.

The single wire tare coil was wound first. It was approximately 10 mm high and had two layers. The main coils were wound on top of the tare coil immediately. This was to maximise the chance of adhesion between all the coils. The main coil was approximately 15 mm in height and consisted of six layers. The intention had been to wind more layers on to the main coil however it was difficult to prevent the bifiar wire from spreading. The coil was finished after six layers to minimise the increase in height and ensure a suitable range of motion inside the magnet. The coils were left in position on the winding system for the epoxy resin to cure over night. The measured resistance of the main coils was approximately 40 Ω per coil and the measured resistance of the tare coil was approximately 28 Ω. The resistance per meter of the wire (ρ_{Cu}/A) was approximately 1.4 Ωm^{-1} calculated from its cross-sectional area ($A = \pi r^2 \approx 1.227 \times 10^{-8} m^2$) and the resistivity of copper ($\rho_{Cu} = 1.68 \times 10^{-8}\,\Omega m$). The measured resistances indicated an approximate length of 28 m for the main coils and 20 m for the tare coil including the additional connection wires. Approximately 2 m of connection wire was retained per coil. Therefore, all coils were slightly longer than

originally planned in the design (section 4.2.1) with the main coils 8% longer and the tare coil 20% longer.

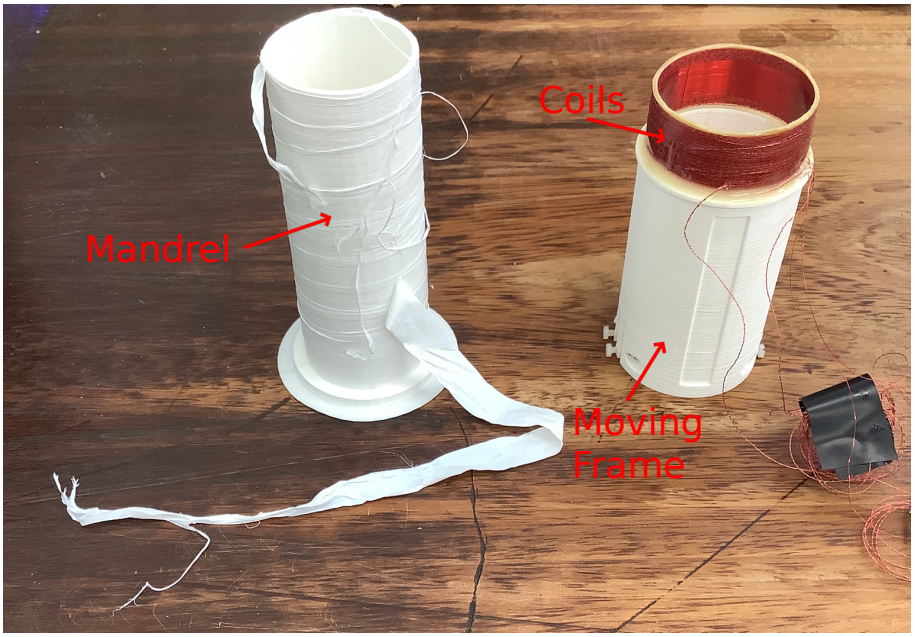

FIGURE 4.27: 3D printed coil alignment mandrel (left) and the moving frame (right) after attaching the coils.

The coils were glued into position on the bottom of the moving frame using Araldite® Ultra Strong epoxy resin and a 3D printed mandrel for alignment (Figure 4.27.) It was imperative to ensure that the coils were affixed concentrically and parallel with the moving frame to prevent fouling on the magnet. The 3D printed mandrel was coated in a layer of polytetrafluoroethylene (PTFE) tape to ensure that the moving frame and coils could be removed once the resin had cured.

4.5.5 Electrical Connections

To ensure a reliable electrical connection of the coils to the electronics box a wire connection plate was designed, printed, and bolted to the support frame of the prototype. It was located in a convenient position to allow the wires from the coils to be routed safely past moving parts of the balance. The wires were loosely coiled to prevent any external force being applied to the moving frame and also to reduce the chance of wires snapping or becoming damaged while the prototype was in use. The plate was designed to accommodate four-pin circular push-pull electrical connectors, one for each coil. The tare coil was connected to the central connector and the main coils on each end.

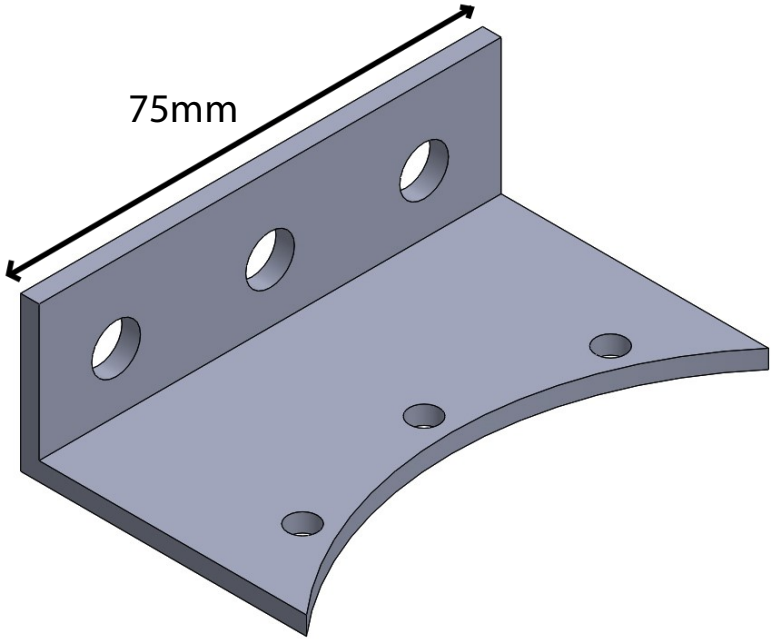

FIGURE 4.28: Wire connection plate CAD model. 3D print shown attached to the prototype in figure 4.21.

4.5.6 Alignment

On initial assembly and integration of the prototype the performance of the mechanical system was not as expected, specifically its motion did not conform to Simple Harmonic Motion (SHM). A number likely causes were discovered and remedial actions taken. These included repair of a broken flexure bearing clamp, removal of PLA "whiskers" (fine needle-like fragments of PLA produced during 3D printing) from the flexure bearings, and removal of a stray washer from inside the magnet gap!

After the improvements were made the alignment of the coil inside the magnet was checked. Although the coils did not appear to be fouling on the magnet they were hanging off-centre. After testing the motion of the mechanical system without the magnet in place it was decided to remove the magnet from its holder. As the alignment of the coils inside the magnet and the motion of the mechanical system are both critical components of the performance of this device an alternative solution for aligning the coils and magnet was created. As shown in figure 4.18 the support frame was firmly secured to an optical board in a raised position using posts and clamps. The magnet was positioned underneath the coil on a laboratory jack with the facility to adjust its level as well as its height. The optical board base was leveled using a bubble level. The laboratory jack platform was found to be level without adjustment. The magnet and coils were aligned concentrically by eye from above. In this

configuration the mechanical system performed as expected. Measurements of the mechanical spring constant of the system are presented in section 5.1.1.

It is possible that the magnet holder could be reintroduced in future iterations of the prototype. An investigation of the manufacturing tolerances will need to be carried out and the 3D printed parts designs updated accordingly. This was not carried out as part of this work due to time constraints.

4.6 Balance Control Software

The software used to operate and control the prototype balance is called Nessus-2. It is in-house software that has been in use and developed by NPL since the early 1990s [106]. It is written in Modula-2 and complied using XDS-C Modula-2 compiler. This is a "via C" type compiler that produces source code which is subsequently compiled by the Free Software GNU Compiler Collection (GCC).

Nessus-2 is a multitasking interpreter based program designed around two data structures: a stack and a dictionary library. Multiple instances of an interpreter can run simultaneously each with access to the same dictionary but maintaining an independent stack. The dictionary contains all the variables and procedures that can be accessed and the stack stores the input and output values of calculations and computations. The user inputs commands and receives information through a command-line style interface. The interpreter language has a similar style to PostScript [107].

Nessus-2 is capable of executing Modula-2 code in real-time through a separate program called RTS (Real Time System). This is essential for the operation of the balance and to facilitate the collection of data at known times. The purpose of RTS is to setup a periodic call to a single routine that carries out all real-time operations on behalf of Nessus-2 by calling relevant sub-routines. This is an interrupt driven system and communication between the two programs is via shared memory blocks. Although separate, the source code for RTS is contained within the source code for Nessus-2. A compiler flag is used to denote which parts of the code should be included in each program.

Chapter 5

Testing and Calibration

Kibble balances are complex instruments that require several independent subsystems to be setup, calibrated, and tested prior to making mass measurements. As part of the setup process it is necessary to measure properties and characteristics of the balance including interactions between subsystems. These preparatory steps assist with optimising the performance of the balance and facilitate the collection of data necessary for estimating Type B uncertainty contributions. This work also allows verification of the design predictions included in chapter 4.

5.1 Prototype Stiffness Characterisation

In this section the stiffness characteristics of the prototype guidance mechanism were measured for the purposes of setup and verification of the design predictions in chapter 4.

5.1.1 Mechanical System Spring Constant

The total spring constant of the guidance system was measured and compared with an analytical calculation to verify the accuracy of the design predictions in chapter 4.

Practical Measurement

By assuming that the mechanical system of the prototype behaves according to the principles of Simple Harmonic Motion (SHM) the total spring constant of the system can be determined by measuring the natural frequency of motion of the moving frame.

$$f = \frac{1}{2\pi}\sqrt{\frac{\kappa}{m}} \tag{5.1}$$

$$\kappa = (2\pi f)^2 m \tag{5.2}$$

Where f is frequency, κ is spring constant and m is mass.

The prototype balance was setup as shown in figure 4.12 where l_r was equal to 50 mm. Brass nuts and washers were used as tare masses at the end of each arm to suspend the moving frame with the arms in the horizontal position. In this configuration the tare mass applied to each prototype arm (m_t) is equal to half of the moving frame mass ($0.5m_{mf}$). The sum of tare mass applied to each arm is equal to the mass of the moving frame. The tare masses were measured using a Kern KB1200-2N table-top digital mass scale (s/n W 1305827) with a 10 mg resolution.

TABLE 5.1: Measured tare mass m_t values and calculated moving frame mass m_{mf} used in spring constant κ calculation.

Tare Mass m_{t1}	**Tare Mass** m_{t2}	**Total** m_{mf}
g	**g**	**g**
28.16	28.01	56.17

The total moving frame mass of 56.17 g is approximately 30% less than the estimated value (80 g) calculated on page 76 during the design process. This is most likely to be due to an error in the assumed density of the 3D printed material and/or the volume of the 3D printed parts.

The natural frequency of the motion of the moving frame was measured using a Siglent SDS1204-E oscilloscope (s/n SDSMMEBX3R2603). The moving frame position indicated by the Renishaw linear encoder (Nessus-2 variable "fracmm") was observed on the oscilloscope. The tare and weighing coils were disconnected from the electronics box and the software was in an idle state to prevent interference from non-mechanical forces. Starting from stationary each time the moving frame was displaced in the negative z direction and released. The resulting oscillation frequency was measured using the oscilloscope "stop" function. The equilibrium position of the moving frame between runs was monitored to ensure the system was behaving like a spring, specifically that the frame returned to the same resting position each time as per a mass on a spring moving according to SHM.

TABLE 5.2: Results from the measurement of the natural frequency f of the mechanical system.

Run	Frequency f	Residual equilibrium position
-	Hz	μm
1	6.13	-0.59
2	6.11	0.77
3	6.12	-0.59
4	6.12	0.47
5	6.11	-0.07
6	6.12	-0.21

The mean natural frequency of 6.12 Hz was calculated from the results in table 5.2. The spring constant κ was calculated to be 83.0 Nm^{-1} according to equation 5.2 using the mass of the moving frame from table 5.1 and the average natural frequency from table 5.2. This value was approximately 33% higher than predicted from the analytical evaluation of the prototype design (62.15 Nm^{-1}).

The cause of the 33% difference between the measured and predicted mechanical spring constants is not immediately clear. Perhaps the stiffness of the pivot bearing clamps contributed more significantly to the force on the moving frame than implied by the theory in section 4.4.3.

The higher spring constant of the mechanical system will have a negative impact on the mass sensitivity of the prototype balance by increasing the predicted mass resolution from 0.127 mg to 0.169 mg. The effect of this difference in mass resolution on measurement uncertainty will be minimal for this prototype design (balance arm length l_r =50 mm) as demonstrated by the predicted uncertainty results presented in figure 4.16.

5.1.2 Force Profile

The forces acting on the moving frame of a Kibble balance are a combination of local gravity and spring force from the mechanical guidance system. The "force profile" of a Kibble balance is the amount of force required to hold the moving frame at each position along the z-axis over its moving range. The Nessus-2 Kibble balance software includes a "tare compensation" system that is designed to negate the force profile of the balance during measurements by applying an opposing force depending on the moving frame position. It does this by flowing the appropriate current through the tare coil.

As described in section 4.5.3, the prototype balance was setup without external tare masses for routine operation (weighing and moving phases). Therefore, the brass nuts and washers used in section 5.1.1 were removed.

The force profile of the prototype was determined using two independent methods. A manual method using physical weights to apply a force and an automated software routine using subsystems of the prototype balance.

Manual

Standard weights from set NPLW3465 were used to deflect the moving frame by applying the known force $F = mg$ where m is the calibrated mass of the standard weight and g is local gravity (9.81 ms^{-2}). This method was performed over the range 0 to -0.05 mm using weights between 50 mg and 1000 mg.

Automatic

DMTMeasF was the Nessus-2 software routine that controlled the position of the moving carriage by supplying current to a main coil. Current measurements were collected at specified z-axis positions. Current was converted to force using the BL product of main coil 1 in the magnetic field. This routine required that the weighing servo system was capable of holding the moving frame position stable to within a few micrometers over the range of positions specified. The range of motion was limited by the maximum current (60 mA) that could be applied to the coil, the length of the coil inside the magnetic field and the stiffness coefficient of the flexures. Data was collected over the range ± 0.4 mm.

Results

Figure 5.1 shows the force profile data collected from the manual and automatic methods. The manual method data was fitted by a linear regression and this fit is shown extrapolated to ± 0.5 mm. The automated force profile 231011a was a close match to the gradient of the data collected manually using weight set NPLW3465 in the region up to ± 0.2 mm. Beyond this range the force profiles do not match. It is unclear why the gradient of force profile 231011a increases significantly and abruptly at ± 0.2 mm. However this was a repeatable observation.

When tested both the gradient from NPLW3465 and force profile 231011a were unsuccessful in producing stability for the weighing servo system. Specifically, a driven oscillation of the moving frame was produced which meant that it was impossible to collect weighing data.

The NPLW3465 gradient profile was adjusted in the software by trial and error to find a force profile that produced the required outcome. A profile with 50% of the gradient

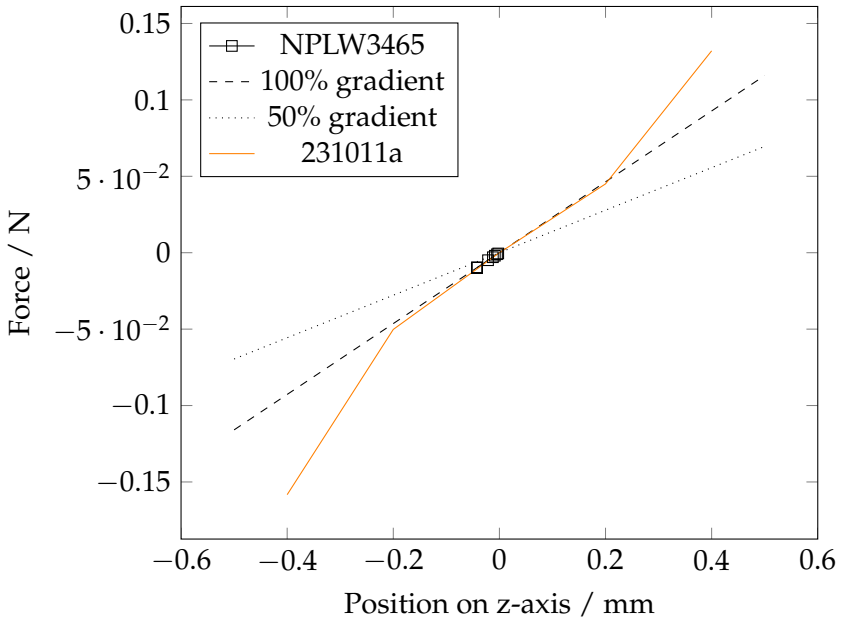

FIGURE 5.1: 3D printed prototype system force profile. The black squares show the data collected using weight set NPLW3465, the black dashed and dotted lines are 100% and 50% of the linear gradient of the weight set data respectively, and the orange line is the force profile collected by the automated software routine on 11th October 2023.

of the NPLW3465 profile successfully produced stability for the weighing servo system and allowed weighing data to be collected.

The total spring constant of the guidance mechanism was estimated from the force profile data. By assuming that the guidance mechanism behaved according to simple harmonic motion ($F = \kappa z$) the spring constant κ was calculated by performing a linear regression on the force profile datasets. The calculated values of the spring constant for the manual data set and the automatic force profile between ± 0.2 mm were very similar, 232 Nm^{-1} and 238 Nm^{-1} respectively (approximately +184% higher than measured in section 5.1.1 and +278% higher than predicted). The calculated spring constants for the automatic force profile outside of the central 0.4 mm were higher, 305 Nm^{-1} from -0.4 mm to -0.2 mm and 361 Nm^{-1} from +0.2 mm to +0.4 mm (approximately +300% higher than measured in section 5.1.1 and +436% higher than predicted). The large discrepancy observed between the measured spring constant in section 5.1.1 and the spring constants calculated from the force profile data may be due to the difference in mechanical system setup between the two tests. For the mechanical measurements in section 5.1.1 the mass of the moving frame was counter balanced by external tare masses attached to the balance arms. This was the configuration assumed for analytical evaluation of the prototype design. For the force profile measurements in this section (5.1.2) the external tare masses were removed. Examples in the literature [108][109][110] have shown that adding or adjusting the position of "trim" masses on a balance mechanism can reduce the total apparent stiffness of the system. Therefore, it is possible that by removing the tare masses from

the balance arms of the prototype the apparent stiffness of the system was increased. Further work will need to be carried out to test this hypothesis.

5.1.3 Summary

TABLE 5.3: Summary of predicted and measured spring constants κ of the guidance mechanism system.

ID	**Measurement Range** z	**Spring Constant** κ
-	**mm**	**Nm**$^{-1}$
Predicted	Not applicable	62.15
Mechanical Measurement	Not recorded	83.0
Manual Force Profile	-0.05 to 0.0	232
Automatic Force Profile	-0.2 to +0.2	238
Automatic Force Profile	-0.4 to -0.2	305
Automatic Force Profile	+0.2 to +0.4	361

The spring constant results measured in this chapter are summarised in table 5.3. These results highlight that the material properties and mechanical design should be carefully considered when scaling to MEMS where minimising flexure stiffness becomes increasingly important for reducing uncertainty as shown by figure 4.17.

Further work will need to be carried out to determine why the measured spring constant of the prototype was higher than predicted in both balance configurations. A dynamic analysis of the guidance mechanism according to principles detailed in [111] and [112] should be considered for future work.

5.2 Subsystem Calibration

The following subsystems were calibrated to determine constant values required for the calculation of mass and its associated uncertainty from the data collected by the prototype balance.

5.2.1 Voltmeter

The prototype balance voltmeter was based on a Thaler Corporation ADC180 Programmable Integrating Analogue to Digital (A/D) Converter. It was configured to work in two gain modes. In "low" gain mode measurements are made by the Thaler ADC180 directly with a nominal gain of 1. In "high" gain mode the voltage signal was passed through a pre-amplifier with a nominal gain of 1005 prior to being measured by the Thaler ADC180. The pre-amplifier was an EM Electronics DC Amplifier Model A22 and was switched in and out of the voltage measurement circuit using

relay switches. Low gain mode was used during the weighing phases of the prototype balance mass measurements and high gain mode was used during the moving phases. Two separate calibrations of the prototype balance voltmeter were performed, one in each gain mode.

Description

The Thaler ADC180 has a $\pm 10.48\,\mathrm{V}$ full scale input range with a 26-bit resolution. It is capable of continuous sampling of 20 MHz with an integration time as programmed by the user [113]. An integration time of two seconds was selected for all voltage measurements in this work.

The EM DC A22 is a low noise amplifier module designed specifically for low signal DC voltage measurements [114].

Low Gain Calibration Method

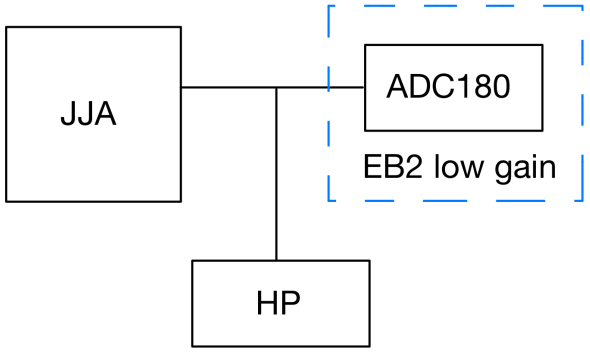

FIGURE 5.2: Connection diagram for the calibration of the prototype balance ADC180 voltmeter (EB2) in low gain mode against a Josephson Junction Array (JJA) primary voltage source. HP nanovoltmeter shown was used to determine the Josephson Voltage step number n.

The prototype balance ADC180 voltmeter (Electronics Box s/n 2, EB2) in low gain mode was calibrated against a primary voltage standard known as a Josephson Junction Array (JJA).

JJAs produce stable quantised voltage steps that are traceable to the SI system of units. They are based on superconducting junctions that operate at the temperature of liquid helium (4 K). The output voltage V_J is dependant only upon the integer step number n, the driving frequency f, elementary charge e, and the Plank constant h [115].

$$V_J = \frac{nfh}{2e} \tag{5.3}$$

The calibration was carried out from +5 V to -5 V and sampled at 0.5 V intervals. This range was selected as the expected range of voltage values for this work. Approximately 24 voltage readings were recorded at each 0.5 V measurement step by the voltmeter under test. The whole measurement run took approximately 16 minutes and was repeated 10 times.

A Nessus-2 software routine (MNCDMeasVseq) was written to collect data from the voltmeter under test. For each voltage measurement the following information was recorded: Modified Julian Date (MJD), nominal gain, ADC180 result index, integration gate time, indicated voltage, and the difference between the current indicated voltage and the previous indicated voltage.

The output voltage of NPL's JJA during the calibration was calculated using data from an EIP Model 578B locking frequency counter (s/n 2021-1539) and a HP 34420A nanovoltmeter (s/n US36000721). The frequency counter was used to monitor the driving frequency f of the JJA and the nanovoltmeter was used to determine the integer step number n of the output voltage. This reference data was recorded every 3 to 4 seconds during the calibration.

$$n = sgn\left(n_{HP}\right)\left\lfloor |n_{HP}| + 0.5 \right\rfloor = -sgn\left(n_{HP}\right)\left\lceil - |n_{HP}| - 0.5 \right\rceil \tag{5.4}$$

$$n_{HP} = \frac{V_{HP}}{V_{step}} \tag{5.5}$$

$$V_{step} = \frac{fh}{2e} \tag{5.6}$$

Where n_{HP} is the non-integer step number of the Josephson voltage according to the HP nanovoltmeter, V_{HP} is the HP nanovoltmeter indicated voltage, $h = 6.626\,070\,15 \times 10^{-34}$ J·s and $e = 1.602\,176\,634 \times 10^{-19}$ C [34].

The average measured driving frequency $f = 76\,917.0$ MHz was used in equation 5.6 to calculate the step voltage $V_{step} \sim 159\,\mu$V.

The timestamp recorded on the reference data set was used to assign the correct Josephson Step number n to each data point recorded by the voltmeter under test. The reference voltage for each measurement was calculated by multiplying V_{step} by the assigned n.

Low Gain Results

The gain and the offset of the voltmeter under test were determined by fitting a straight line (linear regression) to the indicated voltage V_{ind} against the applied Josephson voltage V_J for each ± 5 V measurement sequence. The "least squares" method was used.

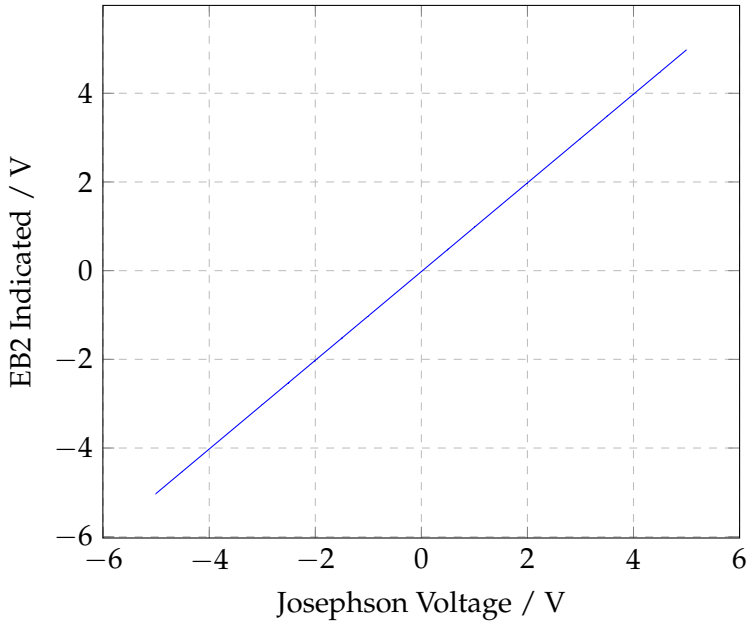

FIGURE 5.3: EB2 voltmeter low gain calibration data from +5 V to -5 V. Run ID 01.

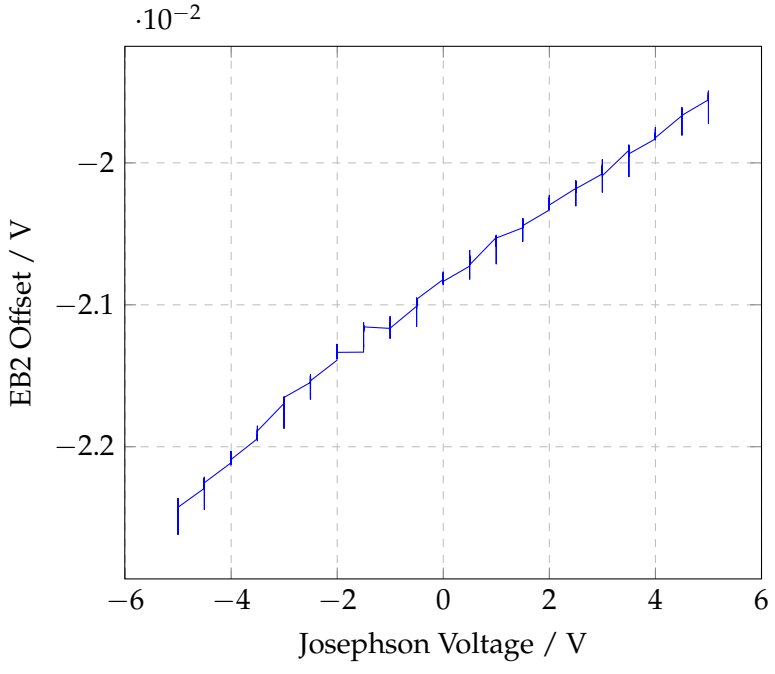

FIGURE 5.4: EB2 voltmeter low gain offset ($V_{ind} - V_J$) from +5 V to -5 V. Run ID 01.

TABLE 5.4: A summary of EB2 voltmeter low gain calibration results.

Run ID	Gain	Gain Standard Error	Offset	Offset Standard Error
-	-	ppm	V	μV
00	1.000 257	0.9	-0.020 7	2.7
01	1.000 285	1.2	-0.020 9	3.6
02	1.000 249	1.0	-0.021 1	3.1
03	1.000 246	0.7	-0.021 2	2.2
04	1.000 237	0.9	-0.021 1	2.7
05	1.000 227	1.2	-0.021 1	3.8
06	1.000 229	1.3	-0.021 0	3.9
07	1.000 224	1.2	-0.021 0	3.6
08	1.000 224	1.2	-0.021 0	3.6
09	1.000 227	1.1	-0.021 0	3.4

Figures 5.3 and 5.4 are plots of the voltage data collected during calibration run ID 01. These plots are typical of the data collected during this calibration.

Table 5.4 contains the calculated gain and offset for each calibration run. The mean of the gain G_{EB2L} was 1.000 241 with a standard deviation of 0.000 018. This result shows that the gain of the EB2 voltmeter was stable over the calibration period. The mean offset was -21.0 mV. As shown in figure 5.4 the offset was variable with an average linear gradient of 0.24 mV/V. The magnitude of the offset and its variability with voltage were both larger than expected indicating a possible fault with the Thaler ADC180 which requires further investigation. The methods of measuring by difference in both weighing and moving phases will negate the majority of the offset however the gradient will need to be included the uncertainty budget as a known source of error (0.002 4%).

Low Gain Uncertainty Budget

TABLE 5.5: EB2 voltmeter low gain calibration uncertainty budget.

Note	Contribution	Value	Unit	Unc. ($k = 1$)	Unit	Distribution	Sensitivity	Unc. ($k = 1$) V	%
i	Low gain coefficient Type A	1.000241	-	5.83E-06	-	1	1.59E-04	9.3E-10	0%
ii	Voltmeter offset	2	V	4.80E-04	V	1	1	4.8E-04	90%
iii	JJA frequency	76917000000	Hz	5	Hz	1	2.07E-15	1.0E-14	0%
iv	JJA step number	1	-	1	-	1	1.59E-04	1.6E-04	10%
							Total ($k = 1$) V	0.0005	100%

As shown in table 5.5 the total uncertainty of the EB2 voltmeter calibration was calculated to be 0.5 mV at $k = 1$. The low gain coefficient type A uncertainty was calculated from the gain calibration results according to the equation for standard error of the mean.

$$u = \frac{\sigma}{\sqrt{N}} \tag{5.7}$$

where u is the standard uncertainty, σ is the standard deviation of the mean, and N is the number of data points.

A maximum of 2 V difference between measured values in the two mass states has been assumed to calculate the uncertainty due to variable offset of the voltmeter observed in figure 5.4. An uncertainty of 5 Hz has been allocated to the frequency source applied to the JJA during the calibration. The HP nanovoltmeter used to determine the step number of the JJA during the calibration had a 50 μV offset. As this offset was $\sim$3 times smaller than the step voltage of $\sim$ 159 μV it was assumed that the maximum error in step number could only be a single step.

High Gain Calibration Method

The prototype balance EB2 voltmeter in high gain mode (ADC180 plus A22) was calibrated using a Keysight 3458A multimeter (s/n MY45053792), a Fluke 720A Kelvin-Varley voltage divider (s/n FL720A-1 2525002 VOLT) and a Time Electronics Type 2003 0.05% grade battery powered voltage source. The calibration was carried out in two steps.

Stage 1

The 3458A multimeter was calibrated against the EB2 voltmeter in low gain mode at the following voltage values $\pm$1 V, $\pm$4 V, $\pm$6 V, and $\pm$10 V. The battery powered voltage source was connected to the 3458A and EB2 in parallel as shown in figure 5.5a. The 3458A was set to indicate average readings over 500 power line cycles (approximately 10 seconds). The EB2 was set to record voltage measurements every 2 seconds using the Nessus-2 software routine MNCDMeasVseq. The voltage source was changed to a new value every 2 minutes. The 3458A indication was recorded after approximately 1 minute 40 seconds of stabilisation time. The average of 5 readings recorded by the EB2 voltmeter were calculated for each voltage. These were selected to be at a time close to when the 3458A indication was recorded. The results are presented in table 5.6.

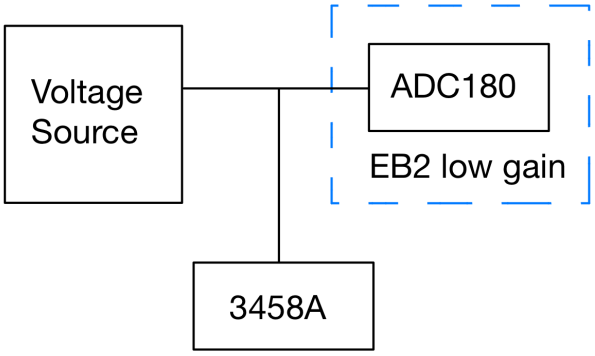

(A) Stage 1: Connection diagram for 3458A multimeter calibration against the EB2 (ADC180) voltmeter in low gain mode.

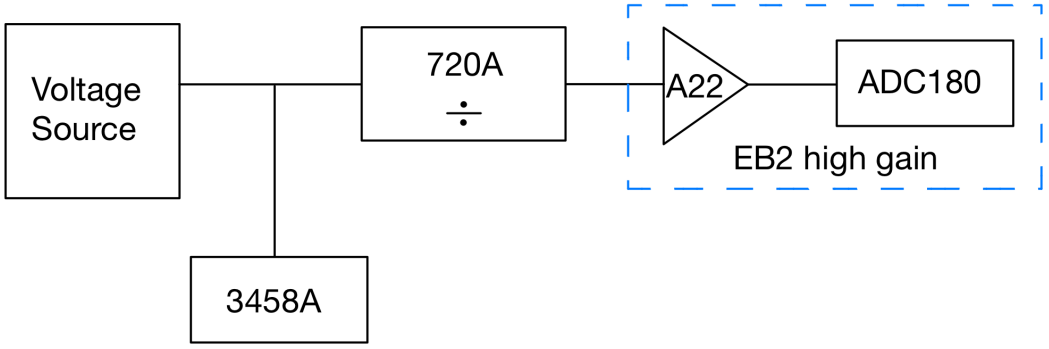

(B) Stage 2: Connection diagram for the EB2 (ADC180) voltmeter calibration in high gain mode showing the source voltage attenuation by the 720A voltage divider and subsequent amplification by the A22 pre-amplifier.

FIGURE 5.5: Connection diagrams for the two stages of the calibration of the prototype balance EB2 voltmeter (ADC180) in high gain mode.

TABLE 5.6: 3458A calibration against the EB2 voltmeter in low gain mode over the range ± 10 V.

Nominal	EB2 Low Gain Ind	3458A Ind	Average EB2 Corr	Average 3458A
V	V	V	V	V
10	9.995 497	9.997 853	9.995 528	9.997 843
-10	-10.000 368	-9.997 832		
6	5.995 862	5.998 231	5.996 833	5.998 253
-6	-6.000 688	-5.998 274		
4	3.996 100	3.998 449	3.997 5 14	3.998 452
-4	-4.000 852	-3.998 455		
1	0.997 066	0.999 415	0.999 185	0.999 433
-1	-1.001 758	-0.999 452		

The positive and negative indicated voltage values for each voltmeter were combined to remove instrument voltage offset from the calibration.

$$2V_{av} = (V_+ + V_o) - (V_- + V_o) \tag{5.8}$$
$$2V_{av} = V_+ - V_- \tag{5.9}$$
$$V_{av} = \frac{V_+ - V_-}{2} \tag{5.10}$$

Where V_{av} is average voltage, V_+ is positive voltage, V_- is negative voltage, and V_o is offset voltage.

$$V_{corr} = \frac{V_{av}}{GD} \tag{5.11}$$

Where V_{corr} is corrected voltage, G is the gain coefficient, and D is the input division ratio.

The average EB2 data were corrected according to equation 5.11 using gain coefficient G_{EB2L} calculated during the low gain calibration and input division ratio D of 1. The gain of the 3458A was determined by fitting a straight line (linear regression) to the final two columns in table 5.6. The calculated gain G_{3458A} was 1.000 230 with a standard error of 2.2 ppm.

Stage 2

The EB2 voltmeter in high gain mode was calibrated using the 720A voltage divider and the calibrated 3458A multimeter. The battery powered voltage source was connected to the 3458A and the input of the 720A voltage divider in parallel. The 720A was adjusted following the manufacturer's procedure and checked against the linearity of the 3458A prior to use. The division by 1 000 was found to be accurate to within 3 ppm. The output of the 720A was connected to the input of the EB2 in high gain mode. The above measurement sequence at ± 1 V, ± 4 V, ± 6 V, and ± 10 V was repeated in the new connection configuration. The results are presented in table 5.7.

The average 3458A data were corrected according to equation 5.11 using gain coefficient G_{3458A} calculated during the first stage of this high gain calibration and input division ratio of 1 000 from the 720A voltage divider. The gain of the EB2 voltmeter in high gain mode was determined by fitting a straight line (linear regression) to the final two columns in table 5.7. The calculated gain G_{EB2H} was 1004.401 with a standard error of 3.6 ppm.

TABLE 5.7: EB2 voltmeter in high gain mode calibration against the 3458A over the range ±10 V.

Nominal	3458A Ind	EB2 High Gain Ind	Average 3458A Corr	Average EB2
V	V	V	V	V
10	9.998 200	10.038 039	9.995 888	10.039 864
-10	-9.998 174	-10.041 689		
6	5.998 264	6.021 577	5.996 901	6.023 317
-6	-5.998 296	-6.025 057		
4	3.998 550	4.013 552	3.997 632	4.015 238
-4	-3.998 553	-4.016 924		
1	0.999 468	1.017 847	0.999 248	1.003 634
-1	-0.999 488	-1.005 349		

High Gain Uncertainty Budget

TABLE 5.8: EB2 voltmeter high gain calibration uncertainty budget.

Note	Contribution	Value	Unit	Unc. ($k = 1$)	Unit	Distribution	Sensitivity	Unc. ($k = 1$) V	%
i	Low gain coefficient Type A	1.000241	-	5.83E-06	-	1	1.58E-07	9.2E-13	0%
ii	Voltmeter offset	0.6	V	1.44E-04	V	1	9.96E-04	1.4E-07	45%
iii	JJA frequency	76917000000	Hz	5	Hz	1	2.06E-18	1.0E-17	0%
iv	JJA step number	1	-	1	-	1	1.58E-07	1.6E-07	55%
v	High gain coefficient Type A	1004.401	-	0.005	-	1	5.95E-10	3.1E-12	0%
							Total ($k = 1$) V	2.1E-07	100%

As shown in table 5.8 the total uncertainty of the EB2 voltmeter calibration in high gain mode was calculated to be 0.2 μV at $k = 1$. This calculation included the low gain calibration contributions (low gain coefficient type A, JJA frequency and JJA step number) as in table 5.5 in addition to an updated voltmeter offset contribution and a high gain coefficient contribution. A maximum of 0.6 V difference between measured induced voltage in the two moving directions ($V_+ - V_-$) has been assumed to calculate the uncertainty due to variable offset of the voltmeter observed in figure 5.4.

TABLE 5.9: Pre-amplifier calibration uncertainty budget.

Note	Contribution	Value	Unit	Unc. ($k = 1$)	Unit	Distribution	Sensitivity	Unc. ($k = 1$)	%
i	A22 gain fit error	1004.401	-	0.003589691	-	1	1	3.6E-03	48%
ii	720A divider	1000	-	0.003	-	1	1	3.0E-03	34%
iii	3458A gain fit error	1.00023003	-	2.17138E-06	-	1	999.540	2.2E-03	18%
iv	3458A resolution	0.000001	V	0.0000005	V	1.732	999.540	2.9E-04	0%
							Total ($k = 1$)	0.005	100%

The high gain coefficient uncertainty was calculated to be approximately 5 ppm as shown in table 5.9. Contributions include 3.6 ppm from the standard error of the

gradient from the linear fit of the calibration data for G_{EB2H} in stage 2, 3 ppm for the maximum error of 720A voltage divider, 2.2 ppm for the standard error of the gradient of the linear fit of the calibration data for G_{3458A} in stage 1.

Summary

The calibration coefficients in low gain and high gain mode were determined to a high level of accuracy with traceability to the SI unit of voltage. The results of these calibrations show that the prototype voltmeter was capable of meeting the measurement requirements for this work.

5.2.2 Resistor

As discussed in section 3.1, a Kibble balance in weighing phase measures the current passing through the weighing coil by using a resistor to convert current I_W to voltage V_W. Therefore the value of the resistor R used needs to be known accurately in order to calculate mass.

Description

The resistor included in the prototype balance electronics box (s/n 2, EB2) for the purpose of converting current in the weighing coil I_W to voltage V_W is a UFPB100RV TE Connectivity high precision metal film leaded resistor with a nominal value of 100 Ω. It is specified with a 0.02% resistance tolerance, a Temperature Coefficient of Resistance (TCR) of 5 ppm/°C, and a 0.5 W power rating [116].

Calibration Method

The resistor under test was calibrated in-situ on the coil control board inside the electronics enclosure with the lid removed. An Isotech microK Resistance Bridge (s/n 381482/1) and a Tinsley 100 Ω Standard Resistor Model 5685A (s/n 267732) were used to carry out the calibration. Each of the 4-wire channels on the microK resistance bridge was setup to measure against its internal 100 Ω resistor using a 1 mA sensing current. The rolling average and standard deviation of up to 100 readings for each channel was continuously displayed.

Channel 2 was used to measure the resistor under test. See below for connection details. Channel 3 was used to measure the 5685A standard resistor. Channel 1 was used to measure the temperature of the 5685A standard resistor using a Platinum

Resistance Thermometer (PRT) (s/n 14/10286-07) with a recent calibration (certificate number 2023070242/4/PM04).

The microK bridge internal 100 Ω resistor was adjusted using the 5685A standard resistor (certificate number 2023070375-2 (RM 35.179)) according to the manufacturer's procedure prior to starting calibration measurements.

The calibration was carried out at two temperatures 20°C and 22.5°C. This was achieved by changing the air temperature of the laboratory and allowing the equipment to equilibrate at measurement conditions for a minimum of 16 hours.

Connection Details

The resistor under test was connected to the microK bridge using a 4-wire connection. The 4-wire voltage sense was connected directly to the resistor terminals using connection point SK19 on the coil control board. The 4-wire current input was connected through SK18 which usually connects the current source to the coils. A relay was operated such that weighing coil 1 was switched into moving mode and therefore weighing coil 2 was in weighing mode. A shorting connector was used on SK15 to complete the circuit.

Results

TABLE 5.10: Resistor calibration data.

5685A Temp. T	**5685A Indicated Average**	**5685A Standard Deviation**	**5685A Certified Value** R_T	**microK Corretion** $R_{corr}(T)$	**EB2 Indicated Average**	**EB2 Standard Deviation**	**EB2 Corrected**
°C	Ω	Ω	Ω	Ω	Ω	Ω	Ω
19.934	99.999 617	0.000 012	99.999 615	-0.000 002	99.992 856	0.000 039	99.992 854
19.935	99.999 614	0.000 011	99.999 615	+0.000 001	99.992 970	0.000 016	99.992 971
22.442	100.000 070	0.000 011	100.000 071	-0.000 002	99.993 139	0.000 014	99.993 137
22.452	100.000 075	0.000 010	100.000 076	+0.000 001	99.993 138	0.000 011	99.993 139

TABLE 5.11: Resistor Temperature Coefficient of Resistance (TCR) data.

Resistor ID	**Average Temperature Difference**	**Average Resistance Difference**	**Temperature Coefficient of Resistance**	**Temperature Coefficient of Resistance**
-	**°C**	Ω	**Ω/°C**	**ppm**
5685A	2.512	0.000 458	0.000 182 49	1.82
EB2	2.512	0.000 225	0.000 089 75	0.90

The TCR of the 5685A standard resistor and the resistor under test were determined using an average of the data in table 5.10. For this calculation, the temperature of the resistor under test was assumed to be the same as the temperature of the 5685A standard resistor. The results show that both resistors have a very low TCR consistent

with their respective manufacturer specifications, ±5 ppm/°C [116] and 2 ppm/°C [117].

The calculated TCR for the 5685A standard resistor of 1.82 ppm/°C was used in conjunction with its certified resistance value at 20°C to calculate a correction for the indicated values on the microK bridge as per equations 5.12 and 5.13.

$$R_T = R_{20^\circ C} + (T - 20)\alpha \tag{5.12}$$

Where R_T is the value of the 5685A standard resistor at temperature T in °C, and $R_{20^\circ C}$ is the certified resistance value at 20°C and α is the TCR of the 5685A standard resistor in $\Omega/^\circ C$ respectively.

$$R_{corr}(T) = R_{ind}(T) - R_T \tag{5.13}$$

Where $R_{corr}(T)$ is the resistance correction, $R_{ind}(T)$ is the indicated value of the 5685A standard reference resistor and R_T is the calculated reference value of the 5685A standard reference resistor at temperature T.

The resistance of the resistor under test at 20°C was calculated to be 99.992 919 Ω using average values of the results in table 5.10 and the measured TCR in table 5.11.

Uncertainty Budget

TABLE 5.12: EB2 100 Ω resistor calibration uncertainty budget.

Note	Contribution	Value	Unit	Unc. ($k = 1$)	Unit	Distribution	Sensitivity	Unc. ($k = 1$) Ω	%
i	EB2 Resistor - Type A	99.9929	Ω	1.60E-06	Ω	1	1	1.6E-06	0%
ii	EB2 Resistor - Temperature	20	°C	5	°C	1	0.0005	2.5E-03	100%
iii	Standard Resistor - Calibration	99.9996	Ω	5.00E-06	Ω	2	1	2.5E-06	0%
iv	Standard Resistor - Temperature Coefficient	20	°C	0.005	°C	2	0.0002	5.0E-07	0%
v	Standard Resistor - Temperature Coefficient Error	20	°C	0.05	°C	1	0.0002	1.0E-05	0%
							Total ($k = 1$) Ω	0.0025	100%

The total uncertainty of the prototype resistor calibration was calculated to be ∼25 ppm at $k = 1$ including contributions due to the type A uncertainties of the measurements, the properties of the resistors, and the environmental conditions as shown in table 5.12.

The temperature of the prototype balance resistor was not measured directly during this calibration procedure. It is likely that it was not at exactly the same temperature as the 5685A standard reference resistor. However it can be assumed that it was at a temperature that could be considered typical during "normal" operation ($20 \pm 5\,°C$). A value of 5 ppm/°C has been assumed as a conservative estimate of the TCR. The calculated TCR of 0.90 ppm/°C has not been used as this appears to be an underestimate and the temperature of resistor was not measured directly. For future work it is advised to measure the temperature variation within the electronics box during operation of the prototype balance. This will allow a more accurate estimate of error due to temperature variation of the resistor. Ideally, the calibration procedure should be repeated with a PRT allocated specifically to measure the temperature of the resistor under test.

Summary

The results of this calibration show that the prototype balance $100\,\Omega$ resistor meets its specification. The measured resistance of $99.992\,919\,\Omega$ was within 0.02% of nominal value and its measured TCR of 0.90 ppm/°C was below 5 ppm/°C quoted on the UFPB100RV data sheet [116].

5.2.3 Frequency Counter

The prototype balance uses a frequency counter (s/n Counter 2) to analyse the signal received from the optical encoder used to observe the linear scale attached to the moving frame. During the weighing phase this subsystem is used to record the position of the moving frame and during the moving phase it is used to measure the velocity of the moving frame.

Description

The counter under test is designed to accept two sinusoidal signals with a phase shift of 90° from either a laser interferometer or an incremental encoder. The prototype uses a Renishaw TONiC™Incremental Encoder for position and velocity measurement. This device outputs two sinusoidal signals of $1\,V_{pp}$ with a 90° phase shift.

Calibration Method

A Siglent SDG2042X Function Generator (s/n SDG2XCA2161285) was used to supply signals of known characteristics to the counter under test. A Tektronics FCA3100

Frequency Counter (s/n 338622) was used to measure the frequency output of the SDG2042X. A Stanford Research Systems (SRS) FS752 GNSS 10 MHz Reference (s/n 75200023) was used as the external reference for both the SDG2042X and the FCA3100. The FS752 GNSS 10 MHz reference was used in conjunction with an SRS FS730 Distribution Amplifier (s/n 141087) to allow multiple references to be supplied simultaneously. Three checks of this system were performed prior to starting measurements of the counter under test.

Firstly, the FCA3100 frequency counter was used to compare the output signal of the FS752 GNSS 10 MHz reference with the NPL Maser 10 MHz Reference Signal. The result was $10.000\,000\,000 \pm 0.000\,000\,001$ MHz measured with a 2 s gate time. Agreement to 1 part in 10^{10} between the two references meant that either could be used as the external standard for this calibration. The signals supplied by each reference were observed on an oscilloscope. The FS752 GNSS reference signal had a higher amplitude (1 V_{PP}) than the NPL Mazer reference signal (20 mV_{PP}). The FS752 was selected for use a it had a higher amplitude signal.

Secondly, the FCA3100 frequency counter was used to compare the output channels of the FS730 distribution amplifier. The result was $10.000\,000\,000\,01 \pm 0.000\,000\,000\,10$ MHz measured with a 2 s gate time. Agreement to 1 part in 10^{11} between the two channels showed that the distribution amplifier was operating to a level appropriate for this calibration.

Thirdly, the SDG2042X function generator was setup to generate two output signals of identical frequency and 1 V_{PP} amplitude with a phase offset of 90°. This was checked by observing the two output signals simultaneously on an oscilloscope.

In addition, the checks involving the FCA3100 frequency counter showed that it was performing adequately to measure the frequency of the signals supplied by the SDG2042X function generator during the calibration of the counter under test.

A Nessus-2 software routine (MNCDfmm) was written to collect data from the counter under test. This was configured to match the settings during a moving measurement block. 20 measurements were collected back-to-back with a gate time of 0.5 s each and this was repeated 5 times to collect 100 individual measurements.

The output signal from the SDG2042X function generator was measured by the FCA3100 frequency counter with a gate time of 10 s and was recorded manually.

The calibration was carried out at four nominal frequencies: 5 Hz, 10 Hz, 100 Hz and 1000 Hz. The linear scale attached to the moving frame has 20 μm scale divisions therefore the nominal frequencies are equivalent to 0.1 mm/s, 0.2 mm/s, 2 mm/s, and 20 mm/s respectively.

Results

TABLE 5.13: Frequency counter (s/n Counter 2) calibration data.

FCA3100 Indicated Frequency	FCA3100 Standard Deviation	Counter 2 Indicated Frequency	Counter 2 Standard Deviation	Counter 2 Correction	Counter 2 Correction
Hz	Hz	Hz	Hz	Hz	ppm
4.999 997	0.000 014	5.000 016	0.000 035	-0.000 019	-3.8
9.999 995 7	0.000 007 4	10.000 032	0.000 033	-0.000 036	-3.6
100.000 002 5	0.000 004 9	100.000 321	0.000 055	-0.000 319	-3.2
1000.000 000 0	0.000 001 6	1000.003 25	0.000 13	-0.003 25	-3.2

Uncertainty Budget

TABLE 5.14: Frequency counter calibration uncertainty budget.

Note	Contribution	Value	Unit	Unc. ($k = 1$)	Unit	Distribution	Sensitivity	Unc. ($k = 1$) Hz	%
i	Counter 2 - Cal Error	5.000016	Hz	1.90e-05	Hz	1	1	1.9E-05	91%
ii	Counter 2 - Cal Type A	5.000016	Hz	0.0000035	Hz	1	1	3.5E-06	3%
iii	Ref - Type A	4.999997	Hz	4.66667E-06	Hz	1	1	4.7E-06	6%
							Total ($k = 1$) Hz	2.0E-05	100%

The total estimated uncertainty of the frequency counter calibration is $\sim$4 ppm at $k = 1$. Including the absolute error of the counter under test at 5 Hz and its type A uncertainty. The type A uncertainty of the counter used to measure the signal from the function generator was also included. As shown in table 5.14, the largest contribution is due to the absolute error of the counter indication.

Summary

The results in table 5.13 show that the prototype counter has a consistently low error of approximately 3.5 ppm across the range of frequency values calibrated resulting in a maximum uncertainty of 4 ppm. This is likely to have a low impact on the measurements of velocity and position required for mass measurement and therefore a correction has not been applied to the calculated velocity results.

5.3 Performance Assumptions

There were a few measurement components of the prototype that could not be re-calibrated or measured post-assembly without significant additional equipment. These included the scale divisions of the linear encoder system and the consistency of alignment of the coils with the axis of local gravity. In addition a constant value of local gravity was assumed. All of these aspects have an impact on the measured mass. In this section details of the assumption made are presented.

5.3.1 Linear Encoder System

A critical assumption of the Kibble balance principle is that the motion of the coils is aligned with the axis of local gravity. The prototype balance includes a Renishaw TONiC™linear encoder system to detect the position of the coils during the weighing phases and measure their velocity during the moving phases. The system includes a stainless steel linear tape scale (part number RTLC20-S) with 20 μm scale divisions. It has been assumed that the scale meets its manufacturers accuracy specifications of $\pm 5\,\mu\mathrm{m/m}$ and coefficient of thermal expansion of $10.1 \pm 0.2\,\mu\mathrm{m/m/°C}$ [84]. The coils were mounted on the moving frame as described in section 4.5.4 using a former to ensure a concentric and parallel fit. A vertical recess matching the width of the tape scale was included on the side of the moving frame to ensure alignment of the scale to the vertical axis of the moving frame. The scale was attached to the moving frame using the supplied self-adhesive backing tape. The linear encoder readhead was mounted on a 3D printed support that allowed the rideheight and angle with respect to the scale to be adjusted. The readhead includes two LED indicators that show when alignment within manufacturer specified tolerance with respect to rideheight (2.10 ± 0.15 mm), pitch ($\pm 1°$), roll ($\pm 0.5°$) and yaw ($\pm 0.4°$), have been achieved. During setup the encoder readhead was secured at an appropriate position and checked to ensure that alignment was maintained over the moving range of the moving frame (± 0.7 mm).

After installation into the prototype the angle of the moving frame was observed by placing a bubble level on the mass pan. It was assumed that if the mass pan was level then the moving frame was aligned vertically with local gravity. In the direction parallel with the balance arms the bubble indicated that the mass pan was level. In the direction perpendicular to the balance arms the bubble indicated that the mass pan was slightly off level. The angle was estimated to be approximately 1.5° which is equivalent to an error of 350 ppm (cosine error).

Table 5.15 shows an estimate of uncertainty of ∼375 ppm at $k = 1$ including contributions due to the specification of the linear tape scale, the alignment of the

TABLE 5.15: Linear encoder uncertainty budget.

Note	Contribution	Value	Unit	Unc. ($k = 1$)	Unit	Distribution	Sensitivity	Unc. ($k = 1$) m	%
i	Scale Div Uncert	2.00E-05	m	1.00E-10	m	1	1	1.0E-10	0%
ii	Scale - TCE	2.00E-05	m	2.02E-10	m	1	1	2.0E-10	0%
iii	Angle wrt local g	1.5	°	6.85E-09	m	1	1	6.9E-09	83%
iv	Angle wrt scale	1	°	3.05E-09	m	1	1	3.0E-09	16%
							Total ($k = 1$) m	7.5E-09	100%

optical readhead, and the alignment of the system with the axis of gravity. The largest contribution was due to the measured misalignment to the axis of local gravity.

5.3.2 BL Product

In the original Kibble balance theory another key assumption was that the value of the BL product in the weighing phase was the same as the measured value of the BL product in the moving phase. This assumption relies on several parameters being constant or changing very slowly with time.

Magnetic Field

The strength of magnetic field B is known to vary with temperature. This effect can be mitigated by controlling the temperature of the magnet and also by measuring the BL product frequently during the measurement run and interpolating the value at the time of the weighing phases. The prototype contains a single CotS NdFeB ring magnet. Typical NdFeB material has a temperature coefficient of approximately 1000 ppm/K [118]. For this work it was assumed that the air temperature control in the laboratory (20 ± 1 °) was sufficient to keep the rate of change of the magnetic field strength to below 1 mT between moving phases.

Length of Coil

The length of the main coil inside the magnetic field is known to vary with angle. Providing the alignment of the coil does not change between weighing and moving phases then the length of the coil inside the magnetic field is constant. To mitigate the effect of any change in alignment of the coil due to lowering or raising the test mass measurement data has been collected in both mass states (on and off) during both measurement phases (weighing and moving) as described in section 4.3.1.

5.3.3 Gravity

In order to determine the mass of an object using a Kibble balance the value of local gravity g at the time of measurements needs to be known. For this work a constant value of 9.811 84 m/s^2 has been assumed. This value is based on previous measurements of local gravity in the laboratory where the prototype was located [79]. The uncertainty on the gravity correction for the NPL Mark II balance was 15 ppb in 2007 and reduced to 4 ppb in 2008. A conservative estimate of 100 ppm uncertainty for the assumed value of local gravity has been used for this work based on published measurements of surface gravity [119]. This error will not significantly impact the mass results.

Chapter 6

Results

In this chapter the mass measurement performance of the prototype is presented and evaluated. The results are compared with the predicted performance calculated in chapter 4 and a traditional mass calibration.

6.1 Test Masses

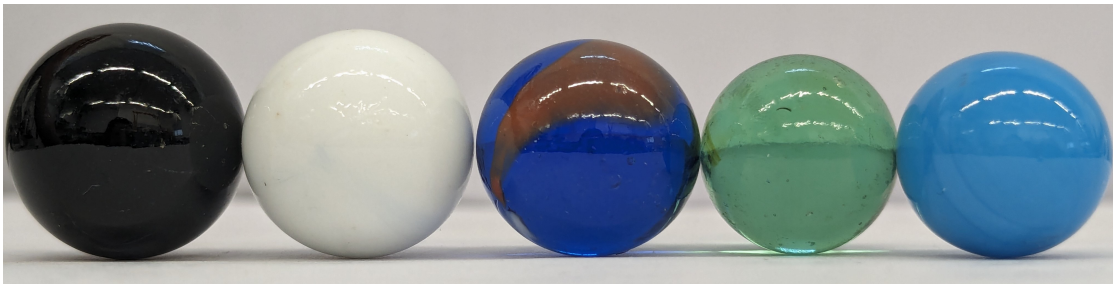

FIGURE 6.1: Spherical test masses used to determine the mass measurement performance of the 3D printed prototype system. Colour ID and nominal mass from left to right: Black 6.0 g, White 5.2 g, Blue and Orange 4.7 g, Green 3.5 g, Pale Blue 3.5 g.

Five glass spheres with masses in the range 3.5 g to 6.0 g were chosen for testing the mass measurement performance of the prototype. These were sourced from a mixed set of ordinary marbles. The advantages of using marbles for this purpose were threefold. Firstly, the prototype balance was designed to be compatible with spherical masses. As discussed in section 4.3 this is beneficial for repeatability of artefact placement on the balance pan. Secondly, glass is an inert material and therefore it can be assumed that its mass will remain stable both during the measurement and over a longer period of time (weeks/months) between measurement runs. Thirdly, marbles are available commercially-off-the-shelf in the mass range required for this work and in a variety of colours for easy identification. The only disadvantage was that were no marbles of nominal mass close to 1 g and 10 g in the set purchased.

The Black, White, Blue and Orange, and Green test masses were selected for assessing the mass measurement performance of the prototype in comparison with a traditional mass calibration. The Pale Blue test mass and no test mass (None) were used to check the operation of the balance and provide additional insight into the prototype characteristics and performance.

6.2 Measurement Sequence

Two types of measurement sequence or "run" were implemented according to the simplified bifilar coil measurement theory described in section 4.3.2. The measurement runs consisted of alternating weighing and moving phases in mass on and off states as shown in figure 6.2. The roles of the main coils (1 and 2) were fixed for each measurement run.

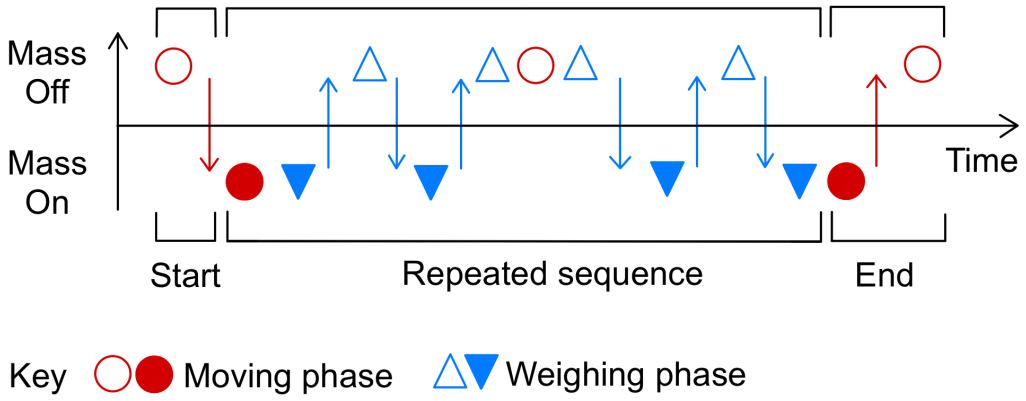

FIGURE 6.2: Measurement sequence illustration of a short run showing the order of moving and weighing phase measurements including mass state. Arrows indicate the changing of mass state. This pattern ensures all weighing phase measurements are bracketed by two moving phases (one in each mass state).

The "short" measurement run lasted approximately 3.25 hours and included 21 moving phases plus 18 weighing phases. Figure 6.2 shows the building blocks of the measurement sequence. Each moving phase contained 100 individual data points of 0.5 s duration with a single mass state (red circle). The mass state (on or off) was alternated every other moving phase. The sequence started and ended with two moving phases (one in each mass state). Each weighing phase comprised a total of 48 individual data points of 2 s duration and alternated between mass states (on and off) every 12 data points (blue triangle).

The "long" measurement run took approximately 11 hours and included 11 moving phases plus 8 weighing phases. The moving phases were implemented in the same way as in the short measurement run and similarly the sequence started and ended with two moving phases (one in each mass state). Each weighing phase comprised a

total of 480 individual data points of 2 s duration and alternated between mass states every 12 data points.

The data for each measurement run was processed using software written in MATLAB®. It was created for use with any Kibble balance developed at NPL that operates in a single mode with time-separated measurement phases.The data collected during each measurement phase was saved to a comma-separated values (csv) file and stored in a single directory per measurement run. Directories were named according to the format YYMMDDll where the letters (ll) started from aa each day and incremented through the alphabet, specifically ab, ac, etc... Files were named sequentially according to the type of measurement phase starting from Moving01.dat and Weighing01.dat. All data points were labelled with appropriate metadata such as the mass state (on or off) and the number of the main coil carrying the weighing current (1 or 2).

Firstly, the analysis software computed the evolution of $(BL)_s$ of the main coil with time for each mass state (on and off) using the moving phase data sets. The following data were calculated for each moving data point: mean time (t), mean position (z), coil velocity (u), and induced voltage (V). $(BL)_s$ in each mass state was determined by fitting these data by multiple regression. The software allows the position of the coil to be a fitted parameter however for this work the $(BL)_s$ models were determined at position $z = 0$. Next the weighing phase data was processed. For each weighing data point the following data were calculated: mean time (t), mean position (z), and weighing current (I). $(BL)_s(z = 0)$ at the time of each weighing data point was determined by interpolating the appropriate $(BL)_s$ model (mass state on or off). The mass value (m_s) for each weighing data point was calculated according to $m_s = \frac{BLI}{g}$ (equation 2.13) where g is local gravity with an assumed value of 9.81 m/s^2. The non-corrected mass of the object under test was determined by multiple regression of the weighing data. It was assumed that the mass of the object was constant during the measurement run. Other fitted parameters included the tare force (switched on at all times) and the drift in the tare force. The tare drift parameter was included to provide an indication of changes in the balance system with time such as temperature changes.

Corrections due the coil-current effect described in section 4.3.4 and air buoyancy described in section 2.1 were applied to determine the reported true mass values in table 6.1.

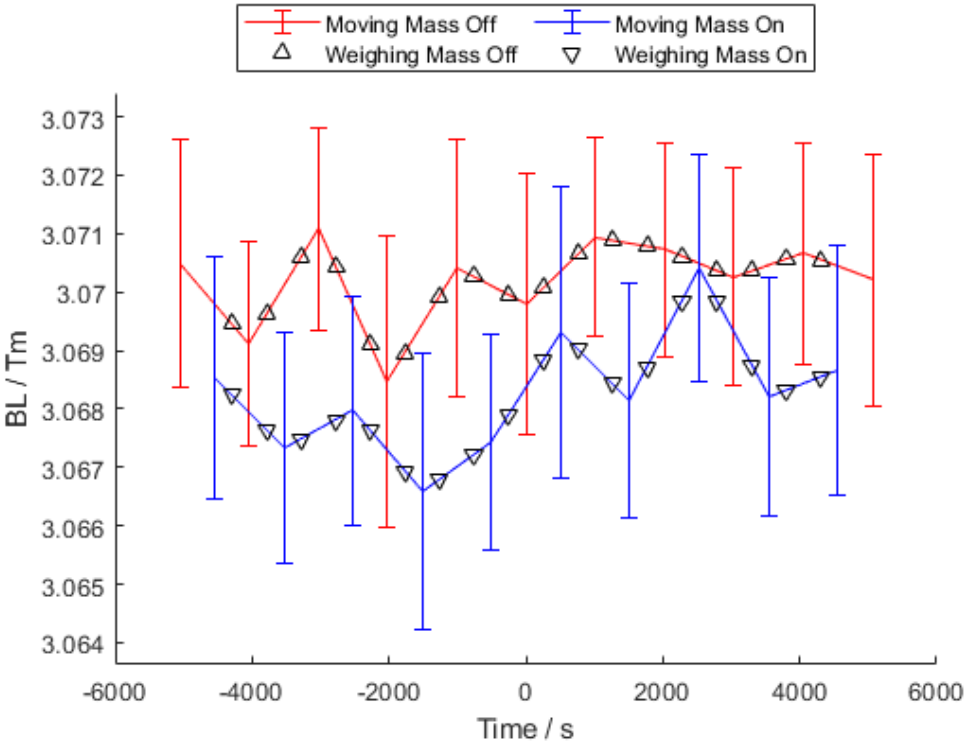

FIGURE 6.3: Main coil $(BL)_s(z = 0)$ data from the moving phases of the short measurement run of the Black test mass in each mass state (on and off) with the interpolated values at the time of the weighing phases indicated by the triangles.

6.3 Prototype Results

TABLE 6.1: Calculated true mass and uncertainty of five test masses and none measured according to short and long measurement sequences. The datasets were collected between 24th October and 30th November 2023.

ID	Dataset	Duration	Weighing coil	Mass	Uncertainty ($k = 1$)	Uncertainty ($k = 1$)
-	-	Hours	-	g	g	%
Black	231024ab	3.25	1	6.197	0.008	0.13
	231024ac	11	1	6.177	0.008	0.12
White	231026aa	3.25	1	5.388	0.008	0.14
	231031aa	11	1	5.367	0.011	0.21
Blue/Orange	231026ab	3.25	1	4.873	0.006	0.13
	231026ac	11	1	4.885	0.009	0.18
Green	231101aa	3.25	1	3.623	0.006	0.17
	231101ab	11	1	3.625	0.008	0.23
Pale Blue	231025aa	3.25	1	3.618	0.006	0.17
	231025ab	11	1	3.625	0.011	0.30
	231109aa	3.25	2	3.631	0.008	0.21
	231109ab	3.25	1	3.626	0.006	0.18
	231130aa	3.25	1	3.637	0.005	0.15
None	231103aa	11	1	0.012	0.016	-
	231104aa	3.25	1	-0.004	0.011	-

The results in table 6.1 show the calculated true mass value for each measurement run. These values include a correction according equation (4.29) to account for the co-location of the tare and main coils in the same magnetic field and a buoyancy correction according to equation (2.4) assuming a constant air density of $1.2\,\mathrm{kg/m^3}$[120].

During each measurement run the two strands of the main coil were permanently assigned to specific roles. For 14 out of 15 measurement runs, main coil 1 was assigned to carrying the weighing current ("Weighing Coil") and main coil 2 was assigned to carrying the induced voltage during moving phase ("Moving Coil"). For one short measurement run the roles were reversed (Pale Blue 231109aa). As discussed on page 83 and 132 it has been assumed that main coils 1 and 2 are equivalent in terms of length and position in the magnetic field.

Figure 6.4 shows a histogram containing 166 residual mass data points collected from the five test masses with the prototype configured to use main coil 1 as the Weighing Coil. This histogram demonstrates that the mass result data follows a Gaussian distribution with a sigma of 8.1 mg.

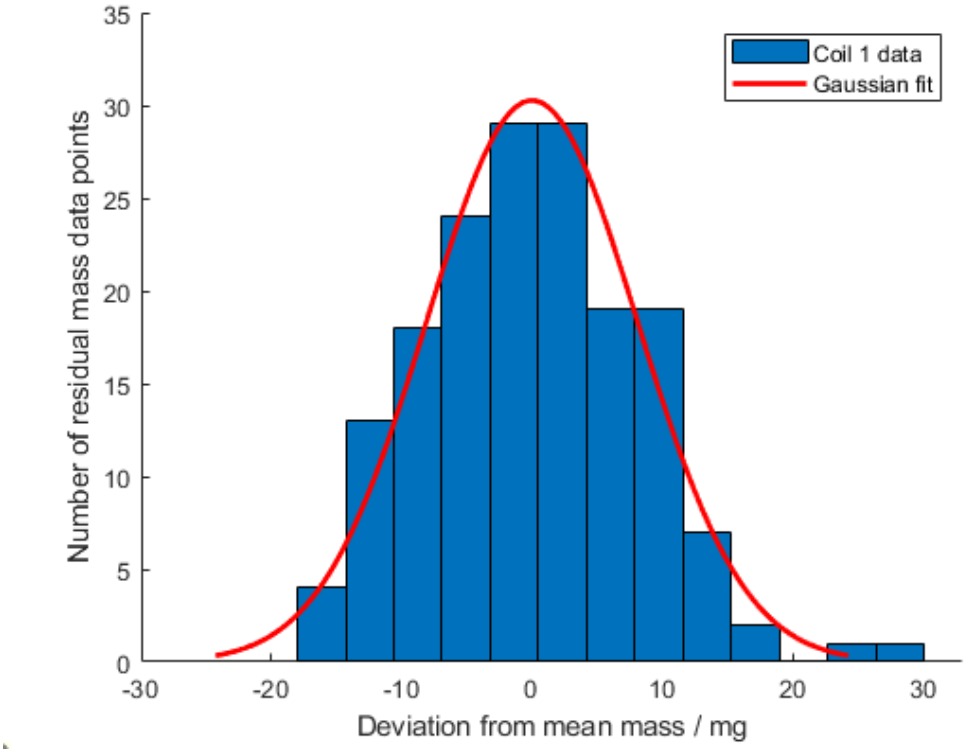

FIGURE 6.4: Histogram of mass residuals from the calculated mean for each test mass (Black, White, Blue and Orange, Green and Pale Blue). Data collected with main coil 1 assigned to carry the weighing current, n = 166.

6.4 Moving Phase

The moving frame was driven up and down at a target speed of 0.1 mm/s over a distance of 1.4 mm ($\pm$0.7 mm about the zero position) and data was collected over the central 1 mm.

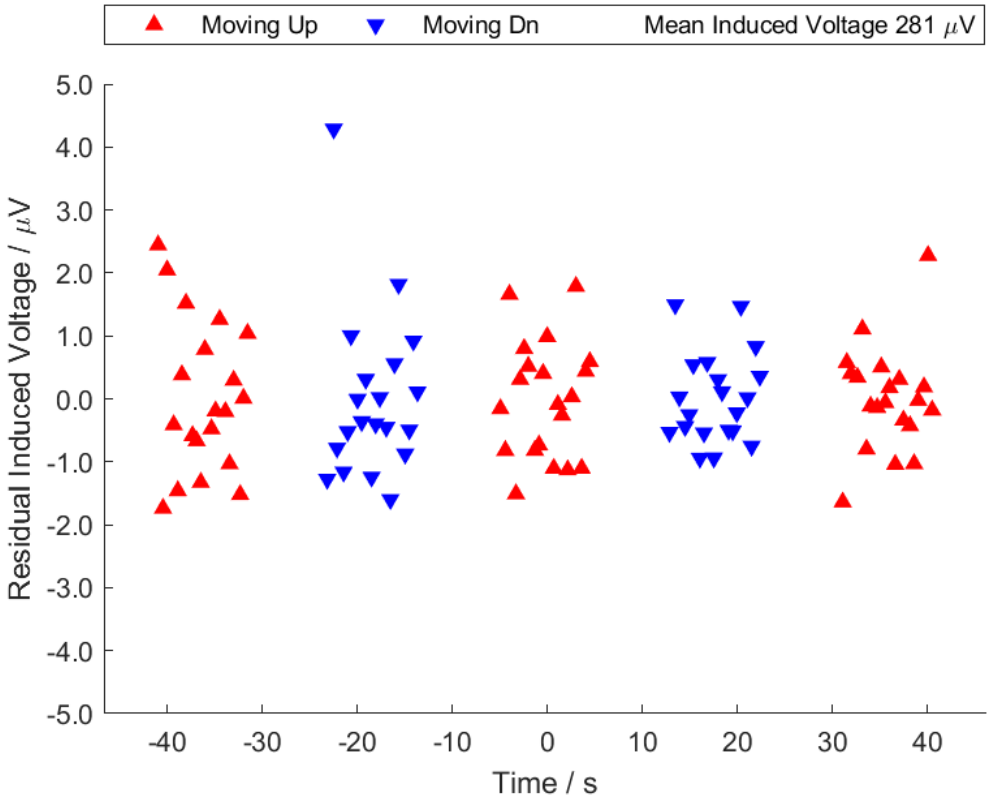

FIGURE 6.5: Residual induced voltage data (Move 01) of dataset 231024ab.

The induced voltage in the moving coil was measured 100 times per moving phase. Each data point had a nominal gate time of 0.5 s. Figure 6.5 shows typical induced voltage residuals from the short measurement run of the Black test mass (nominal 6.0 g, Move01, 231024ab). The induced voltage was approximately 280μV which was amplified 1004.401 times by the A22 pre-amplifier prior to being measured by the Thaler ADC180. The spread of voltage residuals was typically $\pm$2.8 μV (10 000 ppm) with the occasional outlier up to $\pm$ 4.2 μV (15 000 ppm). Moving phase plots from all black test mass data sets are included in appendix B.

The velocity of the moving coil was measured simultaneously. Figure 6.6 shows typical measured speed data during a moving phase in the mass off state (Move01, 231024ab). The average coil speed for dataset 231024ab was 0.091 952 mm s^{-1} with a standard deviation of 0.000 034 mm s^{-1}. This average includes data collected in both mass states ($n = 2100$). Figure 6.6 indicates that the speed of the moving coil was subject to position dependent damping, specifically it appears to be independent of the direction of motion.

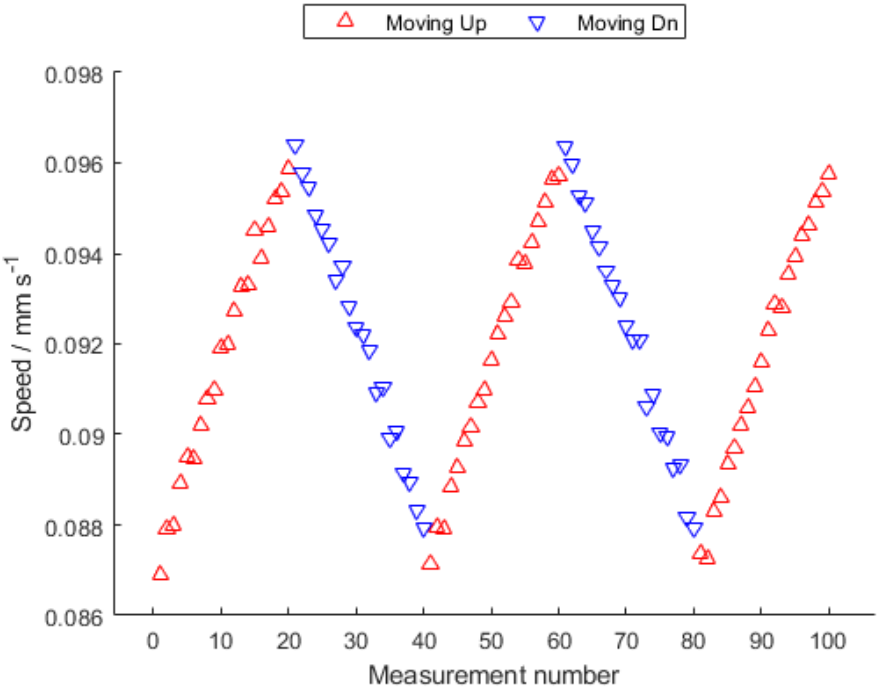

FIGURE 6.6: Moving coil speed data from a single moving phase with mass off (Move01 231024ab).

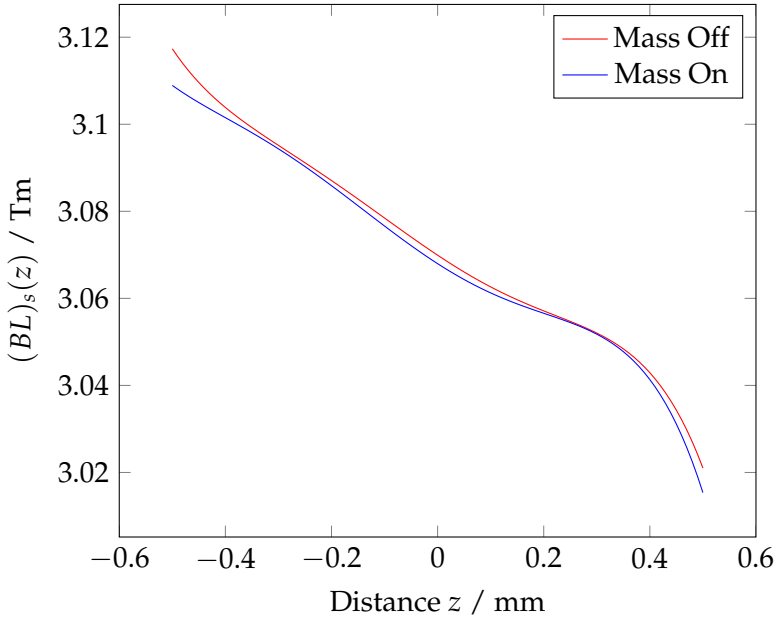

FIGURE 6.7: $(BL)_s$ plotted as a function of z for mass off and mass on states (Move01 and Move02 from dataset 231024ab).

The measured induced voltage and speed were used to calculate $(BL)_s(z)$. Figure 6.7 shows the fifth order multiple regression fits of the $(BL)_s(z)$ data from two moving phases of the short measurement run of the Black test mass (231024ab) with mass off and mass on respectively. The shape of $(BL)_s$ with z was approximately consistent

between the mass off and mass on states. For this work, these data fits were used to calculate the $(BL)_s$ at the assumed weighing position of $z = 0$. Ideally, $(BL)_s(z)$ should be constant in the moving range of the main coil. However, it varied by approximately 2.6% over the moving phase measurement distance of 1 mm (assuming a linear fit). The position of the moving frame during the weighing phase was controlled by the servo system. For the Black test mass measurement runs the average weighing position difference from $z = 0$ was 48 μm resulting in 0.004 Tm (0.12%) systematic error in the calculated $(BL)_s(z = 0)$. This increased to 0.014 Tm (0.44%) for the largest recorded weighing position deviation from $z = 0$ in this data set. To remove this systematic error the NPL Kibble balance analysis software should be implemented with calculation of $(BL)_s(z)$ at the measured weighing position for each data point. In addition further work should be carried out to determine the location of the magnetic field centre of the prototype magnet. If not already aligned, the prototype design should be adjusted to align the weighing position with the magnetic field centre of the magnet. Otherwise an additional correction for the coil-current effect will need to be determined and applied as mentioned in section 4.3.3.

Figure 6.3 shows the calculated $BL(z = 0)$ results from all moving phases of the short measurement run of the Black test mass (231024ab). The error bars are given by the estimate of the fit error for each data point. Typically this is about 0.002 Tm in both mass off and mass on states.

The average $(BL)_s(z = 0)$ across all datasets included in table 6.1 and for both mass states is 3.0695 Tm with a standard deviation of 0.0021 Tm. This average value is approximately 25% lower than the predicted value of 4 Tm calculated during the design phase (page 75). A lower BL product is a disadvantage as it reduces the sensitivity in both measurement phases. The lower value is likely to be due to a combination of the spreading problem when winding the coils noted in section 4.5.4 and the distribution of the magnetic field. The main coils were 15 mm in height rather than the planned 10 mm. This increase of 50% meant that the coil was not concentrated within the planned volume. If the distribution of the magnetic field in the z-axis was narrower than 15 mm then it is likely that part of the coil was always outside of the magnetic field. This would result in a lower than planned $(BL)_s$. Further investigation of the magnetic field distribution is recommended to optimise the coil design.

Figure 6.8 shows the residual $(BL)_s(z = 0)$ for each dataset. The plot shows that $(BL)_{on}$ is generally lower in magnitude than $(BL)_{off}$. It also shows that the measured values of $(BL)_s$ for dataset 231130aa are significantly adrift from the group average. However they appear to have maintained a similar relationship to each other. Dataset 231130aa was collected three weeks later than the previous dataset 231109ab therefore the observed change in $(BL)_s$ could be due to a change in environment such as room temperature causing a change in the magnetic field of the permanent magnet.

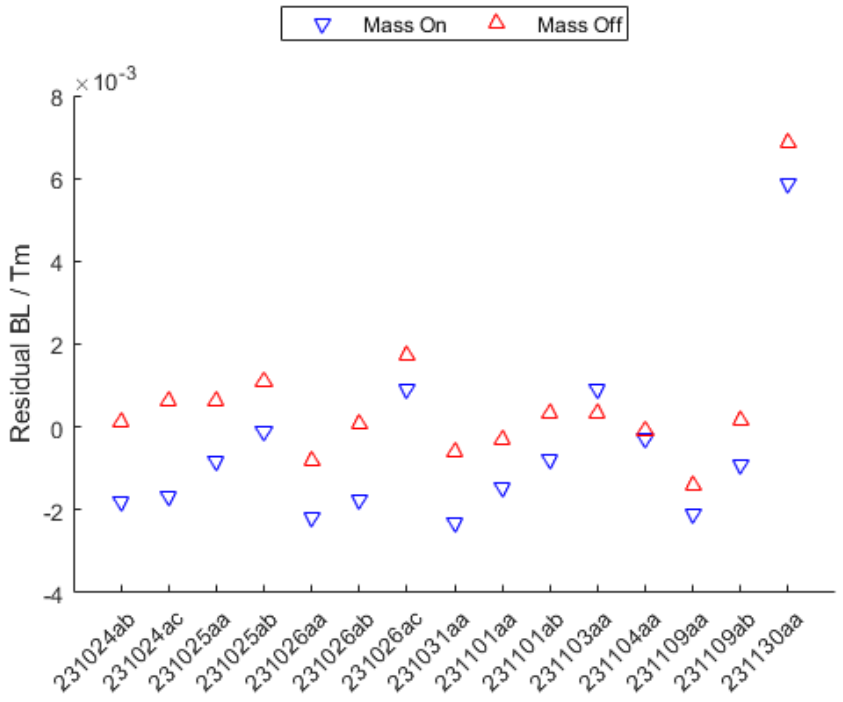

FIGURE 6.8: Residual $(BL)_s(z = 0)$ for both mass states for all datasets.

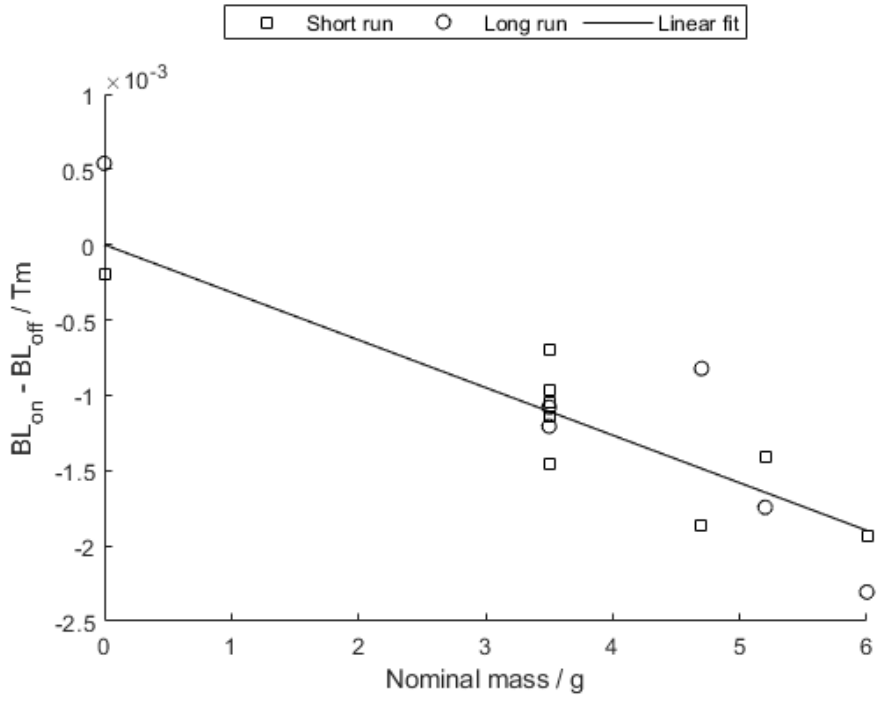

FIGURE 6.9: Difference between the $(BL)_s(z = 0)$ measured in each mass state against the nominal value of the test mass for all datasets.

Figure 6.9 is a plot of the difference between the measured $BL(z = 0)$ in the mass on state and the mass off state for each dataset against the nominal mass of the test mass.

The data point markers are categorised by measurement run type. A single straight line (linear regression through zero) has been fitted to all the data points resulting in a gradient of -0.000 32 Tm/g with a standard error of 0.000 02 Tm/g and R squared of 0.95. This relationship is a key characteristic of the prototype as it directly impacts mass measurement performance through the magnetic field correction due to the change in weighing current between mass on and mass off states (equation 4.29). The correction factor due to this effect is approximately -0.59% of the test mass being measured.

6.5 Weighing Phase

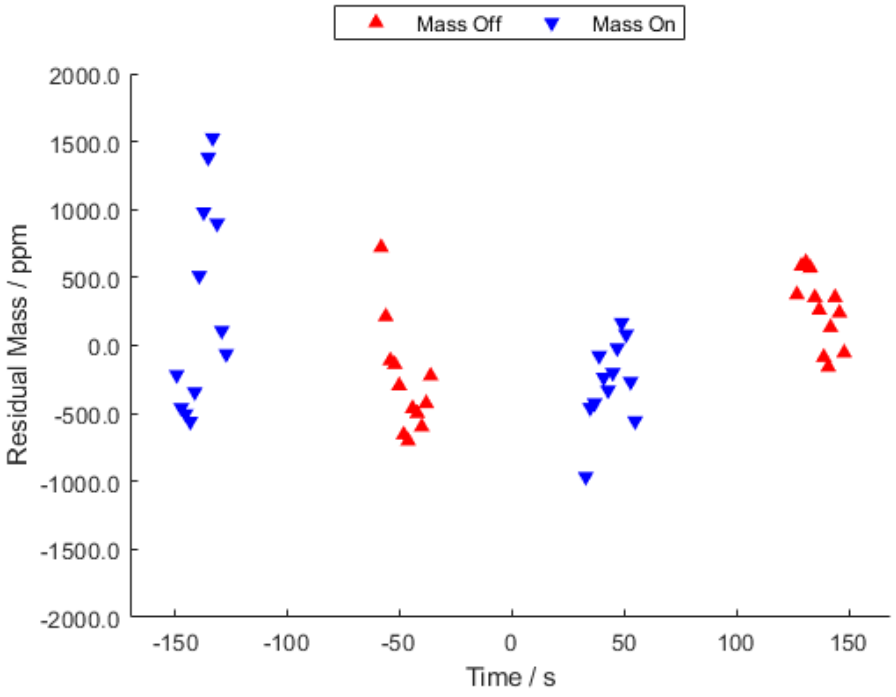

FIGURE 6.10: Weighing phase residual mass from a short run (Weigh02 231024ab) with a nominal 6.0 g test mass.

Figure 6.10 shows typical residual mass results from a short run weighing phase lasting 5 minutes. The spread of mass residuals is usually no greater than $\pm$2 000 ppm with occasional residuals of up to 5 000 ppm.

Figure 6.11 shows typical residual mass results from long run weighing phase lasting a total of 67 minutes. The spread of mass residuals is usually no greater than $\pm$5 000 ppm with occasional residuals of up to 10 000 ppm. Weighing phase plots from all black test mass data sets are included in appendix C. The drift observed within each individual weighing phase, typically around 2 000 ppm, was likely to be due to the stability of the guidance mechanism in combination with servo control system. To

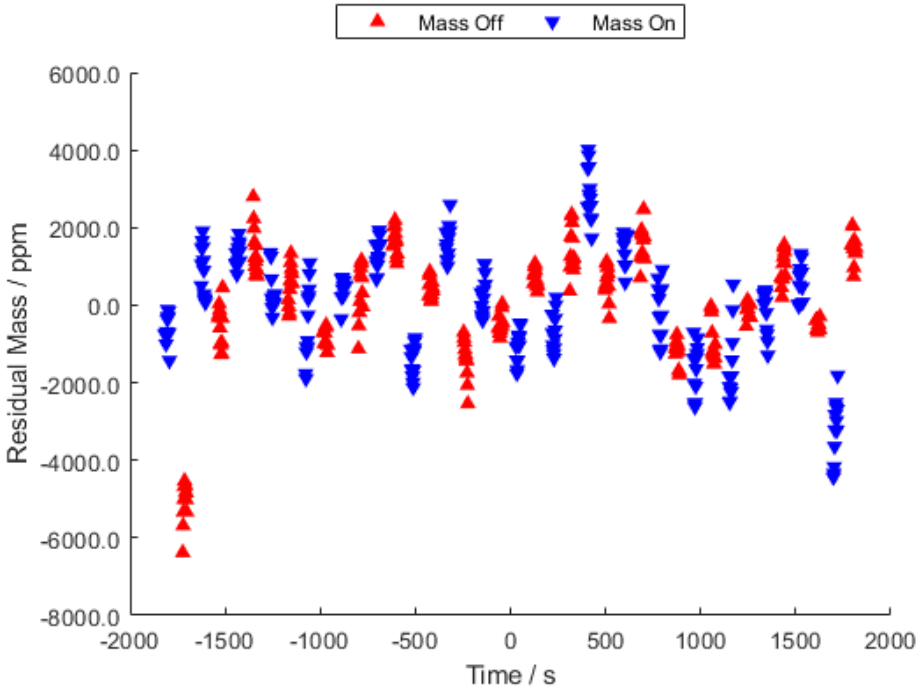

FIGURE 6.11: Weighing phase residual mass from a long run (Weigh02 231024ac) with a nominal 6.0 g test mass.

reduce this variation it is recommended to identify the optimal servo control settings and reduce the effects of mechanical hysteresis either by increasing the settling time prior to measurement or changing the mechanism design. Figure 6.11 also shows a longer term variation in the results, a sinusoidal oscillation of approximately 3 500 ppm peak to peak with a period of approximately 16.5 minutes. This variation could be linked to environmental changes such as temperature. As described in section 4.5 the prototype was exposed to fluctuations in the laboratory temperature which was servo controlled to 22$\pm$1°C. On inspection of the air temperature control system data the period of variation was approximately 11 minutes. To reduce the impact of air temperature changes on the prototype results it is advised to collect weighing data over a period of time significantly shorter than 10 minutes. Also a draft shield could be introduced which would slow the rate of change of the air temperature immediately around the prototype.

6.6 Uncertainty Budget

The total uncertainty on the mass results were calculated by assessing the uncertainty on each part of the measurement and combining the contributions according to the principles of the Guide to the Expression of Uncertainty in Measurement (GUM) [78]. This was carried out for each dataset individually and the total uncertainty at $k = 1$ reported in table 6.1. The uncertainty assessment for dataset 231024ab (nominal 6.0 g test mass) with a total uncertainty of 8 mg is presented in detail to illustrate the relative effects of the sources of uncertainty that contribute to the total.

TABLE 6.2: Mass uncertainty budget for dataset 231024ab.

Note	Contribution	Value	Unit	Unc. ($k = 1$)	Unit	Ratio	%
i	Mass - Type A	6.2291	g	2.0e-03	g	3.2e-04	6%
ii	Voltmeter low gain cal	1.99258	V	5.0e-03	V	2.5e-04	4%
iii	Voltmeter high gain cal	0.000282	V	2.1e-07	V	7.6e-04	34%
iv	Resistor	99.99292	Ω	2.5e-03	Ω	2.5e-05	0%
v	Local gravity	9.811840	m/s^2	9.8e-04	m/s^2	1.0e-04	1%
vi	Linear encoder cal	0.000020	m	7.5e-09	m	3.8e-04	8%
vii	Frequency counter cal	4.597641	Hz	2.0e-05	Hz	4.3e-06	0%
viii	B field current corr	6.1937	g	5.6e-03	g	9.0e-04	48%
ix	Buoyancy corr	6.19661	g	3.7e-04	g	6.0e-05	0%
				Total uncertainty ($k = 1$)		0.008	g

The mass uncertainty budget includes contributions that arise due to the repeatability of the measured mass value, the calibration and performance of the individual subsystems of the prototype, the correction due to the change in magnetic field due to the difference in current in the weighing coil between mass on and mass off states, and the correction due to air buoyancy.

The measured mass value type A standard uncertainty was calculated according to equation 5.7 with N set to the number of weighing phases (18).

The type A uncertainty for the difference in weighing voltage $V_W = V_{on} - V_{off}$ was calculated according to equation 5.7 with N set to the number of weighing phases and the combined standard deviation calculated according to the rules of propagation of uncertainty.

$$f = A - B \tag{6.1}$$

$$\sigma_f = \sqrt{\sigma_A^2 + \sigma_B^2 - 2\sigma_{AB}} \tag{6.2}$$

where f is the calculated result, A and B are the input parameters, σ_A and σ_B are the standard deviations of A and B respectively, and σ_{AB} is the covariance of parameters A and B.

The standard deviations and the covariance of the two weighing voltages were calculated using the "std" and "cov" functions in MATLAB® respectively.

The uncertainty of the voltmeter calibration in low gain mode was included from table 5.5. This component takes into account the ∼2 V difference between the mass on and mass off weighing voltages observed for the Black test mass. The weighing voltage difference for the other test masses varied between 1.1 V and 1.7 V.

The type A uncertainties for the moving voltage and the measured frequency of the linear tape scale marks passing the optical encoder readhead were calculated according to equation 5.7 with N set to the number of moving phases (21).

The voltmeter calibration in high gain mode, resistor calibration, and frequency counter calibration contributions were included from tables 5.8, 5.12, and 5.14 respectively.

The calculated uncertainty of the linear tape scale marks in table 5.15 and the assumed uncertainty of 100 ppm on the value of local gravity discussed in section 5.3.3 were also included.

TABLE 6.3: Magnetic field current correction uncertainty budget.

Note	Contribution	Value	Unit	Unc. ($k = 1$)	Unit	Distribution	Sensitivity	Unc. ($k = 1$) g	%
i	Moving Frame Mass	56.17	g	2	g	1	6.3E-04	1.3E-03	5%
ii	BL_{on}-BL_{off}	-0.0019	Tm	0.0003	Tm	1	1.8E+01	5.4E-03	95%
iii	BL_{off}	3.0696	Tm	0.0003	Tm	1	1.2E-02	3.0E-06	0%
							Total ($k = 1$) g	5.6E-03	100%

The uncertainty on the correction due to the change in magnetic field caused by the change in weighing current between mass states was found to be approximately 5.6 mg as shown in table 6.3. The main contribution was from the type A uncertainty on the difference between the value of $(BL)_s(z = 0)$ in the two mass states. This was calculated according to equations 5.7 and 6.2. The standard deviations and covariance of the parameters were calculated by the relevant functions in MATLAB®. The covariance function required an equal number of data points for each input parameter however all datasets contained differing numbers of mass off and mass on moving phases, specifically 11 and 10 respectively for short measurement runs and 6 and 5 respectively for long measurement runs. This was resolved by removing the last data point in the mass off sets resulting in an N of 10 for short runs and 5 for long runs.

The mass of the moving frame was determined in section 5.1.1. A conservative estimate of uncertainty of 2 g has been assumed due to the indirect method used.

The uncertainty of the correction due to air buoyancy acting on the test mass has been calculated as shown in table 6.4. To determine the buoyancy correction (equation 2.4) the volume of the test mass was calculated by re-arranging equation 2.3.

TABLE 6.4: Air buoyancy correction uncertainty budget.

Note	Contribution	Value	Unit	Unc. ($k = 1$)	Unit	Distribution	Sensitivity	Unc. ($k = 1$) g	%
i	Marble Mass	6.19369	g	0.0094	g	1	4.7E-04	4.4E-06	0%
ii	Air density	0.0012	g/cm^3	0.0001	g/cm^3	1	2.4E+00	2.9E-04	62%
iii	Glass density	2.55	g/cm^3	0.4	g/cm^3	2	1.1E-03	2.3E-04	38%
							Total ($k = 1$) g	3.7E-04	100%

$$v_m = \frac{m}{\rho_m} \tag{6.3}$$

where v_m is the volume of the test mass, m is mass of the test mass and ρ_m is the density of the test mass.

The magnetic field corrected mass with its uncertainty and an assumed density were used for this purpose. The test masses were assumed to be made from glass of density 2 550 kg/m^3 with an uncertainty of 400 kg/m^3 at $k = 2$ as per the traditional mass calibration (see certificate s/n 2024010275 in appendix A). The density of the air was not measured during the measurement runs. A standard air density of 1.2 kg/m^3 with a 10% uncertainty at $k = 1$ has been assumed [120].

The final column in table 6.2 indicates the relative contribution of each source of uncertainty to the total. Three sources of uncertainty dominate: the magnetic field correction due to the change in current between mass off and mass on (35%), the voltmeter calibration in high gain mode (25%) and the type A uncertainty of the voltage measurement during the moving phase (20%). All of these sources are related to the moving phase of the prototype operation. The calibration of the voltmeter in high gain mode could be improved by investigating and removing the fault associated with its variable offset. However this improvement would be negligible (a reduction of only 50 nV). Increasing the induced voltage by a factor of two would have a more significant impact by reducing the total mass uncertainty by ∼2 mg. This assumes that the type A uncertainty of the induced voltage measurement stays at a similar magnitude. There are three options for increasing the induced voltage $V = BLu$. Any or a combination of the following factors can be increased: the velocity of the coil u, the magnetic field B which the coil travels through, and the length of the coil L. The simplest option is to carry out measurements at a higher coil velocity for example at 0.2 mm/s instead of 0.1 mm/s. Another potential option for reducing the type A uncertainty of the induced voltage measurement is to increase the measurement gate time from 0.5 s to 1 s. Doubling the integration time of the voltmeter would allow allow a larger part of the signal to be sampled per measurement and therefore reduce the impact of the noise. However, due to the short moving distance of 1.4 mm, and even shorter sample distance of 1 mm, an increase in velocity and measurement gate time will yield fewer measurements per direction of movement, specifically 5 instead

of 20. In order to keep the total number of data points per moving phase the same (100) the number of movement reversals will need to be increased and the total time per moving phase increase from ∼70 s to ∼140 s. The uncertainty contribution for the magnetic field correction due to the change in current between mass off and mass on is dominated by the uncertainty in the difference between $(BL)_s(z = 0)$ in mass on and mass off states. As $BL = \frac{V}{u}$ the contributing factors to the difference in BL product uncertainty are the induced voltage calibration and measurement in high gain mode (45% total), the linear encoder calibration (6%) and the frequency calibration and measurement ($< 0.5\%$ total). The dominating factor is the induced voltage measurement therefore the proposed changes to the moving phase are also likely to have a positive impact on the uncertainty contribution for the magnetic field correction due to the change in current between mass off and mass on.

Table 6.1 shows that in general the total uncertainty on the mass result was approximately 0.2% which meets the target uncertainty of 0.25% or less stated in section 1.5. This was achieved without optimisation or significant design improvements being made to the system. Time spent on optimising the performance of the system during the moving phase as described above could reduce the total uncertainties further.

6.7 Traditional Mass Calibration Comparison

Four of the test masses, as detailed in table 6.5, were calibrated with traceability to the consensus value for the SI kilogram by comparison with mass standards at NPL. This traditional calibration was carried out as a "blind study" to check for systematic errors in the prototype, specifically the results of the traditional calibration were not revealed until the results from the prototype had been finalised.

TABLE 6.5: Comparison of the prototype mass results compared with mass values obtained through a traditional mass calibration. The uncertainty of the traditional mass calibration was 0.020 mg ($k = 1$) for all test masses.

ID	Dataset	Duration	Prototype Mass	Traditional Mass	Prototype Error
-	-	Hours	g	g	g
Black	231024ab	3.25	6.197	5.972053	0.225
	231024ac	11	6.177		0.205
White	231026aa	3.25	5.388	5.188843	0.199
	231031aa	11	5.367		0.178
Blue/Orange	231026ab	3.25	4.873	4.701402	0.172
	231026ac	11	4.885		0.183
Green	231101aa	3.25	3.623	3.498004	0.125
	231101ab	11	3.625		0.127

The traditional calibration was carried out in air according to a UKAS accredited measurement procedure. To allow the true mass values of the test masses to be

reported their density was assumed to be $2\,550 \pm 400\,\mathrm{kg/m^3}$ (at $k = 2$). The uncertainty of the calibration was 0.020 mg (at $k = 1$). The calibration certificate (s/n 2024010275) has been reproduced in full in Appendix A.

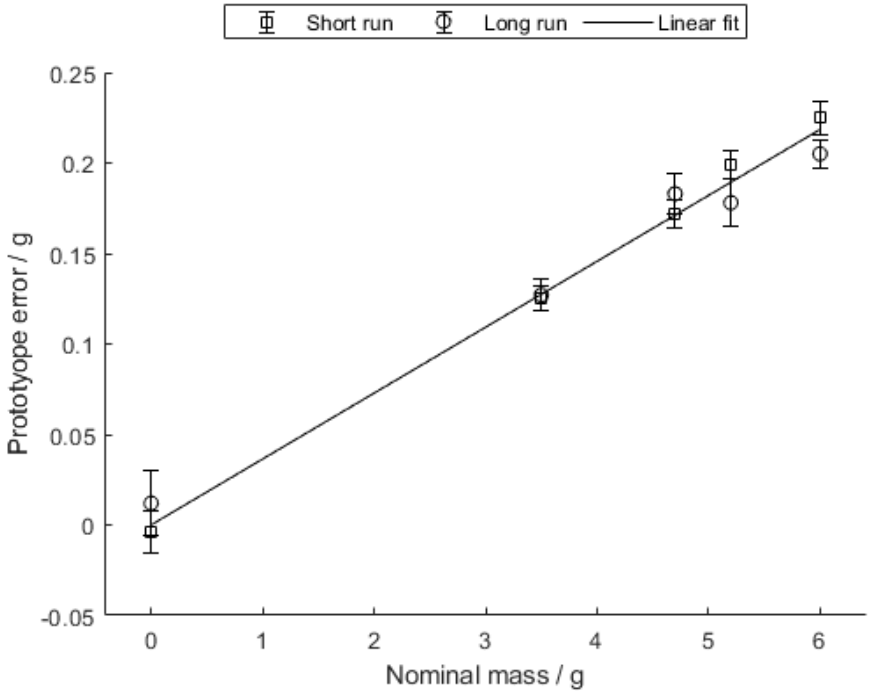

FIGURE 6.12: Comparison of the prototype results with a traditional mass calibration. The error bars are the prototype uncertainty from table 6.1.

Figure 6.12 shows the comparison of the traditional mass calibration with the prototype mass results, specifically the prototype error is plotted against nominal mass of the test mass. The data point markers are categorised by measurement run type. A single straight line (linear regression through zero) has been fitted to all the data points resulting in a gradient of -0.036 4 with a standard error of 0.000 7 and R squared of 0.997, therefore the prototype has a systematic error of +3.6% of the test mass.

The combined total uncertainty is 3.6% as the systematic error dominates the uncertainty of 0.2% calculated in section 6.6. The cause of the systematic error is currently unknown as there was insufficient time remaining to investigate.

There are a few possibilities to explore to identify the source or sources of the systematic error. Effects relating to the weighing current should be considered given that the error varies with the mass of the object under test. For example, the tare force applied to the moving frame resulted in weighing currents that were not symmetrical between the mass off and on states. In theory this should not make a difference, however given the variable offset of the voltmeter discovered during its low gain calibration in section 5.2.1 it would be prudent to investigate this. Further investigation of the variation in mass on BL product ($(BL)_{on}$) with mass of the object

under test shown in figure 6.9 should also be carried out. It will be necessary to improve the high gain voltage measurement performance during the moving phases as described in section 6.6 prior to looking at this aspect. This line of investigation will also have an impact on the correction applied due to the change in magnetic field caused by the change in weighing current between mass states (equation 4.29). This correction also relies upon an accurate value of the moving frame mass and assumes this equates to the force applied to the system from the mechanical components. Both the mass of the moving frame and the magnitude of the force applied by the mechanical system require evaluation. The mass of the moving frame can be found relatively easily by dismantling the prototype and weighing the moving frame on a digital scale. The force applied by the moving frame and associated mechanical components in situ will be more difficult to assess. It could be estimated using the tare system and the amount of current required to keep the moving frame at the zero position.

Another potential source of systematic error could be extraneous forces exerted by the mechanical system. The position dependent damping observed in the moving coil velocity data (figure 6.6) should be investigated. This effect could be linked to the issues experienced when implementing the tare compensation system during initial setup (section 5.1). A force profile with a gradient of 50% of the measured force profile was used as temporary solution for this work.

The type A uncertainties achieved by the prototype were very good considering the balance was set up in a general laboratory without a draft shield or significant vibration isolation. Care was taken to collect data at quiet times such as overnight to ensure minimal disturbance. However it maybe be beneficial to move the prototype system to a solid low vibration plinth and/or trial a draft shield with a large inertial mass. These changes may assist in revealing the cause of the systematic error.

6.8 Summary

In this chapter the results of five test masses in the nominal range 3.5 g to 6.0 g measured by the 3D printed Kibble balance were presented and analysed. The prototype was set up in open air in a temperature controlled laboratory and two measurement sequences were used to gather data. These datasets are the initial results prior to any optimisation of the prototype system. A thorough measurement uncertainty analysis was performed on the data and the combined uncertainty on the mass values was calculated to be 0.2%. This result meets the target of 0.25% or less stated in the aims of this work and there is potential to reduce this uncertainty further. The prototype mass values were compared with a traditional mass calibration in a blind study. This comparison revealed a +3.6% systematic error in the prototype system. The source or sources of this systematic error were not discovered during this project due to the lack of time remaining. Several lines of investigation were suggested as starting points for identifying the cause of this error. However the results of this work show that if the sources of systematic error can be identified and eliminated, the 3D printed Kibble balance has the potential to achieve an uncertainty of 0.5% when miniaturised to the micro-gram range.

Chapter 7

Conclusions and Future Work

7.1 Conclusions

A novel 3D printed Kibble balance was designed, manufactured, and evaluated. The objective of this work was to create a proof-of-concept device at the gram-level that demonstrates potential for miniaturisation to the sub-milligram level via 3D printed MEMS technology.

In the introduction it was established that traceable mass measurement is fundamental to many aspects of daily life. At the lower end of the scale (<1 mg) traceability is not currently available due to a lack of reliable mass standards at this range. A number of applications in industries such as pharmaceutical, environmental, commodities and manufacturing could derive an advantage from traceability at sub-milligram scales.

A Kibble balance does not require mass standards to make traceable mass measurements as the Kibble principle is traceable to the SI kilogram through electrical, dimensional, and time measurements. The Kibble balance was selected as an ideal candidate for creating a traceable mass sensor at low mass scales providing it could be physically miniaturised to the appropriate scale.

In the literature review the principles of a Kibble balance and several existing examples were presented. The literature was also searched for MEMS devices that had components or operation principles in common with Kibble balances. It was found that Kibble balances often have complex 3D mechanical structures that do not lend themselves to traditional MEMS manufacturing methods. However it was noted that 3D printing in MEMS manufacturing is an emerging field that appears to be a viable methodology for production of MEMS devices.

It was reasoned that a proof-of-concept 3D printed Kibble balance at the gram-level, operating with an uncertainty of 0.25% or less, could provide a stepping stone to a 3D

printed MEMS Kibble balance at the sub-milligram level with a target uncertainty of 0.5%. To achieve this aim a number of development phases were implemented.

An analytical feasibility study based on a simplified model of the electromagnetic Kibble principle was carried out for the mass range from 10 g to 1 μg. The simplified model included the electrical, magnetic, time, and distance measurement aspects only. The results of this study showed that there was a reasonable prospect of achieving a competitive uncertainty with a "low cost" miniature Kibble balance sensor at masses of 1 mg and below. It also confirmed that creating a Kibble balance with a competitive uncertainty would be very technically challenging or expensive or both in the range 10 mg to 10 g.

The literature review and feasibility study indicated that the magnetic field and coil interaction was one of the biggest factors in Kibble balance performance. To inform the design of a prototype that could be scaled to MEMS two options were considered, an anti-Helmholtz coil and a pair of permanent magnets, for generation of a radial ($1/r$) magnetic field at an appropriate magnitude (0.1 Tm). A simulation study concluded that anti-Helmholtz coils were not a viable option due to the very low field strength generated. The pair of permanent magnets was shown by simulation and confirmed by experimental results to generate a radial magnetic field of sufficient magnitude to proceed to prototype design.

To create and evaluate a prototype within the timescale of this project it was decided to base the design on components and subsystems from the existing NPL Demonstration Kibble balance, CotS items, and bespoke 3D printed parts. This approach also had the advantage of keeping the manufacture of the prototype at a low cost. The prototype mechanical system and co-wound coils were designed around a single ring magnet from the Demonstration balance. Details of the design, operation principle, and simplified implementation procedure were presented. The expected performance of the prototype was determined using a simplified analytical model of the design including the mechanical system, electromagnetic subsystems, and the velocity and position subsystem. The predicted performance was calculated to be between 0.02% and 0.06% therefore the project proceeded to the manufacturing stages. A few issues were encountered during assembly and integration of the prototype subsystems which resulted in minor design changes as documented in section 4.5.

The properties of subsystems of the prototype were measured and verified against the estimated or required performance. This served two purposes: setting up the software control systems and calibration of individual subsystems for uncertainty calculation. Measurements of the guidance mechanism showed that the total spring constant was 33% higher than expected when configured as designed and approximately +278% higher than predicted with the tare masses removed. It was also noted that the force profile control system could not be optimised. Subsystems including the voltmeter,

resistor, and frequency counter were individually calibrated and found to be operating within specifications and satisfactory levels of uncertainty.

The 3D printed prototype was implemented according to SMTP operation with a bifilar main coil. It was setup on a light-weight plinth without draft shielding in a laboratory temperature controlled to 22±1°C. Five glass spherical test masses were measured over a period of several days according to two measurement routines, one lasting approximately 3 hours and the other 11 hours. The calculated results were reported in chapter 6 and the data from all measurement runs included in appendices B and C. Measurement uncertainty was calculated for each individual run and the average was 0.2% (at k=1). A "blind" comparison with a traditional mass calibration of the test masses revealed a +3.6% systematic error at the end of the project. There was insufficient time remaining to investigate the source of this error.

This work produced an operational 3D printed gram-level Kibble balance prototype with a calculated measurement uncertainty of 0.2% (at k=1). These results were compared with a traditional mass calibration performed at NPL which revealed a +3.6% systematic error in the prototype system. Once identified, the source of this error can be eliminated to allow the device to be scaled to the micro-gram level within a target uncertainty of 0.5% (at k=1).

7.2 Future Work

The next step in the development of the 3D printed Kibble balance is an investigation of the source systematic error present in the current prototype system. Once the root cause is identified a solution can be created to eliminate it.

A number of avenues of investigation should be explored. The magnetic field correction due to the change in weighing current between mass states should be examined to ensure all effects are included. This is a priority given that the systematic error varies with increasing mass. Further work to optimise the control systems such as implementing a symmetrical tare current, measurement of the location of the magnetic centre of the magnet, implementation of an appropriate force profile in the compensation system, and developing an understanding of the behaviour and properties of the guidance mechanism as a whole should be carried out including a detailed dynamic analysis and modelling. Adjustment of the prototype mechanical design may improve the guidance mechanism performance and allow the magnet holder to be reinstated. Manufacturing a new set of co-wound coils would be an opportunity to achieve an increased BL product. This would increase the signal-to-noise ratio on the induced voltage signal during moving phase which would be a significant benefit.

Beyond this prototype, work to miniaturise to a 3D printed MEMS Kibble balance is likely to involve a change of principle to electrostatic Kibble principles. At low mass scales it is very challenging to achieve a sufficient BL product. For example, the feasibility study results in table 3.4 show that the expected BL at 1 μg is 0.02 Tm. The optimum BL product for electromagnetic Kibble balances can be calculated according to $(BL)_{op} = \sqrt{\frac{mgR}{u}}$ where m is the mass of the object under test, g is local gravity, R is the resistor which converts weighing current into voltage for measurement, and u is coil velocity [86]. The optimum BL is approximately 3 Tm for a device operating at 1 μg with the assumed parameters in table 3.4, specifically 150 times higher than predicted. Increasing the magnetic field from 0.1 T to 15 T is not feasible with permanent magnetic material. An electromagnet may achieve this magnitude of field however it would significantly increase the size, cost, and complexity of the system. If the magnetic field could be increased to 0.3 T with a permanent magnet then the length of the coil would need to increase 50 times from 0.2 m to 10 m. This could be achieved however the mass of the coil would be approximately 45,000 times the mass of the object under test. This could cause significant challenges for the design of guidance mechanism, specifically the capability to support the mass of the coil and achieve a very low flexure stiffness. Another issue with increasing the length of the coil is increasing the physical space that it occupies. It is important to concentrate the coil into as small a volume as possible to ensure that all the windings are inside the magnetic field and contribute to the BL product. This is more challenging with a longer coil. Also, increasing the footprint of the device is undesirable if there is a commercial requirement to appeal to users of existing micro-balances.

Once the existing electromagnetic 3D-printed proof-of-concept balance is operating to within satisfactory levels of uncertainty the creation of an electrostatic version should be considered.

The electrostatic principle offers some benefits over the electromagnetic principle for miniaturisation. Firstly, electrostatic actuators such as comb-drives can be fabricated reliably and accurately using existing MEMS fabrication techniques. This is a significant advantage compared with the challenge of fabricating and aligning miniature magnets and coils. Secondly, this approach offers greater flexibility in the design and testing phases. As discussed in section 2.3.3, the sensitivity of an electrostatic Kibble balance is given by $\kappa = \frac{dC}{dz}V$ (equation 2.18) which is equivalent to the BL product in the electromagnetic principle. κ can be optimised by adjusting the capacitance gradient $\frac{dC}{dz}$ or the voltage V between the capacitor plates. For a comb-drive the capacitance gradient can be increased by increasing the number of "fingers" in the comb or increasing the overlapping surface area by increasing the depth of the structure. The sensitivity of the device can also be adjusted by varying the voltage drop between the comb fingers. This will allow greater flexibility to optimise the device post-manufacture.

Appendix A

Traditional Mass Calibration

NATIONAL PHYSICAL LABORATORY
Teddington Middlesex UK TW11 0LW Telephone +44 20 8977 3222
NPL Management Ltd – Registered in England and Wales No 2937881

Certificate of Calibration

UKAS CALIBRATION 0478

SET OF FOUR MARBLES

241M

FOR	National Physical Laboratory Hampton Road Teddington Middlesex TW11 0LW For the attention of Emily Webster
DESCRIPTION	A set of four glass marbles
IDENTIFICATION	Bag labelled 241M Marbles identifiable by colour: Black, White, Blue/Orange and Green
DATE OF CALIBRATION	23 January 2024

Reference: 2024010275 **Page 1 of 3**

Date of Issue: 31 January 2024 **Signed:** **(Authorised Signatory)**

Checked by: J Berry **Name:** Stuart Davidson **on behalf of NPLML**

NATIONAL PHYSICAL LABORATORY

Continuation Sheet

241M

MEASUREMENTS

The true mass of each of these marbles was determined by weighing in air using standards of known mass and density.

TRACEABILITY

The calibration results stated in this certificate are based on the Consensus Value of the kilogram commencing 1st March 2023. The 2023 consensus value for the SI unit of mass, the kilogram, has been determined to be:

1 kg - 7 µg with a standard uncertainty of 20 µg with respect to the mass value of the International Prototype Kilogram (IPK).

RESULTS

The results of the measurements are given in the Table of Results. Each value given in the second column represents the true mass.

The density of the marbles was assumed to be 2 550 kg m^{-3} ± 400 kg m^{-3}.

The results and uncertainties quoted refer to values at the time of calibration and make no allowance for subsequent drift in the values of the weights.

UNCERTAINTY

The reported expanded uncertainties are based on a standard uncertainty multiplied by a coverage factor k = 2, providing a coverage probability of approximately 95 %. The uncertainty evaluation has been carried out in accordance with UKAS requirements.

NATIONAL PHYSICAL LABORATORY

Continuation Sheet

241M

TABLE OF RESULTS

Colour	Measured true mass g	Estimated measurement uncertainty mg
Black	5.972 053	0.040
White	5.188 843	0.040
Orange/Blue	4.701 402	0.040
Green	3.498 004	0.040

Appendix B

Moving Figures

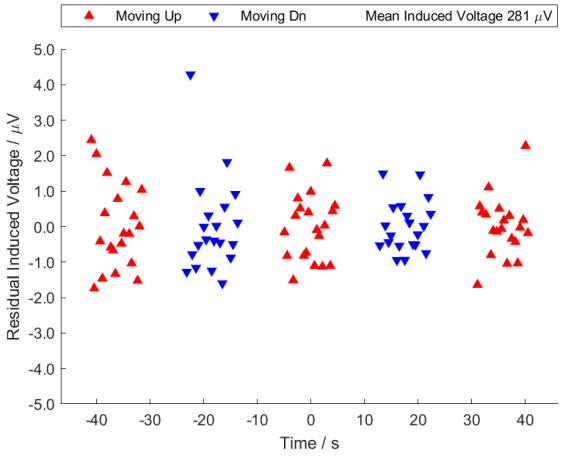

(A) Black 231024ab: Moving 1

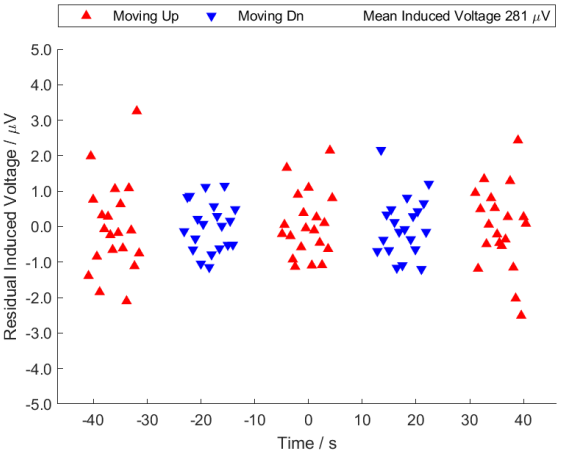

(B) Black 231024ab: Moving 2

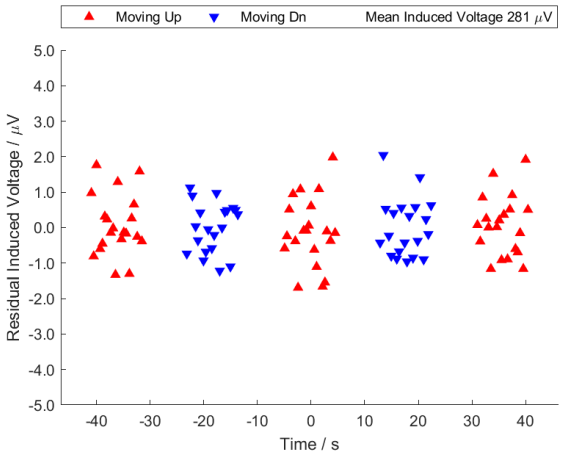

(C) Black 231024ab: Moving 3

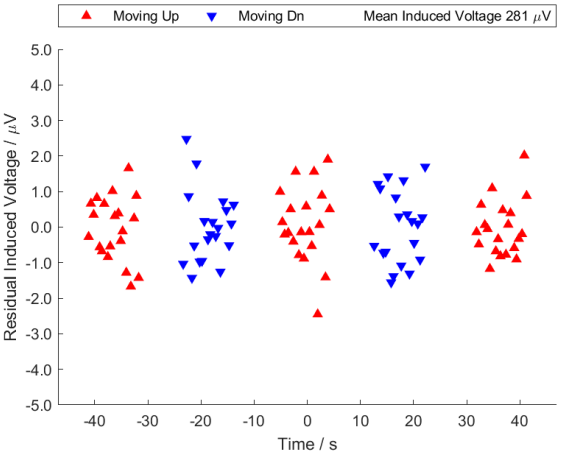

(D) Black 231024ab: Moving 4

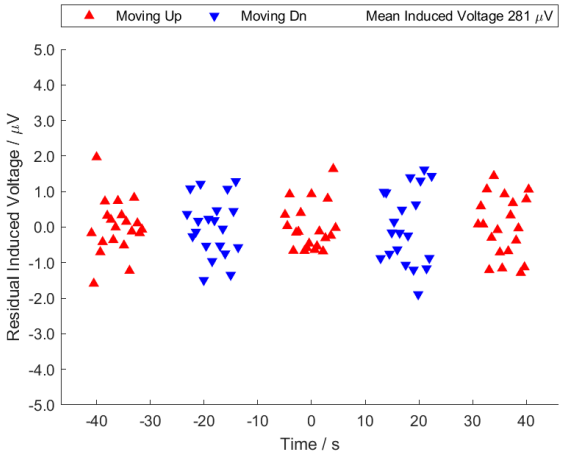

(E) Black 231024ab: Moving 5

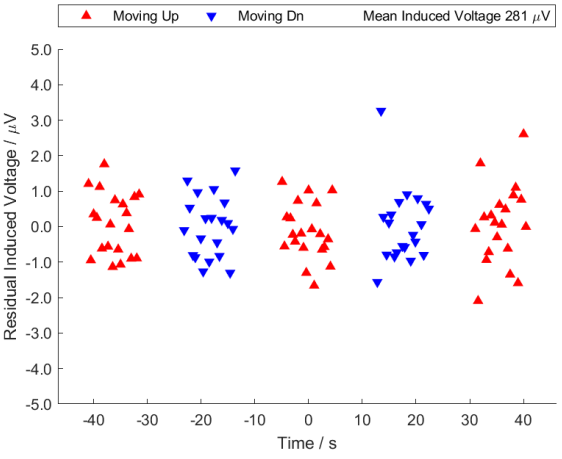

(F) Black 231024ab: Moving 6

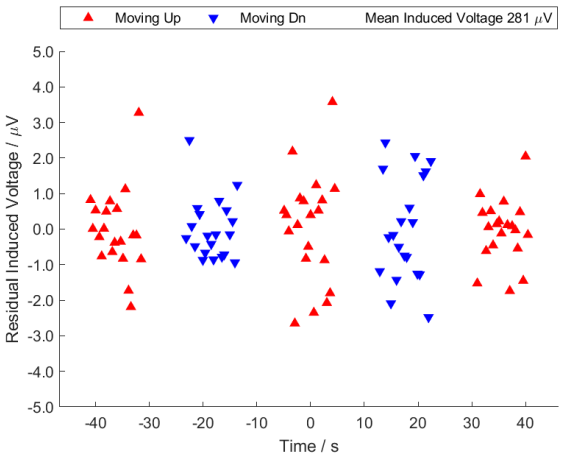

(G) Black 231024ab: Moving 7

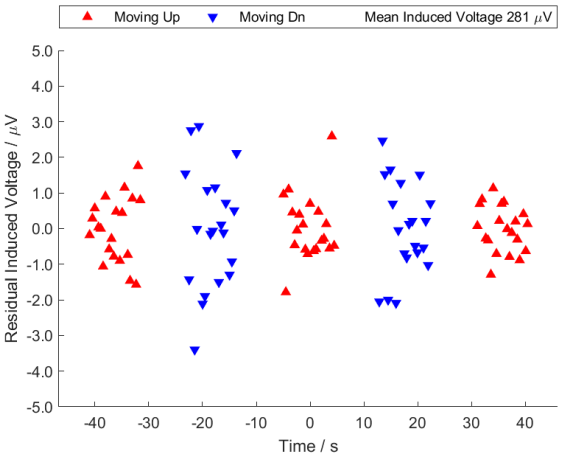

(H) Black 231024ab: Moving 8

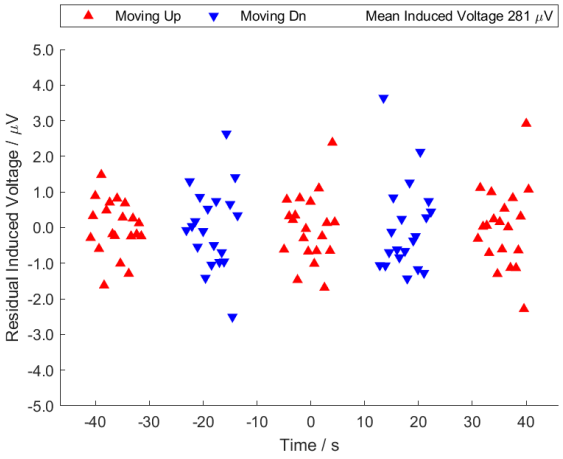

(I) Black 231024ab: Moving 9

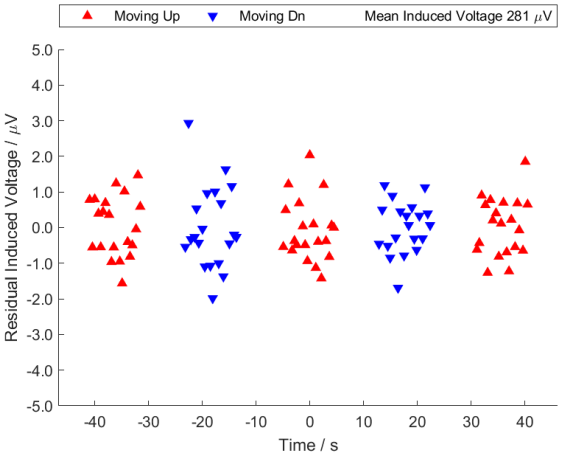

(J) Black 231024ab: Moving 10

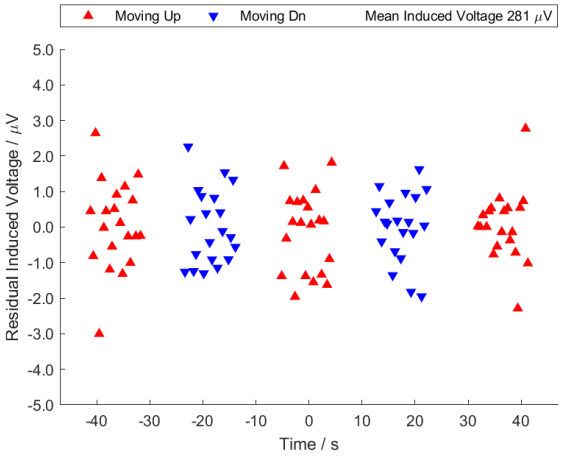

(K) Black 231024ab: Moving 11

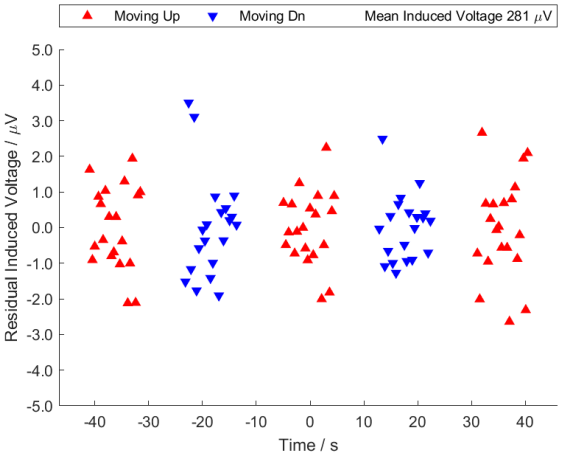

(L) Black 231024ab: Moving 12

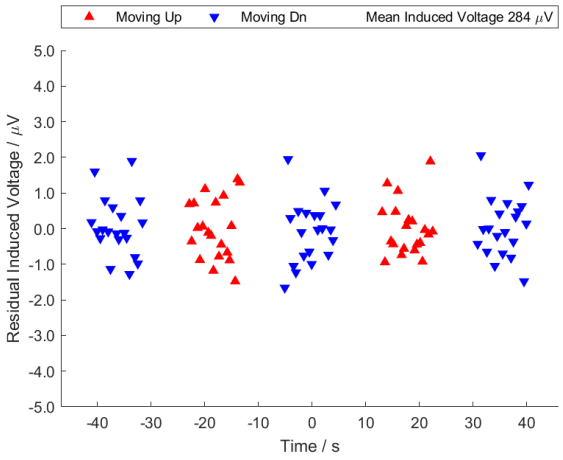

(M) Black 231024ab: Moving 13

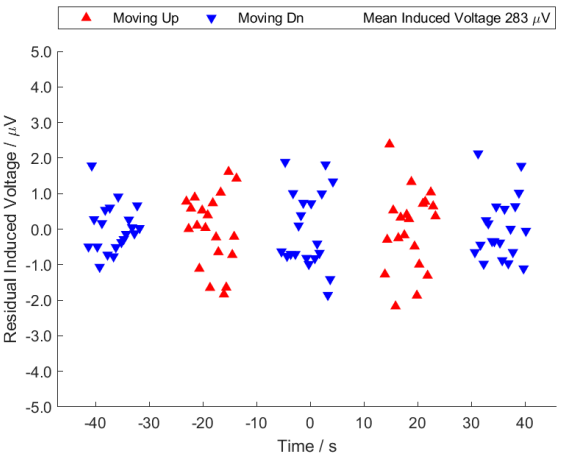

(N) Black 231024ab: Moving 14

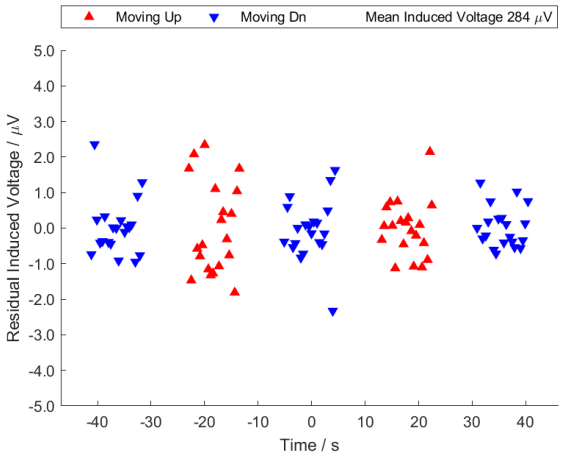

(O) Black 231024ab: Moving 15

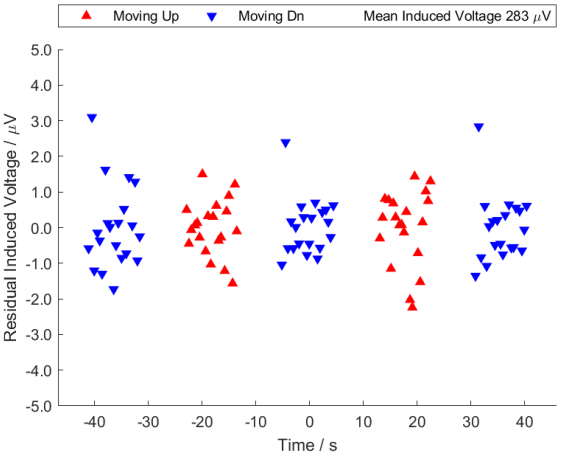

(P) Black 231024ab: Moving 16

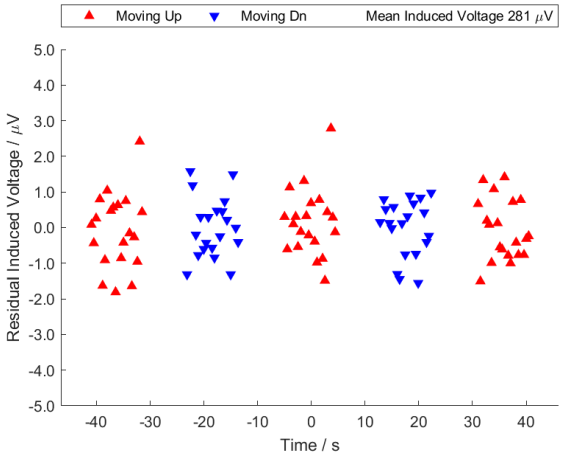

(Q) Black 231024ab: Moving 17

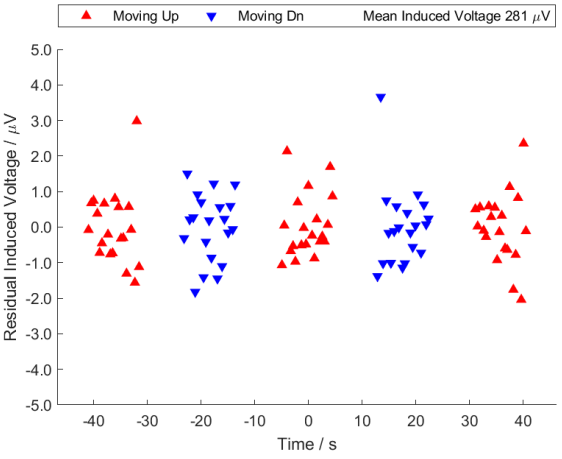

(R) Black 231024ab: Moving 18

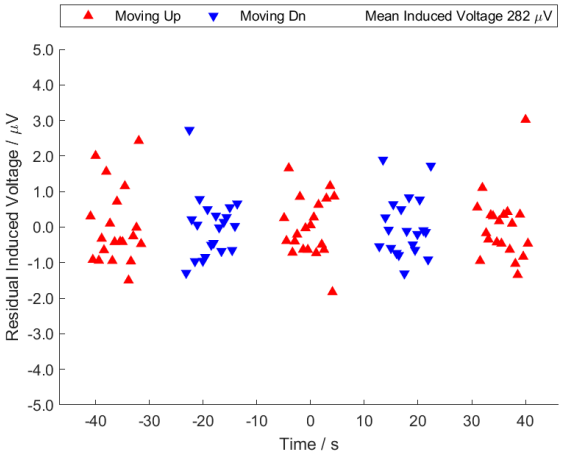

(S) Black 231024ab: Moving 19

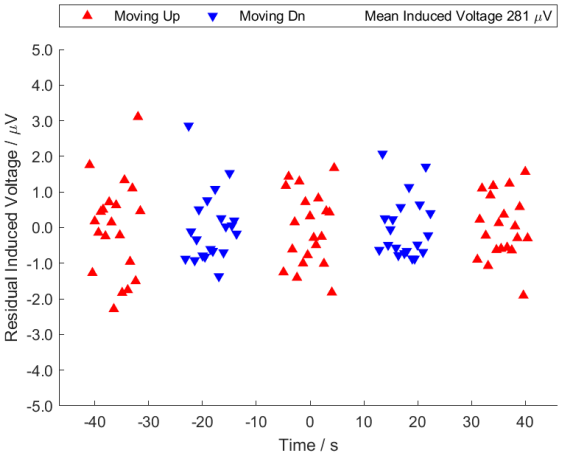

(T) Black 231024ab: Moving 20

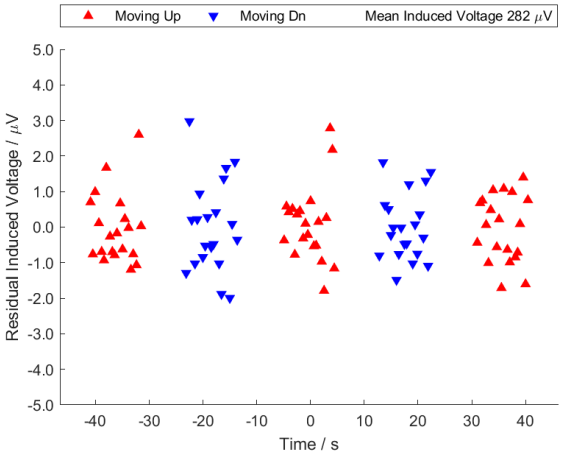

(U) Black 231024ab: Moving 21

FIGURE B.1: Black 231024ab: Moving

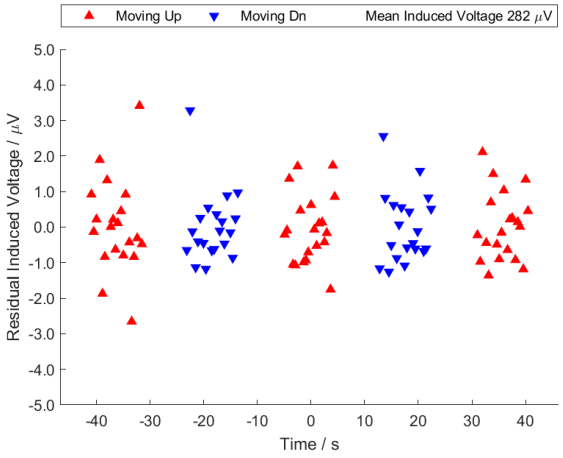

(A) Black 231024ac: Moving 1

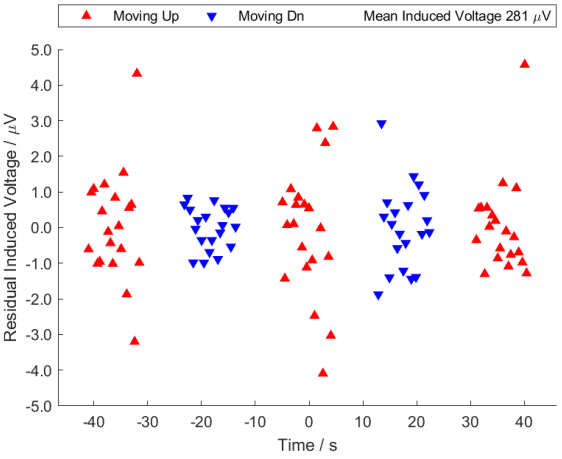

(B) Black 231024ac: Moving 2

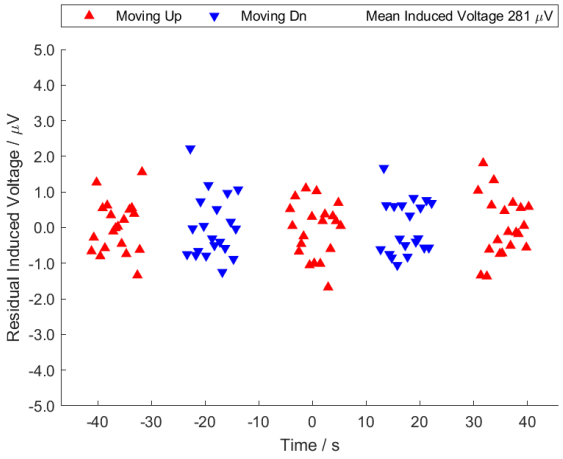

(C) Black 231024ac: Moving 3

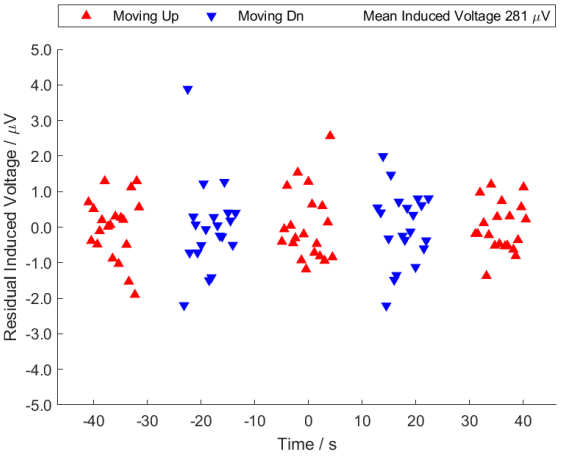

(D) Black 231024ac: Moving 4

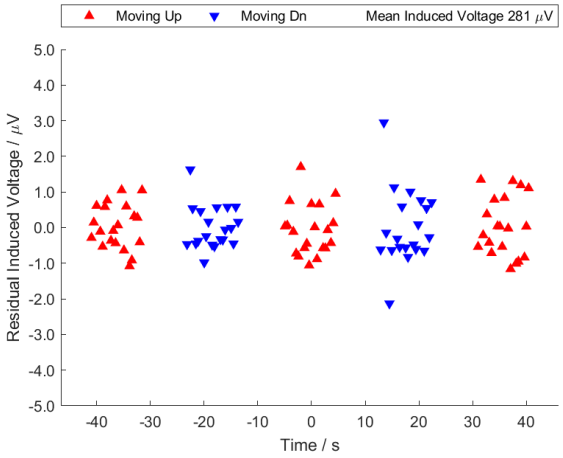

(E) Black 231024ac: Moving 5

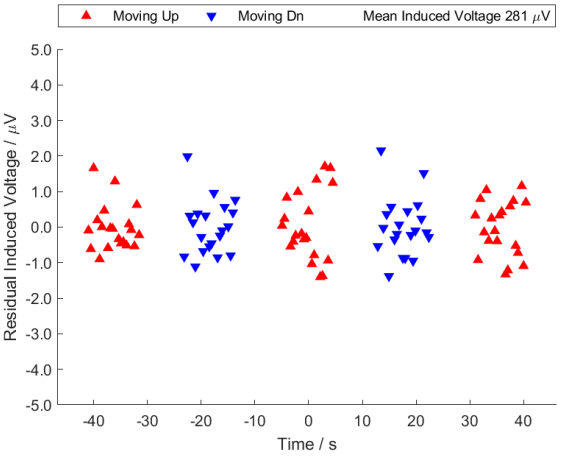

(F) Black 231024ac: Moving 6

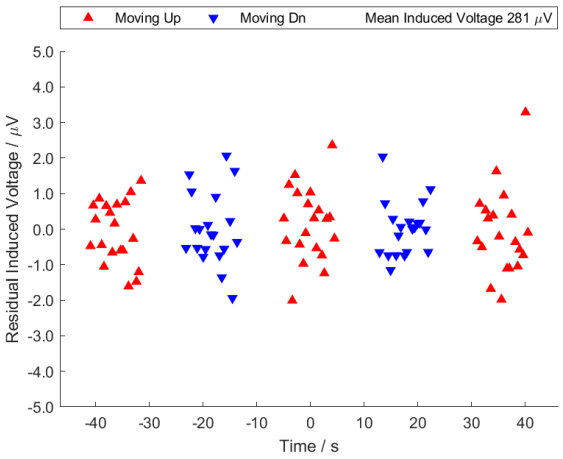

(G) Black 231024ac: Moving 7

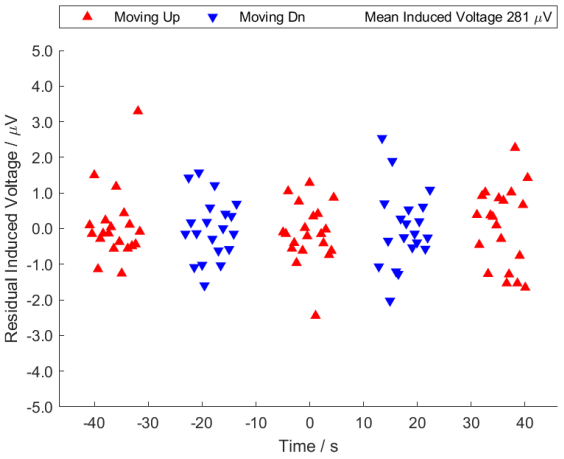

(H) Black 231024ac: Moving 8

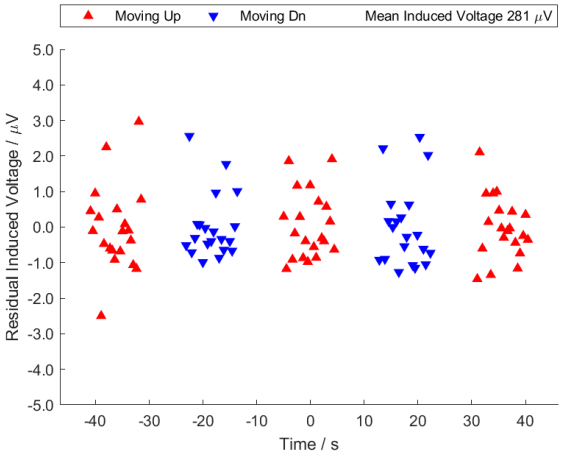

(I) Black 231024ac: Moving 9

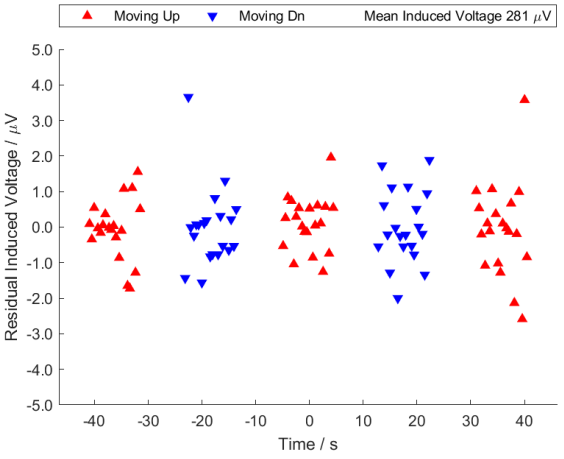

(J) Black 231024ac: Moving 10

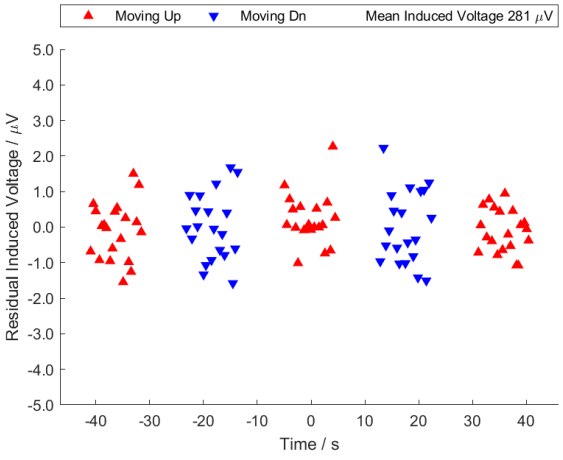

(K) Black 231024ac: Moving 11

FIGURE B.2: Black 231024ac: Moving

Appendix C

Weighing Figures

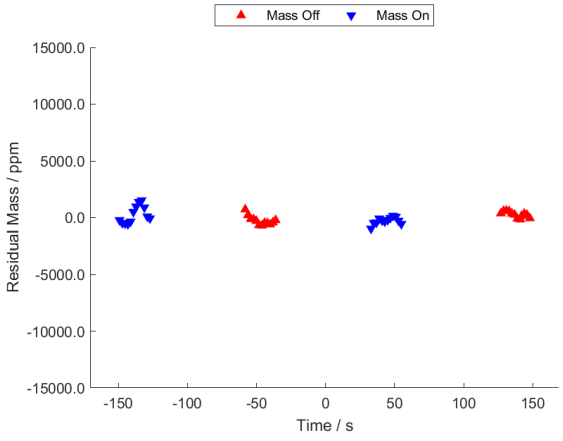

(A) Black 231024ab: Weighing 1

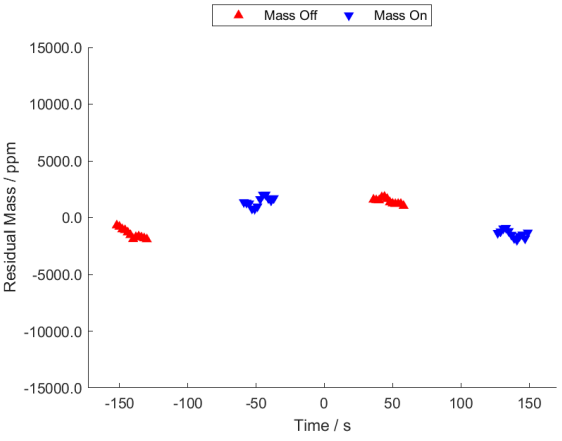

(B) Black 231024ab: Weighing 2

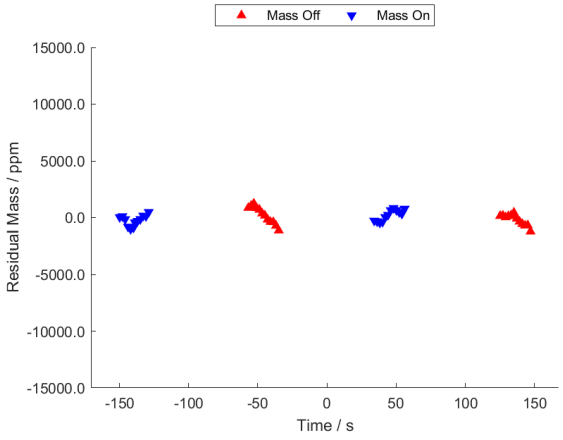

(C) Black 231024ab: Weighing 3

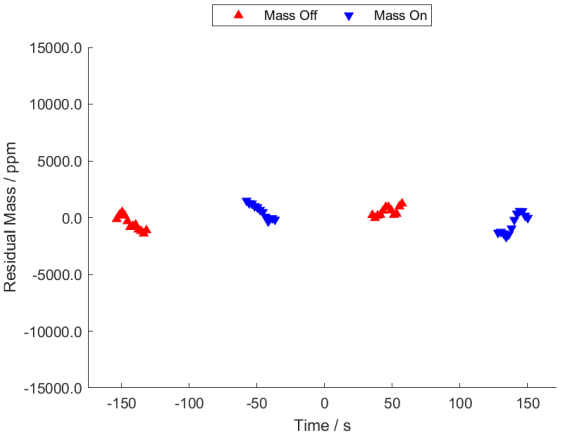

(D) Black 231024ab: Weighing 4

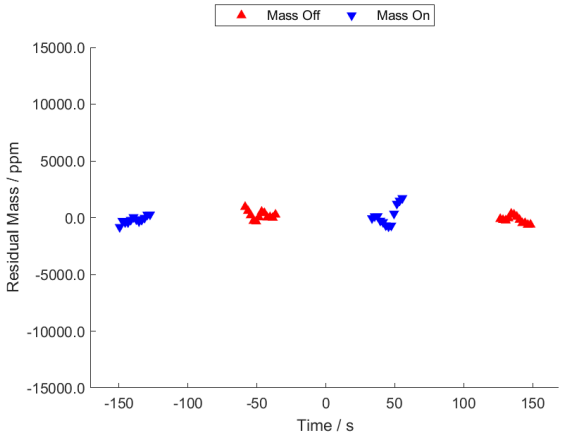

(E) Black 231024ab: Weighing 5

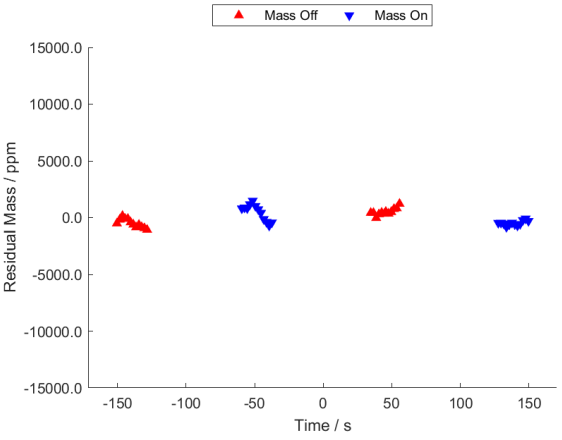

(F) Black 231024ab: Weighing 6

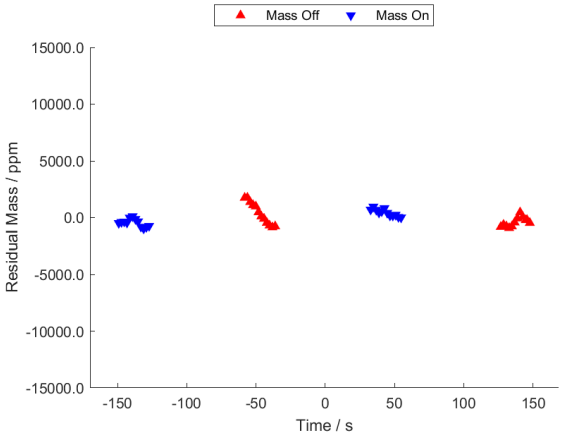

(G) Black 231024ab: Weighing 7

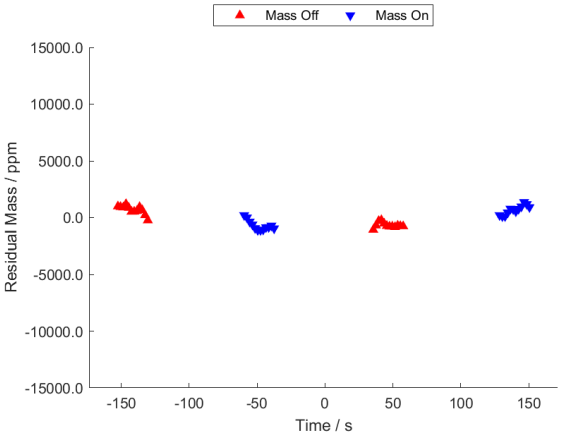

(H) Black 231024ab: Weighing 8

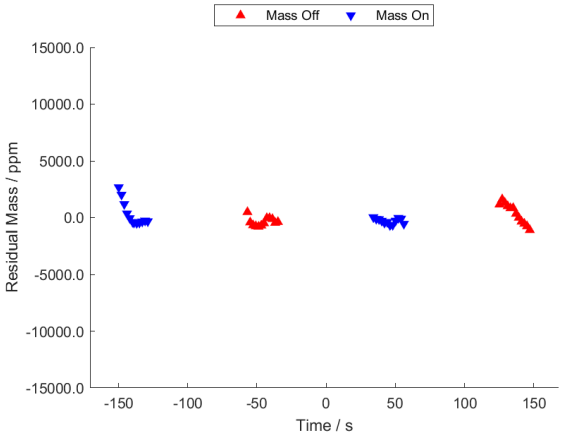

(I) Black 231024ab: Weighing 9

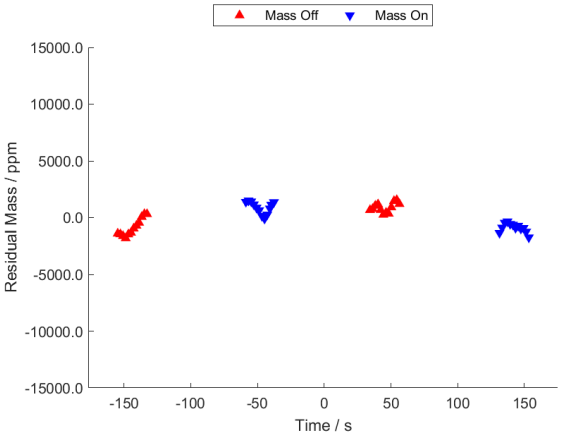

(J) Black 231024ab: Weighing 10

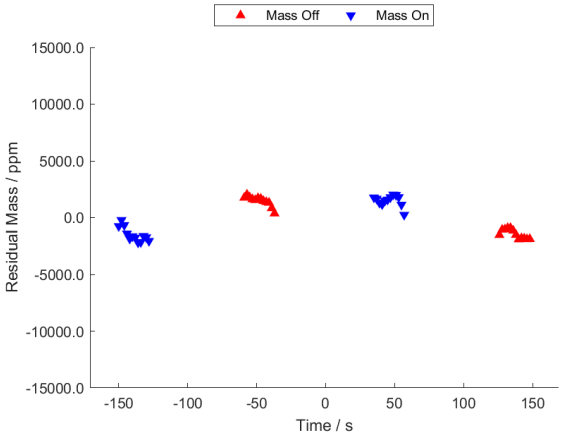

(K) Black 231024ab: Weighing 11

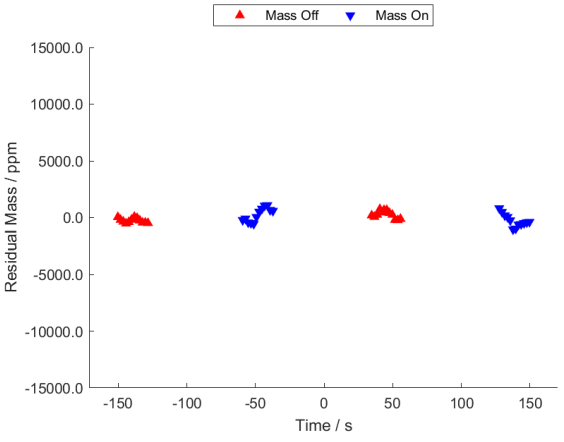

(L) Black 231024ab: Weighing 12

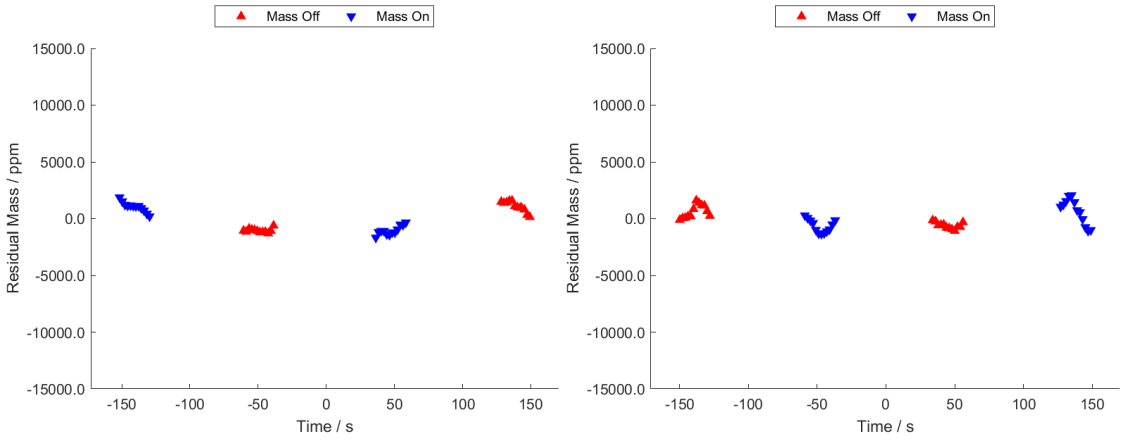

(M) Black 231024ab: Weighing 13

(N) Black 231024ab: Weighing 14

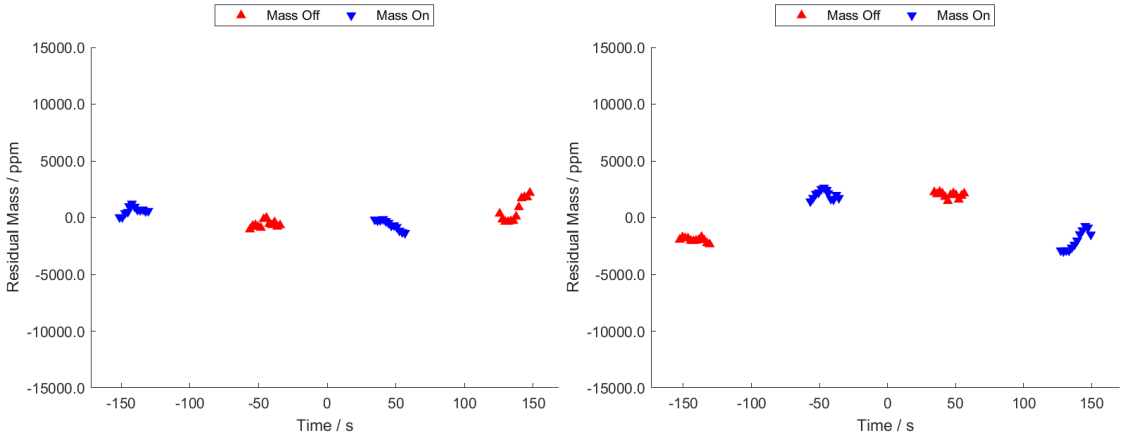

(O) Black 231024ab: Weighing 15

(P) Black 231024ab: Weighing 16

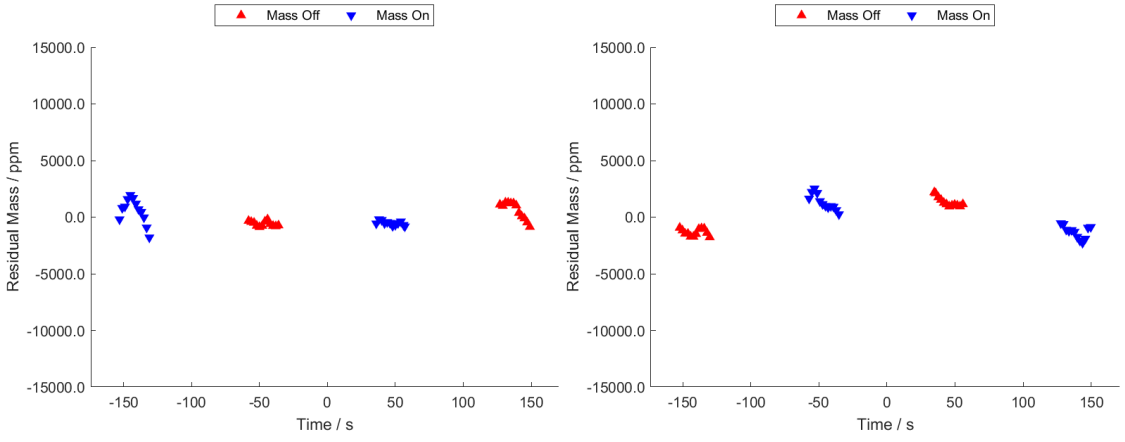

(Q) Black 231024ab: Weighing 17

(R) Black 231024ab: Weighing 18

FIGURE C.1: Black 231024ab: Weighing

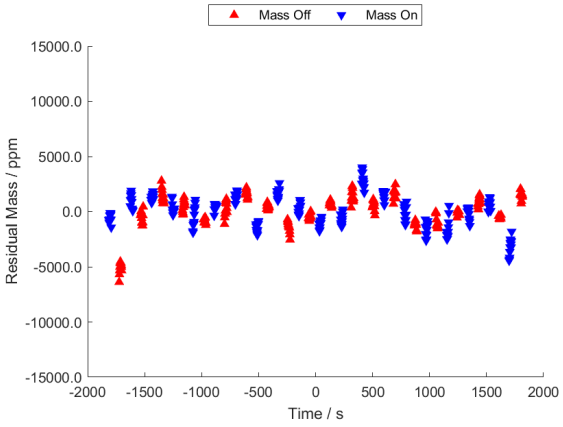

(A) Black 231024ac: Weighing 1

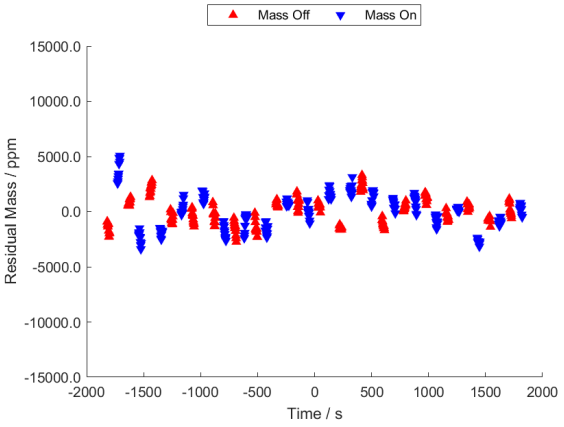

(B) Black 231024ac: Weighing 2

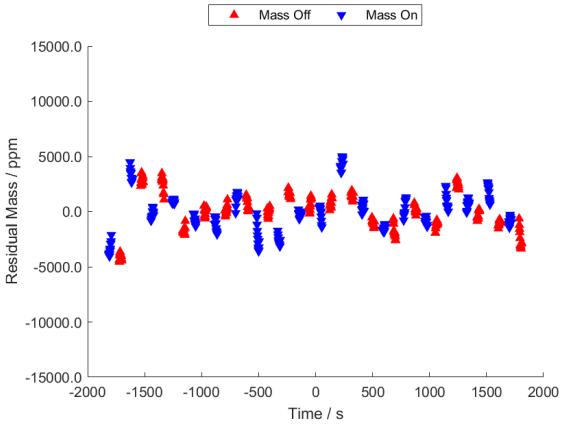

(C) Black 231024ac: Weighing 3

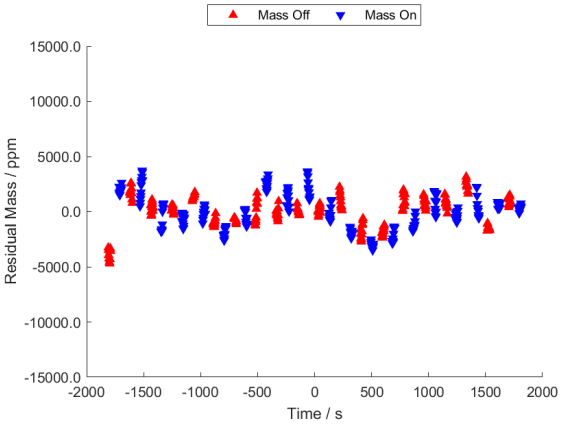

(D) Black 231024ac: Weighing 4

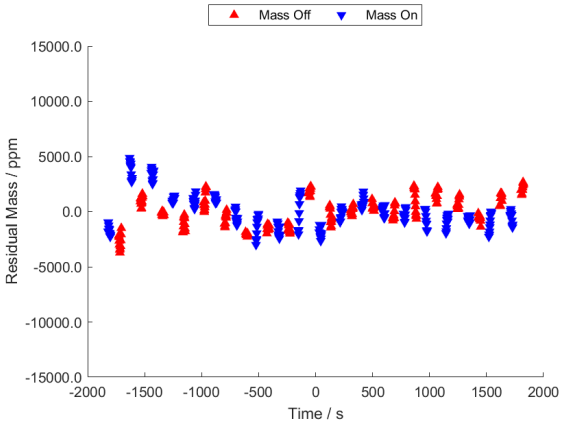

(E) Black 231024ac: Weighing 5

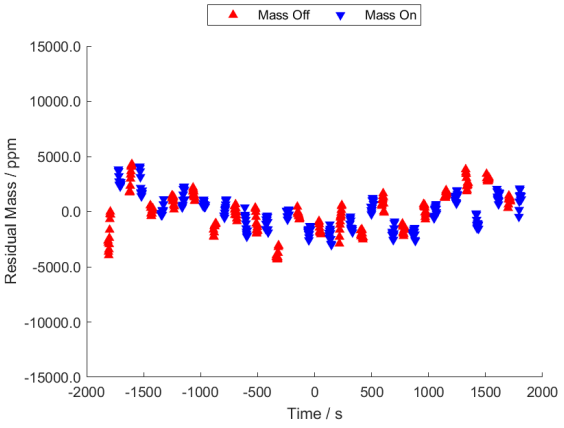

(F) Black 231024ac: Weighing 6

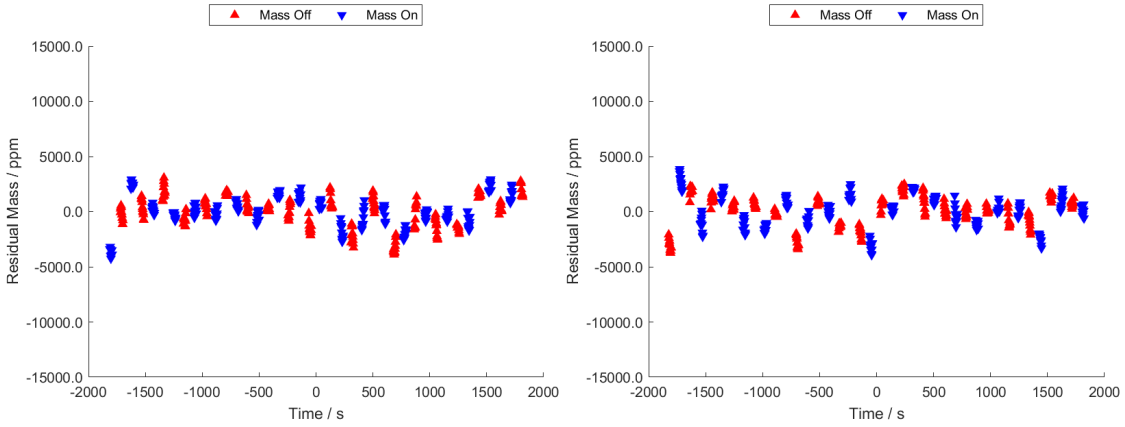

(G) Black 231024ac: Weighing 7

(H) Black 231024ac: Weighing 8

FIGURE C.2: Black 231024ac: Weighing

References

[1] E. Webster, I. A. Robinson, H. Chong, and S. Davidson. Kibble balance for gram level mass measurements. *IMEKO Procedings TC-3*, Oct 2022.

[2] B. P. Kibble and I. A. Robinson. Feasibility study for a moving coil apparatus to relate the electrical and mechanical SI units. Technical Report DES 40, NPL, September 1977.

[3] M Stock, P Conceição, H Fang, F Bielsa, A Kiss, L Nielsen, F Beaudoux, P Espel, M Thomas, D Ziane, H Baumann, A Eichenberger, K Marti, Y Bai, M Hu, Z Li, Y Lu, C Peng, J Wang, Y Wang, D Wu, P Abbott, D Haddad, Z Kubarych, E Mulhern, S Schlamminger, D Newell, K Fujita, H Inaba, K Kano, N Kuramoto, S Mizushima, S Okubo, Y Ota, L Zhang, S Davidson, R G Green, J O Liard, N F Murnaghan, B M Wood, M Borys, D Eppers, D Knopf, E Kuhn, M Hämpke, M Müller, A Nicolaus, F Scholz, M Spoors, and H Ahmedov. Final report on the CCM key comparison of kilogram realizations CCM.M-K8.2021. *Metrologia*, 60(1A):07003, Jan 2023.

[4] R Brown. Report of the 22nd meeting of the CCU to the CIPM, 2016.

[5] B. P. Kibble, R. C. Smith, and I. A. Robinson. A progress report on the moving coil experiment to realise the ampere. In *1980 Conference on Precision Electromagnetic Measurements Digest*, pages 0–1, 1980. ISBN 00.

[6] B. N. Taylor and T. J. Witt. New international electrical reference standards based on the Josephson and quantum Hall effects. *Metrologia*, 26(1):47, 1989.

[7] B. P. Kibble, I. A. Robinson, and J. H. Belliss. A realisation of the SI watt by the NPL moving-coil balance. *Metrologia*, 27:173–192, 1990.

[8] I. A. Robinson. Towards the redefinition of the kilogram: a measurement of the Planck constant using the NPL Mark II watt balance. *Metrologia*, 49:113–156, 2012.

[9] B M Wood, C A Sanchez, R G Green, and J O Liard. A summary of the Planck constant determinations using the NRC Kibble balance. *Metrologia*, 54(3):399, 2017.

[10] M Stock, P Barat, P Pinot, F Beaudoux, P Espel, F Piquemal, M Thomas, D Ziane, P Abbott, D Haddad, Z Kubarych, J R Pratt, S Schlamminger, K Fujii, K Fujita, N Kuramoto, S Mizushima, L Zhang, S Davidson, R G Green, J Liard, C Sanchez, B Wood, H Bettin, M Borys, I Busch, M Hämpke, M Krumrey, and A Nicolaus. A comparison of future realizations of the kilogram. *Metrologia*, 55(1):T1, Jan 2018.

[11] BIPM. Resolution 1 On the revision of the International System of Units (SI). In *Proceedings of the 26th meeting of the General Conference on Weights and Measures (November 2018)*, page 472, 2019.

[12] Abdullah Saleh Algamili, John Ojur Dennis, Abdelaziz Yousif Ahmed, Sami Sultan Alabsi, Saeed Salem Ba Hashwan, and Mohammed M. Junaid. A Review of Actuation and Sensing Mechanisms in MEMS-Based Sensor Devices. *Nanoscale Research Letters*, 16, 2021.

[13] Raju Hajare, Vishnuvardhan Reddy, and R. Srikanth. MEMS based sensors – A comprehensive review of commonly used fabrication techniques. *Materials Today: Proceedings*, 49:720–730, 2022. Web International Conference on Accelerating Innovations in Material Science – 2020 (AIMS-2020).

[14] Tomasz Blachowicz and Andrea Ehrmann. 3D Printed MEMS Technology—Recent Developments and Applications. *Micromachines*, 11(4), 2020.

[15] Sung-Yueh Wu, Chen Yang, Wensyang Hsu, and Liwei Lin. 3D-printed microelectronics for integrated circuitry and passive wireless sensors. *Microsystems and Nanoengineering*, 1, 2015.

[16] Valentina Zega, Caterina Credi, Roberto Bernasconi, Giacomo Langfelder, Luca Magagnin, Marinella Levi, and Alberto Corigliano. The first 3-D-printed z-axis accelerometers with differential capacitive sensing. *IEEE Sensors Journal*, 18(1):53–60, 2018.

[17] OIML. International recommendation on weights of classes E_1, E_2, F_1, F_2, M_1, M_{1-2}, M_2, M_{2-3}, and M_3, part 1: Metrological and technical requirements. Technical Report International Recommendation No. R111-1, Organisation Internationale de Métrologie Légale, 2004.

[18] G. A. Shaw, J. Stirling, J. A. Kramar, A. Moses, P. Abbott, R. Steiner, A. Koffman, J. R. Pratt, and Z. J. Kubarych. Milligram mass metrology using an electrostatic force balance. *Metrologia*, 53(5), 2016.

[19] Gordon A. Shaw and Julian Stirling. Measurement of Submilligram Masses Using Electrostatic Force. *IEEE Transactions on Instrumentation and Measurement*, 68(6):2015–2020, 2019.

[20] Leon Chao, Frank Seifert, Darine Haddad, Jon Pratt, David Newell, and Stephan Schlamminger. The performance of the KIBB-g1 tabletop kibble balance at NIST. *Metrologia*, 57(3):035014, may 2020.

[21] Suren Vasilyan, Norbert Rogge, Christian Rothleitner, Shan Lin, Ivan Poroskun, Dorothea Knopf, Frank Härtig, and Thomas Fröhlich. The progress in development of the Planck-Balance 2 (PB2): A tabletop Kibble balance for the mass calibration of E2 class weights. *tm - Technisches Messen*, 88(12):731–756, 2021.

[22] Mettler Toledo GmbH. Reference Weights and Microgram Weights. https://www.mt.com/gb/en/home/products/Laboratory_Weighing_Solutions/Test_Weights/reference_weights_and_microgram_weights.html. Retrieved May 2024.

[23] C. W. Jones. *Development and characterisation of traceable force measurement for nanotechnology*. PhD thesis, University of Warwick, JUL 2012.

[24] G. A. Shaw. Current state of the art in small mass and force metrology within the International System of Units. *Measurement Science and Technology*, 29(na), 2018.

[25] I. A. Robinson. An optical-fibre ring interface bus for precise electrical measurements. *MeasSciTech*, 2:949–956, 1991.

[26] BIPM. Convention du mètre et règlement annexe. *Bureau international des poids et mesures*, 1875.

[27] BIPM. *Proceedings of the first meeting of the General Conference on Weights and Measures*, 1889.

[28] BIPM. https://www.bipm.org/en/mass-metrology/ipk. Image licensed by BIPM under CC BY 4.0.

[29] G Girard. The Third Periodic Verification of National Prototypes of the Kilogram (1988-1992). *Metrologia*, 31(4):317–336, Jan 1994.

[30] United Kingdom Accreditation Service. NPL Management Ltd Schedule of Accreditation to ISO/IEC 17025:2017, 2021.

[31] BIPM. BIPM Key Comparison Database. https://tinyurl.com/bipmkcd, 12 2021.

[32] S. Davidson, M. Perkin, and M. Buckley. The Measurement of Mass and Weight. *NPL Measurement Good Practice Guide*, 71, JUN 2004.

[33] S. Davidson, A. Valcu, N. Medina, J. Zuda, L. Snopko, and I. Kolozinska. Supplementary comparison of 500 microgram, 200 microgram, 100 microgram and 50 microgram weights—EURAMET.M.M-S9. *Metrologia*, 54(1A), 2017.

[34] BIPM. *Le Système international d'unités / The International System of Units ('The SI Brochure')*. Bureau international des poids et mesures, ninth edition, 2019.

[35] C. Jarvis, E. Webster, S. Davidson, and I. A. Robinson. A μKibble balance for direct realisation of small-scale masses and forces. In *International Congress of Metrology*, page 14002, 2019.

[36] BIPM. *CCM detailed note on the dissemination process after the redefinition of the kilogram*, 2019.

[37] M. Stock, P. Barat, R. S. Davis, A. Picard, and M. J. T. Milton. Calibration campaign against the international prototype of the kilogram in anticipation of the redefinition of the kilogram part I: comparison of the international prototype with its official copies. *Metrologia*, 52(2):310–316, 2015.

[38] M Stock, P Conceição, H Fang, F Bielsa, A Kiss, L Nielsen, D Kim, M Kim, K C Lee, S Lee, M Seo, B C Woo, Z Li, J Wang, Y Bai, J Xu, D Wu, Y Lu, Z Zhang, Q He, D Haddad, S Schlamminger, D Newell, E Mulhern, P Abbott, Z Kubarych, N Kuramoto, S Mizushima, L Zhang, K Fujita, S Davidson, R G Green, J O Liard, N F Murnaghan, C A Sanchez, B M Wood, H Bettin, M Borys, M Mecke, A Nicolaus, A Peter, M Müller, F Scholz, and A Schofeld. Report on the CCM key comparison of kilogram realizations CCM.M-K8.2019. *Metrologia*, 57(1A):07030, Jan 2020.

[39] D Haddad, F Seifert, L S Chao, A Possolo, D B Newell, J R Pratt, C J Williams, and S Schlamminger. Measurement of the Planck constant at the National Institute of Standards and Technology from 2015 to 2017. *Metrologia*, 54(5):633, 2017.

[40] H Fang, F Bielsa, S Li, A Kiss, and M Stock. The BIPM Kibble balance for realizing the kilogram definition. *Metrologia*, 57(4):045009, Jul 2020.

[41] NPL. https://www.npl.co.uk/getmedia/a2745024-9eda-4720-b8d7-bc84b153b46c/kibble-hed-t_1.jpg?width=1024&height=1024&ext=.jpg. Image courtesy of NPL.

[42] NIST. https://www.nist.gov/sites/default/files/styles/1400_x_1400_limit/public/images/photogallery/nist_4_watt_balance.jpg?itok=0pa6j1gv. Image by J.L. Lee, courtesy of NIST.

[43] BIPM. https://www.bipm.org/documents/20126/58070364/wb_500.jpg/02d36f26-da20-03f9-595c-8341ed1e2fe6?t=1625587174412. Image licensed by BIPM under CC BY 4.0.

[44] C. A. Sanchez, B. M. Wood, R. G. Green, J. O. Liard, and D. Inglis. A determination of Planck's constant using the NRC watt balance. *Metrologia*, 51(2):S5–S14, 2014.

[45] L. S. Chao, F. Seifert, A. Cao, D. Haddad, D. B. Newell, S. Schlamminger, and J. R. Pratt. The design of the new NIST-4 watt balance. In *29th Conference on Precision Electromagnetic Measurements (CPEM 2014)*, pages 364–365, 2014.

[46] Darine Haddad, Frank Seifert, Leon Chao, Austin Cao, George Sineriz, Jon Pratt, David Newell, and Stephan Schlamminger. First Measurements of the Flux Integral With the NIST-4 Watt Balance. *IEEETran*, 64(6):1642–1649, JUN 2015.

[47] A. Picard, M. Stock, H. Fang, T. J. Witt, and D. Reymann. The BIPM watt balance. *IEEETran*, 56(2):538–542, 2007.

[48] A. Picard, M. P. Bradley, H. Fang, A. Kiss, E. de Mirandés, B. Parker, S. Solve, and M. Stock. The BIPM watt balance: Improvements and developments. *IEEETran*, 60(7):2378–2386, 2011.

[49] I. A. Robinson. A simultaneous moving and weighing technique for a watt balance at room temperature. *Metrologia*, 49:108–112, 2012.

[50] E. de Mirandés, A. Zeggagh, M. Bradley, A. Picard, H. Fang, A. Kiss, and M. Stock. Superconducting coil system to study the behavior of superconducting coils for a cryogenic watt balance. In *2012 Conference on Precision electromagnetic Measurements*, pages 470–471, 2012.

[51] H. Fang, A. Kiss, E. de Mirandés, J. Lan, L. Robertsson, S. Solve, A. Picard, and M. Stock. Status of the BIPM watt balance. *IEEE Transactions on Instrumentation and Measurement*, 62(6):1491–1498, June 2013.

[52] F. Bielsa, H. Fang, A. Kiss, and Michael Stock. A new interferometric system for the BIPM Kibble Balance. In *Conference on Precision Electromagnetic Measurements (CPEM 2020)*, pages 1–2, 08 2020.

[53] F. Bielsa, K. Fujita, A. Kiss, and H. Fang. Development of a beam mechanism for the BIPM Kibble Balance. In *Conference on Precision Electromagnetic Measurements (CPEM 2024)*, pages 1–2, 2024.

[54] NIST. https://www.nist.gov/sites/default/files/styles/480_x_480_limit/public/images/2021/04/30/kibb-g1.png?itok=5zwILOlv. Image courtesy of NIST.

[55] Sean Kelly/NIST. https://www.nist.gov/sites/default/files/styles/960_x_960_limit/public/images/2023/03/27/Diagram.jpg?itok=VnHlJJea. Image courtesy of NIST.

[56] Leon Shih Chao, Gordon Allan Shaw III, Stephan Schlamminger, and Yusi Cao. Second generation NIST Kibble balance and determining absolute mass. Technical Report US 2023/0375396 A1, United States Patent Application Publication, 2023.

[57] Ch Rothleitner, I Poroskun, S Svitlov, J Kloß, and J Konrad. Erratum: A method for evaluating the force factor in oscillating kibble balances with application to the Planck–Balance (2023 Metrologia 60 055007). *Metrologia*, 60(6):069601, Oct 2023.

[58] J.L. Lee/NIST. https://tinyurl.com/nistefb. Image courtesy of NIST.

[59] C. W. Jones and R. K. Leach. Review of low force transfer artefact technologies. Technical Report ENG 5, NPL, 2008.

[60] S-J. Chen and Pan S-S. A force measurement system based on an electrostatic sensing and actuating technique for calibrating force in a micronewton range with a resolution of nanonewton scale. *MeasSciTech*, 22:045104, 2011.

[61] Sun P., Zhao M., Jiang J., Zheng Y., Han Y., and Song L. The differential method for force measurement based on electrostatic force. *JSens*, page 1857920, 2017.

[62] Yelong Zheng, Le Song, Gang Hu, Meirong Zhao, Yanling Tian, Zihui Zhang, and Fengzhou Fang. Improving environmental noise suppression for micronewton force sensing based on electrostatic by injecting air damping. *Review of Scientific Instruments*, 85(5):055002, 2014.

[63] Song L., Zheng Y., Hu G., Ma J., Werner T., Zhao M., and Fang F. Highly sensitive, precise, and traceable measuremen of force. *InSciTech*, 44:386–400, 2016.

[64] Kim M-S., Choi J-H., Park Y-K., and Kim J-H. Atomic force microscope cantilever calibration device for quantified force metrology at micro- or nano-scale regime: the nano force calibrator (NFC). *Metrologia*, 43:389–395, 2006.

[65] Stenlund L., Riski K., Seppä J., Pudas M., Vähäsöyrinki M., Tuhkanen V., and Röning J. Traceable characterization of a bending millimetre scale cantilever for nanoforce sensing. *MeasSciTech*, 21:075102, 2010.

[66] Nesterov V., Belai O., Nies D., Buetefisch S., Mueller M., Ahbe T., Naparty D., Popadic R., and Wolff H. SI-traceable determination of the spring constant of a soft cantilever using the nanonewton force facility based on electrostatic methods. *Metrologia*, 53:1031, 2016.

[67] Daniel A Buttry. Applications of the Quartz Crystal Microbalance to Electrochemistry. Technical report, Office of Naval Research, 1989.

[68] J. Gilliam and E. Hall. Reference and Equivalent Methods Used to Measure National Ambient Air Quality Standards (NAAQS) Criteria Air Pollutants - Volume I. Technical Report EPA/600/R-16/139, U.S. Environmental Protection Agency, 2016.

[69] Mettler-Toledo GmbH. XPR Microbalances and Ultra-Microbalances. https://www.mt.com/gb/en/home/library/product-brochures/laboratory-weighing/02_Micro_Ultramicro_Balances/01_Brochures/BR_XPR_Micro_Balance.html, 2016.

[70] Rodder J. A. Quartz Fiber Torsion Ultramicrobalance. Technical Report 2,842,351, United States Patent Office, 1958.

[71] P. Punyabrahma and G. R. Jayanth. A magnetometer for estimating the magnetic moment of magnetic micro-particles. *Review of Scientific Instruments*, 88(1):015008, 2017.

[72] Peihong Wang, Katsuhiko Tanaka, Susumu Sugiyama, Xuhan Dai, Xiaolin Zhao, and Jingquan Liu. A micro electromagnetic low level vibration energy harvester based on MEMS technology. *Microsystem Technology*, 15:941, 2009.

[73] Pranay Podder, Peter Constantinou, Dhiman Mallick, Andreas Amann, and Saibal Roy. Magnetic Tuning of Nonlinear MEMS Electromagnetic Vibration Energy Harvester. *Journal of Microelectromechanical Systems*, 26:539, 2017.

[74] E S Leland, P K Wright, and R M White. A MEMS AC current sensor for residential and commercial electricity end-use monitoring. *Journal of Micromechanics and Microengineering*, 19(9):094018, Aug 2009.

[75] M. G. Kisic, N. V. Blaz, K. B. Babkovic, A. M. Maric, G. J. Radosavljevic, L. D. Zivanov, and M. S. Damnjanovic. Passive Wireless Sensor for Force Measurements. *IEEE Transactions on Magnetics*, 51(1):1–4, 2015.

[76] P. Berkelman and H. Abdul-Ghani. Electromagnetic Haptic Feedback System for Use With a Graphical Display Using Flat Coils and Sensor Array. *IEEE Robotics and Automation Letters*, 5(2):1618–1625, 2020.

[77] Junfang Zhu, Toshiyuki Hayashi, Atsuhiro Nishino, and Koji Ogushi. New microforce generating machine using electromagnetic force. *ACTA IMEKO*, 12 2020.

[78] Working Group 1 of the Joint Committee for Guides in Metrology (JCGM/WG 1). Evaluation of Measurement Data — Guide to the expression of Uncertainty in Measurement. Technical report, BIPM, 9 2008.

[79] I. A. Robinson and B. P. Kibble. An initial measurement of Planck's constant using the NPL mark II watt balance. *Metrologia*, 44:427–440, 2007.

[80] Vishay Precision Group. HZ Series (Z-Foil) with Zero TCR. http://www.vishaypg.com/docs/63120/hzseries.pdf, 2010.

[81] Linear Technology Corporation. LM199/LM399 Precision Reference. https://www.analog.com/media/en/technical-documentation/data-sheets/199399fc.pdf, 2014.

[82] Measurement Computing. Analog to Digital Conversion. https://www.mccdaq.com/PDFs/specs/Analog-to-Digital.pdf, 11 2021.

[83] Vishay Precision Group. Design and Selector Guide for High-Precision Resistors. http://dsg.vishayfoilresistors.com/, 2015.

[84] Renishaw plc. TONiC™ UHV encoder system, 2021. Data sheet: L-9517-9426-03-D.

[85] WikiBooks. Engineering Tables/Standard Wire Gauge. https://en.wikibooks.org/wiki/Engineering_Tables/Standard_Wire_Gauge, 7 2020.

[86] Shisong Li and Stephan Schlamminger. The irony of the magnet system for Kibble balances — a review. *Metrologia*, 59(2):022001, Mar 2022.

[87] S. Schlamminger, D. Haddad, F. Seifert, L. S. Chao, D. B. Newell, R. Liu, R. L. Steiner, and J. R. Pratt. Determination of the Planck constant using a watt balance with a superconducting magnet system at the National Institute of Standards and Technology. *Metrologia*, 51(2):S15–S24, 2014.

[88] F. Seifert, A. Panna, S. Li, B. Han, L. Chao, A. Cao, D. Haddad, H. Choi, L. Haley, and S. Schlamminger. Construction, measurement, shimming, and performance of the NIST-4 magnet system. *IEEE Transactions on Instrumentation and Measurement*, 63(12):3027–3038, December 2014.

[89] Webcraft GmbH. Data sheet article S-20-20-N. https://www.supermagnete.de/eng/data_sheet_S-20-20-N.pdf, 12 2015.

[90] Webcraft GmbH. Data sheet article S-70-35-N. https://www.supermagnete.de/eng/data_sheet_S-70-35-N.pdf, 9 2015.

[91] I A Robinson et al. The NPL Demonstration Kibble Balance: History and development. *in preparation*, 2024.

[92] I. A. Robinson. Simplified fundamental force and mass measurements. *Metrologia*, 53(4):1054–1060, 2016.

[93] B. P. Kibble and I. A. Robinson. Principles of a new generation of simplified and accurate watt balances. *Metrologia*, 51(2):S132–S139, 2014.

[94] X. Jiang, W. Zeng, I. M. Smith, P. Scott, and F. X. Maletras. The detection of transient behaviour in environmental vibration for the Watt balance. *MeasSciTech*, 18(5):1487–1494, MAY 2007.

[95] Ian A. Robinson, Aletta E. Karsten, Thapelo Mametja, Landile Mndebele, Karin Cedergren, Tobias Bergsten, and Christopher Bull. Progress on the NPL, NMISA, RISE Kibble Balance Collaboration. In *2024 Conference on Precision Electromagnetic Measurements (CPEM)*, pages 1–2, 2024.

[96] P. Gournay, G. Geneves, F. Alves, M. Besbes, F. Villar, and J. David. Magnetic circuit design for the BNM watt balance experiment. *IEEE Transactions on Instrumentation and Measurement*, 54(2):742–745, April 2005.

[97] Michael Stock. Watt balances and the future of the kilogram. In *Simposio de Metrología 2006*, pages 1–6, 2006.

[98] C-Flex Bearing Co Inc. C-Flex Product Brochure. https://c-flex.com/literature/company-product-brochure/, 2019. Double Ended Bearings Datasheet.

[99] S Li, F Bielsa, M Stock, A Kiss, and H Fang. Coil-current effect in Kibble balances: analysis, measurement, and optimization. *Metrologia*, 55(1):75–83, 2018.

[100] Ian A Robinson. Private communication: Current correction in the Mini Kibble Balance, Mar 2024.

[101] RS Components Ltd. RS PRO 1.75mm White PLA 3D Printer Filament. https://uk.rs-online.com/web/p/3d-printing-materials/8320223. Retrieved August 2025.

[102] L. Auffray, PA. Gouge, and L. Hattali. Design of experiment analysis on tensile properties of PLA samples produced by fused filament fabrication. *The International Journal of Advanced Manufacturing Technology*, 118:4123–4137, 2022.

[103] Houcine Salem, Hamid Abouchadi, and Khalid Elbikri. PLA Mechanical Performance Before and After 3D Printing. *International Journal of Advanced Computer Science and Applications*, 13(3), 2022.

[104] Jibran Khaliq, Dharma Raj Gurrapu, and Farah Elfakhri. Effects of Infill Line Multiplier and Patterns on Mechanical Properties of Lightweight and Resilient Hollow Section Products Manufactured Using Fused Filament Fabrication. *Polymers*, 15(12), 2023.

[105] United Kingdom Accreditation Service. NPL Management Ltd Schedule of Accreditation to ISO/IEC 17025:2017, 2022.

[106] Robinson I. A. Nessus 2 Notes and Tutorial V0.10. Technical report, National Physical Laboratory, 10 2023.

[107] Adobe Systems Incorporated. *Postscript Language Reference Manual*. Addison-Wesley, 1985.

[108] Jon Pratt, David Newell, and John Kramar. A Flexure Balance With Adjustable Restoring Torque for Nanonewton Force Measurement. *IMEKO*, 2002.

[109] M. Darnieder, M. Pabst, R. Wenig, L. Zentner, R. Theska, and T. Fröhlich. Static behavior of weighing cells. *Journal of Sensors and Sensor Systems*, 7(2):587–600, 2018.

[110] Maximilian Darnieder, Markus Pabst, Thomas Fröhlich, Lena Zentner, René Theska, and Yuelin Zeng. Mechanical properties of an adjustable weighing cell prototype. *Euspen's 19th International Conference & Exhibition*, June 2019.

[111] C. C. Speake. Fundamental Limits to Mass Comparison by Means of a Beam Balance. *Proceedings of the Royal Society of London. Series A, Mathematical and Physical Sciences*, 414(1847):333–358, 1987.

[112] T. J. Quinn. The beam balance as an instrument for very precise weighing. *MeasSciTech*, 3:141–159, 1992.

[113] Thaler Corporation. ADC180 Programmable Integrating A/D Converter, 2000. ADC180DS REV H MAR 00.

[114] EM Electronics Ltd. DC Amplifier A22. https://www.emelectronics.co.uk/low-level-dc-voltage-amplifier-modules/em-dc-amplifier-model-a22/, 2020. Retrieved December 2023.

[115] C. A. Hamilton. Josephson voltage standards. *Review of Scientific Instruments*, 71(10):3611–3623, 2000.

[116] TE Connectivity Ltd. High Precision Metal Film Leaded Resistor (UPF series). https://www.te.com/usa-en/product-2176163-2.html, 2022. 1773299-1 Rev. C.

[117] Tinsley Instrumentation Ltd. Standard Reference Resistor Model 5685 and 5695. http://tinsley.co.uk/wp/?page_id=2610, 2018. Version 20180820.

[118] Advanced Magnets. Typical Physical and Chemical Properties of some Magnetic Materials. https://www.advancedmagnets.com/custom-magnets/, 2022. Retrieved July 2024.

[119] D Crossley, J Hinderer, and U Riccardi. The Measurement of Surface Gravity. *Reports on Progress in Physics*, 76(4):046101, mar 2013.

[120] A Picard, R S Davis, M Gläser, and K Fujii. Revised formula for the density of moist air (CIPM-2007). *Metrologia*, 45(2):149, Feb 2008.